UNIVERSITY OF CALIFORNIA SAN DIEGO

Measurements of angle-resolved polarized light scattering by seawater as a tool to characterize natural assemblages of marine particles

A dissertation submitted in partial satisfaction of the
requirements for the degree Doctor of Philosophy

in

Oceanography

by

Daniel Warren Koestner

Committee in charge:

Dariusz Stramski, Chair
Lihini Aluwihare
Farooq Azam
Amato Evan
Alexander Groisman
Rick Reynolds

2019

The dissertation of Daniel Warren Koestner is approved, and it is acceptable in quality and form for publication on microfilm and electronically:

_____

_____

_____

_____

_____

_____

_____

_____

Chair

University of California San Diego

2019

DEDICATION

To all who do not yet believe in their ability to triumph over misfortune and follow their heart wherever it takes them!

EPIGRAPH

Ah, but a man's reach should exceed his grasp, Or what's a heaven for?

Robert Browning

TABLE OF CONTENTS

LIST OF FIGURES

LIST OF TABLES

ACKNOWLEDGEMENTS

I have so much gratitude for the many people and institutions which have supported my growth as a person, and as a scientist. Firstly, I am thankful to the committee members; Dariusz Stramski, Lihini Aluwihare, Farooq Azam, Amato Evan, Alexander Groisman, and Rick Reynolds. Their support has been essential to my success as a graduate student.

Dariusz Stramski has been a key scientific mentor in my life, without whom this work would have never come to fruition. I am so grateful for his unwavering faith and guidance over the course of my doctoral studies. Dariusz is not only a diligent and profoundly meticulous scientist, but also a kind and caring man; his thorough scientific practice and grounded idealism is without parallel and has left a distinct mark on my own idea of what it means to do good science. I appreciate his acceptance and his willingness to listen and guide. Working with Dariusz has been a privilege, and I hope I can continue growing into a scientist who meets his standards.

Several researchers have come and gone over the course of my years at the Ocean Optics Research Lab at SIO, only one of whom remained a near constant in the lab. Rick Reynolds has been as much a mentor to me as Dariusz has been, though in some different ways. Rick taught me about the practical aspects of scientific research at a university, from performing experiments to navigating the bureaucracy and finding balance at work. In addition to Rick, I have been lucky to work with many other scientists cultivating their practice in the Ocean Optics Research Lab. In particular, I am grateful to Linhai Li for our countless discussions about science, life, and Matlab. My figures would certainly not be the same without you, Linhai!

The support I received from my fellow cohort members in our first year was monumental. Whether it was in the classroom, preparing for departmental exams, or unwinding between it all,

I owe my successful start here at SIO to many including Chris Verlinden, Mike Bianco, Travis Schramek, and Ryan Guillemette.

I am also grateful to many people who I have gotten to know outside of SIO. In particular, I do not think I would have seen my doctoral work through without the support of Ramel "Real J" Wallace and the creative community which seems to orbit around him. Over the course of my PhD, Ramel has become one of my closest friends, and our shared creative endeavors have shaped me into a more well-rounded, community-centered, and expressive person.

Another person to whom I am grateful is my mentor in life, Randy Hampton. Randy has been a steadfast support in my times of need, and has relentlessly guided me in my pursuit of a life lived in line with my deepest principles. His gentle nudges which encouraged me to start jogging regularly, among other things, have forever changed me physically, mentally, emotionally, and spiritually.

I would also like to acknowledge Andrew Scott, a dear friend and confidant, whose mindfulness practice and friendship have contributed greatly to my recent successes. I am grateful to have shared such meaningful experiences with Andrew, and am looking forward to sharing many more.

My partner, Shea Cheatham, played an instrumental role as a loving presence, editor, listener, and friend. I feel so fortunate to have met Shea during my most trying and most successful year of graduate life. She has contributed to my work in so many direct and indirect ways. Countless paragraphs in this document were clarified and refined as a result of her dedicated efforts. Complex concepts were better fleshed out by her sharp and inquisitive mind, stressful moments dissolved with her love, and creative expressions fueled by her being. I cannot express in words how grateful I am to share my life with Shea and our cats, Juniper and Lani, though I

hope I can demonstrate my gratitude in each moment we share. Me, this document, and the world are better with you as a part of them.

I want to thank my parents for their support and encouragement throughout my life to pursue my interests, whether academic or extracurricular. I feel very fortunate to have a family which has supported and enabled my success before and during graduate school in so many ways. Special thanks to my father, Kevin Koestner, for his excitement about science and learning, and the encouragement he gave me to excel academically. I will never forget learning about multiplication and the notion of infinity from my dad at home long before the public school system catered to my interest in mathematics. I would also like to thank my mother, Marsha Tepper, for her unfailing support and willingness to listen under any and all circumstances. She never failed to believe in my potential, and I always knew that I was accepted and loved by her. Lastly, I would like to thank my stepdad Roy Post, for encouraging us to travel, and for planning trips which allowed for me to experience truly remarkable places on Earth. My passion for environmental science is without a doubt a product of our many trips, and was deeply inspired by Roy and my mother's fascination with the natural world.

Finally, to the broader communities which have carried me through life; I thank you with all my heart!

Chapter 1, in full, has been published in the Outstanding Topics in Ocean Optics special issue of Applied Sciences. The dissertation author was the primary investigator and author of the paper: Koestner, D., D. Stramski, and R. A. Reynolds. 2018. Measurements of the volume scattering function and the degree of linear polarization of light scattered by contrasting natural assemblages of marine particles. Appl. Sci. **8**: 2690, doi:10.3390/app8122690.

Chapter 2, in full, has been accepted for publication at Limnology and Oceanography. The dissertation author was the primary investigator and author of the paper: Koestner, D., D. Stramski, and R. A. Reynolds. 2019. Assessing the effects of particle size and composition on light scattering through measurements of size-fractionated seawater samples. Limnol. Oceanogr. *In press*.

Chapter 3 material is currently being prepared to be submitted for publication with authors Koestner, D., D. Stramski, and R. A. Reynolds. The dissertation author will be the primary investigator and author of this paper.

VITA

2012 Bachelor of Science (Environmental Engineering), Rensselaer Polytechnic Institute

2015 Master of Science (Oceanography), University of California San Diego

2019 Doctor of Philosophy (Oceanography), University of California San Diego

PUBLICATIONS

Koestner, D., D. Stramski, and R. A. Reynolds. 2018. Measurements of the volume scattering function and the degree of linear polarization of light scattered by contrasting natural assemblages of marine particles. Appl. Sci. **8**: 2690, doi:10.3390/app8122690.

Koestner, D., D. Stramski, and R. A. Reynolds. 2019. Assessing the effects of particle size and composition on light scattering through measurements of size-fractionated seawater samples. Limnol. Oceanogr. *In press*.

ABSTRACT OF THE DISSERTATION

Measurements of angle-resolved polarized light scattering by seawater as a tool to characterize natural assemblages of marine particles

by

Daniel Warren Koestner

Doctor of Philosophy in Oceanography

University of California San Diego, 2019

Dariusz Stramski, Chair

The light scattering properties of seawater play important roles in oceanic radiative transfer and optically-based methods for characterizing marine suspended particles from in situ and remote sensing measurements. In order to realize the full gamut of potential applications associated with light scattering in the ocean, advancements in the fundamental understanding of the effects of particle size and compositional characteristics on variability in scattering across various marine environments must be made.

The recently commercialized LISST-VSF instrument measures the volume scattering function, $\beta_p(\psi)$, the degree of linear polarization, $DoLP_p(\psi)$, and scattering matrix element $p_{22}(\psi)$ associated with particle scattering at a single light wavelength (532 nm) with high angular resolution over the range ~0.1° to 155°. This thesis presents the first independent and thorough evaluation of LISST-VSF performance, including the development of necessary corrections for improved results and validation of such corrections using measurements and Mie scattering calculations for polystyrene bead suspensions.

Seventeen seawater samples representing contrasting natural assemblages of particles from coastal environments near San Diego, California have been comprehensively characterized with laboratory measurements of angle-resolved polarized light scattering, particle size distribution (PSD), and particle composition in terms of various metrics derived from mass concentration and particulate absorption. Measurements of angle-resolved light scattering and PSD were made on original (unfiltered) seawater samples and particle size-fractionated samples obtained using 5 μm and 20 μm mesh filters.

Although the effects of particle size and composition are complex, small particles (< 5 μm in size) consistently produced a major or dominant contribution (~50–80%) to the particulate backscattering coefficient, b_{bp}, in both phytoplankton and non-algal dominated organic samples regardless of significant variations in PSD. The notable exception was a sample dominated by large-celled diatoms from microphytoplankton size range, which exemplifies a scenario when large particles (> 20 μm) can produce a considerable contribution (~40%) to b_{bp}. Samples dominated by inorganic material, by contrast, consistently exhibited weaker contributions (~30−40%) of small particles to b_{bp}. The maximum value of $DoLP_p(\psi)$, $DoLP_{p,max}$, was found to be weakly dependent on particle composition, but exhibited negative correlation with the

proportion of relatively large sized particles in samples. The scattering matrix element $p_{22}(\psi)$ exhibited similiar trends as $DoLP_{p,max}$ for ψ = 100º. In contrast, $p_{22}(20°)$ was relatively unaffected by the presence of large sized particles but showed negative correlation with inorganic content of particulate assemblages. Finally, simple optically-based proxies for the estimation of particle size and compositional parameters which rely on polarized light scattering measurements at only one or two angles were developed.

Introduction

For most of the Earth, the availability of radiant energy including visible light—the "birth" of photons— originates with the Sun. Nearly all life on this planet is deeply reliant on the solar emission of radiant energy, and its role in the history and sustenance of life on Earth is difficult to exaggerate. The absorption of visible light—or, the "death" of a photon— often involves the transformation of its energy into other forms, such as heat or the chemical energy used for primary production. The scattering of light is then most aptly described as the process of life for a photon. It describes the redirection and propagation of photons which maintain their original properties (in the case of elastic scattering) until their conversion into some other form of energy. While absorption dictates which colors, or more generally wavelengths (or frequencies) of radiation, are removed from its spectrum, it is the scattered light which is eventually observed. For example, the familiar light blue color of the sky can be predominantly explained as a function of the enhanced scattering of the wavelengths which compose the color blue relative to those which are green or red by molecules in the air; the perceived blue of the ocean is similar in nature, although in addition to this molecular scattering, there is strong absorption of green and red wavelengths by water molecules as well as the absorption and scattering effects of other seawater constituents that can further affect the ocean color. Blue and red light are predominantly absorbed in the case of photosynthetic activity in both terrestrial and aquatic organisms, leaving predominantly green light to be scattered and observed.

The conception of mathematical solutions to describe the propagation of electromagnetic radiation, including visible light (Maxwell 1865), heralded breakthroughs across fields ranging from astronomy to oceanography. In oceanography, optical assessment of marine environments has been achieved through technological advancements along with support from advancements in

theoretical understanding of hydrologic optics (Preisendorfer 1976). The field of ocean optics has quickly become vital in the study of ocean biogeochemistry as a result of improved abilities to make observations at unsurpassed temporal and spatial scales (Yentsch and Yentsch 1984). More specifically, and as it pertains to this thesis, the inherent light scattering properties of natural waters are of crucial importance in ocean optics, with potentially broad applications in oceanography. These properties are essential inputs to the radiative transfer models used to compute the ambient light fields in natural water bodies (Gordon et al. 1974; Kattawar and Adams 1989; Mobley 1994; Mobley et al. 2002; Li et al. 2014; Mobley et al. 2015). Furthermore, measurements of the inherent light scattering by seawater enable sophisticated characterization of marine particles.

The variability in the light scattering properties of seawater is primarily driven by the concentration of suspended particles, particle size distribution, and composition through particle refractive index, internal structure, and shape. For this reason, scattering measurements carry potentially useful information about the characteristics of natural particle assemblages. For example, the particulate scattering and backscattering coefficients have been examined as proxies for estimating the mass concentrations of suspended particulate matter SPM (Babin et al. 2003; Neukermans et al. 2016), particulate inorganic carbon PIC (Balch et al. 1999; 2001), particulate organic carbon POC (Stramski et al. 1999; 2008), and chlorophyll-*a* Chla (Huot et al. 2008; Barbieux et al. 2018) in ocean waters. Multi-angle light scattering measurements provide a means to estimate the particle size distribution (Bale and Morris 1987; Agrawal et al. 2008; Reynolds et al. 2010), including in the submicrometer size range (Wyatt and Villalpando 1997; Uitz et al. 2010). Spectral properties of particulate backscattering have also been demonstrated to potentially provide a means for the estimation of particle size information (Kostadinov et al. 2009; Slade and Boss 2015). The angular pattern of light scattering can also contain useful information about the

composition of particulate assemblages, including the bulk refractive index of particles (Morel 1973; Ackleson and Spinrad 1988; Twardowski et al. 2001; Boss et al. 2004; Sullivan et al. 2005; Zhang et al. 2013). Furthermore, measurements of the scattering matrix which provide information about the polarization effects of light scattering (Morel 1973; Bohren and Huffman 1983; Bickel and Bailey 1985; Jonasz and Fournier 2007) may aid in the identification and differentiation between different types of particles, such as phytoplankton species or minerals, which are present in complex natural assemblages (Fry and Voss 1985; Quinby-Hunt et al. 1989; Wyatt and Jackson 1989; Volten et al. 1998; Svensen et al. 2011; Muñoz et al. 2012).

Most obviously from the time of the launch of the first ocean color observing satellite (Coastal Zone Color Scanner CZCS; 1978), applications of optical information in ocean biogeochemistry have in some ways eclipsed fundamental knowledge of the manner in which natural assemblages of marine particles interact with visible light. From a very fundamental perspective, it is still unclear which particle sizes may contribute most significantly to backscattering in the ocean, which is essentially the observed signal in many optical applications including ocean color remote sensing. Modeling studies suggest that this signal can be dominated by small sized-particles (< 2 μm in diameter) in typical open ocean conditions (Stramski and Kiefer 1991), however many oversimplifying assumptions about particle size distribution, shape, and composition may underestimate the role of larger sized-particles (Kitchen and Zaneveld 1992; Organelli et al. 2018). Many studies exist which examine the inherent light scattering properties of individual phytoplankton, bacteria, and mineral particles using measurements (Stramski and Kiefer 1991; Stramski and Reynolds 1993; Stramski and Mobley 1997; Stramski et al. 2001; Stramski et al. 2007; Muñoz et al 2012); however the complexity and variability of natural particulate assemblages impose significant challenges for an understanding of bulk light scattering

properties of seawater in terms of detailed particle size and compositional characteristics (Babin et al. 2003; Stramski et al. 2004). This complexity is, for example, reflected in significant variations in the relationships between light scattering properties and measures of phytoplankton and particle concentrations (Huot et al. 2008; Woźniak et al. 2010; Neukermans et al. 2012) and the lack of robust relationship between the spectral slope of backscattering and particle size across different water types (Reynolds et al. 2016). In order to realize the full gamut of potential applications associated with light scattering in the ocean, advancements in the fundamental understanding of the effects of particle size and compositional characteristics on variability in scattering across various marine environments must be made.

Both polarized and unpolarized angular light scattering are foremostly a function of particle size, shape, and composition including internal structure. Additionally, both vary depending on scattering angle from the incident photon direction, ψ, and light wavelength in vacuum, λ. However, particle scattering of polarized light is far more complex, given its dependence on the incident polarization state of light. This interaction is described using a 4 x 4 scattering matrix, or Mueller matrix, which represents how a particle, or ensemble of particles, linearly transforms the 4-component incident Stokes vector into a 4-component scattered Stokes vector (Bohren and Huffman 1983). The current study focuses primarily on three of these matrix elements: $p_{11}(\psi,\lambda)$, $p_{12}(\psi,\lambda)$ and $p_{22}(\psi,\lambda)$.

One of the most fundamental inherent optical properties (IOPs) of seawater is the spectral volume scattering function, $\beta(\psi,\lambda)$ [m^{-1} sr^{-1}], which describes the scattered intensity at light wavelength as a function of scattering angle per unit incident irradiance per unit volume of water (Mobley 1994). The first scattering matrix element, $p_{11}(\psi,\lambda)$, is proportional to $\beta(\psi,\lambda)$ and carries no information about the polarization state of scattered light (Bohren and Huffman 1983).

Integrating $\beta(\psi,\lambda)$ over all scattering directions gives the spectral scattering coefficient, $b(\lambda)$ [m^{-1}]. In this integration, it is commonly assumed that light scattering by an assemblage of randomly-oriented scatterers (molecules and particles) in natural waters is azimuthally symmetric about the direction of incident light beam. Similarly, integration within the range of backward scattering angles yields the spectral backscattering coefficient, $b_b(\lambda)$ [m^{-1}]. It is common to include a subscript p in the notation of these inherent scattering properties (and other IOPs) to denote the contribution specifically by particles in suspension, with the contribution of molecular water (subscript w) removed, e.g., $\beta_p(\psi,\lambda) = \beta(\psi,\lambda) - \beta_w(\psi,\lambda)$.

The degree of linear polarization of light scattered by particles, $DoLP_p(\psi,\lambda)$, describes the proportion of linearly polarized light relative to total intensity of the scattered light beam. This quantity can be derived from $p_{11}(\psi,\lambda)$ and $p_{12}(\psi,\lambda)$, which require measurements involving linear polarization (Volten et al. 1998; Hovenier et al. 2002; Kokhanovsky 2003). The $p_{22}(\psi,\lambda)$ element also describes how linearly polarized light is transformed and has the unique property of being equal to $p_{11}(\psi,\lambda)$ for a collection of optically inactive homogeneous spheres (Hovenier et al. 1985). Few studies exist which examine both $DoLP_p(\psi,\lambda)$ and $p_{22}(\psi,\lambda)$ using measurements on natural seawater samples (Beardsley 1968; Kadyshevich 1977; Voss and Fry 1984). However, the role of different particle types in the variability of $DoLP_p(\psi,\lambda)$ and $p_{22}(\psi,\lambda)$ is unclear, as particle assemblages were not characterized beyond location of sampling in these studies.

Despite the relative importance of the angle-resolved polarized light scattering properties of seawater, the ocean optics community has historically relied on simplified theoretical models (such as Mie scattering theory for homogenous spheres) and a limited dataset of measurements developed using custom-built light scattering instruments. For example, over the past several decades, a limited dataset of $\beta_p(\psi,\lambda)$ measurements made by Petzold (1973) has been widely used

as a standard input for the particulate scattering phase function for radiative transfer modeling in the ocean. More recently, several light scattering sensors have been developed for in situ deployments and laboratory use (Lee and Lewis 2003; Sullivan and Twardowski 2009; Tan et al. 2013; Chami et al. 2014), though none have yet been made commercially available. The majority of studies which have comprehensively measured angle-resolved polarized light scattering by natural marine particle assemblages are well over three decades old. Given the technological advancements of today, a reevaluation of angle-resolved polarized light scattering by marine particles using measurements along with comprehensive characterization of particles in terms of particle size distribution and composition is warranted. Recently, a new light scattering instrument, the LISST-VSF (Sequoia Scientific, Inc., Bellevue, WA, USA), has become commercially available. This instrument is capable of determining $\beta_p(\psi,\lambda)$, $DoLP_p(\psi,\lambda)$ and $p_{22}(\psi,\lambda)$ at a single light wavelength (λ = 532 nm) with high angular resolution over the range ~0.1° to 155° (Slade et al. 2013), and is capable of both in situ and benchtop measurements on water samples. This commercial instrument is expected to enable routine measurements by a variety of investigators, and thus has the potential to improve understanding of light scattering properties of seawater and marine particles, advancing many related applications by proxy. Note that λ is hereafter omitted from notation for brevity.

This thesis is separated into three chapters and is based mainly upon seventeen laboratory experiments using measurements with the LISST-VSF on seawater samples representing contrasting natural assemblages of particles from coastal environments near San Diego, California, including near-shore samples dominated by organic particulate matter with predominant role of small-celled or large-celled phytoplankton, estuarine samples dominated by inorganic particles, and offshore samples representative of phytoplankton-dominated subsurface chlorophyll-a

maximum and near-surface water dominated by organic non-algal particles. The first chapter titled "Measurements of the volume scattering function and the degree of linear polarization of light scattered by contrasting natural assemblages of marine particles" focuses on presenting results of $\beta_p(\psi)$ and $DoLP_p(\psi)$ for natural seawater samples which have been characterized in terms of particle size distribution and composition. Additionally, it is acknowledged here that the LISST-VSF is a new commercially available instrument and great effort is spent evaluating the instrument, developing necessary corrections, and validating corrected results using suspensions of National Institute of Standards and Technology (NIST) certified standard polystyrene beads ranging in diameter between 100 nm and 2 μm. The second chapter titled "Assessing the effects of particle size and composition on light scattering through measurements of size-fractionated seawater samples" seeks to investigate the role of particle size and composition in $\beta_p(\psi)$ by collecting measurements on eight highly contrasting seawater samples before and after particle size-fractionation with 5 μm and 20 μm mesh filters. This study focuses primarily on the development of particle size-based budgets for $\beta_p(\psi)$, b_p, and b_{bp} with the ultimate goal of describing the characteristics of particulate assemblage responsible for various scenarios of the particle size-based budgets. The third chapter titled "Development of an approach based on polarized light scattering measurements of seawater for characterizing size and composition of marine particles" utilizes the rich dataset acquired throughout sixteen of the experiments involving particle size-fractionation and comprehensive particle characterization. Here, the focus on angle-resolved polarized light scattering by marine particles is twofold. Firstly, the scattering measurements of $DoLP_p(\psi)$and $p_{22}(\psi)$ on well-characterized seawater samples are described for the purpose of interpretation in terms of particle size distribution and composition. Finally, the thesis culminates

with the development of simple optical relationships which characterize marine assemblages as functions of polarized light scattering measurements at one or several angles.

References

Ackleson, S. G. and R. W. Spinrad. 1988. Size and refractive index of individual marine particulates: a flow cytometric approach. Appl. Opt. **27**: 1270–1277.

Agrawal, Y. C., A. Whitmire, O. A. Mikkelsen, and H. C. Pottsmith. 2008. Light scattering by random shaped particles and consequences on measuring suspended sediments by Laser Diffraction. J. Geophys. Res. **113**: C04023.

Balch, W. M., D. Drapeau, J. Fritz, B. Bowler, and J. Nolan. 2001. Optical backscattering in the Arabian Sea: Continuous underway measurements of particulate inorganic and organic carbon, Deep Sea Res. Part I **48**: 2423–2452.

Balch, W. M., D. T. Drapeau, T. L. Cucci, R. D. Vaillancourt, K. A. Kilpatrick, and J. J. Fritz. 1999. Optical backscattering by calcifying algae: Separating the contribution by particulate inorganic and organic carbon fractions, J. Geophys. Res. **104**: 1541–1558.

Bale, A. J. and A. W. Morris. 1987. In situ measurement of particle size in estuarine waters. Estuar. Coast. Shelf Sci. **24**: 253–263.

Beardsley, G. F. Jr. 1968. Mueller Scattering Matrix of Sea Water. J. Opt. Soc. Am. **58**: 52.

Bickel, W. S. and W. M. Bailey. 1985. Stokes vectors, Mueller matrices, and polarized scattered light. Am. J. Phys. **53**: 468–478.

Bohren, C. F. and D. R. Huffman. 1983. Absorption and Scattering of Light by Small Particles; Wiley: New York, NY, USA.

Boss, E., W. S. Pegau, M. Lee, M. Twardowski, E. Shybanov, G. Korotaev, and F. Baratange. 2004. Particulate backscattering ratio at LEO 15 and its use to study particle composition and distribution. J. Geophys. Res. **109**: C01014,

Chami, M., A. Thirouard, and T. Harmel. 2014. POLVSM (Polarized Volume Scattering Meter) instrument: an innovative device to measure the directional and polarized scattering properties of hydrosols. Opt. Express **22**: 26403–26428.

Fry, E. S. and K. J. Voss. 1985. Measurement of the Mueller matrix for phytoplankton. Limnol. Oceanogr. **30**: 1322–1326.

Hovenier, J. W., H. C. van de Hulst, and C. V. M. van der Mee. 1985. Conditions for the elements of the scattering matrix. Astron. Astrophys. **157**: 301–310.

Hovenier, J. W., H. Volten, O. Muñoz, W. J. Van der Zande, and L. B. F. M. Waters. 2002. Laboratory studies of scattering matrices for randomly oriented particles: Potentials, problems, and perspectives. J. Quant. Spectrosc. Radiat. Transf. **79**: 741–755.

Huot, Y., A. Morel, M. S. Twardowski, D. Stramski, and R. A. Reynolds. 2008. Particle optical scattering along a chlorophyll gradient in the upper layer of the eastern South Pacific Ocean. Biogeosciences **5**: 495–507.

Jonasz, M. and G. Fournier. 2007. Light scattering by particles in water: Theoretical and experimental foundations. Elsevier.

Kadyshevich, Y. A. 1977. Light-Scattering Matrices of Inshore Waters of the Baltic Sea. Izv. Acad. Sci. USSR Atmos. Oceanic Phys. **13**: 77.

Kitchen, J. C. and J. R. V. Zaneveld. 1992. A three-layered sphere model of the optical properties of phytoplankton. Limnol. Oceanogr. **37**: 1680–1690.

Kokhanovsky, A. A. 2003. Parameterization of the Mueller matrix of oceanic waters. J. Geophys. Res. **108**: 3175, doi:10.1029/2001JC001222.

Kostadinov, T. S., D. A. Siegel, and S. Maritorena, 2009. Retrieval of the particle size distribution from satellite ocean color observations. J. Geophys. Res. **114**: 1–22.

Lee, M., and M. Lewis. 2003. A new method for the measurement of the optical volume scattering function in the upper ocean. J. Atmos. Ocean. Technol. **20**: 563–572.

Li, L., D. Stramski, and R. A. Reynolds. 2014. Characterization of the solar light field within the ocean mesopelagic zone based on radiative transfer simulations. Deep Sea Res. I. **87**: 53–69, doi:10.1016/j.dsr.2014.02.005.

Maxwell, J. C. 1865. A dynamical theory of the electromagnetic field. Philosophical Transactions of the Royal Society of London. **155**: 459–512.

Mobley, C. D. 1994. Light and water: Radiative transfer in natural waters. Academic Press.

Mobley, C. D., F. Chai, P. Xiu, and L. K. Sundman. 2015. Impact of improved light calculations on predicted phytoplankton growth and heating in an idealized upwelling-downwelling channel geometry, J. Geophys. Res. Oceans **120**: 875–892, doi:10.1002/2014JC010588.

Mobley, C. D., L. K. Sundman, and E. Boss. 2002. Phase function effects on oceanic light fields. Appl. Opt. **41**: 1035–1050.

Morel, A. Diffusion de la lumière par les eaux de mer: Resultats expérimentaux et approche théorique. In *Optics of the Sea*; North Atlantic Treaty Organization AGARD Lecture

Series, No. 61; Technical Editing and Reproduction Ltd, London, England, 1973; pp. 3.1.1–3.1.76.

Muñoz, O., F. Moreno, D. Guirado, D. D. Dabrowska, H. Volten, and J. W. Hovenier. 2012. The Amsterdam–Granada light scattering database. J. Quant. Spectrosc. Radiat. Transf. **113**: 565–574.

Neukermans, G., H. Loisel, X. Meriaux, R. Astoreca, and D. McKee. 2012. In situ variability of mass-specific beam attenuation and backscattering of marine particles with respect to particle size, density, and composition. Limnol. Oceanogr. **57**: 124–144.

Organelli, E., G. Dall'Olmo, R. J. W. Brewin, G. A. Tarran, E. Boss, and A. Bricaud. 2018. The open-ocean missing backscattering is in the structural complexity of particles. Nat. Commun. **9**: 5439, doi:10.1038/s41467-018-07814-6.

Petzold, T.J. 1972. *Volume Scattering Functions for Selected Ocean Waters*. SIO Ref. 72–78, Scripps Institution of Oceanography Visibility Lab: University of California, San Diego, CA, USA.

Preisendorfer, R.W., 1976. Hydrologic optics.

Quinby-Hunt, M. S., A. J. Hunt, K. Lofftus, and D. Shapiro. 1989. Polarized-light scattering studies of marine Chlorella. Limnol. Oceanogr. **34:** 1587–1600.

Reynolds, R. A., D. Stramski, V. M. Wright, and S. B. Woźniak. 2010. Measurements and characterization of particle size distributions in coastal waters. J. Geophys. Res. **115**: C08024.

Slade, W. H., Y. C. Agrawal, and O. A. Mikkelsen. 2013. Comparison of measured and theoretical scattering and polarization properties of narrow size range irregular sediment particles. In *Oceans San Diego*; IEEE: San Diego, CA, USA, 2013; pp. 1–6.

Slade, W. H. and E. Boss. 2015. Spectral attenuation and backscattering as indicators of average particle size. Appl. Opt. **54**: 7264–7277.

Stramski, D., M. Babin, and S. B. Wozniak. 2007. Variations in the optical properties of terrigenous mineral-rich particulate matter suspended in seawater. Limnol. Oceanogr. **52**: 2418–2433.

Stramski, D., and C. D. Mobley. 1997. Effects of microbial particles on oceanic optics: A database of single-particle optical properties. Limnol. Oceanogr. **42**: 538–549.

Stramski, D., and R. A. Reynolds. 1993. Diel variations in the optical properties of a marine diatom. Limnol. Oceanogr. **38**: 1347–1364.

Stramski, D., S. B. Wozniak, and P. J. Flatau. 2004. Optical properties of Asian mineral dust suspended in seawater. Limnol. Oceanogr. **49**: 749–755.

Stramski, D., A. Bricaud, and A. Morel. 2001. Modeling the inherent optical properties of the ocean based on the detailed composition of planktonic community. Appl. Opt. **40**: 2929–2945.

Stramski, D. and D. A. Kiefer. 1991. Light scattering by microorganisms in the open ocean. Prog. Oceanogr. **28**: 343–383.

Stramski, D., E. S. Boss, D. J. Bogucki, and K. J. Voss. 2004. The role of seawater constituents in light backscattering in the ocean. Prog. Oceanogr. **61**: 27–56.

Stramski, D., R. A. Reynolds, M. Babin, S. Kaczmarek, M. R. Lewis, R. Röttgers, A. Sciandra, M. Stramska, M. S. Twardowski, B. A. Franz, and H. Claustre. 2008. Relationships between the surface concentration of particulate organic carbon and optical properties in the eastern South Pacific and eastern Atlantic Oceans. Biogeosciences **5**: 171–201.

Stramski, D., R. A. Reynolds, M. Kahru, and B. G. Mitchell. 1999. Estimation of particulate organic carbon in the ocean from satellite remote sensing. Science **285**: 239–242.

Sullivan, J. M., and M. S. Twardowski. 2009. Angular shape of the oceanic particulate volume scattering function in the backward direction. Appl. Opt. **48**: 6811–6819.

Sullivan, J. M., M. S. Twardowski, P. L. Donaghay, and S. A. Freeman. 2005. Use of optical scattering to discriminate particle types in coastal waters. Appl. Opt. **44**: 1667–1680.

Svensen, Ø., J. J. Stamnes, M. Kildemo, L. M. S. Aas, S. R. Erga, and Ø Frette. 2011. Mueller matrix measurements of algae with different shape and size distributions. Appl. Opt. **50**: 5149–5157.

Tan, H., R. Doerffer, T. Oishi, and A. Tanaka. 2013. A new approach to measure the volume scattering function. Opt. Express **21**: 18697–18711.

Twardowski, M. S., E. Boss, J. B. Macdonald, W. S. Pegau, A. H. Barnard, and J. R. V. Zaneveld. 2001. A model for estimating bulk refractive index from the optical backscattering ratio and the implications for understanding particle composition in case I and case II waters. J. Geophys. Res. **106**: 14129–14142.

Uitz, J., D. Stramski, A. C. Baudoux, R. A. Reynolds, V. M. Wright, J. Dubranna, and F. Azam. 2010. Variations in the optical properties of a particle suspension associated with viral infection of marine bacteria. Limnol. Oceanogr. **55**: 2317–2330.

Volten, H., J. F. De Haan, J. W. Hovenier, R. Schreurs, W. Vassen, A. G. Dekker, H. J. Hoogenboom, F. Charlton, and R. Wouts. 1998. Laboratory measurements of angular

distributions of light scattered by phytoplankton and silt. Limnol. Oceanogr. **43**: 1180–1197.

Woźniak, S. B., D. Stramski, M. Stramska, R. A. Reynolds, V. M. Wright, E. Y. Miksic, M. Cichocka, and A. M. Cieplak. 2010. Optical variability of seawater in relation to particle concentration, composition, and size distribution in the nearshore marine environment at Imperial Beach, California. J. Geophys. Res. **115**: C08027.

Wyatt, P. J., and C. Jackson. 1989. Discrimination of phytoplankton via light-scattering properties. Limnol. Oceanogr. **34**: 96–112.

Wyatt, P. J., and D. N. Villalpando. 1997. High-precision measurement of submicrometer particle size distributions. Langmuir **13**: 3913–3914.

Yentsch, C. M., and C. S. Yentsch. 1984. Emergence of optical instrumentation for measuring biological properties. Oceanogr. Mar. Biol. Ann. Rev. **22**: 55–98.

Zhang, X., Y. Huot, D. J. Gray, A. Weidemann, and W. J. Rhea. 2013. Biogeochemical origins of particles obtained from the inversion of the volume scattering function and spectral absorption in coastal waters. Biogeosciences **10**: 6029–6043.

Chapter 1

Measurements of the volume scattering function and the degree of linear polarization of light scattered by contrasting natural assemblages of marine particles

1.0. Abstract

The light scattering properties of seawater play important roles in radiative transfer in the ocean and optically-based methods for characterizing marine suspended particles from in situ and remote sensing measurements. The recently commercialized LISST-VSF instrument is capable of providing in situ or laboratory measurements of the volume scattering function, $\beta_p(\psi)$, and the degree of linear polarization, $DoLP_p(\psi)$, associated with particle scattering. These optical quantities of natural particle assemblages have not been measured routinely in past studies. To fully realize the potential of LISST-VSF measurements, we evaluated instrument performance, and developed calibration correction functions from laboratory measurements and Mie scattering calculations for standard polystyrene beads suspended in water. The correction functions were validated with independent measurements. The improved LISST-VSF protocol was applied to measurements of $\beta_p(\psi)$ and $DoLP_p(\psi)$ taken on 17 natural seawater samples from coastal and offshore marine environments characterized by contrasting assemblages of suspended particles. Both $\beta_p(\psi)$ and $DoLP_p(\psi)$ exhibited significant variations related to a broad range of composition and size distribution of particulate assemblages. For example, negative relational trends were observed between the particulate backscattering ratio derived from $\beta_p(\psi)$ and increasing proportions of organic particles or phytoplankton in the particulate assemblage. Our results also suggest a potential trend between the maximum values of $DoLP_p(\psi)$ and particle size metrics, such that a decrease in the maximum $DoLP_p(\psi)$ tends to be associated with particulate assemblages exhibiting a higher proportion of large-sized particles. Such results have the potential to advance optically-based applications that rely on an understanding of relationships between light scattering and particle properties of natural particulate assemblages.

1.1. Introduction

It has long been recognized that inherent light-scattering properties of natural waters are of crucial importance and have strong potential for wide-ranging applications in aquatic sciences, including oceanography. These properties are essential inputs to the radiative transfer models used to compute the ambient light fields in natural water bodies [1−4]. The variability in the light scattering properties of seawater is driven primarily by the concentration of suspended particles, particle size distribution, and composition through particle refractive index, internal structure, and shape. Hence, scattering measurements carry potentially useful information about characteristics of natural particle assemblages. For example, the scattering and backscattering coefficients of suspended particles have been shown to provide useful proxies of mass concentration of total suspended particulate matter (SPM), particulate inorganic carbon (PIC), and particulate organic carbon (POC) in the ocean [5−7]. Multi-angle light scattering measurements provide a means to estimate the particle size distribution [8−11], including the submicrometer size range [12−14]. The angular pattern of light scattering can also contain useful information about the composition of particulate assemblages, including the bulk refractive index of particles [15−19]. In addition, measurements of the scattering matrix that provide information about polarization effects of light scattering [15,20−23] have the potential for identifying and discriminating different types of particles, such as phytoplankton species or minerals, which are present in complex natural assemblages [24−34]. Despite the potential usefulness of information provided by light scattering measurements, the complexity and variability in composition of natural particulate assemblages impose significant challenges in achieving an understanding of bulk light-scattering properties of seawater in terms of detailed compositional characteristics of particulate matter [35].

The volume scattering function, $\beta_p(\psi, \lambda)$, and the degree of linear polarization, $DoLP_p(\psi, \lambda)$ of light scattered by marine particles are of primary interest in this study. Here, ψ denotes the scattering angle, λ the light wavelength in vacuum, and the subscript p indicates that the quantity is associated with particles. When the subscript p is omitted, the quantity describes the scattering by the entire suspension with additive contributions from both water molecules and suspended particles. The volume scattering function, $\beta(\psi, \lambda)$ [in units of m^{-1} sr^{-1}], is one of the fundamental inherent optical properties (IOPs) of seawater, which describes the scattered intensity as a function of scattering angle per unit incident irradiance per unit volume of small sample of water [2]. Several light-scattering related IOPs can be derived from $\beta(\psi, \lambda)$. For example, integrating $\beta(\psi, \lambda)$ over all scattering directions gives the total spectral scattering coefficient, $b(\lambda)$ [m^{-1}]. In this integration, it is commonly assumed that light scattering by an assemblage of randomly-oriented scatterers (molecules and particles) in natural waters is azimuthally symmetric about the incident direction of light beam. When $\beta(\psi, \lambda)$ is normalized by $b(\lambda)$, the resulting scattering phase function $\tilde{\beta}(\psi, \lambda)$ [sr^{-1}] provides a useful indicator of the angular shape of the volume scattering function. In optical remote sensing applications based on measurements with above-water sensors (e.g., from satellites or aircraft), the spectral backscattering coefficient, $b_b(\lambda)$ [m^{-1}], is particularly useful. This coefficient can be obtained by integrating $\beta(\psi, \lambda)$ over the range of backward scattering angles [2].

The volume scattering function provides incomplete information, in the sense that it does not contain information about polarization effects associated with light scattering. A complete characterization of elastic incoherent interactions of light at arbitrary wavelength λ with a sample volume of seawater is provided by a 4 × 4 scattering matrix, often referred to as the phase matrix or Mueller matrix [20−23]. This matrix describes a linear transformation of irradiance and

polarization of an incident beam described by a 4-component Stokes vector into the intensity and polarization of the scattered beam that is also described by its corresponding Stokes vector. $\beta(\psi,\lambda)$ is related to the first element of the scattering matrix, $p_{11}(\psi,\lambda)$, and can be obtained from a measurement using unpolarized light for illumination of sample and measuring the total scattered intensity. The degree of linear polarization of scattered light, $DoLP(\psi,\lambda)$, describes the proportion of linearly polarized light relative to total intensity of the scattered light beam. As described in greater detail below, for various assemblages of particles including suspended marine particles and when the incident light beam is unpolarized, this quantity can be derived from the first two elements of the scattering matrix, which requires measurements involving linear polarization [29,36,37].

Despite the relative importance of $\beta(\psi,\lambda)$ and $DoLP(\psi,\lambda)$ of seawater and the associated particulate components $\beta_p(\psi,\lambda)$ and $DoLP_p(\psi,\lambda)$, the ocean optics community has historically relied mostly on simplified theoretical models (such as Mie scattering theory for homogenous spheres) and a limited dataset of measurements made with custom-built light scattering instruments. For example, over the past several decades, a limited dataset of $\beta(\psi,\lambda)$ measurements made by Petzold [38] was widely used as a standard input for the particulate scattering phase function for radiative transfer modeling in the ocean. Comprehensive determinations of the scattering matrix for natural seawater have been very scarce [39−42]. These determinations showed that the off-diagonal matrix elements for seawater are very small or negligible, indicating very small effects associated with optical activity or orientational anisotropy of seawater scatterers [37,42]. More recently, several light scattering sensors have been developed for in situ deployments or laboratory use [43−46], but to our knowledge, none of these sensors are commercially available. While measurements with these new sensors have already significantly

contributed to the increase of available datasets of $\beta(\psi,\lambda)$ (or $\beta_p(\psi,\lambda)$ which can usually be satisfactorily estimated by subtracting the contribution associated with water molecules) in various oceanic environments [44,47,48], the determinations of $DoLP_p(\psi,\lambda)$ for natural assemblages of marine particles remain very scarce, as indicated by the rarity of scattering matrix measurements of seawater.

Recently, a new light scattering instrument, the LISST-VSF (Sequoia Scientific, Inc., Bellevue, WA, USA), has become commercially available, and provides the capability of determining both the volume scattering function and the degree of linear polarization of scattered light at a single light wavelength (532 nm) with high angular resolution over the range ~0.1° to 155° [49]. It is capable of both in situ and benchtop measurements on water samples. This commercial instrument is expected to enable routine measurements by different groups of investigators, so it has the potential to enhance our understanding of light scattering properties of seawater and marine particles and advance the related applications. In this study, we report on LISST-VSF measurements of $\beta_p(\psi)$ and $DoLP_p(\psi)$ and size and compositional characteristics for contrasting natural particulate assemblages from marine coastal and offshore environments. The particulate scattering (b_p) and backscattering (b_{bp}) coefficients have also been determined from measured $\beta_p(\psi)$.

To fully realize the potential of such quantitative determinations for seawater samples from this new instrument, we also conducted an evaluation of the LISST-VSF performance through a series of laboratory experiments using samples of National Institute of Standards and Technology (NIST) certified standard polystyrene beads ranging in diameter between 100 nm and 2 μm. These measurements were compared with theoretical simulations of light scattering by bead suspensions using Mie scattering computations. With this approach, we developed corrections to the

determinations of $\beta_p(\psi)$ and $DoLP_p(\psi)$ from LISST-VSF measurements. A validation of the corrected measurements was performed using independent measurements of multi-angle light scattering with another instrument, the DAWN-EOS (Wyatt Technology Corporation, Santa Barbara, CA, USA).

1.2. Methods

The description of methods includes two main parts: first, a description of laboratory experiments and Mie scattering calculations for standard polystyrene beads which were carried out to evaluate the performance of the LISST-VSF instrument and develop a calibration correction; second, a description of measurements on natural assemblages of marine particles from coastal and offshore oceanic environments.

1.2.1. Laboratory Experiments and Mie Scattering Calculations to Evaluate LISST-VSF

In order to evaluate the LISST-VSF instrument, light scattering and beam attenuation measurements were made in the laboratory on samples of nearly monodisperse standard polystyrene spherical beads with mean nominal diameters of 100, 200, 400, 500, 700, and 2000 nm, which were suspended in water (Table 1.1). In addition to LISST-VSF, two other instruments were used in these experiments, a DAWN-EOS for measuring multi-angle light scattering and a dual beam UV/VIS spectrophotometer Lambda 18 (Perkin-Elmer, Inc., Waltham, MA, USA) equipped with a 15-cm integrated sphere (Labsphere, Inc., North Sutton, NH, USA) for measuring the beam attenuation coefficient of particles in suspension. The use of standard beads ensures that Mie scattering calculations for homogeneous spherical particles can be used to calculate the Mueller matrix elements for these particles to determine reference (expected) values of the volume scattering function and the degree of linear polarization. The comparison of measurements with

such reference values allows for evaluation of performance of LISST-VSF instrument and formulation of calibration correction functions for improved determinations of the volume scattering function and the degree of linear polarization from this instrument. This type of approach, which combines measurements on standard well-characterized particles with accurate scattering calculations, has been previously used for the evaluation, calibration, and characterization of light scattering instruments [29,43,44,50]. Although the evaluation results presented in this study are relevant to the specific version of the LISST-VSF instrument used in our laboratory, most methodological aspects are generally applicable to evaluation of other light scattering instruments.

1.2.1.1. Instrumentation

A LISST-VSF instrument (S/N 1475) was equipped with a custom designed 2 L sample chamber for benchtop laboratory use. This chamber effectively rejects ambient light and promotes good mixing conditions to maintain particles in suspension. For sample illumination the LISST-VSF uses a frequency-doubled YAG laser to produce a beam of light at a wavelength of 532 nm with a Gaussian beam profile of 3 mm in diameter. A single measurement takes approximately 4 s and consists of two scans of a 15-cm path within the sample, each with a different linear polarization state of the incident beam, i.e., parallel and perpendicular to the scattering plane. Scattered intensity is measured at multiple scattering angles ψ from 0.09° to 15.17° with 32 logarithmically-spaced ring detectors and from 14° to 155° with 1° interval using a fixed axis Roving Eyeball sensor equipped with photomultiplier tubes (PMTs). For the Roving Eyeball, scattered light is split between two PMTs with a polarizing prism allowing for only parallel or perpendicularly polarized light to be detected by each PMT. To enable measurements of large dynamic range of scattered intensity with a single PMT, the laser power is dimmed by a factor of

8 for the angular range 14–63° and returned to full power for 64–155°. The beam attenuation coefficient, c, is also measured at light wavelength of 532 nm for the 15-cm path length of the sample.

For incoherent elastic scattering of light at a given wavelength λ by a collection of particles suspended in water, the Stokes vector of incident light beam, $S_i = [I_i\ Q_i\ U_i\ V_i]^T$, where T represents the transpose operation, is transformed into the Stokes vector of scattered beam, $S_s(\psi)$, by a scattering matrix, $P(\psi)$. For an ensemble of randomly-oriented particles exhibiting certain symmetry properties and no optical activity, the scattering matrix simplifies to 6 independent non-zero elements [20,36,51]

$$S_s(\psi) = \begin{bmatrix} I_s(\psi) \\ Q_s(\psi) \\ U_s(\psi) \\ V_s(\psi) \end{bmatrix} = P(\psi)S_i = C\begin{bmatrix} p_{11}(\psi) & p_{12}(\psi) & 0 & 0 \\ p_{12}(\psi) & p_{22}(\psi) & 0 & 0 \\ 0 & 0 & p_{33}(\psi) & p_{34}(\psi) \\ 0 & 0 & -p_{34}(\psi) & p_{44}(\psi) \end{bmatrix}\begin{bmatrix} I_i \\ Q_i \\ U_i \\ V_i \end{bmatrix}, \quad (1.1)$$

where λ has been omitted for brevity, C is a constant factor (for a given sample, light wavelength, and measurement geometry), $p_{11}(\psi)$ represents the scattering phase function, and the reference plane is the scattering plane containing the incident and scattered directions [20,51,52]. This form provides a reasonable description of the measured scattering matrix by suspensions of randomly-oriented marine particles, including various specific types of particles present in seawater [24,29,33,36,37,42]. In the case of unpolarized incident light (i.e., Q_i, U_i, and V_i are all zero), the volume scattering function $\beta(\psi)$ equals (to within a constant factor) $p_{11}(\psi)$, and the degree of linear polarization $DoLP(\psi)$ can be determined from [29,36,37,53]

$$DoLP(\psi) = \frac{-p_{12}(\psi)}{p_{11}(\psi)} = \frac{-Q_s(\psi)}{I_s(\psi)} . \quad (1.2)$$

Positive values of $DoLP(\psi)$ are for dominantly perpendicular polarization and negative values for dominantly parallel polarization. We note that this definition of $DoLP(\psi)$ has been widely used for characterizing the inherent scattering properties of various types of particles beyond aquatic particles, such as aerosol particles and cosmic dust [30,54–58].

The LISST-VSF measurements of forward scattering within the angular range 0.09–15.17° are made with two linear polarization states of the incident beam, but with no polarization analyzers of the ring detectors. For the ring detectors, the calibrated $\beta(\psi)$ in absolute units is a standard output of the manufacturer's processing software. The absolute calibration is based on the manufacturer-provided conversion from ring detector counts to physical units using radiant sensitivity of ring detectors [59,60]. Detection of scattered light within the angular range 14–155° using the Roving Eyeball sensor employs measurements made with two linear polarization states of the incident beam and the corresponding two linear polarization states of the scattered light. The four measurement configurations allow for the determination of relative values of $p_{11}(\psi)$, $p_{12}(\psi)$, and $p_{22}(\psi)$. The calibrated $\beta(\psi)$ values within the Roving Eyeball angular range are obtained by scaling the $p_{11}(\psi)$ data from the Roving Eyeball sensor. Specifically, the scattering measurements from the first angles of the Roving Eyeball sensor are forced to match the calibrated $\beta(\psi)$ values from the overlapping last ring detectors. The $DoLP(\psi)$ values are obtained from Equation (1.2) using $p_{11}(\psi)$ and $p_{12}(\psi)$, and are also included in the standard output of the manufacturer's processing code.

We also used a DAWN-EOS multi-angle light scattering instrument which provided independent measurements of $\beta(\psi)$ and $DoLP(\psi)$ of polystyrene beads suspended in water. These

measurements were made with a sample placed in a 20 mL cylindrical glass vial. The DAWN-EOS instrument used in this study has been previously characterized and calibrated for such measurement configuration [61]. This instrument uses a diode-pumped frequency-doubled Nd-YAG laser at light wavelength 532 nm with a Gaussian beam profile of 62 μm in diameter. The interrogated sample volume is on the order of 10 nL. The incident beam can be linearly polarized both parallel and perpendicular to the scattering plane. The intensity of scattered light is measured simultaneously with eighteen photodiode detectors and no polarization analyzers, enabling measurements within a range of scattering angles from 22.5° to 147°. To encompass the large dynamic range of scattered intensity, three selectable gain settings are available for each detector (gain factors of 1, 21, or 101).

As the DAWN-EOS detectors have no polarization analyzers, they only measure the first parameter of Stokes vector of the scattered light, $I_s(\psi)$. Here we define $I_{s\parallel}(\psi)$ for the parallel polarization of the incident beam and $I_{s\perp}(\psi)$ for the perpendicular polarization of the incident beam. The matrix elements $p_{11}(\psi)$ and $p_{12}(\psi)$ can be obtained (to within a constant factor) from DAWN-EOS measurements as

$$p_{11}(\psi) = \frac{I_{s\parallel}(\psi) + I_{s\perp}(\psi)}{2} \tag{1.3}$$

$$p_{12}(\psi) = \frac{I_{s\parallel}(\psi) - I_{s\perp}(\psi)}{2}, \tag{1.4}$$

which allows for determination of $DoLP(\psi)$ from Equation (2). The calibration procedure described in Babin et al. [61] allows for determination of $\beta(\psi)$ in absolute units. Importantly, the calibration procedure of DAWN-EOS is fundamentally different from the calibration procedure of LISST-VSF. The manufacturer's calibration of LISST-VSF is based on a nominal radiant sensitivity of ring detectors (amperes of photoelectric current per watt of optical power) traceable

to the National Institute of Standards and Technology [59,60]. In contrast, the calibration of DAWN-EOS is based on measurements of light scattered at 90° by pure toluene with the incident beam having a linear perpendicular polarization [61]. This calibration relies on the known magnitude of molecular scattering by toluene. The two different methods employed in calibration of LISST-VSF and DAWN-EOS allow for comparisons of independent estimates of $\beta(\psi)$ obtained by these instruments. We also recall that the $DoLP(\psi)$ estimates obtained with the two instruments within the common range of scattering angles are based on different polarization measurement configurations used by these instruments.

A Lambda 18 spectrophotometer was used to collect independent measurements of the spectral beam attenuation coefficient, $c(\lambda)$, of polystyrene beads suspended in water. These measurements were made for comparisons with the beam attenuation data obtained with LISST-VSF, and also to aid in the preparation of samples with appropriate concentrations of polystyrene beads to ensure that measurements with LISST-VSF and DAWN-EOS were made within the single scattering regime. The spectrophotometric measurements were made in the spectral range from 290nm to 860 nm with 1 nm interval, but only data at 532 nm are used in this study. The general applicability of laboratory spectrophotometers with proper modifications to enable measurements of beam attenuation of particle suspensions, including colloidal samples, has long been recognized [62,63]. In our study, a sample of particle suspension was measured in a 1-cm quartz cuvette placed at a significant distance from the detector (~25 cm from the entrance of the integrating sphere), and field stops were aligned within the light path to reduce the size of the beam and acceptance angle of the detector to less than 1°. This measurement geometry has been used in our previous studies of spectral beam attenuation by various particle assemblages [64,65].

1.2.1.2. Experimental Procedure

Baseline measurements of 0.2 μm filtered water were collected with all three instruments used in the experiments; LISST-VSF, DAWN-EOS, and Lambda 18 spectrophotometer. These baseline measurements were subtracted from subsequent measurements taken on particle suspensions to determine the optical properties associated with suspended particles only, i.e., the particulate volume scattering function, $\beta_p(\psi)$, the particulate degree of linear polarization, $DoLP_p(\psi)$, and the particulate beam attenuation coefficient, c_p.

Original manufacturer's stock samples of standard polystyrene beads (100, 200, 400, 500, 700, and 2000 nm in diameter) were used to generate master samples using 0.2 μm filtered, deionized, and degassed water as a medium (with the exception of 2000 nm beads which used 0.2 μm filtered seawater). In the process of preparation of master samples, the particle concentration was optimized to ensure that spectrophotometric measurements of beam attenuation coefficient can be performed either directly or with small dilution factor (~3) on these samples over 1-cm path length with sufficiently high signal but negligible multiple scattering effects. The c_p values for master samples ranged from about 18 m^{-1} to 58 m^{-1} (Table 1.1).

The master sample was diluted for measurements with the LISST-VSF to avoid oversaturation of PMT detectors and multiple scattering over the longer path length (15 cm). For baseline measurements, the LISST-VSF sample chamber was filled with 1900 mL of 0.2 μm filtered water. The final samples of particle suspensions were created by addition of 20 to 100 mL of master sample to the LISST-VSF chamber. For most beads examined in our experiments, more than one particle suspension differing in terms of particle concentration was measured with LISST-VSF (Table 1.1). The different particle concentrations were achieved by different dilution of master sample within LISST-VSF chamber. Owing to different dilution factors ranging from 20

to 96 (labeled as DF1, DF2, and DF3 in Table 1.1), the c_p values of LISST-VSF samples ranged from about 0.5 m^{-1} to 1.8 m^{-1}. For a single bead size, concentration, and PMT gain, a series of LISST-VSF measurements was composed of 200 measurements taken in rapid succession (recall that a measurement refers to two scans, each with a different polarization of incident beam). This measurement series was divided into five sets of 20 measurements and one set of 100 measurements to enable manual gentle mixing of sample before each set of measurements. In addition, for the 2000 nm bead suspensions a magnetic stir bar which operated on low speed and changed direction of rotation every 30 s was used to prevent particle settling during the measurement.

Several LISST-VSF baseline measurements of 0.2 μm filtered water were collected for each experiment, i.e., for each examined bead size. However, for reasons of consistency and out of the desire to use an optimal baseline representative of the least contaminated 0.2 μm filtered water, a single baseline was used for processing of all experimental data collected for various bead sizes and concentrations except for 2000 nm sized beads which used 0.2 μm filtered seawater. This baseline was determined on the basis of finding a measurement which exhibited minimal scattering signal detected by Roving Eyeball and ring detectors and maximum directly transmitted light detected by the laser transmission sensor. We note, however, that for each PMT gain setting of the Roving Eyeball sensor a separate baseline was determined.

Measurements using the DAWN-EOS instrument were collected for 100, 200, 400, and 700 nm beads. Dilution factors of master samples for DAWN-EOS measurements were between 300 and 3000, depending on bead size. The gain settings for each detector were adjusted to the highest setting that would avoid saturation of signal with incident perpendicular polarization of light. For 400 and 700 nm bead suspensions, two different dilutions were measured. For each

polarization state (i.e., perpendicular and parallel) of incident light, we acquired 1440 measurements with a sampling frequency of 8 Hz over 3 min. For a given sample, this data acquisition protocol was repeated three times. Each of these three replications was made with a different randomly-chosen orientation of sample cylindrical vial within the instrument. The sample was gently mixed between these replicate measurements. The baseline measurements of 0.2 μm filtered water were acquired using the same protocol.

As mentioned above, the optical measurements were made on sufficiently-diluted samples to ensure negligible effects of multiple scattering over a pathlength used by a given instrument. A criterion for a single scattering regime is generally defined in terms of small optical thickness of the sample, $\tau << 1$, where τ is a product of the beam attenuation coefficient, c, and pathlength, r [51,66]. Also, a simple practical test for ensuring that multiple scattering effects are negligible is to verify a direct proportionality between the measured optical signal and the concentration of particles in suspension by conducting a series of measurements on the same sample with different dilutions [51]. Our measurements on bead samples with different dilutions showed an excellent 1:1 relationship between the LISST-VSF measurement and the bead concentration over the range of beam attenuation coefficient up to at least 2 m^{-1}. The single scattering regime can also be determined by the condition $\tau (1-g) << 1$, where g is the average cosine of the scattering angle of the volume scattering function [23,66]. For the 100 nm polystyrene beads, the g value is 0.115, which yields the most restrictive condition in our study, $\tau << 1.13$. For all bead samples measured with LISST-VSF, including all bead sizes and sample dilutions, τ was always less than about 0.3. This condition was also satisfied for samples measured with a spectrophotometer. For the measurements with DAWN-EOS, the τ values were even smaller. For the natural seawater samples examined in our study (which is described below in section 1.2.2), the g values (for the total

volume scattering function including the contribution by pure seawater) were about 0.9 or somewhat higher, which yields less restrictive criterion $\tau << 10$. Our measurements of natural samples clearly satisfied this single scattering condition, as the highest value of c for the natural samples measured with LISST-VSF was about 2.6 m^{-1}, so τ was always less than about 0.45, given that the maximum pathlength for LISST-VSF is 17.5 cm for the scattering angle of 150°.

1.2.1.3. Data Processing

Processing of LISST-VSF data was done with a standard processing code provided by manufacturer (version of 2013) to determine $\beta_p(\psi)$, $DoLP_p(\psi)$, and c_p, denoted hereafter as $\beta_p^{LISST*}(\psi)$, $DoLP_p^{LISST*}(\psi)$, and c_p^{LISST*} respectively (the asterisk indicates that the variable is derived from the standard processing code without additional corrections developed in this study). Some details specific to the processing and quality control of our experimental data are provided below.

As a first step in data processing, the baseline values in raw counts were subtracted from each LISST-VSF measurement of raw counts acquired on samples of bead suspensions. To account for light attenuation along the path between the scattering volume and the detector, an attenuation correction factor was calculated using the average c_p^{LISST*} from the series of measurements and the length of the path for each scattering angle. Further, to account for the difference in sensitivity of the two Roving Eyeball PMT detectors, a factor α is used to adjust the measured counts of one PMT detector relative to the other [67]. The value of $\alpha = 0.9335$ was determined by averaging all median values of α derived from each series of measurements for each bead size, particle concentration, and PMT gain. The α parameter was observed to be nearly constant over the period of experiments (~18 months, the coefficient of variation < 5%). For each

series of measurements a specific scaling factor was determined to convert $p_{11}(\psi)$ in PMT counts to $\beta_p^{LISST*}(\psi)$ in absolute units [m^{-1} sr^{-1}] for scattering angles 14–155° measured by the Roving Eyeball sensor. First, for each measurement from a given series of measurements, a scaling factor was determined by matching the PMT counts measured with Roving Eyeball sensor between 15° and 16° with $\beta_p^{LISST*}(\psi)$ in absolute units obtained from measurements with the last two ring detectors at 13.01° and 15.17°. Then, using these determinations, the average scaling factor for a given series of measurements was calculated and used for further data processing. Note that this scaling was not needed for the determination of $DoLP_p^{LISST*}(\psi)$ for the Roving Eyeball angular range, which is calculated from $p_{11}(\psi)$ and $p_{12}(\psi)$ determined in PMT counts following Equation (1.2).

Quality control of data was performed by removing the first set of 20 measurements (the remaining four sets with 20 measurements each were retained) and the first 20 measurements from the set of 100 measurements. We observed that this was necessary to ensure reasonable stability in the measured scattering signal. The mean and standard deviation values for each angle based on all of the 160 remaining measurements in the series were determined, and the outlying single measurements within the series were identified and rejected from subsequent analysis. Typically, 120 to 130 measurements from a given series of 200 measurements passed the quality criteria.

Example data of uncorrected $\beta_p^{LISST*}(\psi)$ for 200 nm and 2000 nm bead suspensions are shown in Figure 1.1. The series of measurements that remained after quality control and the median values of $\beta_p^{LISST*}(\psi)$ derived from the series of measurements are shown. We also note that the median values were very close to mean values for our data (<1% difference for most scattering angles). The results for 2000 nm beads show a distinct pattern with several scattering maxima and minima due to constructive and destructive interference of the scattered light from a nearly

monodisperse population of beads that are large relative to the wavelength of light. The 200 nm beads are smaller than the wavelength of light leading to a more featureless shape of $\beta_p^{LISST*}(\psi)$. The variability between the individual measurements is largest at very small scattering angles, i.e., approximately <4°, where the scattering signal for submicron particles is low relative to our baseline measurements. Apart from small scattering angles, the coefficient of variation (*CV*) for each scattering angle calculated from a series of measurements on 200 nm beads is generally very small, ranging from ~3% to <1%, with the smallest values at angles greater than 64° where full laser power is used. The measurements of 2000 nm beads exhibit somewhat higher *CV*, i.e., between about 3% and 6%. The higher values of *CV* are observed mostly near the angles where minima of $\beta_p^{LISST*}(\psi)$ occur.

The DAWN-EOS measurements for four bead sizes were also used to calculate $\beta_p(\psi)$ and $DoLP_p(\psi)$, denoted as $\beta_p^{DAWN}(\psi)$ and $DoLP_p^{DAWN}(\psi)$. First, for each time series of 1440 measurements with DAWN-EOS, the highest 2% of data was rejected, as these data are assumed to result from sample contamination with rare, larger particles. Each set of measurements then consists of 1411 measurements of both $I_{s\parallel}(\psi)$ and $I_{s\perp}(\psi)$ for a specific orientation of sample vial. These measurements were averaged to represent that orientation. Such results were then averaged for three vial orientations. This protocol was applied to both the sample and baseline measurements, with the exception that baseline values were calculated by averaging the lowest 5% of data. The final $I_{s\parallel}(\psi)$ and $I_{s\perp}(\psi)$ for the beads were calculated by subtracting the average baseline from the average sample data. These particulate $I_{s\parallel}(\psi)$ and $I_{s\perp}(\psi)$ were then used to determine $p_{11}(\psi)$ and $p_{12}(\psi)$ according to Equations (1.3) and (1.4), from which $\beta_p^{DAWN}(\psi)$ [61] and $DoLP_p^{DAWN}(\psi)$ [Equation (1.2)] were determined. Note that two dilutions of the master suspension for 400 and 700 nm beads were measured with DAWN-EOS and the average of the

two was used to represent these bead sizes. As a final step, the determined $\beta_p^{DAWN}(\psi)$ values were rescaled using relevant dilution factors to obtain final results representing the particle concentration in LISST-VSF samples and enable direct comparisons with LISST-VSF measurements. Note that such rescaling is not necessary for $DoLP_p^{DAWN}(\psi)$.

With regard to processing of data acquired with a Lambda 18 spectrophotometer, the spectral data of measured optical density $OD(\lambda)$ (i.e., measurements made in the absorbance mode of the spectrophotometer) were converted (after subtraction of baseline measurement) into the particulate beam attenuation coefficient [m^{-1}] using the relationship $c_p(\lambda)$ = ln(10) $OD(\lambda)$/0.01, where ln is the natural logarithm and 0.01 is the path length in meters. The final particulate beam attenuation coefficient obtained from spectrophotometric measurements is denoted as c_p^{SPEC}. The estimates of c_p^{LISST*} from LISST-VSF measurements were calculated with the standard manufacturer's processing code. Because each LISST-VSF measurement consists of two linear polarization states of the incident beam, the average of these two is used as the final estimate of c_p^{LISST*}. As a final step, the determined c_p^{SPEC} values were multiplied by relevant dilution factors to obtain final results representing particle concentration in LISST-VSF samples and enable direct comparisons with LISST-VSF measurements.

1.2.1.4. Determination of Correction Functions

In addition to $\beta_p^{LISST*}(\psi)$, Figure 1.1 shows results for the 200 nm and 2000 nm polystyrene beads based on Mie scattering calculations (more details about these calculations are provided below). These results are significantly higher (nearly a factor of 2) than the measured values of $\beta_p^{LISST*}(\psi)$. We assume that the Mie scattering calculations for samples of spherical polystyrene beads are sufficiently accurate to provide reference values for such samples.

In order to correct for the mismatch between the measured and reference values, a calibration correction function $CF(\psi)$ is defined as

$$CF(\psi) = \frac{\beta_p^{REF}(\psi)}{\beta_p^{LISST*}(\psi)} , \quad (1.5)$$

where $\beta_p^{REF}(\psi)$ is a reference volume scattering function determined according to

$$\beta_p^{REF}(\psi) = \tilde{\beta}_p^{Mie}(\psi)\, b_p^{REF} , \quad (1.6)$$

where $\tilde{\beta}_p^{Mie}(\psi)$ is the scattering phase function [sr^{-1}] obtained from Mie scattering computations and b_p^{REF} is the reference particulate scattering coefficient [m^{-1}]. Note that all quantities in Equations (1.5) and (1.6) are for the LISST-VSF light wavelength of 532 nm.

For each examined suspension of standard polystyrene beads, $\tilde{\beta}_p^{Mie}(\psi)$ was determined from Mie scattering computations for homogeneous spherical particles. We used the Mie scattering code for homogeneous spheres of Bohren and Huffman [20], which included our modifications to account for polydispersity of the sample, i.e., to use particle size distribution as input to the code rather than just a single particle diameter as in the original code. The computations were performed assuming a relative particle size distribution (PSD) of Gaussian shape, with 300 evenly spaced size bins about the nominal mean diameter ± 3 standard deviations, as provided by the manufacturer for each bead size (Table 1.1). The use of such PSDs allows us to account for the realistic, small degree of polydispersity of each sample. The Mie computations also require input of the refractive index of particles. Based on the study of Ma et al. [68] we assumed that the complex refractive index of polystyrene relative to water at 532 nm is $m = 1.193 + 0.0003i$, where the first component is the real part and the second component is the imaginary part of refractive index. Note that the

imaginary part is very small because polystyrene is a weakly absorbing material in the examined spectral region.

Equation (1.6) also requires b_p^{REF}, which was determined from the combination of beam attenuation measurements and Mie scattering calculations as

$$b_p^{REF} = c_p^{LISST*} \frac{Q_b^{Mie}}{Q_c^{Mie}}, \quad (1.7)$$

where Q_b^{Mie} and Q_c^{Mie} are the single-particle scattering and attenuation efficiency factors, respectively, obtained from Mie computations. Because the populations of examined beads exhibit a slight degree of polydispersity, the calculated Q_b^{Mie} and Q_c^{Mie} represent the average values of efficiency factors for a given particle population [69]. Given very weak light absorption of polystyrene beads at 532 nm, the ratio $\frac{Q_b^{Mie}}{Q_c^{Mie}}$ was found to be >95%. We also note that in addition to c_p^{LISST*}, we have another potential measurement of beam attenuation coefficient from the spectrophotometer (c_p^{SPEC}). Figure 1.2 shows that the measurements of c_p^{LISST*} and c_p^{SPEC} are consistent, and generally agree very well.

By combining Equations (1.6) and (1.7), $\beta_p^{REF}(\psi)$ can be determined for each LISST-VSF measurement as

$$\beta_p^{REF}(\psi) = \tilde{\beta}_p^{Mie}(\psi)\ c_p^{LISST*} \frac{Q_b^{Mie}}{Q_c^{Mie}}. \quad (1.8)$$

Note that the estimates of $\beta_p^{REF}(\psi)$ can vary between individual measurements because of variations in c_p^{LISST*}. Finally, by combining Equations (1.5) and (1.8), $CF(\psi)$ can be determined for each LISST-VSF measurement as

$$CF(\psi) = \frac{\tilde{\beta}_p^{Mie}(\psi)\ c_p^{LISST*}\ \frac{Q_b^{Mie}}{Q_c^{Mie}}}{\beta_p^{LISST*}(\psi)}\ . \tag{1.9}$$

The application of this protocol to every individual measurement of $\beta_p^{LISST*}(\psi)$ helps to better capture the variability between individual measurements during a given series of LISST-VSF measurements on a given sample, for example due to imperfect mixing in the 2 L sample chamber or potential electronic fluctuations in the instrument.

The smaller-sized particle standards (<500 nm in diameter) appear as the best candidates for determination of $CF(\psi)$ because they produce a relatively featureless pattern of angular scattering (see the results for 200 nm beads in Figure 1.1). The measurements with larger beads (500 nm to 2000 nm) were not used in these determinations because the angular scattering pattern includes multiple maxima and minima (see the results for 2000 nm beads in Figure 1.1), which render the comparison of $\beta_p^{LISST*}(\psi)$ and $\beta_p^{REF}(\psi)$ particularly sensitive to even small uncertainties in measurements or theoretical calculations. The results obtained with beads of 100, 200, and 400 nm in diameter were considered in the determinations of final correction function $CF_f(\psi)$ within four angular ranges, as described below:

$$CF_f(\psi) = (CF_{100}(\psi) + CF_{200}(\psi) + CF_{400}(\psi))/3\ for\ \psi = 0.09\text{–}60° \tag{1.10a}$$

$$CF_f(\psi) = CF_{200}(\psi)\ \ for\ \psi = 61\text{–}128° \tag{1.10b}$$

$$CF_f(\psi) = (CF_{200}(\psi) + CF_{400}(\psi))/2\ for\ \psi = 129\text{–}150° \tag{1.10c}$$

$$CF_f(\psi) = (CF_{100}(\psi) + CF_{200}(\psi) + CF_{400}(\psi))/3\ for\ \psi = 151\text{–}155°. \tag{1.10d}$$

The $CF_{200}(\psi)$ data obtained with 200 nm beads provide the main contribution to the determination of $CF_f(\psi)$. The $CF_{100}(\psi)$ data obtained with 100 nm beads are used partially

because of increased uncertainty in the PSD of these beads (*CV* of nominal mean diameter is 7.8%, see Table 1.1). The $CF_{400}(\psi)$ data obtained with 400 nm beads are also used partially and cover the backscattering angles, where these particular data are useful for correction of an apparent artifact near 130–140°, which is rather minor but has been consistently observed with our LISST-VSF instrument for various natural particle assemblages. The calculations of $CF_{100}(\psi)$, $CF_{200}(\psi)$, and $CF_{400}(\psi)$ were made using data for particle concentrations and PMT gains which ensured sufficient signal for the ring detectors while avoiding PMT saturation of the Roving Eyeball sensor (see dilution factors in italic font in Table 1.1). For a given bead standard, the final values of correction function at different angles were determined as the median values of all the relevant determinations.

The final $CF_f(\psi)$ was smoothed in the angular range 2.56–155° with a 3-point and then a 5-point moving average. In addition, $CF_f(\psi)$ within the near-forward angular range 0.09–4.96° was set to a constant value of $CF_f(\psi_{32})$, where ψ_{32} = 15.17° corresponds to the last ring detector. The rationale for this assumption is that the scattering signal produced by the examined beads for the first 25 rings (ψ = 0.09–4.96°) is comparable to the baseline, while there is good signal relative to the baseline for the last ring detector.

The final correction simply involves the multiplication of uncorrected $\beta_p^{LISST*}(\psi)$ by the correction function $CF_f(\psi)$,

$$\beta_p^{LISST}(\psi) \;=\; \beta_p^{LISST*}(\psi)\;\; CF_f(\psi)\;\;, \qquad (1.11)$$

where $\beta_p^{LISST}(\psi)$ is the corrected LISST-VSF measurement of volume scattering function (note that the superscript * is removed from this symbol).

We also determined a correction function for $DoLP_p^{LISST*}(\psi)$,

$$BF(\psi) = DoLP_p^{LISST*}(\psi) - DoLP_p^{REF}(\psi) , \quad (1.12)$$

where $BF(\psi)$ quantifies a correction for potential bias in $DoLP_p^{LISST*}(\psi)$ obtained from the standard processing code applied to LISST-VSF measurements and $DoLP_p^{REF}(\psi)$ is a reference degree of linear polarization determined from Mie scattering calculations of the two scattering matrix elements, $p_{11}^{Mie}(\psi)$ and $p_{12}^{Mie}(\psi)$, for a given sample of standard beads. The results for $BF_{100}(\psi)$, $BF_{200}(\psi)$, $BF_{400}(\psi)$, and the final correction function $BF_f(\psi)$ were obtained using a procedure similar to that for $CF_{100}(\psi)$, $CF_{200}(\psi)$, $CF_{400}(\psi)$, and $CF_f(\psi)$. The correction of $DoLP_p^{LISST*}(\psi)$ simply requires a subtraction of $BF_f(\psi)$,

$$DoLP_p^{LISST}(\psi) = DoLP_p^{LISST*}(\psi) - BF_f(\psi) , \quad (1.13)$$

where $DoLP_p^{LISST}(\psi)$ is the corrected degree of linear polarization within the range of scattering angles from 16° to 150°. Because the $DoLP_p^{LISST*}(\psi)$ data output from standard processing of LISST-VSF measurements begins at ψ = 16°, no correction for the forward scattering angles of the ring detectors (ψ < 16°) was determined.

1.2.2. Measurements and Analysis of Natural Seawater Samples

Optical measurements with the LISST-VSF and ancillary analyses of natural particle assemblages were performed on seawater samples collected between summer 2016 and spring 2017 in contrasting marine environments, namely, in open ocean waters off the coast of Southern California, nearshore ocean waters at the pier of the Scripps Institution of Oceanography (SIO Pier) in La Jolla, and the tidal estuary of the San Diego River. Overall 17 samples representing a broad range of natural particle assemblages were analyzed. Most samples (number of samples *N* = 11) were collected at the SIO Pier. These samples were collected during typical dry weather

conditions, phytoplankton bloom events, and after heavy rain. The tidal estuary samples ($N = 3$) include three tidal states between low and high tide. The offshore samples ($N = 3$) were collected in the Santa Barbara Channel, about 8 km off San Diego Bay, and about 2 km off SIO Pier. Seawater samples were collected just beneath the sea surface using either Niskin bottles or a bucket, except for one offshore sample (off San Diego Bay) that was collected at the subsurface chlorophyll-*a* maximum at a depth of 18 m. All samples were analyzed in the laboratory within 24 h of sampling.

To characterize the concentration and composition of particulate matter for each sample, we determined the dry mass concentration of total suspended particulate matter, SPM [g m^{-3}], mass concentration of particulate organic carbon, POC [mg m^{-3}], and mass concentration of the pigment chlorophyll-*a*, Chla [mg m^{-3}]. For these determinations, the particles were collected on glass-fiber filters (GF/F Whatman) by filtration of appropriate volumes of seawater (150–2100 mL depending on the sample). SPM was determined following a gravimetric method using pre-washed and pre-weighted filters [7,70]. The determinations of POC were made on precombusted filters with a standard CHN analysis involving high temperature combustion of sample filters [7,71,72]. Chla was determined spectrophotometrically using a Lambda 18 spectrophotometer and placing 1-cm cuvettes containing acetone extracts of the samples inside the integrating sphere. The measured absorbance values at 630, 647, 665, and 691 nm (after subtraction of acetone baseline values) were used in the calculation of Chla [73]. For each seawater sample, replicate determinations of SPM and POC were made on separate sample filters. The final SPM and POC are average values of replicate determinations. The replicates for SPM and POC agreed generally to within 15% and 10%, respectively. No replicates were taken for Chla. In addition to information about particle concentration, SPM, POC, and Chla provide useful proxies of bulk composition of

particulate matter. The organic and inorganic fractions of SPM can be characterized using the ratio POC/SPM, and the contribution of phytoplankton to SPM using Chla/SPM [65]. These ratios are expressed on a [g/g] basis.

The measurements of particle size distribution (PSD) were made with a Coulter Multisizer 3 (Beckman Coulter, Brea, CA, USA) equipped with a 100 μm aperture, which allows particle counting and sizing in the range of volume-equivalent spherical diameter from 2 μm to 60 μm. Within this size range we used 300 log-spaced size bins to provide high resolution PSDs. For each experiment, 0.2 μm filtered seawater was used as a blank that was subtracted from sample measurements. Approximately 10 to 15 replicate measurements of 2 mL subsamples of each seawater sample were collected. After removing outliers, the remaining measurements were summed and divided by the total analyzed volume to produce an average density function of PSD in particle number per unit volume per width of size bin. For each sample the power function fit with a slope parameter, ζ, was determined using these PSD data over the size range 2–50 μm. In these determinations, the linear regression analysis was applied to log-transformed data, and the last size bins with very low particle counts were ignored. Although the measured PSDs often showed significant deviations from the power function fits, we use the slope parameter ζ as a particle size metric, because this is the most common parameterization of size distribution of marine particles [23,74]. Additionally, assuming spherical particles, the particle volume distributions were determined from particle number distributions for each sample. From particle volume distributions, we calculated the percentile-based particle diameters such as the median diameter, D_V^{50}, and the 90$^{\text{th}}$ percentile diameter, D_V^{90}. These parameters have been shown to provide potentially useful metrics in the analysis of relationships between the optical and particle size properties in seawater [65].

Measurements and processing of data collected with LISST-VSF for natural seawater samples were made following a protocol similar to that described above for standard polystyrene bead samples. For each experiment, baseline measurements were taken on 0.2 μm filtered seawater obtained from a given seawater sample. However, a single baseline selected from the lowest measured baselines was used for data processing of all seawater samples to ensure a consistent baseline unaffected by possible variations associated with the imperfect purity of 0.2 μm filtered seawater prepared during different experiments. To ensure scattering measurements were acquired in a single-scattering regime, samples with an average c_p over 3.0 m^{-1} were diluted using 0.2 μm filtered seawater. Dilution was necessary only for the two most turbid samples collected in the San Diego River Estuary. Between four and eight sets of 50 measurements were collected for each seawater sample with gentle hand mixing between the measurement sets, while a magnetic stir bar was on very low speed changing direction of rotation every 30 s. All results from LISST-VSF measurements for natural seawater samples shown in this paper represent the $CF_f(\psi)$-corrected volume scattering function of particles, $\beta_p^{LISST}(\psi)$, and $BF_f(\psi)$-corrected degree of linear polarization of particles, $DoLP_p^{LISST}(\psi)$. For a given sample the final values of $\beta_p^{LISST}(\psi)$ and $DoLP_p^{LISST}(\psi)$ correspond to the median values of the series of measurements that passed the quality control criteria.

To determine the particulate scattering, b_p^{LISST}, and particulate backscattering, b_{bp}^{LISST}, coefficients, the corrected measured $\beta_p^{LISST}(\psi)$ was first extrapolated in the angular range 150–180°. The extrapolated portion of $\beta_p^{LISST}(\psi)$ was obtained by fitting a specific function to the data of $\beta_p^{LISST}(\psi)$ in the angular range 90–150°. We used two methods for fitting and extrapolating $\beta_p^{LISST}(\psi)$. The first method is based on a non-linear least squares best fit of the analytical function proposed by Beardsley and Zaneveld [75]. The second method is based on a linear mixing model

that finds a non-negative least squares best fit for combined contributions of four end members representing shapes of volume scattering functions associated with scattering by small and large particles, as described in Zhang et al. [76].

A backscattering factor, κ, was determined for the fitted volume scattering function as

$$\kappa = \frac{b_{bp}^{fit}}{b_{bp,150}^{fit}}, \tag{1.14}$$

where b_{bp}^{fit} is the particulate backscattering coefficient determined by the integration of the fitted function in the angular range 90–180° and $b_{bp,150}^{fit}$ is the coefficient determined by the integration of the fitted function in the range 90–150°. The final estimate of backscattering coefficient, b_{bp}^{LISST}, was calculated as

$$b_{bp}^{LISST} = \kappa \; b_{bp,150}^{LISST}, \tag{1.15}$$

where $b_{bp,150}^{LISST}$ is obtained by the integration of $\beta_p^{LISST}(\psi)$ in the angular range 90–150°. The final estimate of scattering coefficient, b_p^{LISST}, was calculated as the sum of b_{bp}^{LISST} and the forward scattering coefficient obtained from the integration of $\beta_p^{LISST}(\psi)$ in the angular range 0.09–90°.

The calculations of b_p^{LISST} and b_{bp}^{LISST} were made for each seawater sample using the two methods for fitting and extrapolation. The particulate backscattering ratio, $\tilde{b}_{bp}^{LISST} = b_{bp}^{LISST} / b_p^{LISST}$ was also calculated. We note that the κ values for all examined seawater samples were found to range between 1.125 and 1.138 and 1.118–1.120 for the Beardsley and Zaneveld [75] and Zhang et al. [76] methods, respectively. An example illustration of fitting and extrapolation methods for one sample collected during high tide at the San Diego River estuary is depicted in Figure 1.3. As seen, both the Beardsley and Zaneveld [75] and Zhang et al. [76] fitted functions are in good

agreement with the measured data of $\beta_p^{LISST}(\psi)$ in the angular range 90–150°. However, the extrapolated portion of the Beardsley and Zaneveld [75] function in the angular range 150–180° has somewhat higher values compared with the Zhang et al. [76] function. Nevertheless, the estimates of b_{bp}^{LISST} for this sample obtained from the two extrapolation methods differ only by 0.5%. For all other seawater samples the difference was also small, not exceeding 1.5%. The final results of b_p^{LISST} and b_{bp}^{LISST} for seawater samples presented in this study are based on the Zhang et al. [76] method.

1.3. Results and Discussion

1.3.1. Correction Functions for LISST-VSF

The results for $CF_{100}(\psi)$, $CF_{200}(\psi)$, $CF_{400}(\psi)$, and $CF_f(\psi)$ are plotted in Figure 1.4. The final correction function $CF_f(\psi)$ indicates that $\beta_p^{LISST*}(\psi)$ is lower than $\beta_p^{REF}(\psi)$ by a factor of about 2, and also exhibits some angular variability. One consistent feature in the forward scattering region, which is independent of the bead size, is a sharp increase in $CF_f(\psi)$ with a peak at ring 26 (ψ = 5.84°). We observed a similar but inverse feature consistently in natural seawater samples, which suggests that the behavior of the correction function at these angles is credible. Within the angular range of data from the Roving Eyeball sensor (16–150°), the $CF_f(\psi)$ values remain generally in the range between 1.7 and 1.9. For angles larger than 150°, we did not obtain consistent results of the correction function for different bead sizes (not shown), so this angular range is omitted from our analysis of LISST-VSF measurements. Note also that $CF_{400}(\psi)$ differs greatly from $CF_{100}(\psi)$ and $CF_{200}(\psi)$ within the angular range between about 65° and 120°. This can be attributed to the uncertainty in the determinations of $CF_{400}(\psi)$ associated with a well-

pronounced minimum in the volume scattering function for the 400 nm beads in this angular range. Therefore, the $CF_{400}(\psi)$ data in this angular range were not used in the determination of final $CF_f(\psi)$.

The results for $BF_{100}(\psi)$, $BF_{200}(\psi)$, $BF_{400}(\psi)$, and $BF_f(\psi)$, are shown in Figure 1.5. As seen, $BF_f(\psi)$ is negative within the examined angular range and varies within a relatively narrow range of values between about −0.02 and −0.04. Similar to the results for $CF_{400}(\psi)$, the distinct feature of positive bias observed in the $BF_{400}(\psi)$ data around the scattering angle of 80° can be attributed to the uncertainty associated with a minimum in the volume scattering function for the 400 nm beads in this angular range. This portion of $BF_{400}(\psi)$ data was not used in the determination of final $BF_f(\psi)$.

The performance of the final correction function $CF_f(\psi)$ within the range of scattering angles from 0.09° to 150° was evaluated by comparing the corrected LISST-VSF measurements of volume scattering function, $\beta_p^{LISST}(\psi)$, with reference values of $\beta_p^{REF}(\psi)$ for six samples of polystyrene beads (100, 200, 400, 500, 700, and 2000 nm in diameter; see the dilution factors for these samples indicated in boldface in Table 1.1). The beads with diameters of 500, 700, and 2000 nm were not used in the generation of the final correction function, so they provide completely independent data for evaluating the performance of $CF_f(\psi)$. The evaluation with the data for 100, 200, and 400 nm beads is also useful because the final $CF_f(\psi)$ was determined by averaging the results obtained with multiple bead sizes and concentrations of these samples, and not from a single bead size and concentration. Results of independent measurements obtained with the DAWN-EOS on four bead suspensions (100, 200, 400, and 700 nm) are also included in the evaluation analysis for additional comparisons.

The comparisons of $\beta_p^{LISST}(\psi)$ and $\beta_p^{REF}(\psi)$ are shown in Figure 1.6 for the six polystyrene bead samples. The presented values of $\beta_p^{LISST}(\psi)$ are the median values for each angle from each measurement series. The measured values of $\beta_p^{DAWN}(\psi)$ are additionally depicted for the 100, 200, 400, and 700 nm diameter beads. In general, the magnitude and angular dependence of $\beta_p^{LISST}(\psi)$ exhibits good agreement with reference values for all bead diameters. Notable differences occur within the minima of volume scattering function, for example near the angle of 80° for the 400 nm beads (Figure 1.6c). This issue has been mentioned above in the context of determinations of $CF_f(\psi)$ and $BF_f(\psi)$. The agreement observed between $\beta_p^{LISST}(\psi)$ and $\beta_p^{DAWN}(\psi)$ lends additional credence to the determined correction function $CF_f(\psi)$ and its application to LISST-VSF measurements.

Figure 1.7a illustrates the relationship between $\beta_p^{LISST}(\psi)$ measured at all angles between 3.02° and 150° and $\beta_p^{REF}(\psi)$ for the corresponding angles for the six bead samples. The overall agreement is quite good over a range spanning nearly 4 orders of magnitude. The regions of largest disagreement correspond to angles measured with the ring detectors, as well as angles corresponding to sharp minima or maxima in volume scattering function which are observed for the larger beads. Although the measured minima and maxima occur essentially at the same angles as predicted by Mie scattering calculations, the measured magnitude of minima or maxima can differ by a few tens of percent from the reference values. This is illustrated by plots of percent differences between the measured and reference values (Figure 1.7b). The oscillations and peaks (both positive and negative) in percent differences correspond to the minima and maxima in the angular patterns of volume scattering function.

Table 1.2 includes several statistical parameters that quantify the agreement between the data of $\beta_p^{LISST}(\psi)$ and $\beta_p^{REF}(\psi)$ illustrated in Figure 1.7a. In this analysis we ignore $\psi < 3.02°$ due

to generally low scattering signal relative to baseline for these ring detectors. The values of statistical parameters support the overall good agreement; for example, the median ratio (*MR*) of $\beta_p^{LISST}(\psi)$ to $\beta_p^{REF}(\psi)$ is very close to 1, and the median absolute percent difference (*MAPD*) between $\beta_p^{LISST}(\psi)$ and $\beta_p^{REF}(\psi)$ is only ~4%. These median values indicate no overall bias in the corrected measurements of $\beta_p^{LISST}(\psi)$ relative to the reference values of $\beta_p^{REF}(\psi)$ and small statistical differences between $\beta_p^{LISST}(\psi)$ and $\beta_p^{REF}(\psi)$. Table 1.2 also includes the statistical parameters for a subset of data presented in Figure 1.7a. In this subset, the forward scattering measurements with ring detectors were excluded, so the angular range is 16–150°. The statistical parameters for this subset are generally improved compared with the dataset covering the angular range 3.02–150°. For example, the root mean square difference (*RMSD*) is smaller (0.015 m^{-1} sr^{-1} vs. 0.21 m^{-1} sr^{-1}) and the slope of linear regression is closer to 1 (0.958 vs. 0.723). The improvements in the statistical parameters after removing the ring detector data are related primarily to much larger values of volume scattering function at forward scattering angles compared with larger angles, and a tendency to negative bias in $\beta_p^{LISST}(\psi)$ relative to $\beta_p^{REF}(\psi)$ at forward angles.

To further validate the correction of LISST-VSF measurements with the $CF_f(\psi)$ function, we performed comparisons for approximate scattering and backscattering coefficients, $b_{p,150}$ and $b_{bp,150}$, respectively. The approximate scattering coefficient $b_{p,150}$ was obtained by integrating the volume scattering function within the angular range from 0.09° to 150°. The approximate backscattering coefficient $b_{bp,150}$ was obtained by the integration from 90° to 150°. These calculations were made for the uncorrected measured $\beta_p^{LISST*}(\psi)$, CF_f-corrected measured $\beta_p^{LISST}(\psi)$, and reference $\beta_p^{REF}(\psi)$. We also used Mie scattering calculations to estimate the

underestimation of the scattering and backscattering coefficients for the examined polystyrene beads caused by the integration of $\beta_p^{REF}(\psi)$ up to 150° as opposed to 180°. We found that the approximate scattering coefficient, $b_{p,150}^{REF}$, can be lower by as much as 7% compared with the "true" scattering coefficient b_p^{REF}. This result was observed for 100 nm beads. For backscattering the approximate coefficient $b_{bp,150}^{REF}$ was found to be lower by as much as 24% for the 500 nm beads. Although the LISST-VSF measurements extend to 150° rather than 180°, the approximate coefficients are still useful for our validation exercise because most of the angular range and magnitude of total scattering and backscattering coefficients are included in the integration up to 150°. In addition, this validation analysis includes all 20 experiments conducted in this study, and not just the six example experiments presented in Figures 1.6 and 1.7.

Figure 1.8 compares the reference values of $b_{p,150}^{REF}$ and $b_{bp,150}^{REF}$ with LISST-VSF values determined from uncorrected $\beta_p^{LISST*}(\psi)$ and CF_f-corrected $\beta_p^{LISST}(\psi)$. In these calculations we used the median values of $\beta_p^{LISST*}(\psi)$ and $\beta_p^{LISST}(\psi)$ for each measurement series from all 20 experimental combinations of bead sizes, concentrations, and PMT gains listed in Table 1.1. For all experiments, the approximate coefficients, $b_{p,150}^{LISST*}$ and $b_{bp,150}^{LISST*}$, derived from uncorrected $\beta_p^{LISST*}(\psi)$ are nearly half of the reference values of $b_{p,150}^{REF}$ and $b_{bp,150}^{REF}$. After $CF_f(\psi)$ correction the approximate coefficients $b_{p,150}^{LISST}$ and $b_{bp,150}^{LISST}$ exhibit a nearly 1:1 relationship with $b_{p,150}^{REF}$ and $b_{bp,150}^{REF}$. The statistical parameters that quantify the overall good agreement between $b_{p,150}^{LISST}$ and $b_{p,150}^{REF}$ and between $b_{bp,150}^{LISST}$ and $b_{bp,150}^{REF}$ are listed in Table 1.2.

Similarly to the validation analysis of $CF_f(\psi)$, the performance of the correction function $BF_f(\psi)$ was evaluated by comparing the corrected LISST-VSF measurements of the degree of linear polarization, $DoLP_p^{LISST}(\psi)$, with reference values of $DoLP_p^{REF}(\psi)$ for six samples of

polystyrene beads (100, 200, 400, 500, 700, 2000 nm in diameter). Figure 1.9 depicts these comparisons. The values of $DoLP_p^{DAWN}(\psi)$ measured with DAWN-EOS are also depicted for the 100, 200, 400, and 700 nm beads. For all bead sizes, the magnitude and angular dependence of $DoLP_p^{LISST}(\psi)$ exhibits generally a very good agreement with both the reference values and DAWN-EOS measurements. For larger beads, notable differences occur within the minima of the degree of linear polarization, for example near the angle of 80° for the 400 nm beads (Figure 1.9c).

Figure 1.10a is a scatter plot of $DoLP_p^{LISST}(\psi)$ vs. $DoLP_p^{REF}(\psi)$ which includes all data for the six bead samples presented in Figure 1.9. In the region of negative values which correspond to the minima in the angular pattern of the degree of linear polarization, the $DoLP_p^{LISST}(\psi)$ exhibits a positive bias relative to $DoLP_p^{REF}(\psi)$. This bias is seen in the form of peaks in the angular pattern of the difference between $DoLP_p^{LISST}(\psi)$ and $DoLP_p^{REF}(\psi)$ for larger bead sizes (Figure 1.10b). The peak amplitudes generally range from 0.05 to 0.3. Importantly, however, aside from these features the data of $DoLP_p^{LISST}(\psi)$ vs. $DoLP_p^{REF}(\psi)$ are distributed close to the 1:1 line within the major part of the region of positive values (Figure 1.10a). This includes the region of maximum values of the degree of linear polarization of scattered light from natural seawater samples, which are observed at scattering angles near 90° or greater. The overall good agreement between BF_f-corrected measured $DoLP_p^{LISST}(\psi)$ and $DoLP_p^{REF}(\psi)$ is supported by the statistical parameters shown in Table 1.2 which are calculated on the basis of the entire dataset presented in Figure 1.10 For example, the *RMSD* and *MAPD* values are small, 0.065 and 5%, respectively. Also, despite some negative bias for data with negative values of the degree of linear polarization, the *MR* for the ratio of $DoLP_p^{LISST}(\psi)$ to $DoLP_p^{REF}(\psi)$ for the entire dataset is 0.993, indicating essentially no bias. These statistics would improve if the data within the minima in the angular pattern of the degree of linear polarization were removed from the analysis.

1.3.2. Measured Light Scattering Properties of Natural Particulate Assemblages

Figure 1.11 depicts the corrected measured volume scattering function, $\beta_p^{LISST}(\psi)$, and the degree of linear polarization, $DoLP_p^{LISST}(\psi)$, for three contrasting natural assemblages of particles. The selected parameters describing the particulate and optical properties of these samples are provided in Table 1.3. Sample A was obtained ~8 km offshore from the subsurface chlorophyll-*a* maximum at a depth of 18 m, sample B was collected just beneath the sea surface at SIO Pier during a calm sunny summer day, and sample C was collected ~2 km inland at the San Diego River Estuary during low tide. The SPM range covers about one order of magnitude from 0.36 g m^{-3} for sample A to 3.18 g m^{-3} for sample C, which is reflected in significant range of the particulate scattering coefficient, b_p^{LISST}, from 0.36 m^{-1} to 2.23 m^{-1}. Chla was also lowest for sample A (0.75 mg m^{-3}) but highest for sample B (2.5 mg m^{-3}). Thus, whereas the offshore sample A represents a particle concentration that is within the range of observations in relatively clear open ocean waters, sample C is representative of more turbid coastal or nearshore waters [5,7]. Samples A and B have similarly high values of the ratio POC/SPM (0.43 and 0.47, respectively) and relatively high values of Chla/SPM (2.1×10^{-3} and 2.2×10^{-3}, respectively), indicating organic-dominated particulate assemblages with significant contribution of phytoplankton. In contrast, sample C has much lower values of POC/SPM (0.14) and Chla/SPM (3.8×10^{-4}), indicating inorganic-dominated particulate assemblage and relatively small role of phytoplankton, despite significant chlorophyll-*a* concentration (1.21 mg m^{-3}).

These differences in particle properties between the three samples are responsible for the differences in the magnitude and angular shape of $\beta_p^{LISST}(\psi)$ and $DoLP_p^{LISST}(\psi)$ presented in Figure 1.11 and the optical parameters listed in Table 1.3. These optical parameters include the particulate backscattering ratio, $\tilde{b}_{bp}^{LISST}$, the ratio of $\beta_p^{LISST}(45°)$ to $\beta_p^{LISST}(135°)$, and the maximum

value of $DoLP_p^{LISST}(\psi)$ denoted as $DoLP_{p,max}^{LISST}$. This maximum value occurs at a scattering angle ψ_{max} which is also provided in Table 1.3. The offshore sample A has an intermediate value of $\tilde{b}_{bp}^{LISST}$ and the highest $DoLP_{p,max}^{LISST}$ of about 0.77 associated with the smallest ψ_{max} of 92°. Sample B from the SIO Pier has the lowest $\tilde{b}_{bp}^{LISST}$ of 0.008 among the three samples, suggesting a relatively steep slope of particle size distribution, relatively low bulk particle refractive index, or both [17]. This sample also shows the least steep near-forward scattering pattern (Figure 1.11c), which suggests a higher proportion of small particles relative to larger particles compared with the two other samples. Finally, the most turbid and least organic sample, sample C, exhibits an enhanced proportion of backscattering with the highest $\tilde{b}_{bp}^{LISST}$ of 0.027. While this result may suggest a relatively high bulk particle refractive index [17] consistent with the lowest POC/SPM ratio among the three samples, the additional influence of particle size distribution cannot be ruled out. Sample C shows steep near-forward scattering pattern (Figure 1.11c), which is typically indicative of an increased proportion of large particles relative to small particles. Note that sample C also has the lowest $\beta_p^{LISST}(45°)/\beta_p^{LISST}(135°)$ ratio of 12, which indicates a higher degree of symmetry in the angular pattern of scattering about 90°, which is consistent with the relatively high value of $\tilde{b}_{bp}^{LISST}$ for this sample. In addition, sample C has the lowest $DoLP_{p,max}^{LISST}$ of 0.58.

For comparison, Table 1.3 also includes the values for the selected optical parameters estimated from measurements reported by Petzold [38] for clear ocean waters (off Bahamas), coastal waters (San Diego coastal region), and turbid waters (San Diego Harbor). These measurements span a generally similar range of scattering angles as the LISST-VSF (10–180° in 5° increments), but are based on a spectrally broader incident beam (75 nm full width half maximum) centered at 514 nm. The estimates of particulate volume scattering function β_p from Petzold's measurements were obtained by subtracting pure seawater contribution β_w from the

measured total β. The β_w value was calculated assuming a water temperature of 15 °C and salinity of 33 PSU [77]. Although Petzold's data include measurements made in clearer waters compared with our samples, the range of values for the dimensionless parameters associated with the shape of angular scattering pattern, $\tilde{b}_{bp}^{LISST}$ and $\beta_p^{LISST}(45°)/\beta_p^{LISST}(135°)$, is very similar. Specifically, our data for the offshore sample A are similar to Petzold's data from clear waters, sample B from the SIO Pier aligns with Petzold's data from coastal San Diego waters, and sample C from San Diego River Estuary with Petzold's data from the San Diego Harbor.

We note that the dotted lines in Figure 1.11 reflect some variations in $\beta_p^{LISST}(\psi)$ and $DoLP_p^{LISST}(\psi)$ between the individual measurements within a given set of measurements for each sample. For example, on the basis of the collection of 200 to 400 measurements for each of the two linear polarization states of the incident beam and the scattered light, the coefficient of variation at ψ = 90° was 14%, 8%, and 13% for β_p^{LISST} and 20%, 13%, and 15% for $DoLP_p^{LISST}$ for samples A, B, and C, respectively. These variations between the individual measurements that have been taken in rapid succession do not necessarily reflect the measurement precision, as they can also be associated with actual variations in the sample, for example the fluctuations in the presence of relatively rare large particles within the interrogated sample volume. Another important point is that the small negative values of $DoLP_p^{LISST}$ observed for some individual measurements at forward scattering angles <30° (see the 10th percentile dotted lines in Figure 1.11 b,d,f) are not necessarily an indication of measurement uncertainty because the negative values, especially in this angular range, are physically possible for certain types of particles [30,54,56,58].

Figure 1.12 depicts scatter plots of the relationships between the dimensionless optical parameters, $\tilde{b}_{bp}^{LISST}$ and $DoLP_{p,max}^{LISST}$, and the dimensionless particulate compositional properties, POC/SPM and Chla/SPM, for all 17 samples examined in this study. The overall range of

POC/SPM in our dataset is 0.04 to 0.6. The presented data have been divided into three groups according to the values of POC/SPM as follows: the least organic-dominated (or the most mineral-dominated) data with POC/SPM < 0.15; the most organic-dominated data with POC/SPM > 0.3, and the intermediate data with 0.15 ≤ POC/SPM ≤ 0.3. The selected boundary values of POC/SPM for discriminating between the organic-dominated and mineral-dominated groups of data differ from those used in our previous studies [65,78], but appear to adequately reflect the patterns in the present data. In particular, the most mineral-dominated samples with POC/SPM < 0.15 form a clear cluster of data points with the highest $\tilde{b}_{bp}^{LISST}$ (Figure 1.12a) and the lowest Chla/SPM (Figure 1.12b,d). We also note that no data were collected for POC/SPM between 0.15 and 0.2, so we will refer to all data with POC/SPM > 0.2 as highly organic because they all represent highly significant or dominant role of organic particles.

The scatter plot for the data of $\tilde{b}_{bp}^{LISST}$ vs. POC/SPM suggests the presence of a relational trend with significant negative correlation between the variables (the correlation coefficient $R = -0.73$). While the $\tilde{b}_{bp}^{LISST}$ values are clearly highest for POC/SPM < 0.15, the organic-dominated samples have consistently lower $\tilde{b}_{bp}^{LISST}$. This result is consistent with the notion that mineral-dominated particulate assemblages with relatively high bulk refractive index of particles tend to have higher backscattering ratio $\tilde{b}_{bp}$ compared with organic-dominated assemblages with lower refractive index [17]. However, we also note that highly organic samples with POC/SPM > 0.2 show no clear relationship and essentially no correlation between $\tilde{b}_{bp}^{LISST}$ and POC/SPM ($R = -0.11$). This result may be attributable to the effect of other particle characteristics on $\tilde{b}_{bp}^{LISST}$, such as variations in refractive index of particles associated with changes in the composition of particulate organic matter, variations in particle size distribution, or both. The scatter plot of $\tilde{b}_{bp}^{LISST}$ vs. Chla/SPM (Figure 1.12b) provides interesting insight into this question, as this relationship is

significantly better compared with $\tilde{b}_{bp}^{LISST}$ vs. POC/SPM. Whereas the correlation between $\tilde{b}_{bp}^{LISST}$ and Chla/SPM for all data is strong ($R = -0.85$), the subset of data for highly organic samples (POC/SPM > 0.2) has also a relatively high correlation coefficient of -0.51. This is an important result, suggesting that for particulate assemblages with high organic content, the backscattering ratio $\tilde{b}_{bp}$ tends to decrease with increasing proportion of phytoplankton in the particulate assemblage. It is likely that the relationship in Figure 1.12b is largely driven by a decrease in the bulk particle refractive index with increasing proportion of phytoplankton in the particulate assemblage. Because this trend also holds for the subset of highly organic samples, it may indicate that live phytoplankton cells have generally lower refractive index than non-living organic particles.

In contrast to $\tilde{b}_{bp}^{LISST}$, the $DoLP_{p,max}^{LISST}$ data show no clear relational trend and very weak correlation with POC/SPM ($R = 0.31$), indicating that the maximum degree of linear polarization does not provide a useful optical signature for the organic vs. inorganic content of particulate assemblages in our dataset (Figure 1.12c). A similar result with no correlation ($R = 0.07$) is observed for $DoLP_{p,max}^{LISST}$ vs. Chla/SPM, indicating that varying proportion of phytoplankton in total particulate assemblage has no discernible systematic effect on the maximum degree of linear polarization (Figure 1.12d). We also determined that there is no significant correlation between $DoLP_{p,max}^{LISST}$ and $\tilde{b}_{bp}^{LISST}$ in our dataset ($R = -0.22$), as well as between ψ_{max} and POC/SPM or Chla/SPM ($R = -0.09$ and 0.06, respectively). It is also of interest to note that the range of our $DoLP_{p,max}^{LISST}$ data is generally consistent with the range of values reported in literature for natural seawater samples, although the reported range in some earlier studies extends to somewhat lower values, as low as about 0.4 [15,39–42,79,80].

The assessment of potential presence of systematic effects of particle size distribution (PSD) on $\tilde{b}_{bp}^{LISST}$ and $DoLP_{p,max}^{LISST}$ is presented in Figure 1.13. In this assessment, we use two PSD metrics: the 90th percentile diameter, D_V^{90}, derived from the particle volume distribution, and the power function slope, ζ, derived from the particle number distribution. We also tested other percentile-based diameters such as the median D_V^{50} but no improvements in the examined relationships were observed. Figure 1.13a,b shows no trend in the data of $\tilde{b}_{bp}^{LISST}$ associated with variations in the particle size metrics, even though these metrics vary over a significant dynamic range. This is the case for the entire dataset as well as a subset of highly organic samples with POC/SPM > 0.2, which supports the interpretation of results presented in Figure 1.12b in terms of the role of refractive index. The data of $DoLP_{p,max}^{LISST}$ vs. D_V^{90} show the potential for the presence of a relational trend (Figure 1.13c). Although the scatter in these data points is significant and correlation is weak ($R = -0.47$), the lowest values of $DoLP_{p,max}^{LISST}$ tend to occur along with the highest values of D_V^{90}. This result indicates that the decrease in the maximum degree of linear polarization tends to be associated with particulate assemblages exhibiting a higher proportion of large-sized particles. The potential usefulness of the relationship between the degree of linear polarization and particle size has been proposed for the first time in 1930 [81], and the trend observed in our data is consistent with those early results.

1.4. Concluding Remarks

Our laboratory measurements combined with Mie scattering calculations for samples of standard polystyrene beads illustrate the value of such an approach for evaluating the calibration and performance of light scattering instruments. For the specific version of LISST-VSF instrument and data processing code used in our study, we determined the calibration correction functions for

improved determinations of the particulate volume scattering function $\beta_p(\psi)$ and the degree of linear polarization $DoLP_p(\psi)$. The required correction was found to be particularly significant for $\beta_p(\psi)$; a correction factor of ~1.7 to 1.9. The improved determinations of $\beta_p(\psi)$ and $DoLP_p(\psi)$ were validated with measurements on independent samples, and also using another independently-calibrated light scattering instrument, DAWN-EOS. Although the correction functions developed in this study are applicable only to the specific version of LISST-VSF instrument and the data processing code used in this study, our results emphasize a general need for evaluating the performance of light scattering instruments and minimizing the associated uncertainties in quantitative determinations from measurements.

The improved protocol for measurements of light scattering with our LISST-VSF instrument was applied to measurements taken on 17 natural seawater samples from coastal and offshore marine environments characterized by contrasting assemblages of suspended particles. The particulate volume scattering function, degree of linear polarization, and backscattering ratio were determined from LISST-VSF measurements. For our dataset, these light scattering properties exhibit significant variations related to a broad range of measured particle properties characterizing the organic vs. inorganic composition and size distribution of particulate assemblages. For example, we observed negative relational trends between the particulate backscattering ratio and the increasing proportions of organic particles or phytoplankton in the total particulate assemblage. These proportions were parameterized in terms of the measured ratio of particulate organic carbon (POC) or chlorophyll-*a* (Chla) concentration to the total dry mass concentration of suspended particulate matter (SPM). The observed trends can be useful in the development of optical approaches for characterizing the composition of particulate assemblages. Our results also suggest a potential trend between the maximum degree of linear polarization of light scattered by particles

and particle size metrics. Specifically, the decrease in the maximum degree of linear polarization observed at scattering angles close to 90^{o} tends to be associated with particulate assemblages exhibiting a higher proportion of large-sized particles.

Earlier theoretical studies have shown that changes in the angular shape and the maximum value of the degree of linear polarization depend on particle refractive index and size distribution [82,83]; however, the experimental data of the degree of linear polarization of scattered light for natural marine particle assemblages are very scarce. Our results provide a contribution to filling this gap. This type of data can also be useful for improving an understanding of the polarization properties of marine light fields including polarization of water-leaving radiance and advancing related applications, including remote sensing applications [84-90]. The various potential applications of angular light scattering measurements, including the polarization effects associated with light scattering by marine particles, call for further efforts in this research area.

1.5. Acknowledgments

This work was supported by NASA Terrestrial Hydrology and Ocean Biology and Biogeochemistry Programs (Grant #NNX13AN72G) and the NASA Earth and Space Science Fellowship Program (Grant #NNX14AK93H). We acknowledge Edward R. Blocker, Eric Chen, and Linhai Li for assistance during measurements and processing of data. We also thank Xiaodong Zhang for providing computer code for backscattering extrapolation method and related discussions, and Wayne Slade for discussions about LISST-VSF instrument and processing code. We thank Hubert Loisel and three anonymous reviewers for valuable comments on the manuscript.

Chapter 1, in full, has been published in the Outstanding Topics in Ocean Optics special issue of Applied Sciences. The dissertation author was the primary investigator and author of the paper: Koestner, D., D. Stramski, and R. A. Reynolds. 2018. Measurements of the volume

scattering function and the degree of linear polarization of light scattered by contrasting natural assemblages of marine particles. Appl. Sci. **8**: 2690, doi:10.3390/app8122690.

1.6. Figures

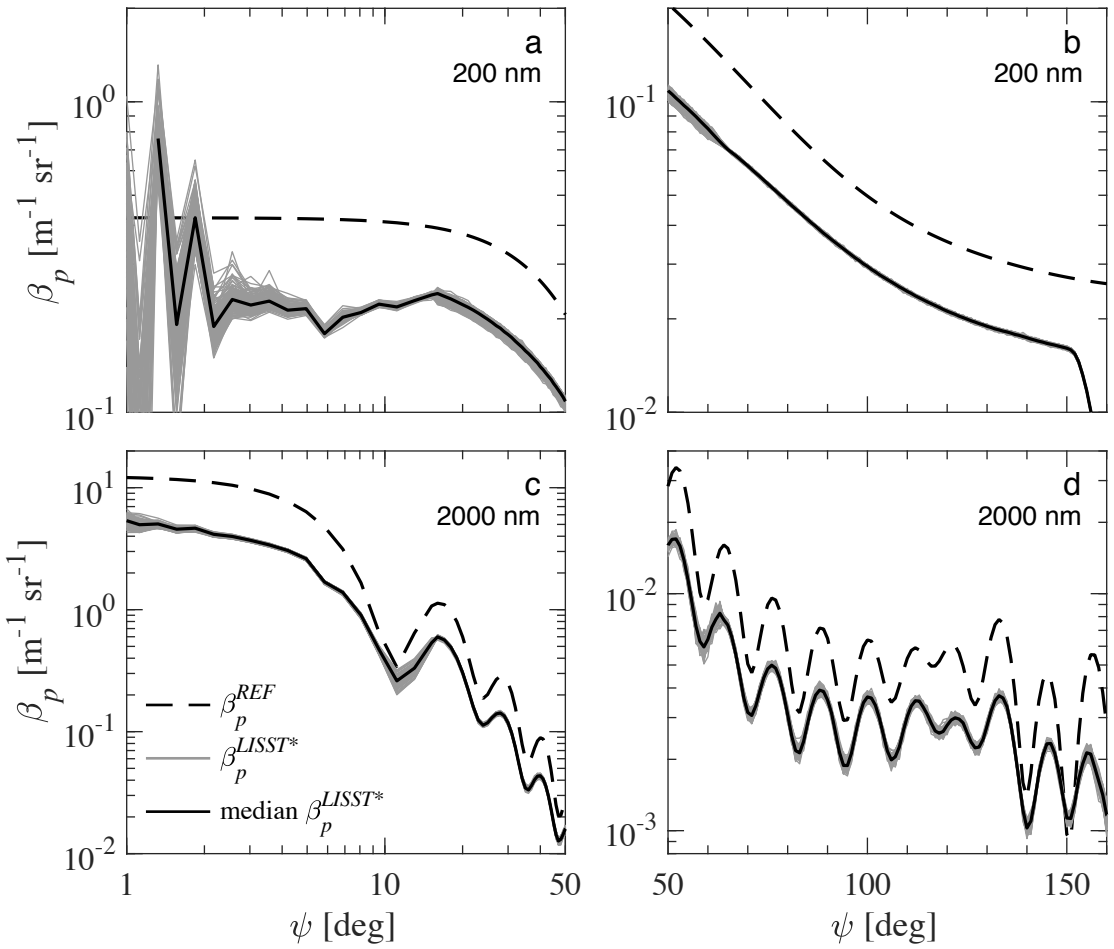

Figure 1.1. Measurements of the particulate volume scattering function, $\beta_p(\psi)$, at light wavelength of 532 nm for 200 nm (**a**,**b**) and 2000 nm (**c**,**d**) diameter polystyrene beads suspended in water. The left panels depict the angular range of 1–50° with logarithmic scaling, and the right panels depict the range 50–160° with linear scaling. The expected reference value, $\beta_p^{REF}(\psi)$, obtained from Mie scattering calculations is indicated as a dashed line. Quality-controlled but uncorrected measurements obtained with the LISST-VSF (gray lines, number of measurements N = 128) and the median value (solid black line) are shown.

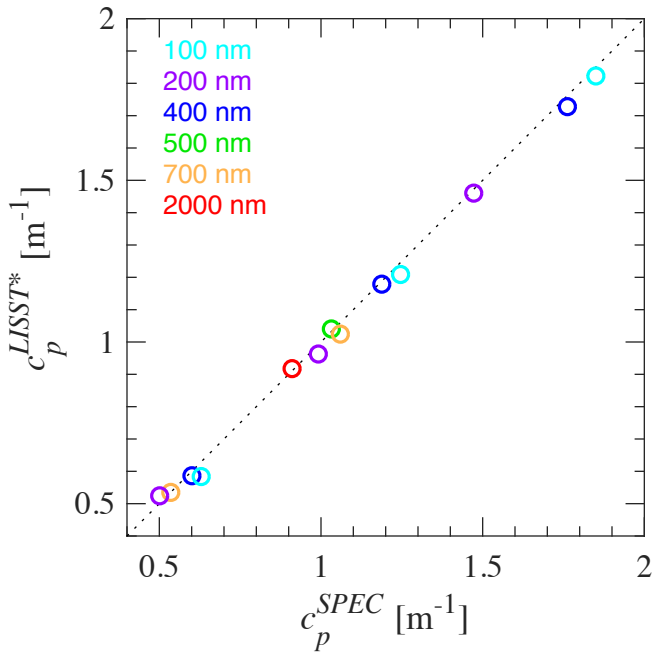

Figure 1.2. Comparison of measurements of the particulate beam attenuation coefficient, c_p, at 532 nm obtained with a spectrophotometer with measurements from the LISST-VSF. The comparison is depicted for suspensions of polystyrene beads of six different diameters as indicated in the legend, and the 1:1 line is plotted for reference (dotted black line). Appropriate dilution factors have been applied to account for the different particle concentrations used in measurements with each instrument. The presented values correspond to samples measured with the LISST-VSF.

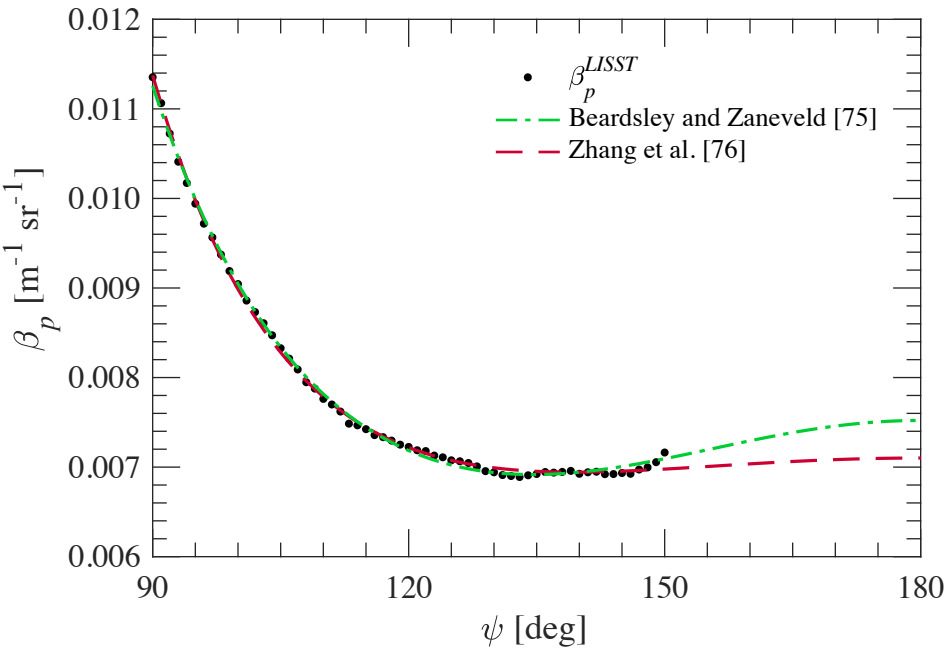

Figure 1.3. Measured values of the particulate volume scattering function $\beta_p(\psi)$ obtained with the LISST-VSF after correction (circles) for scattering angles 90–150° and illustration of the results of two model relationships (Beardsley and Zaneveld [75], Zhang et al. [76]) fitted to the data. The illustrated example measurement was made on a natural sample collected from the San Diego River estuary.

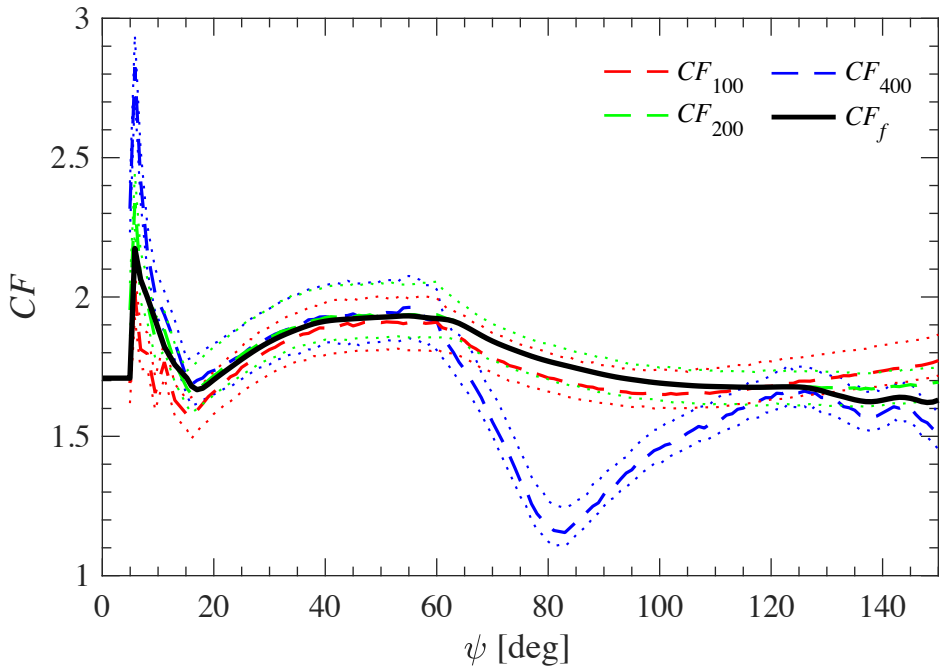

Figure 1.4. Correction functions, $CF(\psi)$, for the LISST-VSF measurements of particulate volume scattering function $\beta_p^{LISST*}(\psi)$ over the angular range 4.96–150° determined for 100, 200, and 400 nm polystyrene bead suspensions. For each individual bead size, dashed lines represent the median values and the dotted lines indicate the 25th and 75th percentiles determined from the series of measurements. The final computed correction function $CF_f(\psi)$ is shown in black, and includes the constant value used for the near-forward angular range from 0.09° to 4.96°.

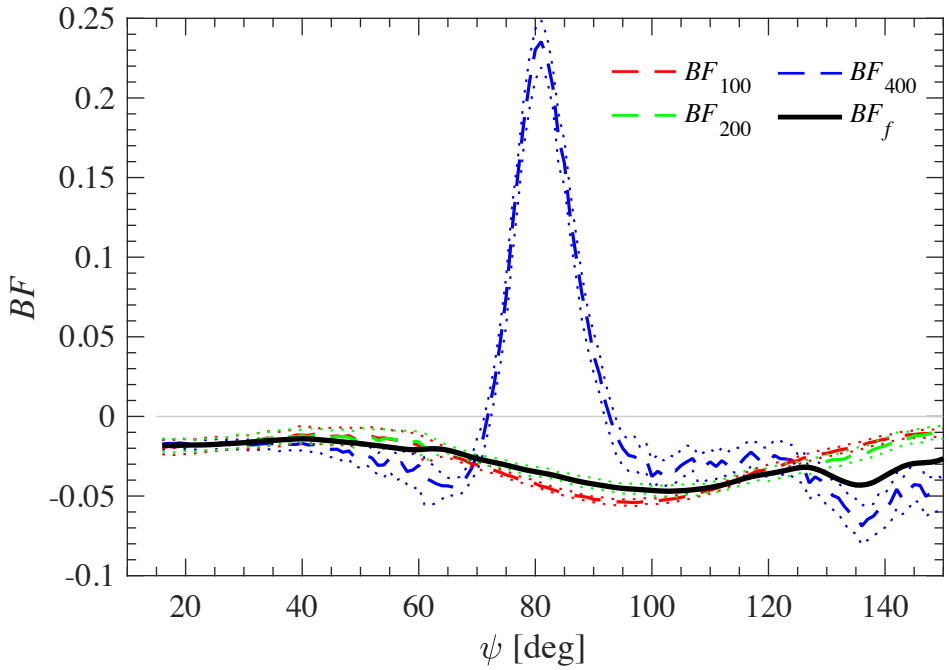

Figure 1.5. Correction functions, $BF(\psi)$, for LISST-VSF measurements of the degree of linear polarization of light scattered by particles, $DoLP_p^{LISST*}(\psi)$ over the angular range 16–150° determined for 100, 200, and 400 nm polystyrene bead suspensions. For each individual bead size, dashed lines represent the median values and the dotted lines indicate the 25th and 75th percentiles determined from the series of measurements. The final computed correction function $BF_f(\psi)$ is shown in black.

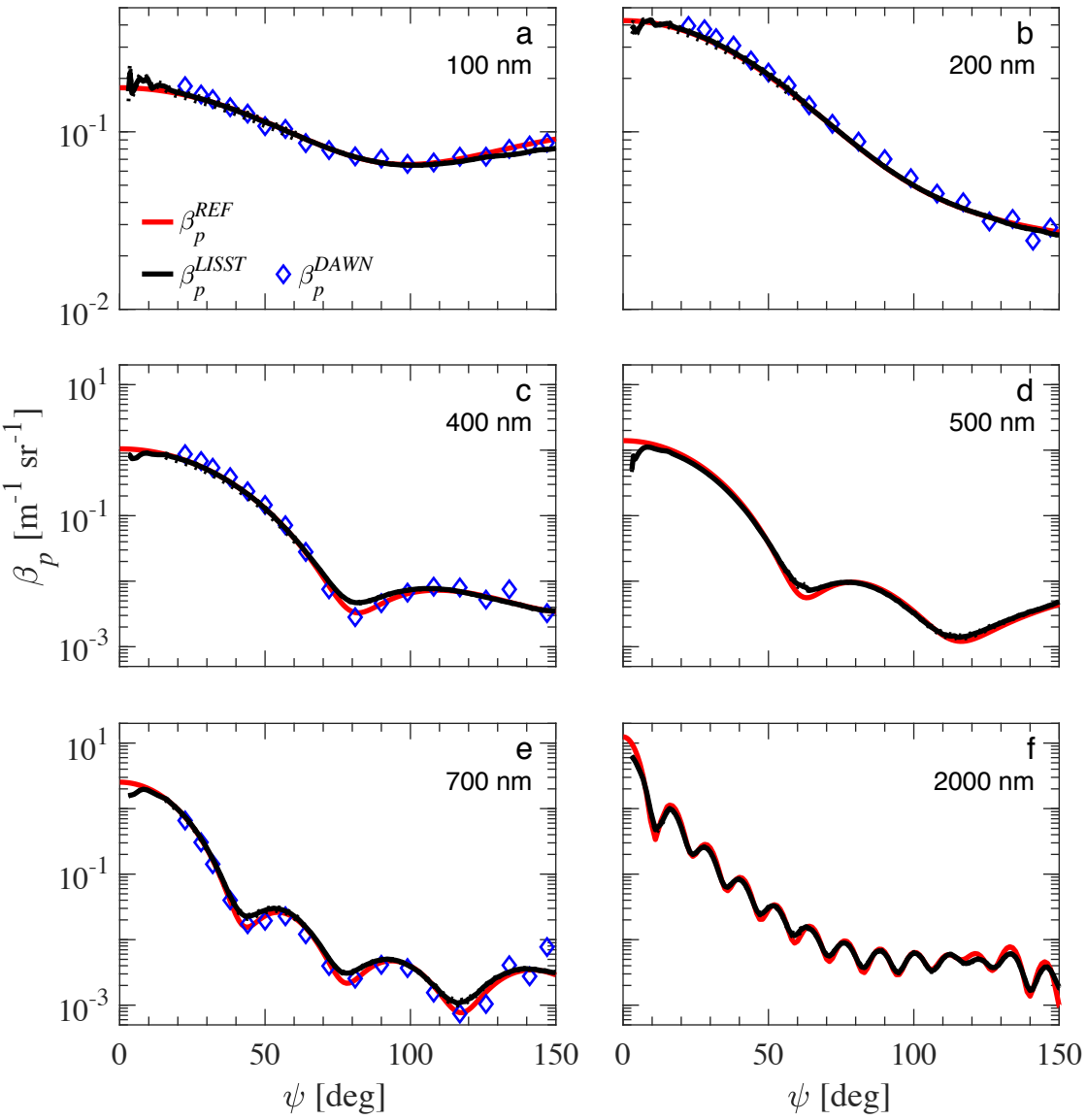

Figure 1.6. Comparison of $\beta_p(\psi)$measurements on suspensions of polystyrene beads of varying diameter with reference values, $\beta_p^{REF}(\psi)$. The $\beta_p^{LISST}(\psi)$ data represent CF_f-corrected median values obtained from a series of measurements with the LISST-VSF. Independent measurements of $\beta_p(\psi)$ obtained with the DAWN-EOS instrument are also shown as diamonds in panels a, b, c and e. The bead diameters are indicated in the legend.

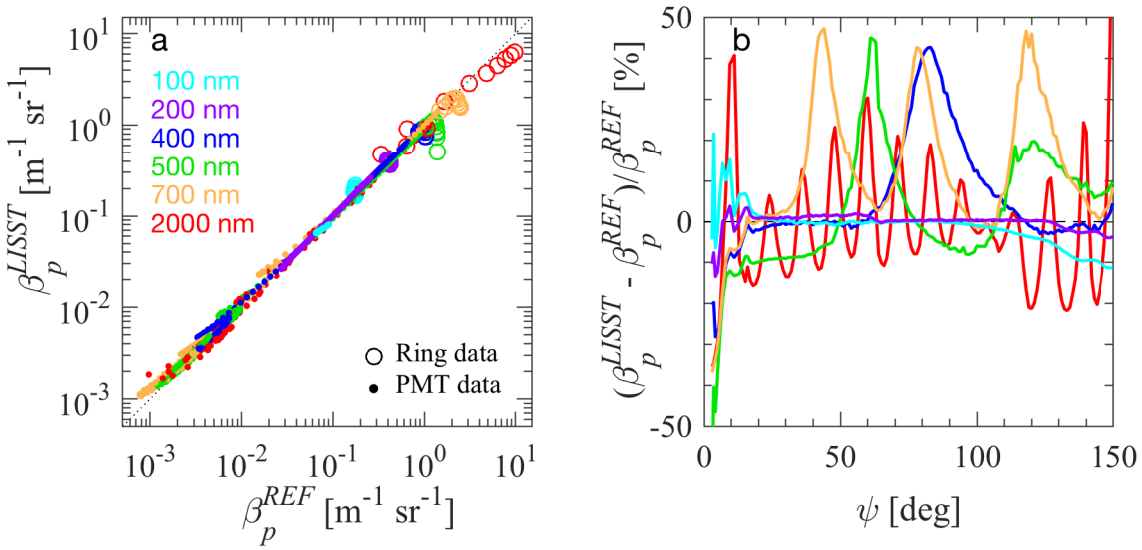

Figure 1.7. (**a**) Scatter plot of β_p^{LISST} vs. β_p^{REF} for polystyrene beads of varying diameters as indicated. Data obtained with the ring detectors and Roving Eyeball sensor are plotted separately, and the 1:1 line is plotted for reference (dotted black line). (**b**) Residuals expressed as percentages between β_p^{LISST} and β_p^{REF} for each bead size as a function of scattering angle.

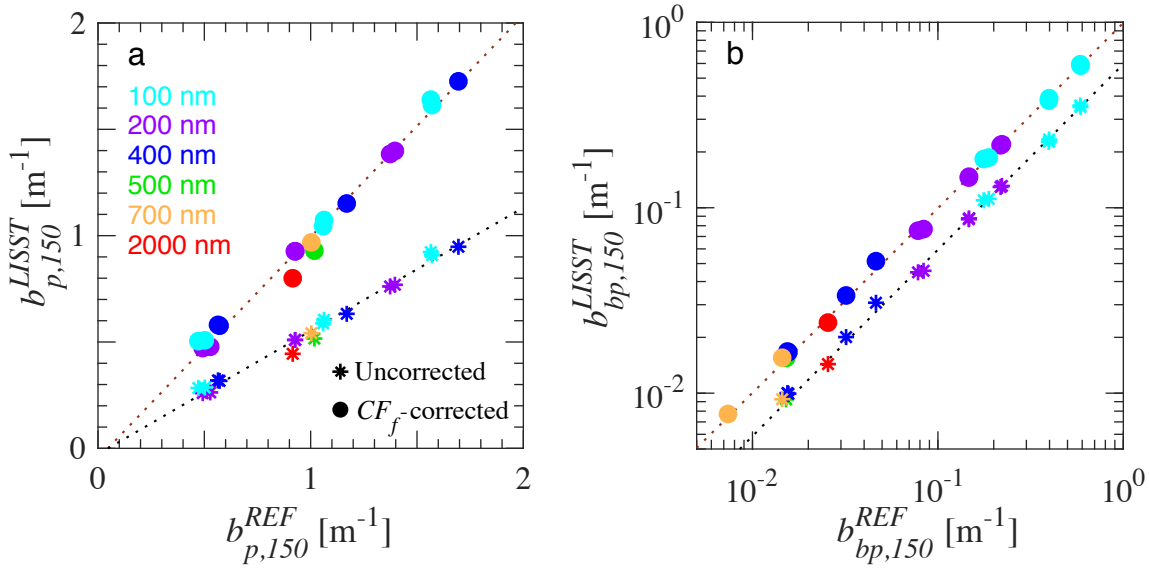

Figure 1.8. (**a**) Scatter plot comparing reference values of the particulate scattering coefficient computed over the angular range 0.09–150°, $b_{p,150}^{REF}$, with values determined from the LISST-VSF, $b_{p,150}^{LISST}$, before (asterisks) and after (circles) correction with CF_f. A type II linear regression model fit to the data is indicated by the dotted lines. (**b**) Similar to (**a**), but for the particulate backscattering coefficient computed over the range 90–150°.

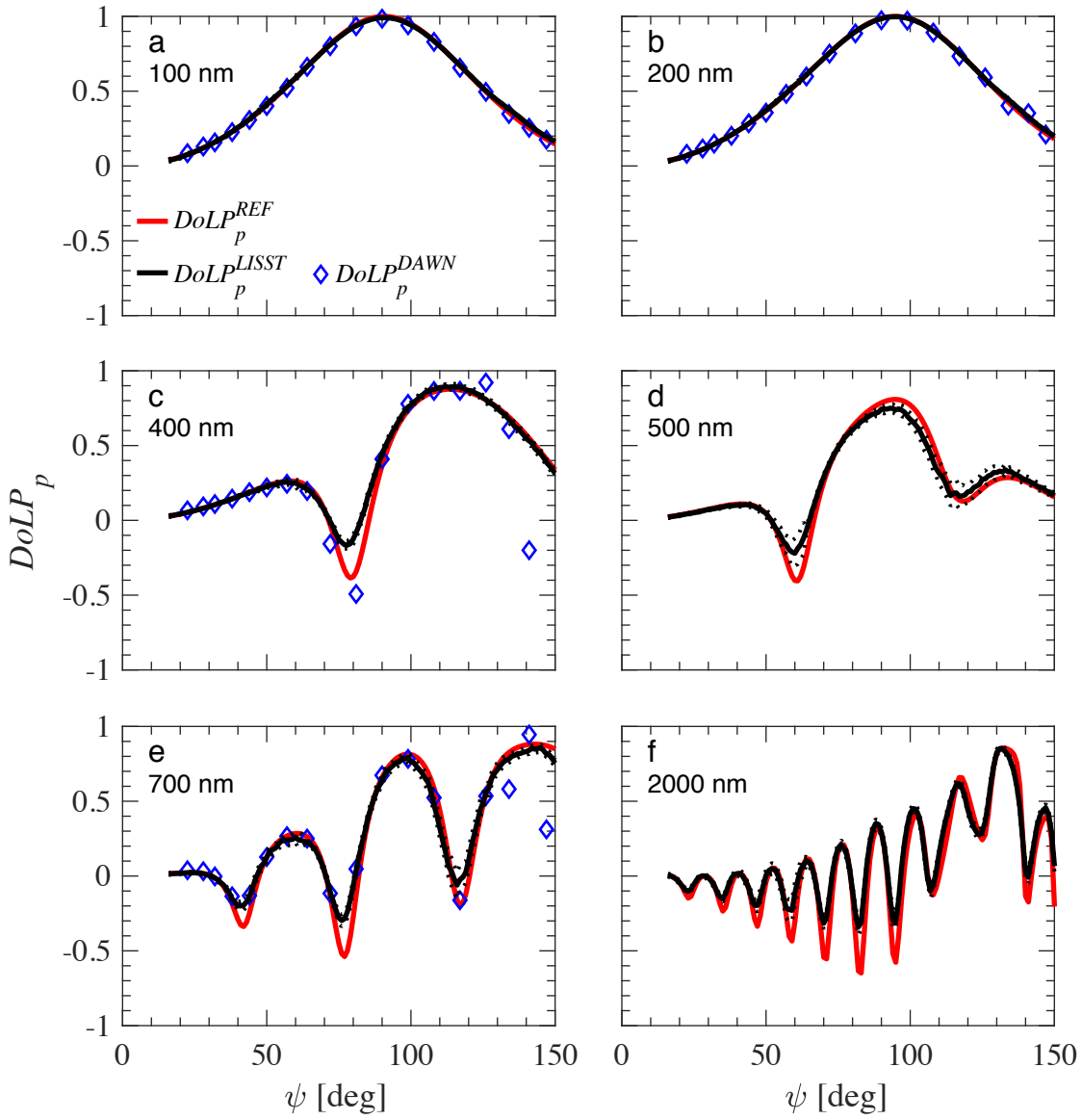

Figure 1.9. Similar to Figure 1.6, but for measured and reference values of particulate degree of linear polarization $DoLP_p$. Measurements obtained with the LISST-VSF were corrected with BF_f.

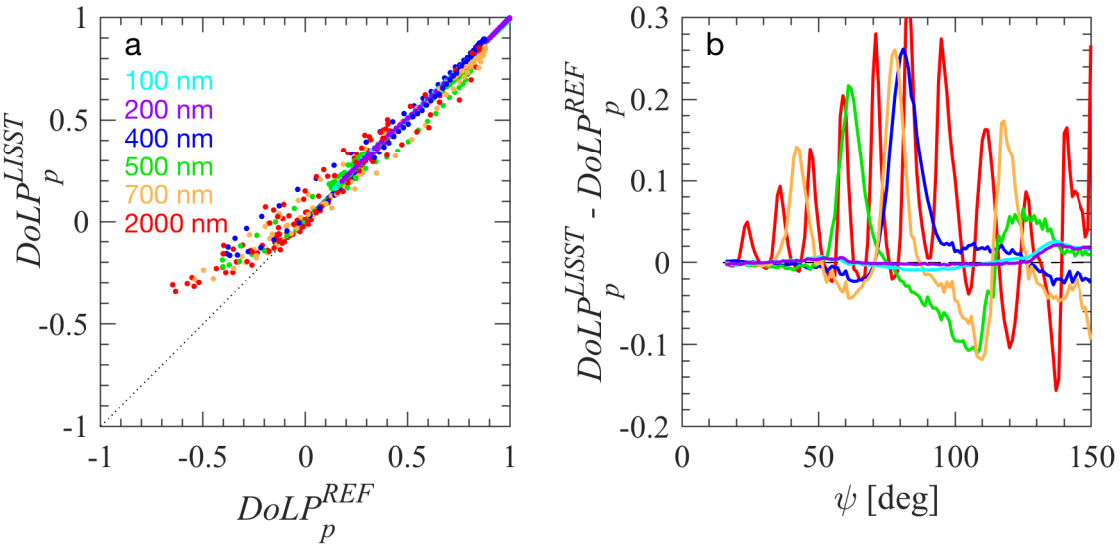

Figure 1.10. Similar to Figure 1.7, but for $DoLP_p$. All data are obtained with the Roving Eyeball sensor, and the residuals between $DoLP_p^{LISST}$ and $DoLP_p^{REF}$ in (**b**) are expressed as absolute differences.

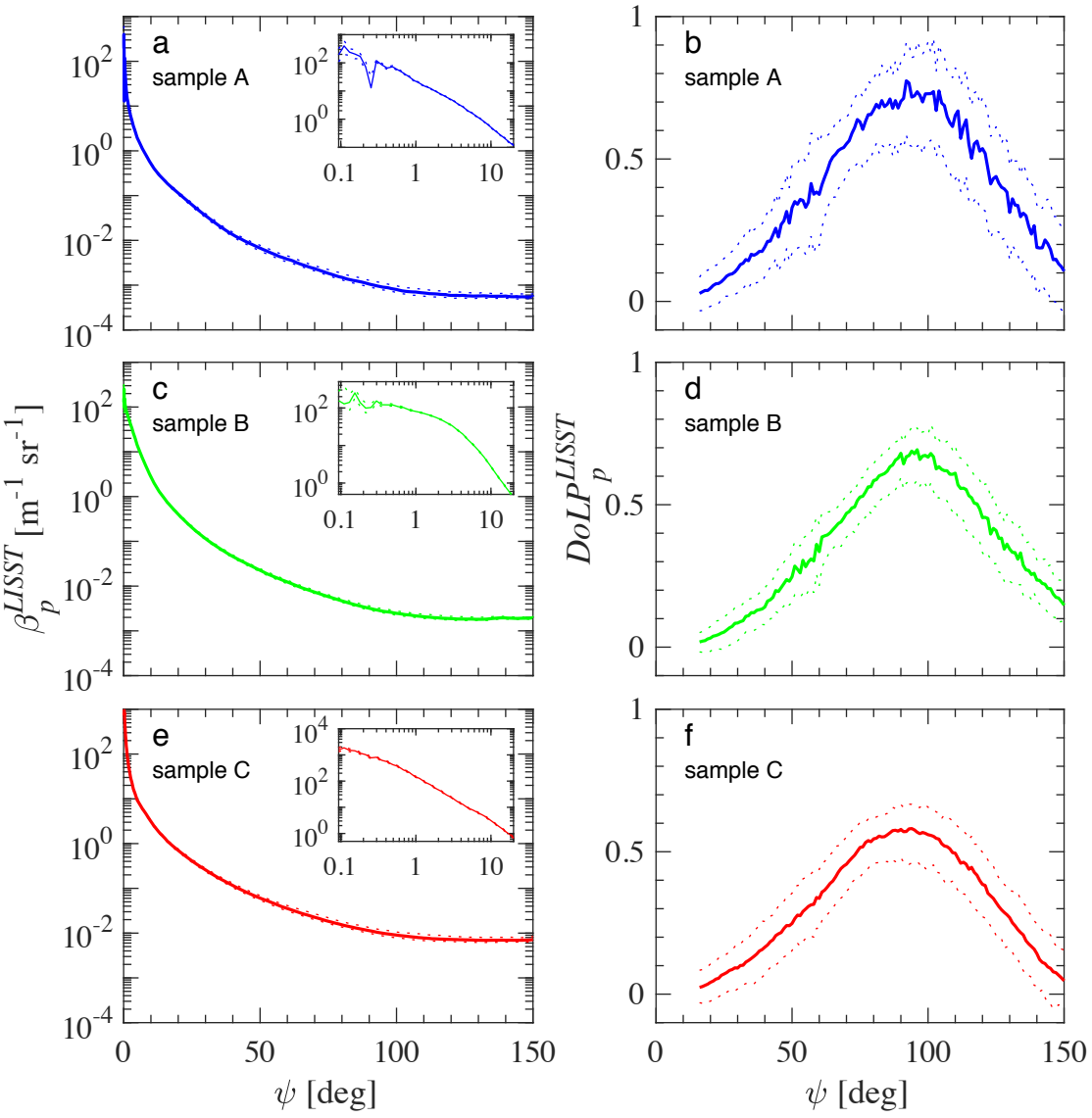

Figure 1.11. Measurements of β_p^{LISST} and $DoLP_p^{LISST}$ obtained with the LISST-VSF on natural seawater samples from the San Diego region representing (**a**,**b**) subsurface offshore waters, (**c**,**d**) SIO Pier, and (**e**,**f**) San Diego River Estuary. Solid lines represent median values while dotted lines indicate the 10th and 90th percentiles obtained from a series of measurements on each sample. Insets in (**a**,**c**,**d**) display greater detail on the near-forward scattering range.

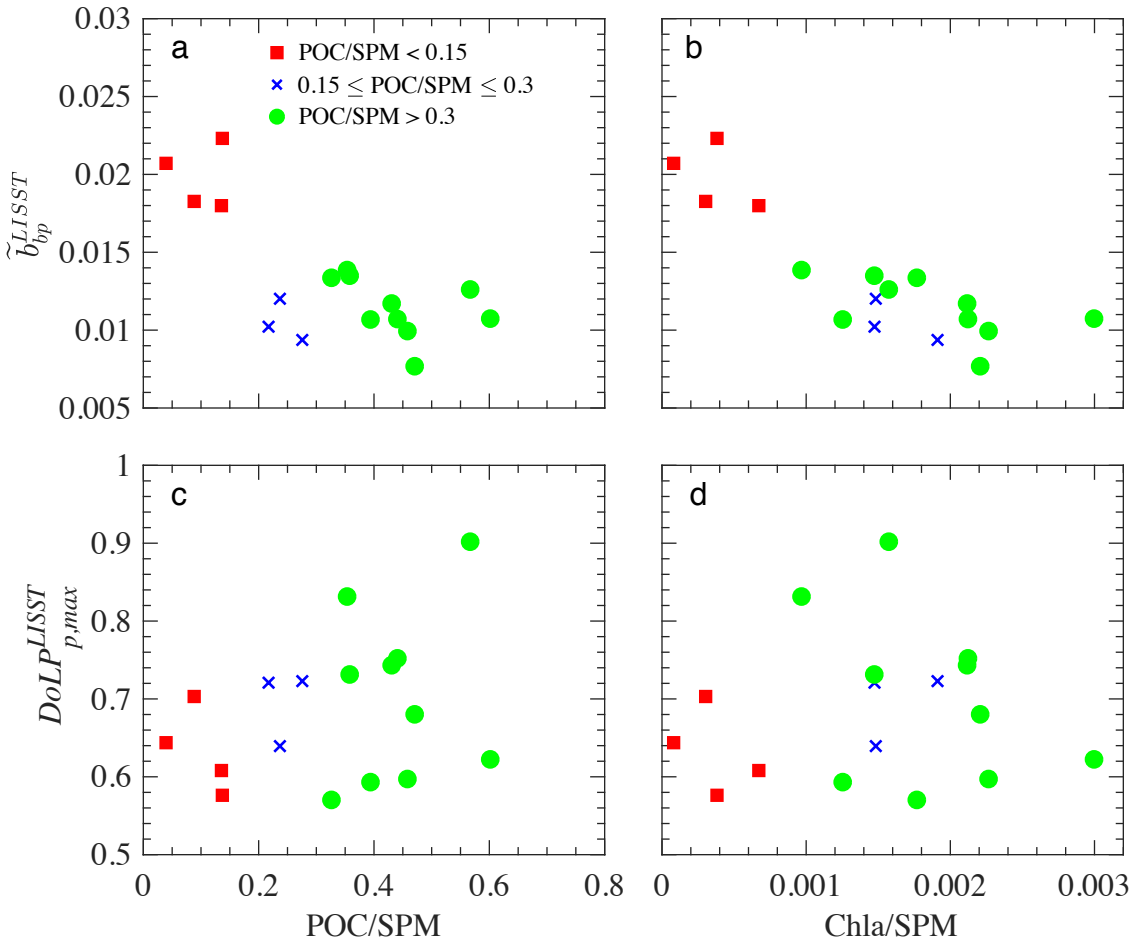

Figure 1.12. LISST-VSF measurements of (**a**,**b**) the particulate backscattering ratio, $\tilde{b}_{bp}^{LISST}$, and (**c**,**d**) the maximum value of the degree of linear polarization of scattered light, $DoLP_{p,max}^{LISST}$, as a function of the POC/SPM or Chla/SPM ratio. The data are divided into three groups defined by the range of POC/SPM as indicated in the legend.

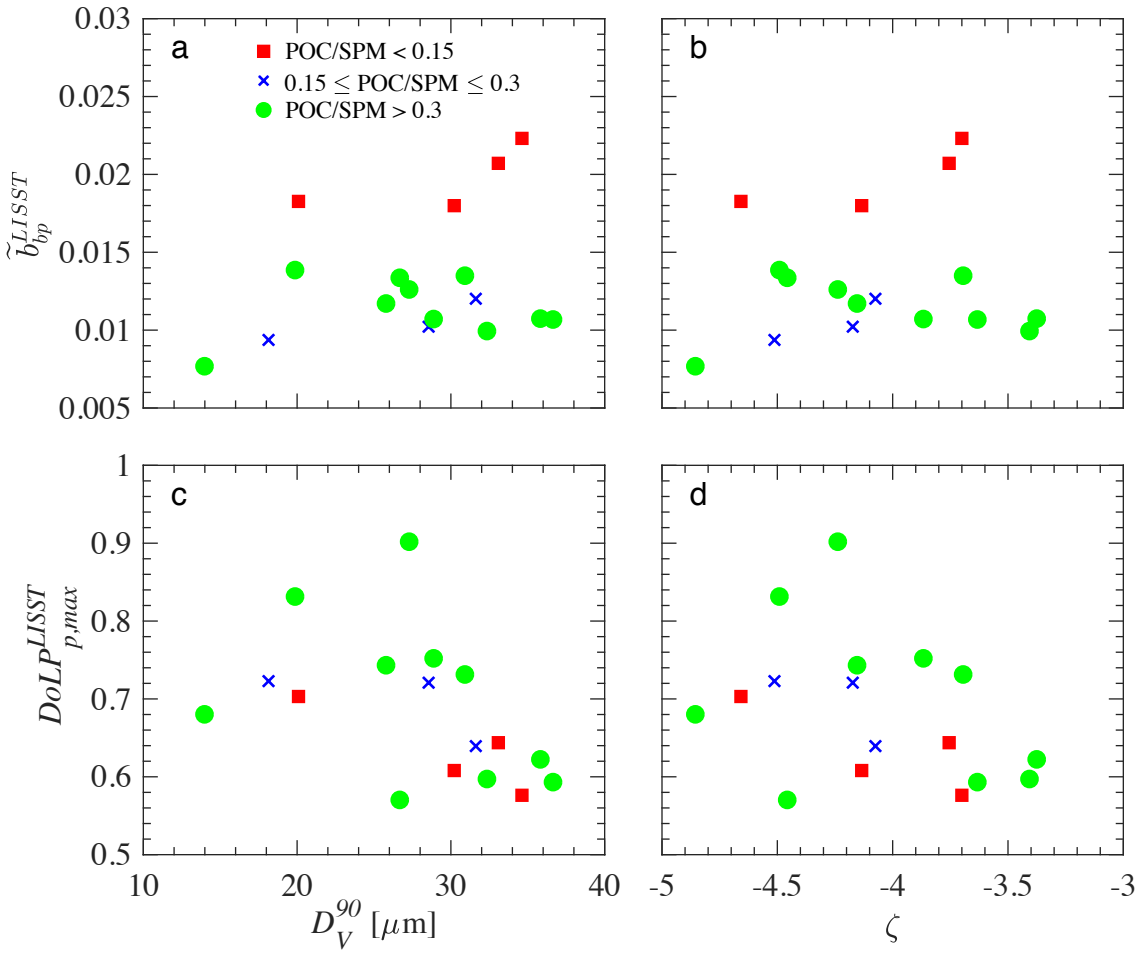

Figure 1.13. Similar to Figure 1.12, but with optical quantities shown as a function of the particle size metrics (**a**,**c**) D_V^{90}, representing the diameter corresponding to the 90th percentile of the particle volume distribution, and (**b**,**d**) ζ, the power law slope of the particle number distribution.

1.7 Tables

Table 1.1. Information on the polystyrene bead size standards used to create laboratory sample suspensions for experiments. The nominal bead diameter (*D*), catalog number, and actual mean diameter $\overline{D}$ (± standard error of estimate) and standard deviation of the mean (*SD*) provided by the manufacturer (Thermo Fisher Scientific, Inc.) is listed. The particulate beam attenuation coefficient at light wavelength 532 nm of the master sample as determined with a spectrophotometer, c_p^{SPEC}, is listed in addition to specific dilution names and factors (e.g., DF1, DF2, etc.) of the master suspension used for LISST-VSF measurements at different PMT gain settings. The dilution factors in italic font denote the experimental data used for generation of the final correction functions CF_f and BF_f, and those in boldface font denote the six examples used for statistical evaluation in Table 1.2.

Nominal *D* [nm]	**Catalog No.**	**$\overline{D}$ [nm]**	***SD* [nm]**	**c_p^{SPEC} [m^{-1}]**	**Dilution Factor (PMT 500)**	**Dilution Factor (PMT 550)**
100	3100A	100 ± 3	7.8	58.63	DF1: 96, DF2: 48.5, *DF3: 32.7*	DF1: 96, ***DF2: 48.5***, *DF3: 32.67*
200	3200A	203 ± 5	5.3	46.26	DF1: 96, *DF2: 48.5, DF3: 32.7*	DF1: 96, *DF2: 48.5,* ***DF3: 32.7***
400	3400A	400 ± 9	7.3	51.44	DF1: 87.4, ***DF2: 44.2***, *DF3: 29.8*	DF1: 87.4
500	3500A	508 ± 8	8.5	20.64	**DF2: 20**	
700	3700A	707 ± 9	8.3	50.93	DF1: 96, **DF2: 48.5**	
2000	4202A	2020 ± 15	21	18.21	**DF2: 20**	

Table 1.2. Statistical results evaluating the comparison of corrected data from the LISST-VSF measurements with reference values obtained from Mie scattering calculations. For β_p^{LISST}, the results are shown for the angular range 3.02–150° which includes the ring data and for the range 16–150° without the ring data. *R* is the Pearson correlation coefficient and the coefficients *A* and *B* are the slope and *y*-intercept, respectively, determined from a type II linear regression between individual pairs of X_i and Y_i values where Y_i represents measured values and X_i reference values. The mean bias (*MB*) was calculated as $1/N \times \sum_{i=1}^{N}(Y_i - X_i)$ and *MR* represents the median ratio of Y_i/X_i. The root mean squared deviation, *RMSD*, was calculated as $\sqrt{\frac{1}{N}\sum_{i=1}^{N}(Y_i - X_i)^2}$, and the median absolute percent difference, *MAPD*, was calculated as the median value of $\left|\frac{Y_i - X_i}{X_i}\right| \times 100$. *N* is the number of data points used in the analysis.

Data	*R*	*A*	*B*	*MB*	*MR*	*RMSD*	*MAPD*	*N*
β_p^{LISST} (w/ rings)	0.987	0.72	0.031 $m^{-1} sr^{-1}$	−0.028 $m^{-1} sr^{-1}$	1.00	0.210 $m^{-1} sr^{-1}$	3.94 %	876
β_p^{LISST} (w/o rings)	0.998	0.96	0.002 $m^{-1} sr^{-1}$	−0.002 $m^{-1} sr^{-1}$	1.00	0.015 $m^{-1} sr^{-1}$	3.39 %	810
$b_{p,150}^{LISST}$	0.995	1.04	−0.048 m^{-1}	−0.007 m^{-1}	1.00	0.043 m^{-1}	2.30 %	20
$b_{bp,150}^{LISST}$	0.999	0.99	0.0001 m^{-1}	−0.001 m^{-1}	1.00	0.006 m^{-1}	3.70 %	20
$DoLP_p^{LISST}$	0.989	0.91	0.046	0.016	0.99	0.065	5.00 %	810

Table 1.3. General information on particle characteristics and median values of optical quantities derived from LISST-VSF measurements for the three example natural seawater samples depicted in Figure 1.11. Values of selected optical quantities estimated from the measurements of Petzold [38] are shown for comparison.

Sample ID	**Chla [mg m^{-3}]**	**SPM [g m^{-3}]**	**POC/SPM [g/g]**	b_p **[m^{-1}]**	$\tilde{b}_{bp}$ **[dim]**	$\frac{\beta_p(45°)}{\beta_p(135°)}$ **[dim]**	$DoLP_{p,max}$ **[dim]**	ψ_{max} **[deg]**
A	0.75	0.36	0.43	0.36	0.012	16.5	0.77	92
B	2.49	1.13	0.47	1.75	0.008	17.1	0.69	96
C	1.21	3.18	0.14	2.23	0.022	12.0	0.58	94
Petzold Measurements								
Clear				0.03	0.015	18.0		
Coastal				0.19	0.009	17.8		
Turbid				1.74	0.020	12.2		

1.8. References

1. Kattawar, G.W.; Adams, C.N. Stokes vector calculations of the submarine light field in an atmosphere–ocean with scattering according to a Rayleigh phase matrix: Effect of interface refractive index on radiance and polarization. *Limnol. Oceanogr.* **1989**, *34*, 1453–1472.

2. Mobley, C.D. *Light and Water: Radiative Transfer in Natural Waters*; Academic Press: San Diego, CA, USA, 1994.

3. Mobley, C.D.; Sundman, L.K.; Boss, E. Phase function effects on oceanic light fields. *Appl. Opt.* **2002**, *41*, 1035–1050.

4. Kattawar, G.W.; Yang, P.; You, Y.; Bi, L.; Xie, Y.; Huang, X.; Hioki, S. Polarization of light in the atmosphere and ocean. In *Light Scattering Reviews 10*; Kokhanovsky, A.A., Ed.; Springer: Berlin, Germany, 2016; pp. 3–39.

5. Babin, M.; Morel, A.; Fournier-Sicre, V.; Fell, F.; Stramski, D. Light scattering properties of marine particles in coastal and open ocean waters as related to the particle mass concentration. *Limnol. Oceanogr*. **2003**, *48*, 843–859.

6. Balch, W.M.; Gordon, R.G.; Bowler, B.C.; Drapeau, D.T.; Booth, E.S. Calcium carbonate measurements in the surface global ocean based on moderate-resolution imaging spectroradiometer data. *J. Geophys. Res.* **2005**, *110*, C07001, doi:10.1029/2004JC002560.

7. Stramski, D.; Reynolds, R.A.; Babin, M.; Kaczmarek, S.; Lewis, M.R.; Röttgers, R.; Sciandra, A.; Stramska, M.; Twardowski, M.S.; Franz, B.A.; et al. Relationships between the surface concentration of particulate organic carbon and optical properties in the eastern South Pacific and eastern Atlantic Oceans. *Biogeosciences* **2008**, *5*, 171–201.

8. Bale, A. J.; Morris, A.W. In situ measurement of particle size in estuarine waters. *Estuar. Coast. Shelf Sci.* **1987**, *24*, 253–263.

9. Agrawal, Y.C.; Pottsmith, H.C. Instruments for particle size and settling velocity observations in sediment transport. *Mar. Geol.* **2000**, *168*, 89–114.

10. Agrawal, Y.C.; Whitmire, A.; Mikkelsen, O.A.; Pottsmith, H.C. Light scattering by random shaped particles and consequences on measuring suspended sediments by Laser Diffraction. *J. Geophys. Res*. **2008**, *113*, C04023, doi:10.1029/2007JC004403.

11. Reynolds, R.A.; Stramski, D.; Wright, V.M.; Woźniak, S.B. Measurements and characterization of particle size distributions in coastal waters. *J. Geophys. Res*. **2010**, *115*, C08024, doi:10.1029/2009JC005930.

12. Wyatt, P.J.; Villalpando, D.N. High-precision measurement of submicrometer particle size distributions. *Langmuir* **1997**, *13*, 3913–3914.

13. Wyatt, P.J. Submicrometer particle sizing by multiangle light scattering following fractionation. *J. Colloid Interface Sci.* **1998**, *197*, 9–20.

14. Uitz, J.; Stramski, D.; Baudoux, A.C.; Reynolds, R.A.; Wright, V.M.; Dubranna, J.; Azam, F. Variations in the optical properties of a particle suspension associated with viral infection of marine bacteria. *Limnol. Oceanogr*. **2010**, *55*, 2317–2330.

15. Morel, A. Diffusion de la lumière par les eaux de mer: Resultats expérimentaux et approche théorique. In *Optics of the Sea*; North Atlantic Treaty Organization AGARD Lecture Series, No. 61; Technical Editing and Reproduction Ltd, London, England, 1973; pp. 3.1.1–3.1.76.

16. Ackleson, S.G.; Spinrad, R.W. Size and refractive index of individual marine particulates: a flow cytometric approach. *Appl. Opt*. **1988**, *27*, 1270–1277.

17. Twardowski, M.S.; Boss, E.; Macdonald, J.B.; Pegau, W.S.; Barnard, A.H.; Zaneveld, J.R.V. A model for estimating bulk refractive index from the optical backscattering ratio and the implications for understanding particle composition in case I and case II waters. *J. Geophys. Res*. **2001**, *106*, 14129–14142.

18. Sullivan, J.M.; Twardowski, M.S.; Donaghay, P.L.; Freeman, S.A. Use of optical scattering to discriminate particle types in coastal waters. *Appl. Opt.* **2005**, *44*, 1667–1680.

19. Zhang, X.; Huot, Y.; Gray, D.J.; Weidemann, A.; Rhea, W.J. Biogeochemical origins of particles obtained from the inversion of the volume scattering function and spectral absorption in coastal waters. *Biogeosciences* **2013**, *10*, 6029–6043.

20. Bohren, C.F.; Huffman, D.R. *Absorption and Scattering of Light by Small Particles*; Wiley: New York, NY, USA, 1983.

21. Bickel, W.S.; Bailey, W.M. Stokes vectors, Mueller matrices, and polarized scattered light. *Am. J. Phys.* **1985**, *53*, 468–478.

22. Kattawar, G.W. Polarization of light in the ocean. In *Ocean Optics*; Spinrad, R.W.; Carder, K.L.; Perry, M.J., Eds., Oxford University Press, New York, NY, USA, 1994; pp. 202–202.

23. Jonasz, M.; Fournier, G.R. *Light Scattering by Particles in Water: Theoretical and Experimental Foundations*. Academic Press: San Diego, CA, USA, 2007.

24. Fry, E.S; Voss, K.J. Measurement of the Mueller matrix for phytoplankton. *Limnol. Oceanogr*. **1985**, *30*, 1322–1326.

25. Quinby-Hunt, M.S.; Hunt, A.J.; Lofftus, K.; Shapiro, D. Polarized-light scattering studies of marine Chlorella. *Limnol. Oceanogr.* **1989**, *34*, 1587–1600.

26. Wyatt, P. J.; Jackson, C. Discrimination of phytoplankton via light-scattering properties. *Limnol. Oceanogr*. **1989**, *34*, 96–112.

27. Shapiro, D.B.; Quinby-Hunt, M.S.; Hunt, A.J. Origin of the induced circular-polarization in the light scattered from a dinoflagellate. In *Ocean Optics X*, Spinrad, R.W., Ed.; SPIE: Bellingham, WA, USA, 1990, Volume 1302, pp. 281–289.

28. Witkowski, K.; Wolinski, L.; Turzynski, Z.; Gedziorowska, D.; Zielinski, A. The investigation of kinetic growth of Chlorella vulgaris cells by the method of integral and dynamic light-scattering. *Limnol. Oceanogr.* **1993,** *38*, 1365–1372.

29. Volten, H.; De Haan, J.F.; Hovenier, J.W.; Schreurs, R.; Vassen, W.; Dekker, A.G.; Hoogenboom, H.J.; Charlton, F.; Wouts, R. Laboratory measurements of angular distributions of light scattered by phytoplankton and silt. *Limnol. Oceanogr.* **1998**, *43*, 1180–1197.

30. Volten, H.; Muñoz, O.; Rol, E.; Haan, J.D.; Vassen, W.; Hovenier, J.W.; Nousiainen, T. Scattering matrices of mineral aerosol particles at 441.6 nm and 632.8 nm. *J. Geophys. Res*. **2001**, *106*, 17375–17401.

31. Volten, H.; Muñoz, O.; Hovenier, J.W.; Waters, L.B.F.M. An update of the Amsterdam light scattering database. *J. Quant. Spectrosc. Radiat. Transf.* **2006**, *100*, 437–443.

32. Svensen, Ø.; Stamnes, J.J.; Kildemo, M.; Aas, L.M.S.; Erga, S.R.; Frette, Ø. Mueller matrix measurements of algae with different shape and size distributions. *Appl. Opt.* **2011**, *50*, 5149–5157.

33. Muñoz, O.; Moreno, F.; Guirado, D.; Dabrowska, D.D.; Volten, H.; Hovenier, J.W. The Amsterdam–Granada light scattering database. *J. Quant. Spectrosc. Radiat. Transf.* **2012**, *113*, 565–574.

34. Liu, J.P.; Kattawar, G.W. Detection of dinoflagellates by the light scattering properties of the chiral structure of their chromosomes. *J. Quant. Spectrosc. Radiat. Transf.* **2013**, *131*, 24–33.

35. Stramski, D.; Boss, E.; Bogucki, D.; Voss, K.J. The role of seawater constituents in light backscattering in the ocean. *Prog. Oceanogr.* **2004**, *61*, 27–56.

36. Hovenier, J.W.; Volten, H.; Muñoz, O.; Van der Zande W.J.; Waters, L.B.F.M. Laboratory studies of scattering matrices for randomly oriented particles: Potentials, problems, and perspectives. *J. Quant. Spectrosc. Radiat. Transf.* **2002**, *79*, 741–755.

37. Kokhanovsky, A.A. Parameterization of the Mueller matrix of oceanic waters. *J. Geophys. Res.* **2003**, *108*, 3175, doi:10.1029/2001JC001222.

38. Petzold, T.J. *Volume Scattering Functions for Selected Ocean Waters*. SIO Ref. 72–78, Scripps Institution of Oceanography Visibility Lab: University of California, San Diego, CA, USA,1972.

39. Beardsley, G.F. Mueller scattering matrix of sea water. *J. Opt. Soc. Am.* **1968**, *58*, 52–57.

40. Kadyshevich, Y.A.; Lyubovtseva, Y.S.; Rozenberg, G.V. Light-scattering matrices of Pacific and Atlantic ocean waters. *Izv. Acad. Sci. USSR Atmos. Oceanic Phys.* **1976**, *12*, 106–111.

41. Kadyshevich, Y.A. Light-scattering matrices of inshore waters of the Baltic Sea. *Izv. Acad. Sci. USSR Atmos. Oceanic Phys*. **1977**, *13*, 77–78.

42. Voss, K.J.; Fry, E.S. Measurement of the Mueller matrix for ocean water. *Appl. Opt.* **1984**, *23*, 4427–4439.

43. Lee, M.; Lewis, M. A new method for the measurement of the optical volume scattering function in the upper ocean. *J. Atmos. Ocean. Technol.* **2003**, *20*, 563–572.

44. Sullivan, J.M.; Twardowski, M.S. Angular shape of the oceanic particulate volume scattering function in the backward direction. *Appl. Opt*. **2009**, *48*, 6811–6819.

45. Tan, H.; Doerffer, R.; Oishi, T.; Tanaka, A. A new approach to measure the volume scattering function. *Opt. Express* **2013**, *21*, 18697–18711.

46. Chami, M.; Thirouard, A.; Harmel, T. POLVSM (Polarized Volume Scattering Meter) instrument: an innovative device to measure the directional and polarized scattering properties of hydrosols. *Opt. Express* **2014**, *22*, 26403–26428.

47. Zhang, X.; Lewis, M.; Lee, M.; Johnson, B.; Korotaev, G. The volume scattering function of natural bubble populations. *Limnol. Oceanogr.* **2002**, *47*, 1273–1282.

48. Twardowski, M.S.; Zhang, X.; Vagle, S.; Sullivan, J.; Freeman, S.; Czerski, H.; You, Y.; Bi, L.; Kattawar, G. The optical volume scattering function in a surf zone inverted to derive sediment and bubble particle subpopulations. *J. Geophys. Res.* **2012**, *117*, C00H17, doi:10.1029/2011JC007347.

49. Slade, W.H.; Agrawal, Y.C.; Mikkelsen, O.A. Comparison of measured and theoretical scattering and polarization properties of narrow size range irregular sediment particles. In *Oceans San Diego*; IEEE: San Diego, CA, USA, 2013; pp. 1–6.

50. Slade, W.H.; Boss, E.S. Calibrated near-forward volume scattering function obtained from the LISST particle sizer. *Opt. Express* **2006**, *14*, 3602–3615.

51. Van de Hulst, H.C. *Light Scattering by Small Particles*; Dover Publications: New York, NY, USA, 1981.

52. McCartney, E.J. *Optics of the Atmosphere: Scattering by Molecules and Particles*; Wiley: New York, NY, USA, 1976.

53. Mishchenko, M.I.; Travis, L.D. Light scattering by polydisperse, rotationally symmetric nonspherical particles: linear polarization. *J. Quant. Spectrosc. Radiat. Transf.* **1994**, *51*, 759–778.

54. Yanamandra-Fisher, P.A.; Hanner, M.S. Optical properties of nonspherical particles of size comparable to the wavelength of light: Application to comet dust. *Icarus* **1999**, *138*, 107–128.

55. Petrova E.V.; Jockers, K.; Kiselev, N.N. Light scattering by aggregates with sizes comparable to the wavelength: An application to cometary dust. *Icarus* **2000**, *148*, 526–536.

56. Muñoz, O.; Volten, H.; Hovenier, J.W.; Min, M.; Shkuratov, Y.G.; Jalava, J.P.; van der Zande, W.J.; Waters, L.B.F.M. Experimental and computational study of light scattering by irregular particles with extreme refractive indices: hematite and rutile. *Astron. Astrophys.* **2006**, *446*, 525–535.

57. Muinonen, K.; Zubko, E.; Tyynelä, J.; Shkuratov, Y.G.; Videen, G. Light scattering by Gaussian random particles with discrete-dipole approximation. *J. Quant. Spectrosc. Radiat. Transf.* **2007**, *106*, 360–377.

58. Zubko, E. Light scattering by irregularly shaped particles with sizes comparable to the wavelength. In *Light Scattering Reviews 6*; Kokhanovsky, A.A., Ed.; Springer: Berlin, Germany, 2012; pp. 39–74.

59. Agrawal, Y.C. The optical volume scattering function: Temporal and vertical variability in the water column off the New Jersey coast. *Limnol. Oceanogr.* **2005**, *50*, 1787–1794.

60. Agrawal, Y.C.; Mikkelsen, O.A. Empirical forward scattering phase functions from 0.08 to 16 deg. for randomly shaped terrigenous 1–21 μm sediment grains. *Opt. Express* **2009**, *17*, 8805–8814.

61. Babin, M.; Stramski, D.; Reynolds, R.A.; Wright, V.M.; Leymarie, E. Determination of the volume scattering function of aqueous particle suspensions with a laboratory multi-angle light scattering instrument. *Appl. Opt.* **2012**, *51*, 3853–3873.

62. Heller, W.; Tabibian, R.M. Experimental investigations on the light scattering of colloidal spheres. II. Sources of error in turbidity measurements. *J. Colloid Sci.* **1957**, *12*, 25–39.

63. Bateman, J.B.; Weneck, E.J.; Eshler, D.C. Determination of particle size and concentration from spectrophotometric transmission. *J. Colloid Sci.* **1959**, *14*, 308–329.

64. Stramski, D.; Babin, M.; Woźniak, S.B. Variations in the optical properties of terrigenous mineral-rich particulate matter suspended in seawater. *Limnol. Oceanogr*. **2007**, *52*, 2418–2433.

65. Woźniak, S.B.; Stramski, D.; Stramska, M.; Reynolds, R.A.; Wright, V.M.; Miksic, E.Y.; Cieplak, A.M. Optical variability of seawater in relation to particle concentration, composition, and size distribution in the nearshore marine environment at Imperial Beach, California. *J. Geophys. Res.* **2010**, *115*, C08027, doi:10.1029/2009JC005554.

66. Bohren, C.F. Multiple scattering of light and some of its observable consequences. *Am. J. Phys.* **1987**, *55*, 524–533.

67. LISST-VSF Multi-angle polarized light scattering meter: User's manual revision A; Sequoia Scientific: Bellevue, WA, USA.

68. Ma, X.; Lu, J.Q.; Brock, R.S.; Jacobs, K.M.; Yang, P.; Hu, X.H. Determination of complex refractive index of polystyrene microspheres from 370 to 1610 nm. *Phys. Med. Biol.* **2003**, *48*, 4165–4172.

69. Morel, A.; Bricaud, A. Inherent optical properties of algal cells including picoplankton: theoretical and experimental results. *Can. Bull. Fish. Aquat. Sci*. **1986**, *214*, 521–559.

70. Van der Linde, D.W. Protocol for determination of total suspended matter in oceans and coastal zones. *JRC Tech. Note I* 1998, *98*, 182.

71. Parsons, T.R.; Maita, Y.; Lalli, C.M. *A Manual of Chemical and Biological Methods for Seawater Analysis*; Elsevier: New York, NY, USA, 1984.

72. Knap, A.; Michaels, A.; Close, A., Ducklow, H.; Dickson, A. *Protocols for the Joint Global Ocean Flux Study (JGOFS) Core Measurements*; UNESCO: Paris, France, 1994.

73. Ritchie, R.J. Universal chlorophyll equations for estimating chlorophylls a, b, c, and d and total chlorophylls in natural assemblages of photosynthetic organisms using acetone, methanol, or ethanol solvents. *Photosynthetica* **2008**, *46*, 115–126.

74. Bader, H. The hyperbolic distribution of particle sizes. *J. Geophys. Res.* **1970**, *75*, 2822–2830. doi:10.1029/JC075i015p02822

75. Beardsley, G.F.Jr; Zaneveld, J.R.V. Theoretical dependence of the near-asymptotic apparent optical properties on the inherent optical properties of sea water. *J. Opt. Soc. Am.* **1969**, *58*, 373–377.

76. Zhang, X.; Fournier, G.R.; Gray, D.J. Interpretation of scattering by oceanic particles around 120 degrees and its implication in ocean color studies. *Opt. Express* **2017**, *25*, A191–A199.

77. Zhang, X.; Hu, L.; He, M. Scattering by pure seawater: Effect of salinity. *Opt. Express* **2009**, *17*, 5698–5710.

78. Reynolds, R.A.; Stramski, D.; Neukermans, G. Optical backscattering by particles in Arctic seawater and relationships to particle mass concentration, size distribution, and bulk composition. *Limnol. Oceanogr*. **2016**, *61*, 1869–1890.

79. Ivanoff, A. Optical method of investigation of the oceans: the p-*ß* diagram. *J. Opt. Soc. Am.* **1959**, *49*, 103–104.

80. Ivanoff, A.; Jerlov, N.; Waterman, T.H. A comparative study of irradiance, beam transmittance and scattering in the sea near Bermuda. *Limnol. Oceanogr.* **1961**, *6*, 129–148.

81. Hatch, T.; Choate, S.P. Measurement of polarization of the Tyndall beam of aqueous suspension as an aid in determining particle size. *J. Franklin Inst.* **1930**, *210*, 793–804.

82. Chami, M.; Santer, R.; Dilligeard, E. (2001). Radiative transfer model for the computation of radiance and polarization in an ocean–atmosphere system: polarization properties of suspended matter for remote sensing. *Appl. Opt.* **2001**, *40*, 2398–2416.

83. Lotsberg, J.K.; Stamnes, J.J. Impact of particulate oceanic composition on the radiance and polarization of underwater and backscattered light. *Opt. Express* **2010**, *18*, 10432–10445.

84. Waterman, T.H. Polarization patterns in submarine illumination. *Science* **1954**, *120*, 927–932.

85. Ivanoff, A. Polarization measurements in the sea. In *Optical Aspects of Oceanography*, Jerlov, N.G., Steeman-Nielsen, E., Eds., Academic Press: London, UK and New York, NY, USA 1974; pp. 151–175.

86. Chami, M. Importance of the polarization in the retrieval of oceanic constituents from the remote sensing reflectance. *J. Geophys. Res.* **2007**, *112*, C05026, doi:10.1029/2006JC003843.

87. Loisel, H.; Duforet, L.; Dessailly, D.; Chami, M.; Dubuisson, P. Investigation of the variations in the water leaving polarized reflectance from the POLDER satellite data over two biogeochemical contrasted oceanic areas. *Opt. Express* **2008**, *16*, 12905–12918.

88. Tonizzo, A.; Gilerson, A.; Harmel, T.; Ibrahim, A.; Chowdhary, J.; Gross, B.; Ahmed, S. Estimating particle composition and size distribution from polarized water-leaving radiance. *Appl. Opt.* **2011**, *50*, 5047–5058.

89. Ibrahim, A.; Gilerson, A.; Chowdhary, J.; Ahmed, S. Retrieval of macro- and micro-physical properties of oceanic hydrosols from polarimetric observations. *Rem. Sens. Environ.* **2016**, *186*, 548–566.

90. Zhai, P.W.; Knobelspiesse, K.; Ibrahim, A.; Franz, B.A.; Hu, Y.; Gao, M.; Frouin, R. Water-leaving contribution to polarized radiation field over ocean. *Opt. Express* **2017**, *25*, A689–A708.

Chapter 2

Assessing the effects of particle size and composition on light scattering through measurements of size-fractionated seawater samples

2.0. Abstract

Measurements of the particulate volume scattering function [$\beta_p(\psi)$] at light wavelength of 532 nm, particle size distribution (PSD), and several metrics of particulate concentration and composition were made on eight contrasting seawater samples from near-shore and coastal oceanic environments including river estuary and offshore locations. Both $\beta_p(\psi)$ and PSDs were measured on original (unfiltered) samples and particle size-fractionated samples obtained through filtration using mesh filters with pore sizes of 5 μm and 20 μm. We present results based on direct size-fractionated measurements and data adjusted for imperfect fractionation, which provide insights into the roles played by particle size and composition in angle-resolved light scattering produced by highly variable natural assemblages of aquatic particles. Despite intricate interplay between the effects of particle size and composition, small particles (< 5 μm in size) consistently produced a major or dominant contribution (~50–80%) to the particulate backscattering coefficient, b_{bp}, in organic, either phytoplankton or non-algal, dominated samples regardless of significant variations in PSD between these samples. The notable exception was a sample dominated by large-celled diatoms from microphytoplankton size range, which exemplifies a scenario when large particles (> 20 μm) can produce a considerable contribution (~40%) to b_{bp}. We also observed a trend for inorganic-dominated samples exhibiting consistently lower contributions (~30−40%) of small particles to b_{bp}. The particle size-based budget for the particulate scattering coefficient, b_p, indicates a significant decrease in the role of small particles accompanied by an increase in the role of larger particles compared to the b_{bp} budget.

2.1. Introduction

The angular distribution of light scattered by natural waters has wide-ranging significance and potential applications in aquatic sciences, especially in oceanography. One of the most fundamental inherent optical properties (IOPs) of seawater is the spectral volume scattering function, $\beta(\psi,\lambda)$ [in units of m^{-1} sr^{-1}], which describes the scattered intensity at light wavelength λ as a function of scattering angle, ψ, per unit incident irradiance per unit volume of water (Mobley 1994). Integrating $\beta(\psi,\lambda)$ over all scattering directions gives the spectral scattering coefficient, $b(\lambda)$ [m^{-1}]. In this integration, it is commonly assumed that light scattering by an assemblage of randomly-oriented scatterers (molecules and particles) in natural waters is azimuthally symmetric about the direction of incident light beam. Similarly, integration within the range of backward scattering angles yields the spectral backscattering coefficient, $b_b(\lambda)$ [m^{-1}]. It is common to include a subscript p in the notation of these inherent scattering properties (and other IOPs) to denote the contribution only by particles in suspension with the contribution of molecular water (subscript w) removed, e.g., $\beta_p(\psi,\lambda) = \beta(\psi,\lambda) - \beta_w(\psi,\lambda)$. As the scattering measurements in this study were made at a single wavelength of 532 nm, we omit λ for brevity hereafter unless otherwise noted.

Because light propagation through the water column depends on scattering, radiative transfer simulations require the input data of the volume scattering function, $\beta(\psi)$, or scattering phase function, $\tilde{\beta}(\psi)$ which is typically defined as $\beta(\psi)$ normalized by b. Such simulations have been used to study numerous problems of ocean optics (Gordon et al. 1974; Mobley et al. 2002; Li et al. 2014) and have also been included in ocean biogeochemical and ecosystem models (Gregg 2002; Mobley et al. 2015). The effect of the angular shape of $\beta(\psi)$ has been explicitly incorporated in an ocean color analytical model which has the potential for improvements of satellite remote

sensing applications (Zaneveld 1995; Twardowski and Tonizzo 2018). Furthermore, light scattering properties depend on the physical and chemical nature of water and its constituents and thus can provide biogeochemically useful information about water composition. For example, the particulate backscattering ratio, b_{bp}/b_p, can provide information about bulk particulate composition such as dominance of organic or inorganic particles in seawater (Twardowski et al. 2001; Boss et al. 2004; Koestner et al. 2018). Inverse methods have also been applied to measurements of $\beta_p(\psi)$ for natural particle assemblages to estimate particulate compositional and size information (Zhang et al. 2013). The particulate scattering and backscattering coefficients have been examined as proxies for estimating the mass concentrations of suspended particulate matter SPM (Babin et al. 2003; Neukermans et al. 2016), particulate inorganic carbon PIC (Balch et al. 1999; 2001), particulate organic carbon POC (Stramski et al. 1999; 2008), and chlorophyll-*a* Chla (Huot et al. 2008; Barbieux et al. 2018) in ocean waters. The spectral slope of backscattering was used for estimating the characteristics of particle size distribution from satellite or in situ measurements (Boss et al. 2001; Kostadinov et al. 2009; Slade and Boss 2015). However, the complexity and variability of natural particulate assemblages impose significant challenges for an understanding of bulk light scattering properties of seawater in terms of detailed particle size and compositional characteristics (Babin et al. 2003; Stramski et al. 2004). This complexity is, for example, reflected in significant variations in the relationships between light scattering properties and measures of phytoplankton and particle concentrations (Huot et al. 2008; Woźniak et al. 2010; Neukermans et al. 2012) and the lack of robust relationship between the spectral slope of b_b and particle size across different water types (Reynolds et al. 2016).

To realize the full potential of applications associated with light scattering in the ocean, further improvements are required in the fundamental understanding of the effects of particle size

and compositional characteristics on variability in scattering across various marine environments. It has recently been demonstrated that classifying samples in terms of the ratio of POC/SPM, which serves as a bulk compositional proxy for the relative organic and inorganic contributions to particulate matter, has the potential to provide improved estimates of particle characteristics from optical measurements including light scattering (Woźniak et al. 2010; Reynolds et al. 2016). This approach deserves further investigation. Further studies of the role of the particle size distribution in light scattering associated with diverse particle assemblages encountered across different marine environments are also needed.

The size of optically significant marine particles varies from submicron range to at least several hundreds of micrometers (Jonasz and Fournier 2007; Davies et al. 2014), thus the particle size distribution (PSD) is a major driver of variability in particulate scattering in the ocean. For example, theoretical modeling of idealized assemblages of homogenous spherical particles obeying a Junge-type power-law of PSD predicts that very small particles in the picoplankton and colloidal size range, i.e., less than about 2 μm in diameter, can be a dominant source of b_{bp} under typical open ocean conditions in the absence of phytoplankton bloom or significant presence of coccolithophores (Stramski and Kiefer 1991). The idealized assumptions about marine particles imply that such theoretical modeling must be interpreted with caution, especially in terms of quantitative predictions for natural particle assemblages, as various scenarios of the scattering dominance by different particle-size fractions or types can be encountered in various environments (Stramski et al. 2004). Theoretical computations have also shown that non-homogenous particles, for example layered spheres, produce enhanced backscattering compared with homogenous spheres (Meyer 1979). This suggests that marine particles > 1 μm in size, especially phytoplankton cells, can play a greater role in b_{bp} within the surface ocean waters than predicted from the

assumption of homogenous spherical particles (Kitchen and Zaneveld 1992; Whitmire et al. 2010). Only a few studies have used an experimental approach based on particle-size fractionation of natural seawater samples to address the role of particle size in backscattering. One such study in the equatorial Pacific Ocean suggested that particles < 3 μm in size contribute significantly to b_{bp}, accounting for over 50% of the bulk signal in most samples (Dall'Olmo et al. 2009). Twelve samples from mainly oligotrophic waters (Chla < 0.25 mg m^{-3}) with low particle concentration were analyzed using a flow-through system with and without a 3 μm cartridge filter. In another study Organelli et al. (2018) also used a flow-through system to collect and filter seawater for measurements of PSD and b_{bp} for 22 samples collected along an Atlantic meridional transect. Compared to Dall'Olmo et al. (2009), a broader range of oceanic conditions was included and Organelli et al. (2018) concluded that particles < 1 μm accounted for about 30–55% of b_{bp}. In both studies, light scattering was measured only at one scattering angle and no significant assessment of the observed variability in light scattering as it relates to particulate characteristics such as size distribution and composition was made. In addition, these studies performed limited investigation into how the reported size-based b_{bp} budgets may have been affected by imperfect fractionation.

To improve our understanding of the effects of particle size and composition on the light scattering properties of seawater we conducted laboratory measurements of $\beta_p(\psi)$ combined with comprehensive characterization of the particulate assemblages of natural seawater samples before and after particle-size fractionation. The experiments were made for eight seawater samples collected near San Diego, California, which represent significant variability in terms of concentration of suspended particles, particle size distribution, and composition as assessed by the contributions of organic vs. inorganic and phytoplankton vs. non-algal particulate components. Unlike previous light scattering studies involving size-fractionation (Dall'Olmo et al. 2009;

Organelli et al. 2018), we investigate the roles of particle size and composition for a broad angular range of light scattering from less than 1º to 150º using a comprehensive suite of parameters for particle characterization in parallel with angle-resolved scattering measurements. The fractionation of samples was made with mesh filters of 5 μm and 20 μm pore sizes, which allows for the investigation of the fraction of particles which are small-sized and large-sized. To our knowledge, the role of large-sized particles (> 20 μm) has not been evaluated experimentally in the past. Our study also includes the assessment of the effects on our results associated with unavoidable limitations of particle fractionation methodology.

2.2. Methods

2.2.1. Water samples

Seawater samples were collected in the region of San Diego, California, from June 2016 through March 2017. Two samples were collected at offshore locations aboard the R/V Sproul in mid-September. One sample was collected ~8 km offshore with Niskin bottles at a depth of ~20 m coinciding with the measurement of maximum chlorophyll-*a* fluorescence. The other sample was collected ~2 km offshore at a near-surface depth using the ship's surface seawater intake. Four near-shore samples were collected at the Scripps Institution of Oceanography (SIO) Pier, three of which were collected during periods of relatively high phytoplankton abundance in summer 2016 and one collected after a significant rain event in March 2017. Two estuarine samples were collected 2 km inland in the San Diego River Estuary at two stages of high tide. The near-shore and estuarine samples were collected at a depth of about 1 m using either a bucket or a 5 L Niskin bottle. Table 2.1 provides additional description of samples with their corresponding ID used throughout the paper.

Approximately 30–40 L of seawater were collected from a single location for each experiment with onshore laboratory analysis completed within 8 hours after sampling except for offshore samples which were completed within 24 hours after sampling. Before analysis, water was stored in 20 L carboys and protected from light. The water in carboys was homogenized by gentle mixing immediately prior to removing samples for subsequent analysis. Special care was taken to ensure that subsamples of seawater used for different measurements and analyses were treated similarly and collected from carboys within one hour of each other. All measurements were typically completed within a 4-hour period.

2.2.2. Particle fractionation

Seawater for each sample was fractionated using high-precision woven nylon or polyester mesh filters with pore sizes of 5 μm and 20 μm (Spectrum Labs). A 20 x 20 cm square of mesh filter was placed in a customized plastic Buchner funnel with a 15-cm diameter opening for each filtration. Mesh filters were sonicated in a 2% acid detergent solution (Citranox) for at least 10 minutes followed by back-flushing with at least 5 L of 0.2 μm-filtered deionized water before each use. After each use, mesh filters were back-flushed with at least 5 L of 0.2 μm-filtered deionized water followed by soaking in 2% Citranox solution overnight.

Both the 5 μm and 20 μm mesh filters did not require any excess pressure beyond the gravitational force of the water head. The 5 μm mesh filter exhibited mild resistance to flow and seawater was trickled into the Buchner funnel at a rate of ~4 mL/s to limit the overall pressure exerted on suspended particles being retained by the filter. The 20 μm mesh did not produce any noticeable resistance to flow and seawater was poured manually in a swirling pattern.

We acknowledge that the fractionation procedure cannot produce sharp cutoffs at the mesh sizes and we thus choose to refer to particles retained on the 20 μm mesh as “large”, particles

collected in the 5 μm filtrate as "small", and those collected in the 20 μm filtrate but retained on the 5 μm mesh as "medium". To provide a quantitative metric of filtration efficiency, we use a nominal filter rating in percent following Sparks and Chase (2015):

$$F_r^{MD} = \left(1 - \frac{emergent\ \#\ particles\ D\ >\ MD}{incident\ \#\ particles\ D\ >\ MD}\right) \times 100\% \quad (2.1)$$

where D [μm] is an equivalent spherical diameter of the center of a size bin used in measurements with the Coulter technique (see below for more details), MD is the diameter of a sphere corresponding to the pore size of the mesh (i.e., 5 μm or 20 μm in our experiments), *incident # particles* refers to concentration of particles in the original sample before filtration (i.e., unfiltered sample), and *emergent # particles* refers to concentration of particles in the filtrate. In an ideal case of perfect fractionation, the numerator in Eq. 2.1 would be zero and hence F_r^{MD} would be 100%.

2.2.3. Particulate mass concentration and composition

The mass concentrations of suspended particulate matter (SPM), particulate organic carbon (POC), and chlorophyll-*a* (Chla) were determined following filtration of each original seawater sample onto 25 mm Whatman glass fiber filters (GF/F) at low (≤ 120 mm Hg) vacuum. Ratios of these mass concentrations additionally serve as proxies of bulk compositional characteristics of the particulate assemblage. Filtration volumes ranged from 200 mL to 1400 mL depending on particle concentration.

The determinations of SPM were made with a standard gravimetric method (van der Linde 1998). We used pre-rinsed (~500 mL 0.2 μm-filtered deionized water), pre-combusted (5 hours at 450° C), and pre-weighed GF/F filters. Filters with retained particles were gently rinsed with 0.2 μm-filtered deionized water to remove residual salt and then dehydrated in a 60° C convection oven for at least 1 hour before weighting with a high-precision (1 μg) microbalance (MT5, Mettler-

Toledo). Filters were then stored in a desiccator and weighed two more times immediately following additional dehydration in oven. The values of SPM [g m^{-3}] were determined by subtraction of the blank filter mass and dividing by the volume of filtered seawater.

POC samples were filtered onto pre-combusted GF/F filters and organic carbon content was determined using a standard high temperature combustion method (Parsons et al. 1984). Filters with retained particles were dehydrated and stored in acid-washed glass scintillation vials before analysis. Following acidification with 150 μL 10% HCl to remove inorganic carbon, the organic carbon mass of each filter was determined with a CEC 440HA Elemental CHN Analyzer (Control Equipment, now Exeter Analytical). The values of POC [mg m^{-3}] were determined by subtracting the average carbon mass of several blank filters and dividing by the volume of filtered seawater.

Chla was measured using a spectrophotometric method. GF/F filters with retained particles were extracted overnight in 90% acetone, centrifuged, and the absorbance of the clarified acetone extract determined in a dual-beam spectrophotometer (Lambda 18, Perkin-Elmer) equipped with a 15-cm integrating sphere (RSA-PE-18, Labsphere). Following subtraction of the blank (90% acetone solution), values of Chla in the acetone extracts were calculated using the 4-band equation of Ritchie (2008) and scaled by filtration volume to obtain the final Chla [mg m^{-3}] in the seawater sample.

For both the SPM and POC measurements, duplicate sample filters were collected and the results averaged to obtain the final estimates of SPM and POC for a given unfiltered seawater sample. Single filters were also collected to determine both SPM and POC for the 5 μm-filtrate of all seawater samples with the exception of one sample (P_N). Determination of Chla for the unfiltered sample was performed using single filters and no determinations were made for the filtrates.

2.2.4. Particle size distribution

The measurements of particle size distribution, PSD, were made using an electronic impedance method with a Multisizer 3 (Beckman Coulter) equipped with a 100 μm aperture which allows particle counting in the size range of volume-equivalent spherical diameters, D, from 2 μm to 60 μm. Within this range, 300 logarithmically-spaced size bins were used to produce high resolution PSDs. A baseline measurement of 0.22 μm-filtered seawater was subtracted from sample measurements. Approximately 10 to 15 replicate measurements of 2 mL subsamples of each original (unfiltered) and two size-fractionated samples (i.e., the 5 μm and 20 μm filtrates) were collected. Care was taken to ensure particles were well mixed and remained in suspension by manual stirring between replicate measurements. After removing outlier measurements, the remaining measurements were summed and divided by the total volume evaluated to produce an average PSD in particle counts per bin per unit volume of seawater.

We report various metrics of the PSD and provide graphical representation of the density function of particle number distribution, $N(D)$ [cm^{-3} μm^{-1}], which results from the normalization of particle number concentration in each size bin by the width of each bin. Assuming spherical shape of particles, the particle volume distributions, $V(D)$, were determined from the number distributions for each sample. From $V(D)$, the percentile-based particle diameters were calculated such as the median diameter, D_v^{50}, and the 90th percentile diameter, D_v^{90}. These parameters have been shown to provide potentially useful metrics in the analysis of relationships between the optical and particle size properties in seawater (Woźniak et al. 2010).

2.2.5. Light scattering by particles

Measurements of the particulate volume scattering function, $\beta_p(\psi)$ [m^{-1} sr^{-1}], were made with the LISST-VSF instrument (Sequoia Scientific) in a laboratory benchtop configuration. For each sample, $\beta_p(\psi)$ was measured on the original (unfiltered) sample and two size-fractionated samples. The LISST-VSF measures angular scattering at light wavelength of 532 nm with an incident laser beam of ~3.2 mm in diameter. The intensity of light scattered was measured at angles ψ between 0.09º and 15.17° with 32 ring detectors and between 14º and 155° with 1° resolution using a roving eyeball sensor (photomultiplier tube; PMT). The geometry of measurement with the roving eyeball sensor results in interrogated sample volumes in the range ~0.1–0.3 cm^3 depending on the scattering angle. The interrogated volume for the ring detectors is somewhat larger because the scattering contributions to these detectors are generated along a more significant portion of the 15 cm pathlength of the instrument. Beam attenuation was also measured over a 15 cm pathlength to provide an estimate of the particulate beam attenuation coefficient, c_p [m^{-1}], and to correct light scattering measurements for attenuation losses along the interrogated path of the sample. The volume of water necessary for benchtop use of our LISST-VSF is ~1.8 L and each measurement takes ~4 seconds. Extra care was taken to thoroughly clean the benchtop chamber before measurements of each unfiltered and size-fractionated sample by flushing with 0.2 μm-deionized water. A thorough analysis of this specific instrument and measurement configuration has been previously performed, including formulation of a calibration correction and validation of $\beta_p(\psi)$ measurements (Koestner et al. 2018). Therefore, the description below emphasizes only some methodological aspects of LISST-VSF measurements conducted in this study.

All reported data of $\beta_p(\psi)$ represent the particulate scattering with molecular water scattering and scattering from very small particles (less than about 0.2 μm) removed from the

sample measurement via subtraction of a baseline measurement on filtered seawater. Approximately 2 L of 0.22 μm-filtered seawater were prepared via two filtrations at low vacuum; first, with a 47 mm diameter GF/F filter and then with a 47 mm diameter 0.22 μm nitrocellulose membrane filter. The 0.22 μm-filtered seawater was recirculated in the LISST-VSF chamber with a peristaltic pump and 0.2 μm Polycap 36 TC cartridge filter (Whatman) for at least 45 minutes to obtain the least contaminated baseline measurement. The particle concentration of the samples was adequate to ensure that measurements satisfy the single-scattering condition (Van de Hulst 1981; Koestner et al. 2018). One sample (E_L) was diluted to reduce c_p to a value < 2 m^{-1} in order to satisfy this condition. Reported results for E_L account for this dilution.

Between four and eight sequences of 50 replicate measurements were collected for each unfiltered and size-fractionated sample with gentle hand mixing between sequences while a 5 cm magnetic stir bar was rotating at very low speed changing direction every 30 seconds. Thus, the final results of $\beta_p(\psi)$ are based on 200–400 replicate measurements depending on the sample. As a result, the total volumes interrogated with the eyeball sensor in the analysis of our samples varied between ~20 and 120 cm^3 depending on the eyeball scattering angle, and were somewhat larger for the ring detectors. The determinations of final $\beta_p(\psi)$ involved quality control of replicate measurements, removing outliers potentially affected by measurement artifacts, and then deriving the median value at each angle from the remaining measurements.

To estimate the b_p and b_{bp} from the measured $\beta_p(\psi)$, an extrapolation procedure has been used to provide data within the angular range 151–180° as described in Koestner et al. (2018). In brief, a factor κ was determined to estimate the contribution of scattering within the range 151–180° to b_{bp} by finding the best fit function to our measured $\beta_p(\psi)$ between 90º and 150° and then

extrapolating the fit function to 180°. Having determined b_p and b_{bp}, the backscattering ratio was calculated as $\tilde{b}_{bp} = b_{bp}/b_p$.

2.2.6. Light absorption by particles

For the measurement of spectral absorption coefficient of particles, $a_p(\lambda)$ [m^{-1}], unfiltered seawater samples were filtered onto 25 mm GF/F filters at low vacuum. Filtration volumes ranged from 100 mL to 800 mL depending on particle concentration in the samples. The $a_p(\lambda)$ coefficient was determined in the spectral range from 300 to 850 nm at 1 nm intervals using a Lambda 18 UV/VIS spectrophotometer (Perkin Elmer) equipped with a 15 cm integrating sphere (RSA-PE-18, Labsphere). In these measurements we used a special "inside-sphere" configuration of the filter-pad technique with a sample filter placed inside the integrating sphere, which efficiently minimizes the scattering error (Röttgers and Gehnke 2012; Stramski et al. 2015). Duplicate spectral scans were made and averaged for two orientations of the filter to account for any spatial inhomogeneity of particulate matter retained on the filter. An average baseline obtained from measurements of several blank filters saturated with 0.22 μm-filtered seawater was subtracted from the measurements of sample filters. The calculation of $a_p(\lambda)$ involved the use of the pathlength amplification correction recommended by Stramski et al. (2015).

Following the measurement of $a_p(\lambda)$, the sample filters were immediately subject to treatment with 95% methanol which aims at removing the absorption contribution by extractable phytoplankton pigments (Kishino et al. 1985). The methanol-treated filters were then measured with the same inside-sphere spectrophotometric configuration. The result of this measurement is typically referred to as the spectral absorption coefficient of non-algal particles or detrital particles, which is often denoted by $a_d(\lambda)$. The final $a_p(\lambda)$ and $a_d(\lambda)$ spectra were obtained by smoothing

the respective spectral curves with a 5-nm moving average and correcting the $a_d(\lambda)$ spectra with an offset which ensured that the $a_d(\lambda)$ values match the $a_p(\lambda)$ values in the near-infrared spectral region (775–800 nm). As a final step of absorption data processing, the spectral absorption coefficient of phytoplankton was calculated as $a_{ph}(\lambda) = a_p(\lambda) - a_d(\lambda)$.

2.2.7. Light scattering budget based on particle-size fractionation

The measurements of $\beta_p(\psi)$ on unfiltered and size-fractionated samples allow the calculation of a light scattering budget based on particle size. Specifically, we define the scattering budget for $\beta_p(\psi)$ associated with small, medium, and large particle-size fractions as follows:

$$\beta_{ps}(\psi) = \beta_p(\psi)[5\ \mu\text{m filtrate}],$$

$$\beta_{pm}(\psi) = \beta_p(\psi)[20\ \mu\text{m filtrate}] - \beta_p(\psi)[5\ \mu\text{m filtrate}],$$

$$\beta_{pl}(\psi) = \beta_p(\psi)[\text{unfiltered}] - \beta_p(\psi)[20\ \mu\text{m filtrate}], \quad (2.2)$$

where subscripts *s*, *m*, and *l* stand for small, medium and large particle-size fractions, respectively, and [5 μm filtrate], [20 μm filtrate], and [unfiltered] refer to the type of sample used in the measurement of $\beta_p(\psi)$. Note that the lower particle size limit in our measurements is about 0.2 μm because the baseline measurement was made with the 0.22 μm filtered seawater. We also applied the same scheme and notation of scattering budget for b_p and b_{bp}. The percent contributions by each particle-size fraction to total particulate scattering by unfiltered samples were also computed for $\beta_p(\psi)$, b_p, and b_{bp}. For example, the percent contribution of the small particle-size fraction to total b_{bp} of unfiltered sample is $100 \times (b_{bps} / b_{bp})$.

2.2.8. Adjustment for imperfect particle-size fractionation

An analysis to investigate the effect of imperfect fractionation on the results for b_p and b_{bp} budgets was performed using theoretical light scattering computations for measured and idealized PSDs. We made these calculations using a particle scattering model of Xu et al. (2017) under the assumption that scattering calculations for hexagonally-shaped particles can reproduce angular light scattering by natural assemblages of marine particles more adequately than calculations for spherical particles. Adjustment factors describing the fractional difference in theoretical light scattering for idealized fractionation relative to theoretical scattering for actual fractionation were determined as follows:

$$\xi_x = \frac{b_{px}^I}{b_{px}^M} \tag{2.3}$$

$$\xi_{bx} = \frac{b_{bpx}^I}{b_{bpx}^M} \quad , \tag{2.4}$$

where subscript *x* is the particle-size fraction (*s*, *m*, or *l*), ξ_x and ξ_{bx} are the adjustment factors for b_{px} and b_{bpx}, respectively, and superscript *I* or *M* denotes whether the ideal or measured PSD was used as input for the scattering calculations. By ideal, we mean the PSD corresponding to a hypothetical perfect size-fractionation with fractionation efficiency F_r^{MD} of 100% (see Eq. 2.1) and without any effect on particles smaller than the pore size of the mesh filter. Accordingly, the ideal PSD of 5 μm filtrate is equivalent to the measured PSD of unfiltered sample for all size bins associated with particles smaller than 5 μm in diameter and has null particle concentration for all size bins larger than 5 μm. Similarly, the ideal PSD of 20 μm filtrate is equivalent to the measured PSD of unfiltered sample for all size bins associated with particles smaller than 20 μm in diameter and has null particle concentration for all size bins larger than 20 μm.

Because the particle size measurements covered the range 2–60 μm, for the purpose of this analysis we extrapolated the measured PSDs down to 0.2 μm and up to 200 μm which improves the representation of optically significant size range. Extrapolations were performed by determining a slope parameter of power function fit to the measured PSD. The extrapolation from 2 μm to 0.2 μm used a slope parameter determined from size bins between 2.1 μm and 3.5 μm and extrapolation from 60 μm to 200 μm used a slope parameter determined from bins between 20 μm and 55 μm. Note that the idealized PSDs for 5 μm and 20 μm filtrates do not require an independent extrapolation to 0.2 μm because below 5 μm and 20 μm these PSDs are identical to the measured PSDs of unfiltered samples including their extrapolated portions to 0.2 μm.

To compute theoretical scattering and backscattering coefficients for our extrapolated measured and idealized PSDs, we first calculated $\beta_p(\psi)$ for each PSD. Using an idealized PSD for an example,

$$\beta_p^I(\psi, n) = \sum_{D=0.2\ \mu m}^{D=200\ \mu m} N^I(D)\Delta D\ \sigma_b(\psi, n, D)\ , \tag{2.5}$$

where D is an equivalent spherical diameter of the center of a given size bin [m], ΔD is the width of the bin [m], $N^I(D)\Delta D$ is the particle number concentration [m^{-3}] in the bin as obtained from idealized PSD, n is the assumed complex refractive index of particles relative to water, and σ_b is the differential scattering cross section [$m^2\ sr^{-1}$] calculated from the particle scattering model (Xu et al. 2017). We integrated the theoretical $\beta_p(\psi)$ within the angular range from 0.09º to 150º of LISST-VSF instrument and used the κ determined from the measured $\beta_p(\psi)$ (as described above) to derive theoretical values of b_p and b_{bp}. Following Eq. 2.2, we then determined the necessary inputs for Eq. 2.3 and 2.4 and subsequently the corresponding ξ_x and ξ_{bx}.

For each sample, these calculations were repeated for five values of the real part of refractive index which were chosen to reasonably cover a range of the bulk refractive index for natural assemblages of marine particles (Zaneveld et al. 1974; Jonasz and Fournier 2007). For samples dominated by organic particles with the largest contribution of phytoplankton (P_N, P_N, P_D, and O_C as described below in the Results section), we used the refractive index relative to water from 1.03 to 1.07 with a 0.01 step (Aas 1996; Stramski et al. 2001). For samples dominated by inorganic particles with the lowest contribution of phytoplankton (E_L and E_H) we used the values from 1.09 to 1.13 with a step of 0.01 (Carder et al. 1974; Woźniak and Stramski 2004). For the two remaining samples with intermediate contribution of phytoplankton (P_R and O_S), we used the values from 1.06 to 1.10 with a step of 0.01. In all these calculations, we used one value of the imaginary part of refractive index of 0.0005 which reasonably represents weak absorption at 532 nm.

For each sample the final adjustment factors ξ_x and ξ_{bx} were determined for each particle-size fraction as the average of the adjustment factors determined from calculations made for all five values of the refractive index. The final ξ_x and ξ_{bx} were multiplied by our LISST-VSF measured b_{px} and b_{bpx} to yield a final result of our analysis which provides an assessment of the potential effect associated with imperfect fractionation. Using small particle-size fraction as an example,

$$b_{ps}^{*} = b_{ps}\,\xi_s \tag{2.6}$$

$$b_{bps}^{*} = b_{bps}\,\xi_{bs}\,, \tag{2.7}$$

where * indicates that the measured scattering and backscattering coefficients have been adjusted for imperfect fractionation. Compared to the actual size-fractionated measurements the adjusted

coefficients b_{ps}^{*} and b_{bps}^{*} refer more rigorously to particles smaller than 5 μm in diameter, b_{pl}^{*} and b_{bpl}^{*} refer to particles larger than 20 μm, and b_{pm}^{*} and b_{bpm}^{*} refer to particles in the 5–20 μm range.

Finally, using the scattering and backscattering coefficients adjusted for imperfect fractionation, the adjusted percent contributions of each particle-size fraction to total b_p and b_{bp} of unfiltered samples were computed. For example, the adjusted percent contribution of small particle-size fraction, which in this case corresponds more rigorously to particles < 5 μm in size, to total b_{bp} of unfiltered sample is $100 \times (b_{bps}^{*} / b_{bp})$.

2.3. Results

2.3.1. Assessment of particle-size fractionation

Filtration efficiency for natural assemblages of aquatic particles is complex and depends on many factors including filter type, loading rate, and particle composition and shape (Sparks and Chase 2015). As a means of assessing the particle-size fractionation through filtration with the 5 μm and 20 μm mesh filters, we compared measurements of PSD on the unfiltered samples with size-fractionated samples. Figure 2.1 shows an example of such measurements for the E_H sample. In general, there is adequate retention by the mesh of particles larger than the pore size of the mesh. However, fractionation is non-ideal in the sense that some particles smaller than the pore size are retained on the mesh and some particles larger than the pore size are found in the filtrate. For example, in Fig. 2.1 we see that retention of particles by the 20 μm mesh starts to increase significantly around 10 μm and particles larger than 20 μm are still present in the filtrate (solid green line), albeit at much lower concentrations compared with the unfiltered sample (solid red line). Under the condition of ideal fractionation, the PSD of the 20 μm filtrate would be identical to that for the unfiltered sample in the range $D < 20$ μm and the particle concentration would drop

to zero at 20 μm and beyond (dashed green line). Similarly, Fig. 2.1 shows that the 5 μm filtrate contains particles larger than 5 μm although at significantly lower concentrations compared with the unfiltered sample. While the filtration efficiency may be affected by several factors, it is also critical to recognize that our PSDs are determined for volume-equivalent spherical diameters so the unknown degree of non-sphericity of particles suspended in the samples can influence the fractionation results.

Filter ratings for the 5 μm and 20 μm mesh filters calculated following Eq. 2.1 are shown in Table 2.2 for all eight samples examined in this study. We also display the particle diameter associated with F_r = 80% as an additional metric for assessing filtration efficiency. This value denotes the threshold diameter at which 80% of the total counts of particles larger than this threshold have been retained on the mesh and hence removed from the liquid phase of the sample during fractionation. Although this 80% threshold is chosen somewhat arbitrarily it provides a measure of particle diameter at which substantial fractionation is achieved.

Data in Table 2.2 show significant retention of particles > 5 μm by the 5 μm mesh with F_r^5 ranging from 21% to 60%. The threshold diameter associated with 80% retention is less than 16 μm with the exception of two offshore samples. The 20 μm mesh shows a larger range of filter rating, F_r^{20}, compared with that for the 5 μm mesh. The threshold diameter associated with 80% retention of particles by the 20 μm mesh is typically about 30 μm with the exception of three samples with values exceeding 40 μm. The evaluation of the 20 μm mesh is complicated by the fact that particles with D > 20 μm occur typically at very low concentrations in the samples (< 10 particles cm^{-3} μm^{-1}) so the particle counting statistics obtained with the Coulter technique are typically limited for these relatively large diameters. In addition, particles with D > 60 μm were beyond the size range of our PSD measurements. We also note one peculiar case (O_S) which has

a negative F_r^{20} value indicating more particles with $D > 20$ μm in the 20 μm filtrate than in the unfiltered sample. This may result from low particle counts, possible disruption of larger particle aggregates, or both. Nonetheless, the diameter associated with 80% retention is 41 μm in this case.

Not surprisingly, the results from this analysis support the notion that realistically achievable efficiencies of particle-size fractionation can differ considerably from an ideal fractionation scenario (Sheldon 1972; Logan 1993), even if seawater samples are subject to gentle filtration through high-precision mesh filters with relatively large pore size as was done in the present study. Nevertheless, we consider such fractionation a useful experimental approach for addressing the main objectives of our study because the fractionation produces a large change in the PSD which is consistent with the pore size of the filter. However, because the pore size of the filter cannot be used in a quantitative sense as a strict cutoff size in the PSD, the particle-size fractions obtained from measurements on 5 μm filtrates, 20 μm filtrates, and unfiltered samples are qualitatively referred to as representing small, medium, and large particles as has been already explained in relation to Eq. 2.2.

2.3.2. Particle size and composition characteristics

The measured particle size distributions of the eight seawater samples are shown in Fig. 2.2. Each panel includes the additional PSD measurements for the two size-fractionated samples. The particle number concentrations span nearly 7 orders of magnitude within the measured size range 2–60 μm with the P_N and E_L samples exhibiting the highest concentrations approaching or surpassing 10^5 particles cm^{-3} μm^{-1} at a diameter of 2 μm. None of the unfiltered samples (red lines in Fig. 2.2) appear to obey a Junge-type size distribution with a single slope of the log-log plot of PSD over the measured size range. In all cases the slope exhibits significant changes as a function of particle diameter and in some cases large features including maxima (e.g.,

P_N, P_M, and P_D) are superimposed on the general trend of decreasing particle concentration with increasing particle diameter. These results support earlier observations that the Junge-type distribution with a single slope often provides an inadequate approximation of PSD of marine particles (Jonasz and Fournier 2007; Reynolds et al. 2010; 2016). As expected, the deviations from a single slope distribution are much more pronounced for the size-fractionated samples which can also exhibit significant features, especially in some 20 μm filtrates.

Characterization of the PSDs using the percentile particle diameters, $D_v^{50}$and D_v^{90}, is provided in Table 2.3 for the unfiltered samples and the small particle-size fraction corresponding to the 5 μm filtrates. The variations in $D_v^{50}$and D_v^{90} between the samples reflect varying contributions of small vs. large particles to the PSD. For example, the unfiltered samples P_D, P_R, and E_H have D_v^{90} > 30 μm indicating a significant contribution of large-sized particles while samples P_N, E_L and O_S have D_v^{90} close to or less than 20 μm indicating a greater role of small-sized particles. D_v^{50} is also useful in interpreting the PSD of unfiltered samples. For example, sample O_C has a lower D_v^{90} than sample P_M; however, D_v^{50} is higher for O_C indicating that small-sized particles play less significant role in O_C compared to P_M. Among the eight examined samples of unfiltered seawater, sample P_N has the greatest role of small-sized particles (the lowest values of $D_v^{50}$and D_v^{90}) and sample P_D the greatest role of large-sized particles (the highest values of $D_v^{50}$and D_v^{90}). As expected, data for small-sized particles after fractionation with the 5 μm mesh indicate a decrease in D_v^{50} and D_v^{90} compared with the corresponding unfiltered samples. For example, D_v^{50} is less than 7.5 μm for the small-particle fraction of all samples. It is of interest to note that medium or large-sized particles may still play a role in the small-particle fraction of some samples as suggested by relatively large values of D_v^{90}, especially 24.9 μm for E_H and 18.1 μm for P_D.

Table 2.3 also provides a comparison of samples in terms of particle mass concentration and composition characteristics. SPM, POC, and Chla serve as metrics of bulk concentration of total particulate matter, organic particulate matter, and phytoplankton, respectively. The ratios POC/SPM, Chla/SPM, and $a_{ph}(440)/a_p(440)$ are used as metrics of composition of particulate matter. Specifically, POC/SPM provides a proxy for contributions of organic vs. inorganic particles to total mass of particulate matter. Both Chla/SPM and $a_{ph}(440)/a_p(440)$ provide proxies for contributions of phytoplankton vs. non-algal particles although the former in the context of particulate mass concentration and the latter in the context of particulate absorption. In Table 2.3 all these concentration and composition parameters are listed for unfiltered samples and some parameters are also provided for the small particle-size fraction. The spectral information on the ratio $a_{ph}(\lambda)/a_p(\lambda)$ for unfiltered samples is also depicted in Fig. 2.3.

Among the eight original (unfiltered) samples examined, the offshore samples (O_S and O_C) have the lowest SPM (~0.5 g m^{-3} or less) and the samples collected in the San Diego River Estuary (E_L and E_H) have the highest SPM in the range from about 3 to 10 g m^{-3}. The samples from the SIO Pier have intermediate values of SPM. The offshore samples also have the lowest POC and Chla. The offshore values of Chla ranged from about 0.5 to 0.75 g m^{-3}, which is significantly higher than the average near-surface Chla of about 0.2 mg m^{-3} within the global ocean (Gregg and Conkright 2002). Only one SIO Pier sample (P_R) has POC and Chla that are comparable to the offshore values; the remaining samples are characterized by significantly higher values, including Chla > 2 mg m^{-3} for P_N, P_D, and E_L. These data indicate that in terms of particle concentration, our samples are not representative of vast areas of oligotrophic open ocean where Chla is less than 0.5 mg m^{-3}.

The composition of particulate assemblages also varies significantly among the unfiltered samples as characterized by the large range of POC/SPM from 0.09 to 0.6, i.e. from inorganic-dominated (E_L) to highly organic-dominated (P_D). The samples from San Diego River Estuary are inorganic-dominated with the lowest POC/SPM. Despite the relatively high Chla, we presume phytoplankton to have minimal relative contribution to E_L and E_H as indicted by the lowest Chla/SPM and $a_{ph}(440)/a_p(440)$ values (see also the spectra $a_{ph}(\lambda)/a_p(\lambda)$ in Fig. 2.3). Only one SIO Pier sample (P_R) has comparatively low POC/SPM of 0.14; the remaining samples have significantly higher values indicating a major or dominant role of organic particles.

Two SIO Pier samples (P_N and P_D) are totally dominated by organic matter with POC/SPM in the range 0.47–0.60. These samples also have relatively high values of Chla/SPM and $a_{ph}(\lambda)/a_p(\lambda)$ indicating a dominant role of phytoplankton. We use some ancillary information (not shown) to help further characterize these samples. The P_N sample is most likely nano- or perhaps even picophytoplankton dominated. We note that the highest concentration of picoeukaryotes observed with flow cytometry measurements during summer 2016 (Brian Palenik, personal communication) corresponded to the period of collecting the P_N sample. Despite a conspicuous particle (most likely phytoplankton) population near 25 μm in the PSD of P_N (Fig. 2.2), half of the measured particle volume is associated with particles smaller than about 5 μm (Table 2.3) which, along with very high $a_{ph}(440)/a_p(440)$, supports the major role of small-sized phytoplankton cells in this sample. The P_D sample is considered to represent highly productive conditions related to the strong presence of microphytoplankton. This conjecture is supported by observations of an abundance of the chain-forming diatom *Hemiaulus hauckii* with the Scripps Plankton Camera System operated by the Jaffe Laboratory for Underwater Imaging during the time of collecting our P_D sample. This is also consistent with the PSD of P_D which

shows a large particle population centered around 30 μm. These diatom chains consist of individual cells of about 15 μm in base diameter by 100 μm in length which produces a volume-equivalent spherical diameter of about 32 μm.

The offshore samples O_S and O_C are also highly organic-dominated with POC/SPM ranging from 0.35 to 0.43. However, as indicated by Chla/SPM and $a_{ph}(\lambda)/a_p(\lambda)$ the role of phytoplankton in the particulate assemblage of surface sample O_S is significantly reduced compared to sample O_C that was collected within the subsurface chlorophyll maximum. We therefore presume O_S to be mostly organic and non-algal in nature while O_C is phytoplankton dominated.

Our analysis also includes one SIO Pier sample (P_M) which has an intermediate value of POC/SPM of 0.22. This value indicates a major role of organic particles with a non-negligible effect of inorganic particles. This particulate assemblage also has the second highest ratio of $a_{ph}(440)/a_p(440)$ of 0.77 (see also Fig. 2.3) suggesting a very important role of phytoplankton.

Table 2.3 also includes SPM, POC, and POC/SPM data for the small particle fractions corresponding to the 5 μm filtrates. Based on these data the percent contribution of SPM associated with the small particle fraction to the total SPM associated with the unfiltered sample ranges between 13% and 67%. For POC this range is 34% to 81%. For samples P_M, O_S, and O_C over half of the total SPM and POC is associated with small particle fraction. With the exception of one sample (P_D), the ratio POC/SPM is higher in the small particle fraction compared with unfiltered sample, indicating that the small particle fraction is usually more organic than the entire particulate assemblage. For example, the POC/SPM value for the small particle fraction of sample E_L increased almost 3-fold compared with the entire particulate assemblage (0.24 vs. 0.09), suggesting that while the entire assemblage is inorganic-dominated, the small particle fraction is

organic-dominated and therefore the medium and large-sized particles are even further dominated by inorganic particles (i.e., POC/SPM < 0.09). A similar trend is observed for sample P_R which exhibits an important role of inorganic particles in its unfiltered assemblage.

2.3.3. Particulate scattering properties

Figure 2.4 shows the particulate volume scattering functions, $\beta_p(\psi)$, and scattering phase functions, $\tilde{\beta}_p(\psi)$, measured on the eight unfiltered seawater samples. The San Diego River Estuary samples have the largest magnitude of $\beta_p(\psi)$ for nearly all scattering angles while offshore samples have the lowest values (Fig. 2.4a,b). Although the angular scattering patterns share the common features of a strong peak at forward angles and flattening in the backscattering region ψ > 100º, which are characteristic for natural assemblages of aquatic particles (Morel 1973; Jonasz and Fournier 2007; Sullivan and Twardowski 2009), there are significant differences amongst our samples in the angular shape of scattering as shown by the scattering phase functions (Fig. 2.4c,d). In particular, the $\tilde{\beta}_p(\psi)$ functions of the estuary samples exhibit enhancements within the range encompassing intermediate and backscattering angles, ψ > 45º. The SIO Pier samples generally have the lowest values of $\tilde{\beta}_p(\psi)$ in this range of scattering angles while the offshore samples have the intermediate values. Within the near-forward scattering region where ψ is less than about 10º, the angular shapes of $\tilde{\beta}_p(\psi)$ are generally similar between the samples, although the SIO Pier sample P_N stands out in this region with enhancement between about 2º and 8º and a flattening for ψ < 1º, while data for all other samples continue to rise more substantially with further decrease in scattering angle (Fig. 2.4d).

Table 2.4 shows b_p and b_{bp} computed from the measured β_p as well as the backscattering ratio, $\tilde{b}_{bp}$, for the unfiltered samples and 5 μm filtrates (i.e., small particle fraction). The b_p and

b_{bp} coefficients generally follow the trends observed in the magnitude of $\beta_p(\psi)$ as displayed in Fig. 2.4a,b, while $\tilde{b}_{bp}$ generally reflects the variations in $\tilde{\beta}_p(\psi)$ shown in Fig. 2.4c,d. The estuary samples (E_L and E_H) have the highest values for both b_p and b_{bp}, which is consistent with the highest particle mass concentration of these samples (SPM in Table 2.3). The offshore samples (O_S and O_C) have the lowest values of b_p and b_{bp}, which is consistent with the lowest values of SPM for these samples. For the SIO Pier samples, b_p and b_{bp} assume intermediate values between the estuary and offshore samples. There are, however, notable differences between the pier samples. For example, whereas b_{bp} for P_N and P_R are nearly identical, b_p for P_N is over twice as large as it is for P_R. The P_D sample has the lowest values of b_p and b_{bp} among the pier samples, which is especially well pronounced for b_{bp}.

The backscattering ratio $\tilde{b}_{bp}$ varies over a 2.75-fold range between 0.008 for P_N and 0.022 for E_H. This range is consistent with earlier observations of $\tilde{b}_{bp}$ in different marine environments (Boss et al. 2004). The most inorganic-dominated samples with the lowest POC/SPM ratio, P_R, E_L, and E_H, have the highest $\tilde{b}_{bp}$values, which suggest that these assemblages are dominated by particles having a relatively high refractive index (Twardowski et al. 2001). The sample P_N with the lowest $\tilde{b}_{bp}$ is highly organic and phytoplankton-dominated (Table 2.3). Interestingly, although P_N also has the lowest values of particle size metrics as shown in Table 2.3, this relative importance of small particles does not seem to have a clear enhancement effect on $\tilde{b}_{bp}$. We also recall that, in contrast to other samples, P_N exhibits enhancement in the phase function $\tilde{\beta}_p(\psi)$ between about 2º and 8º (Fig. 2.4d), which may contribute to lower $\tilde{b}_{bp}$ by means of increased b_p.

Data in Table 2.4 also show that the $\tilde{b}_{bp}$ values of the small particle-size fraction are generally very similar (to within ±0.001) to the values of unfiltered samples. The only exception

is sample P_R for which $\tilde{b}_{bp}$ of the small particle-size fraction decreased by 0.004 compared to the unfiltered sample. This sample is characterized by the noteworthy increase of POC/SPM in the small size fraction compared to the unfiltered sample (0.24 vs. 0.14, Table 2.3). Nevertheless, the interpretation of the potential effect of changes in particle composition on $\tilde{b}_{bp}$ of sample P_R as a result of size fractionation is not straightforward because most other samples also showed an increased POC/SPM in the small size fraction (Table 2.3). In addition, $\tilde{b}_{bp}$ is dependent on particle size which, on average, is smaller in the small particle-size fraction than the unfiltered sample (Table 2.3) and, hence, expected to reduce $\tilde{b}_{bp}$ (Morel and Bricaud 1986).

With regard to data for the small particle-size fraction, Table 2.4 also shows an expected decrease in the magnitudes of b_p and b_{bp} compared with the unfiltered samples. This reduction is a component of the particle size-based scattering budget which is discussed in greater detail in the next section. In brief, the data for the eight examined samples displayed in Table 2.4 indicate a significant range in the extent to which b_p and b_{bp} are reduced in the small particle-size fraction compared to the unfiltered samples. For example, this reduction for backscattering is only about 20–30% for P_N, O_S, and O_C and as much as 65–70% for E_L and E_H. This result indicates that our study includes a range of contrasting samples with highly different scenarios for particulate backscattering in terms of the roles of the small particle-size fraction.

Figure 2.5 shows the relative contributions of small [$\beta_{ps}(\psi)$], medium [$\beta_{pm}(\psi)$], and large [$\beta_{pl}(\psi)$] particle-size fractions to the total particulate volume scattering function, $\beta_p(\psi)$, for each experiment using the notation described in Eq. 2.2. Generally, the small particles dominate $\beta_p(\psi)$ at nearly all scattering angles for all samples except E_L and E_H. Samples P_N and O_C exhibit the highest contributions of $\beta_{ps}(\psi)$ to $\beta_p(\psi)$, generally greater than 75%, and samples P_M and O_S also have very high contributions generally in the range of 65−75%. For samples P_D and P_R, the

contributions vary between about 40% and 55%. For sample E_L the scattering by medium-sized particles, $\beta_{pm}(\psi)$, is the most important contributor to $\beta_p(\psi)$ while E_H exhibits a pattern with most similar contributions of all three particle-size fractions. We also note that, with the exception of E_L, the contributions of $\beta_{pm}(\psi)$ and $\beta_{pl}(\psi)$ to $\beta_p(\psi)$ are quite comparable to one another. Another interesting feature is a significant decrease in the contribution of $\beta_{ps}(\psi)$ to $\beta_p(\psi)$ at small scattering angles less than about 10º, which is consistent with the notion of general dominance of near-forward scattering by larger particles (Morel and Bricaud 1986; Jonasz and Fournier 2007). Otherwise, the scattering-budget curves in Fig. 2.5 are mostly flat as a function of ψ.

2.4. Discussion

This study is based on a suite of simultaneous measurements of light scattering and several metrics of particulate concentration, composition, and size distribution of contrasting natural seawater samples, including measurements on particle size-fractionated samples. Owing to this approach, our results provide unique insights into the complexity of the roles played by particle size and composition in light scattering produced by highly variable natural assemblages of aquatic particles. We examined eight contrasting samples from near-shore and coastal oceanic environments including river estuary and offshore samples. Samples P_N, P_D (from SIO Pier) and O_C (from subsurface chlorophyll-a maximum at offshore location) are all highly dominated by organic particulate matter, which includes strong contribution of phytoplankton as indicated by the highest values of POC/SPM accompanied by high values of Chla/SPM and a_{ph}/a_p (Table 2.3). Despite sharing these common features, these three samples are highly contrasting because P_N exhibits the greatest relative role of small-sized particles (mainly nano- and picophytoplankton cells) and P_D the greatest role of large-sized particles (mainly chain-forming diatoms) among all

examined samples (Table 2.3). Samples E_L and E_H (from San Diego River Estuary) provide strong contrast with other samples because of predominance of inorganic particles and the smallest relative role of phytoplankton (Table 2.3). Again, despite sharing common features, E_L and E_H differ significantly from one another in terms of particle size characteristics with E_L having a higher proportion of small vs. large sized particles (Table 2.3). Samples P_M, P_R (SIO Pier), and O_S (surface water at offshore location) provide additional contrasting features (Table 2.3). Specifically, O_S is dominated by organic particles but it is the non-algal component, rather than phytoplankton, which is most important. Sample P_R was collected after rain event and hence is characterized by dominant presence of inorganic particles although phytoplankton still make an important contribution to particulate absorption. Finally, sample P_M appears to represent an intermediate scenario of transition between inorganic and organic dominated particulate assemblage that includes, however, a major role of phytoplankton.

Our results obtained with such contrasting samples support long-recognized challenges for the use of particulate scattering and backscattering coefficients as empirical proxies for phytoplankton or particulate concentration metrics, such as Chla (Huot et al. 2008; Barbieux et al. 2018), POC (Stramski et al. 2008; Woźniak et al. 2010), and SPM (Babin et al. 2003; Neukermans et al. 2016). For example, samples P_N and P_R are characterized by nearly identical b_{bp} and SPM but differ greatly from one another in terms of b_p, POC and Chla, as well as all particulate composition and size metrics determined in our experiments (Tables 2.3 and 2.4). Another example is provided by a comparison of samples P_R and O_C, which are characterized by nearly identical Chla and POC but very different b_p, b_{bp}, SPM, and particulate composition metrics.

In view of such complexities, our data obtained for the original (unfiltered) and size-fractionated samples provide particularly useful insights on the intricate effects of particle size and

composition on light scattering. Specifically, measurements of angle-resolved scattering provided information on the contributions of three particle-size fractions, referred to as small, medium, and large size fractions, to total magnitude of particulate volume scattering function, $\beta_p(\psi)$, at different scattering angles ψ for each examined sample (Fig. 2.5). These measurements also allow the determination of similar particle size-based budgets for the particulate scattering, b_p, and backscattering, b_{bp}, coefficients. Because of specific needs to advance an understanding of the backscattering coefficient owing to its effect on ocean reflectance and ocean color remote sensing (Morel and Prieur 1977; Gordon and Morel 1983) as well as increasing potential for applications associated with extensive use of backscattering sensors on autonomous in situ platforms (Organelli et al. 2017; Barbieux et al. 2018), we here put special emphasis on the discussion of particle size-based budgets for b_{bp}. These budgets are illustrated using the results obtained directly from our measurements (Fig. 2.6a) and after adjustment for imperfect size-fractionation (Fig. 2.6b), as described in Methods section 2.2.8.

Figure 2.6a suggests that the samples can be grouped into three categories based on the contribution of the small particle-size fraction to b_{bp}. The first group includes the four samples, P_N, P_M, O_S and O_C, with the highest contribution of small particles as indicated by b_{bps}/b_{bp} > 60%. The samples with b_{bp} most dominated by small particles are P_N and O_C with b_{bps}/b_{bp} around 80%. These samples are highly organic in nature with high values of POC/SPM, and are dominated by phytoplankton (Table 2.3). Interestingly, while P_N distinguishes itself in terms of the smallest values for particle size metrics, D_v^{50} and D_v^{90}, and hence the largest relative role of small-sized particles in the PSD, this feature is not observed in O_C (Table 2.3). We note that although the metrics of particulate composition, especially Chla/SPM and a_{ph}/a_p, suggest a dominant role of phytoplankton, this result does not automatically imply that phytoplankton cells are the dominant

direct source of backscattering in these samples. An important relevant point is that the abundance of non-algal particles in seawater can often be higher compared with phytoplankton cells across the optically significant size range (Stramski and Kiefer 1991; Jonasz and Fournier 2007). Therefore, the question of partitioning backscattering between different types of particles cannot be unambiguously resolved without quantitative information on various properties, including the concentration and size distribution, of separate phytoplankton and non-algal particulate components present in the samples. Such information is, however, beyond the reach of present experimental methods. Another organic-dominated sample in the first group, O_S, also has a high value of b_{bps}/b_{bp} above 70% but in this case organic non-algal particles are considerably more important than phytoplankton (Table 2.3). Finally, the fourth sample in the first group, P_M, with b_{bps}/b_{bp} of about 64% is more balanced in terms of organic and inorganic particulate matter as indicated by lower POC/SPM of 0.22, however phytoplankton play a major role, especially in terms of high value of a_{ph}/a_p (Table 2.3). It is also remarkable that the values for particle size metrics, D_v^{50} and D_v^{90}, vary significantly among the four samples from this first group (Table 2.3). In summary, the results for this first group of samples indicate that particulate backscattering can be dominated by the small size fraction in samples that are characterized by quite different particulate compositions and size distributions.

The second group includes the samples with the lowest contribution of small particles, $b_{bps}/b_{bp} < 40\%$, and therefore highest combined contribution of medium and large particles. This group includes the two inorganic-dominated samples collected in the San Diego River Estuary, E_L and E_H, which also exhibit the weakest role of phytoplankton among the examined samples. Because the particle size metrics for these two samples are quite different (Table 2.3), our results suggest that the scenario of relatively weak contribution of small particles to backscattering can

occur in samples with significant differences in PSD. However, it is important to note that these two samples also differ in terms of the proportions of organic and inorganic particles both in the small particle-size fractions and original unfiltered samples (Table 2.3).

The third group includes the samples with intermediate, but still considerable contribution of small particles, 40% < b_{bps}/b_{bp} < 50%, and accordingly, similar or somewhat larger combined contribution of medium and large particles. This group includes two samples from the SIO Pier with very different compositional characteristics, P_D and P_R. P_D was collected during enhanced presence of diatom *Hemiaulus hauckii* and is apparently dominated by these large-sized microphytoplankton as corroborated by the highest values of particle size metrics, D_v^{50} and D_v^{90}, among all examined samples (Table 2.3). In contrast, P_R was collected after a rain event and is dominated by inorganic particles although phytoplankton appear to have a considerable presence in this sample. P_R has a value of D_v^{50} that is nearly 3-fold lower compared with P_D; however the difference for D_v^{90} is not as substantial between the two samples (Table 2.3).

Figure 2.6b shows that the particle size-based budget for backscattering coefficient after adjustment for imperfect size-fractionation is qualitatively similar to that based on measurements without adjustment. Specifically, the grouping of samples remains similar with P_N, P_M, O_S, and O_C still having the greatest role of small particles that are now defined more rigorously as particles < 5 μm in size. For these samples, b_{bps}^*/b_{bp} ranges from about 50% to 75%. These percent contributions are, however, slightly lower compared with those based directly on size-fractionated measurements. The percent contributions of small particles to b_{bp} for E_L and E_H are still amongst the lowest (33−36%) in Fig. 2.6b, but in this case the adjustment for imperfect fractionation has not resulted in consistent reduction of these contributions. For sample P_D, which is dominated by diatoms from microphytoplankton size range, this adjustment resulted in the most significant

reduction of percent contribution of small particle-size fraction from about 49% (Fig. 2.6a) to 32% (Fig. 2.6b). Thus, in the adjusted budget, this sample along with E_L and E_H represent the weakest role of small particles in backscattering. For sample P_R, the adjustment for imperfect fractionation made no significant effect on the contribution of small-particle fraction to b_{bp}, which is about 42%.

The effects of adjustment for imperfect fractionation on the backscattering budget for the medium and large particle-size fractions, especially how the contributions are partitioned between these fractions, are more convoluted. In general, however, the adjustment resulted in an increase of the contribution of medium-sized particles to b_{bp} for all samples except for E_H. With regard to the role of large particles > 20 μm in size, the most noteworthy result is that the adjustment resulted in an increase of the contribution from about 29% to 40% for sample P_D. This result suggests that under conditions leading to an abundance of large-celled diatoms, the microphytoplankton size range can produce a very important contribution to particulate backscattering extending to, or perhaps even exceeding, 40%.

Figure 2.7 shows the particle size-based budgets in the same fashion as Fig. 2.6, except that it is for the particulate scattering coefficient, b_p. In agreement with data for $\beta_p(\psi)$ in Fig. 2.5, the results based on size-fractionated measurements in Fig. 2.7a show that small particle-size fraction is the most important contributor to b_p for all samples, except for E_L and E_H. The percent contributions of small particles to b_p in Fig. 2.7a are generally higher than or about the same as the corresponding contributions for b_{bp} in Fig. 2.6a. However, the adjustment for imperfect fractionation resulted in a significant decrease in the contribution of small-sized particles (< 5 μm) to b_p (Fig. 2.7b). For example, the contribution of small-sized particles to b_p decreased from 84% to 26% for sample O_C and from 71% to 40% for sample O_S. Similar decreases were observed for

the other two samples that belong to the first group of samples (P_N and P_M), as described above in relation to the backscattering budget. As a result of adjustment for imperfect fractionation the contribution of medium-sized particles to b_p increased for most samples, in some cases to values over 50% (P_N, P_M, and O_C). For a few samples (P_M, P_D, and O_S) this adjustment also resulted in considerable increase in the contribution of large-sized particles (> 20 μm) to b_p. In particular, for diatom-dominated sample P_D, the percent contribution increased more than 2-fold from about 35% (Fig. 2.7a) to 75% (Fig. 2.7b). The contribution of large-sized particles to b_p did not, however, increase for all samples and, in some cases, decreased slightly (P_R).

The patterns in Fig. 2.7 indicate that the particle size-based budget for b_p is considerably more sensitive to imperfect fractionation than the budget for b_{bp} (Fig. 2.6). This result is consistent with earlier modeling studies of light scattering by polydisperse particle assemblages, which indicated that the particle size-based contributions to b_p are more heavily weighted towards larger particles compared with contributions to b_{bp} (Stramski and Kiefer 1991). Accordingly, our data show that the adjustment for the presence of particles larger than 5 μm in the 5 μm filtrate has a greater effect on the b_p budget than the b_{bp} budget. As a result, while 4 out of 8 samples exhibit the small-particle (< 5 μm) contributions to b_{bp} greater than 50% in the adjusted budget (Fig. 2.6b), all samples have contributions less than 45% to b_p (Fig. 2.7b). Along the same lines, while in the adjusted budgets the highest large-particle (> 20 μm) contribution is about 40% for b_{bp}, it is 75% for b_p.

Although size-fractionated measurements and scattering computations to assess the effect of imperfect fractionation are unavoidably subject to some limitations, the combination of these results provided significant insights into the roles of particle size and composition in light

scattering by particulate assemblages in seawater. Our study supports the notion that assemblages with contrasting particle size and compositional characteristics can produce very different scenarios for particulate scattering (b_p) and backscattering (b_{bp}) budgets in terms of relative contributions of different particle-size fractions (Stramski et al. 2004). Our results also indicate that particle assemblages with contrasting characteristics can produce similar scenarios for particle size-based b_p and b_{bp} budgets.

Our results quantitatively demonstrate several highly different scenarios of particle size-based scattering budgets on the basis of analysis of eight contrasting samples from coastal environments, including near-shore samples dominated by organic particulate matter with predominant role of small-celled or large-celled phytoplankton, estuarine samples dominated by inorganic particles, and offshore samples representative of phytoplankton-dominated subsurface chlorophyll-a maximum and near-surface water dominated by organic non-algal particles. Despite intricate interplay between the effects of particle size and composition on light scattering, we observed that small particles (< 5 μm in size) consistently produced a major or dominant contribution to b_{bp} (close to or more than 50%) in organic, either phytoplankton or non-algal, dominated samples in spite of significant variations in particle size metrics between these samples. The notable exception was a sample dominated by large-celled diatoms from microphytoplankton size range, which exemplifies a specific scenario when large particles (> 20 μm) can play a considerable role in backscattering (about 40%). In addition, we observed a trend for inorganic-dominated samples exhibiting consistently lower contributions of small particles to b_{bp} (~30−40%). This trend for reduced contribution of small particles associated with inorganic-dominated assemblages having generally higher refractive index of particles, compared with organic-dominated assemblages with generally lower refractive index, is consistent with earlier

predictions based on light scattering modeling of idealized populations of marine particles with low and high refractive index (Stramski and Kiefer 1991).

The chlorophyll-a concentration in our coastal samples was greater than 0.5 mg m^{-3}, so these samples are not representative of vast open-ocean areas where Chla is typically less than 0.5 mg m^{-3}. Our two offshore samples (O_S and O_C) and the near-shore sample with the highest proportion of small particles (P_N) most closely resemble the characteristics of samples from open-ocean oligotrophic waters. For these three samples, the contribution to b_{bp} of particles < 5 μm was estimated to range from 64% to 75%. Because the open-ocean oligotrophic samples are also expected to be organic-dominated with similar or perhaps even higher relative abundance of small particles, the contribution of small-sized particles to b_{bp} can also be expected to be similarly high or higher than our estimates for these three samples. Given such relatively high estimates of percent contributions for the size fraction < 5 μm, it is conceivable that very small particles from picoplankton and colloidal size range (< 2 μm) can play a major or dominant role in backscattering under non-bloom conditions in open-ocean waters. While this supposition is generally consistent with earlier theoretical and experimental results (Stramski and Kiefer 1991; Dall'Olmo et al. 2009; Organelli et al. 2018) it requires further research. There are also other related questions that are difficult to address but demand special attention in future research. For example, the role of phytoplankton cells as a direct source of backscattering versus the role of co-existing non-algal particles that are typically more abundant than phytoplankton, except perhaps for specific particle-size range under bloom conditions, is poorly understood. Another example is the need to consider the effects of variations in particle shape on light scattering by natural assemblages, which present particular challenges for theoretical and experimental studies and receive less attention that the effects associated with particle size and composition.

2.5. Acknowledgments

This work was supported by NASA Terrestrial Hydrology and Ocean Biology and Biogeochemistry Programs (Grants NNX13AN72G and 80NSSC18K0956) and the NASA Earth and Space Science Fellowship Program (Grant NNX14AK93H). We acknowledge Eric Chen, Linhai Li, and Hugh Runyan for assistance during measurements and processing of data. We thank Xiaodong Zhang for providing software to calculate light scattering by hexahedrally-shaped particles and to extrapolate backscattering measurements, and Wayne Slade for discussions regarding the LISST-VSF instrument. We also thank two anonymous reviewers for valuable comments on the manuscript. POC analysis of seawater samples was done at the Marine Science Institute, University of California Santa Barbara.

Chapter 2, in full, has been accepted for publication at Limnology and Oceanography. The dissertation author was the primary investigator and author of the paper: Koestner, D., D. Stramski, and R. A. Reynolds. 2019. Assessing the effects of particle size and composition on light scattering through measurements of size-fractionated seawater samples. Limnol. Oceanogr. *In press*.

2.6. Figures

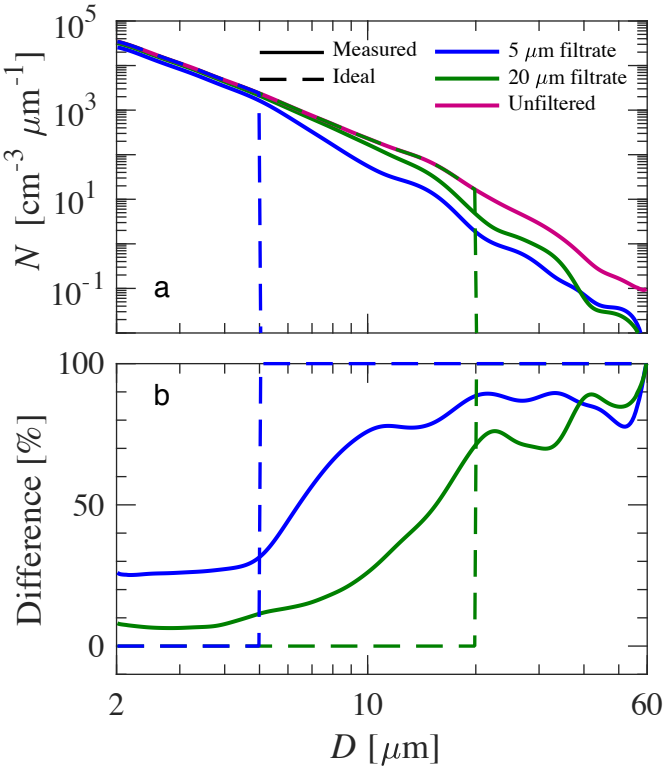

Figure 2.1. (a) Particle size distributions as probability density functions, *N*, for unfiltered and size-fractionated samples from the San Diego River Estuary (sample E_H). (b) Percent difference between the size-fractionated samples and the unfiltered sample shown in (a). Solid lines represent the measured size distribution and dashed lines represent idealized size-fractionation.

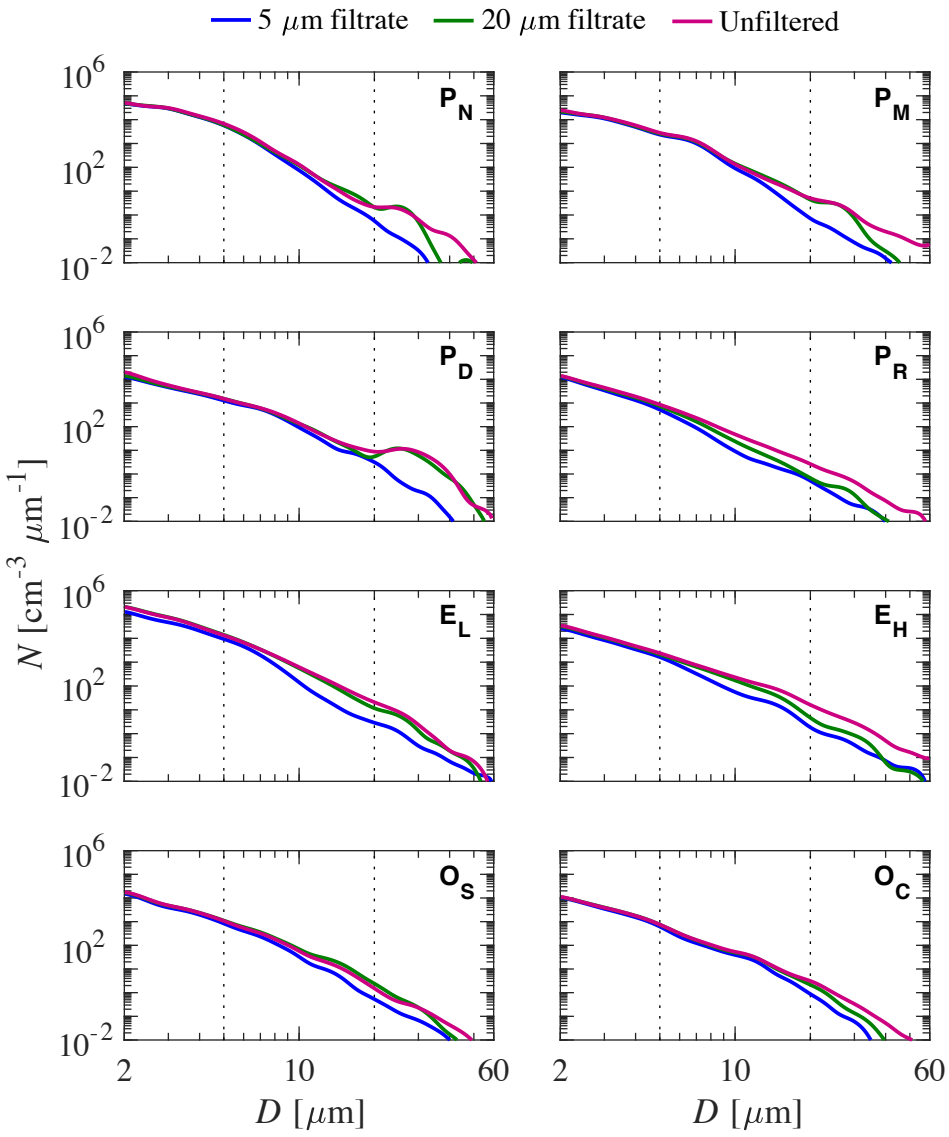

Figure 2.2. Measured particle size distributions for unfiltered and size-fractionated samples for the eight seawater samples as indicated. Vertical black dotted lines are shown to represent the expected cutoff of the mesh filters at 5 μm and 20 μm.

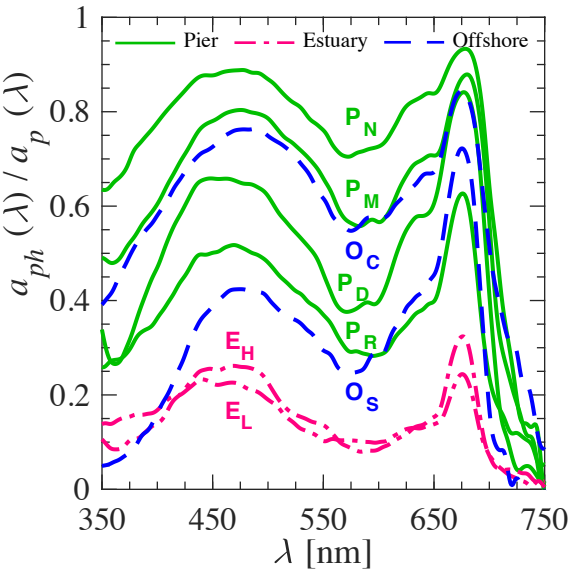

Figure 2.3. The proportion of spectral particulate absorption coefficient associated with phytoplankton for the eight seawater samples as indicated.

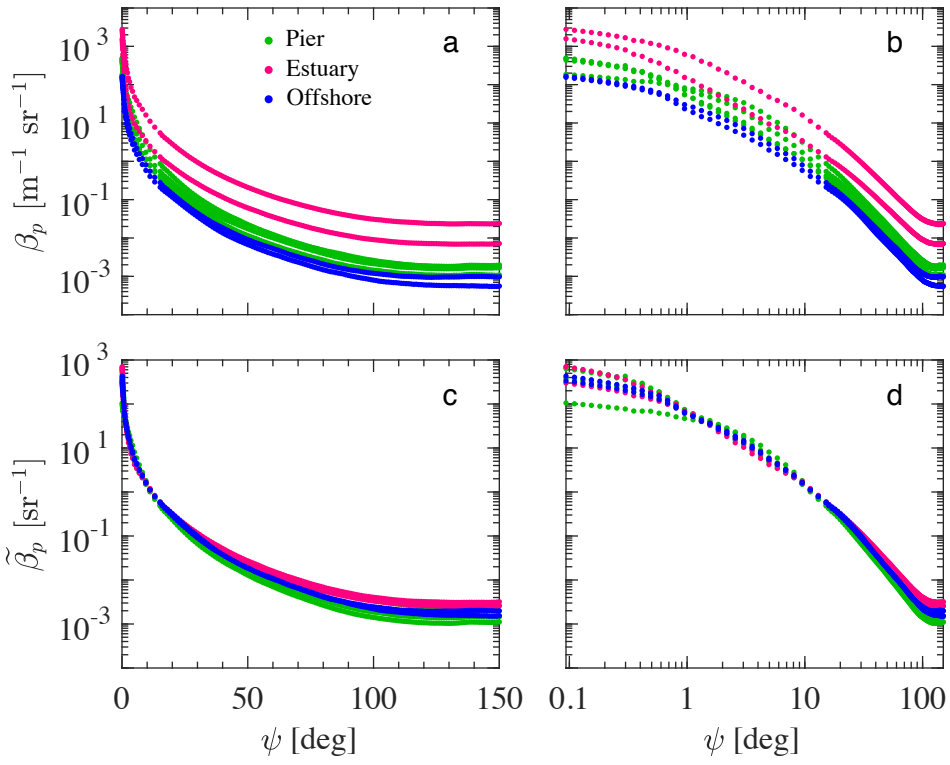

Figure 2.4. (a,b) Measurements of the particulate volume scattering function, $\beta_p(\psi)$, and (c,d) the particulate scattering phase function, $\tilde{\beta}_p(\psi)$, at light wavelength of 532 nm for the unfiltered seawater samples as indicated. The left panels (a,c) depict $\beta_p(\psi)$ and $\tilde{\beta}_p(\psi)$ with linear scaling of scattering angles between 0° and 150° while the right panels (b,d) depict $\beta_p(\psi)$ and $\tilde{\beta}_p(\psi)$ with logarithmic scaling of angles between 0.1° and 150°. Data points represent median values.

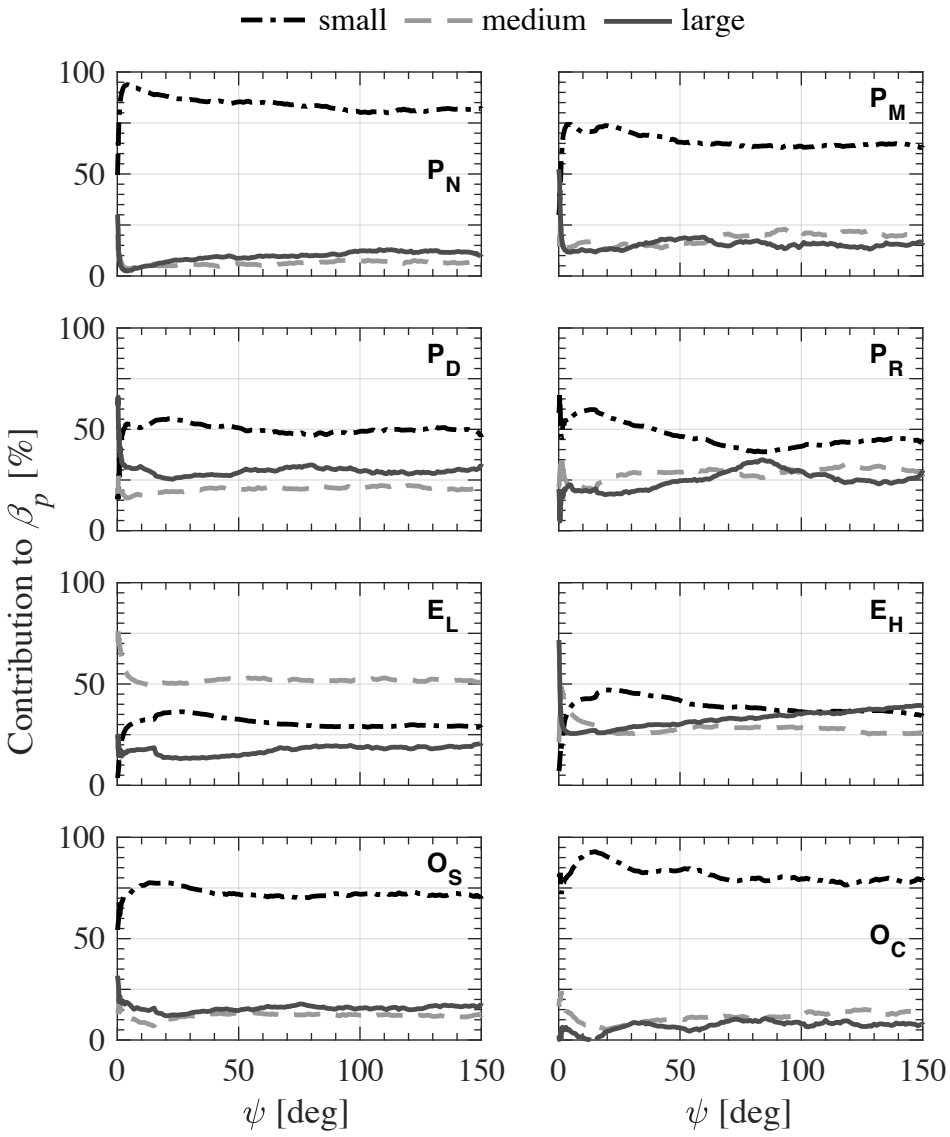

Figure 2.5. Particulate scattering budget in terms of contributions of particle-size fractions to the total particulate volume scattering function $\beta_p(\psi)$ in the range of scattering angles 0.09–150° for the eight seawater samples as indicated. Results for small, medium, and large particle-size fractions are shown as a percentage of the total $\beta_p(\psi)$.

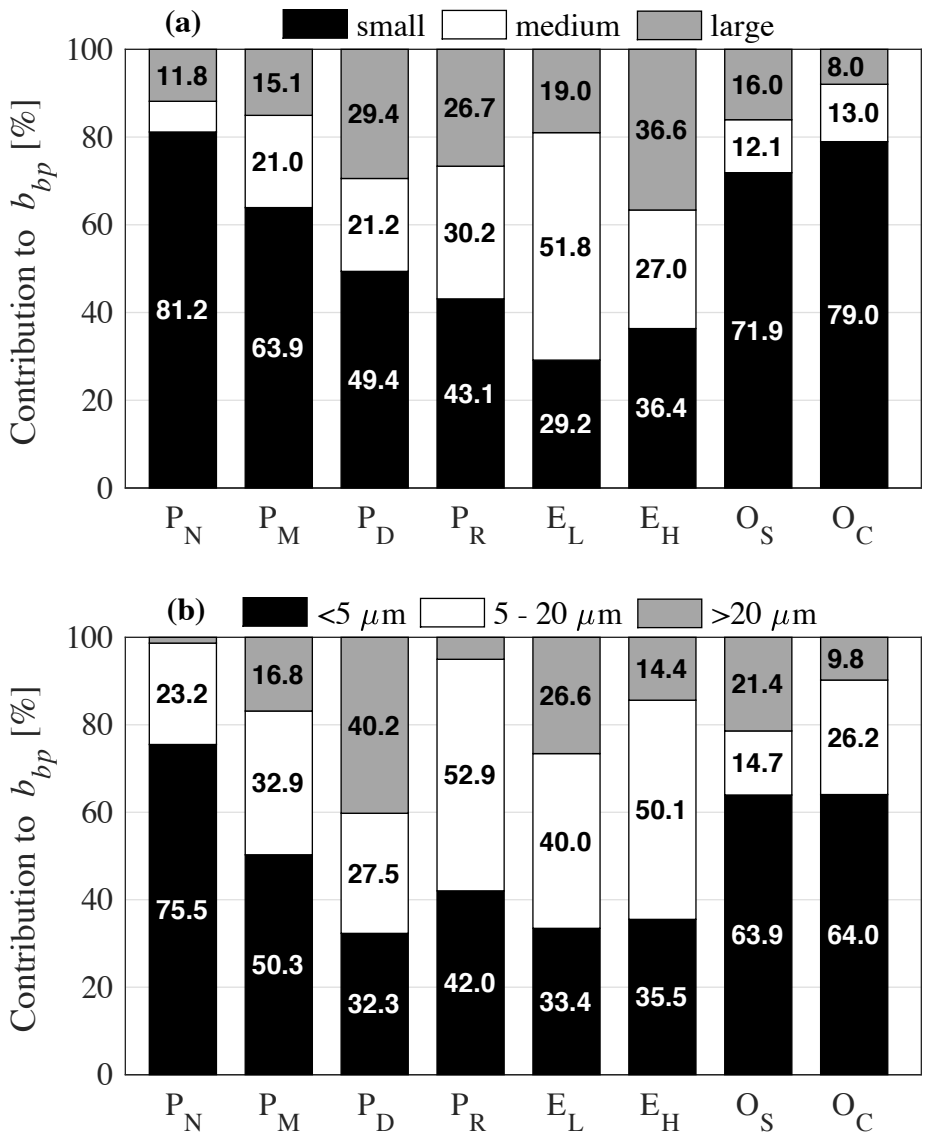

Figure 2.6. (a) Particulate backscattering budget in terms of contributions of particle-size fractions to total particulate backscattering coefficient b_{bp} for the eight samples as indicated below each set of bars. Results for small, medium, and large particle-size fractions are shown as a percentage of total b_{bp} on the basis of measurements on original (unfiltered) and size-fractionated samples. (b) Same as panel (a) but results were obtained after adjustment for imperfect fractionation. Number values [in %] for the size fractions are displayed within the bar when possible.

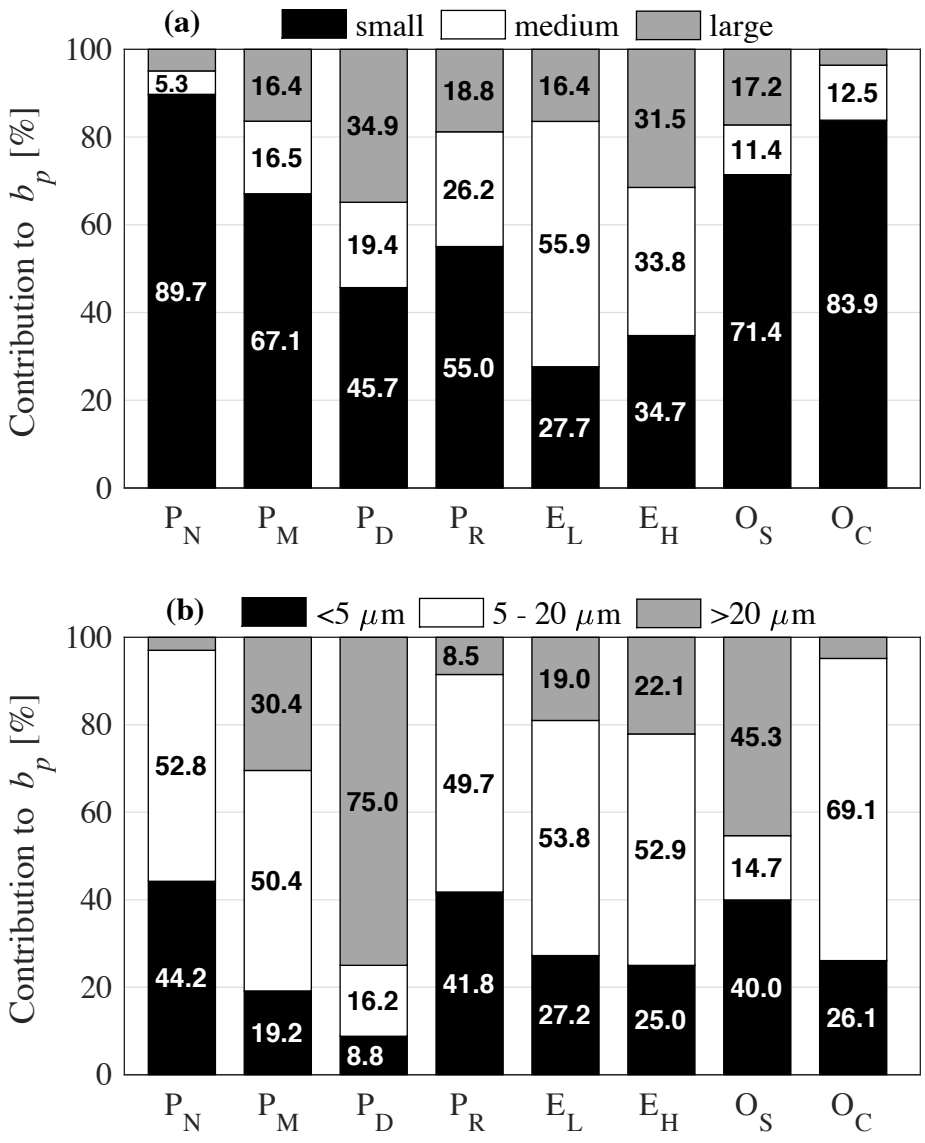

Figure 2.7. Same as Figure 2.6 but for the particulate scattering coefficient, b_p.

2.7. Tables

Table 2.1. General sample information for the eight experiments including identifier used throughout the paper (ID), location of sampling, date of sampling, and some key characteristics used as a general descriptor. The pier samples were collected at the Scripps Institution of Oceanography (SIO) Pier, the estuary samples were collected in the San Diego River Estuary, and offshore samples were collected at various locations offshore of San Diego.

ID	Location	Date	Key characteristics
P_N	Pier	6/30/2016	Nanophytoplankton abundant
P_M	Pier	7/12/2016	Mixed assemblage
P_D	Pier	7/26/2016	Microphytoplankton abundant
P_R	Pier	3/01/2017	After heavy rain
E_L	Estuary	8/09/2016	Lower high tide
E_H	Estuary	8/18/2016	Higher high tide
O_S	Offshore	9/15/2016	Surface water
O_C	Offshore	9/19/2016	Subsurface Chla maximum

Table 2.2. Filter ratings, F_r^{MD} where *MD* is the pore size of filter mesh in μm, and the volume-equivalent spherical diameter *D* associated with F_r = 80% for the 5 μm and 20 μm mesh filters. F_r^{MD} was calculated using Eq. 2.1 and PSD data from each experiment.

ID	5 μm mesh		20 μm mesh	
	$\boldsymbol{F_r^5}$ **[%]**	$\boldsymbol{D(F_r = 80\%)}$ **[μm]**	$\boldsymbol{F_r^{20}}$ **[%]**	$\boldsymbol{D(F_r = 80\%)}$ **[μm]**
P_N	24	16.0	10	28.6
P_M	21	14.0	24	28.9
P_D	21	14.8	15	49.2
P_R	60	8.02	74	28.2
E_L	42	8.58	36	47.0
E_H	56	10.2	75	31.6
O_S	30	33.8	−29	41.0
O_C	28	19.0	45	33.5

Table 2.3. Mass concentrations of SPM [g m^{-3}], POC [mg m^{-3}] and Chla [mg m^{-3}] and particulate composition and size parameters derived from measurements on the unfiltered seawater samples from the eight experiments. Information is also displayed when available for the small particle-size fraction in the 5 μm filtrates. The absorption ratio is given at λ = 440 nm. The particle size parameters, D_v^{50} and D_v^{90}, are the diameters in μm associated with the 50th and 90th percentile, respectively, of the particle volume distribution.

	Concentration			Composition			Size	
ID	**SPM**	**POC**	**Chla**	$\frac{\mathbf{POC}}{\mathbf{SPM}}$	$\frac{\mathbf{Chla}}{\mathbf{SPM}}$	$\frac{a_{ph}(440)}{a_p(440)}$	D_v^{50}	D_v^{90}
Unfiltered seawater								
P_N	1.13	532	2.49	0.47	0.0022	0.88	5.10	14.0
P_M	1.19	259	1.76	0.22	0.0015	0.77	7.41	28.6
P_D	0.75	453	2.26	0.60	0.0030	0.65	24.9	35.8
P_R	1.13	153	0.76	0.14	0.0007	0.50	8.78	30.2
E_L	9.90	873	3.00	0.09	0.0003	0.23	6.39	20.1
E_H	3.18	436	1.21	0.14	0.0004	0.25	13.5	34.6
O_S	0.54	192	0.53	0.35	0.0010	0.36	7.08	19.9
O_C	0.36	153	0.75	0.43	0.0021	0.71	9.84	25.8
Small particle fraction								
P_N	-	-	-	-	-	-	4.55	8.11
P_M	0.62	181	-	0.29	-	-	6.11	11.5
P_D	0.32	157	-	0.49	-	-	7.49	18.1
P_R	0.26	63	-	0.24	-	-	4.76	16.9
E_L	1.25	296	-	0.24	-	-	4.93	9.95
E_H	0.96	165	-	0.17	-	-	6.54	24.9
O_S	0.36	151	-	0.41	-	-	5.77	13.5
O_C	0.24	124	-	0.53	-	-	6.77	16.2

Table 2.4. Particulate scattering (b_p) and backscattering (b_{bp}) coefficients at λ = 532 nm determined from measurements of $\beta_p(\psi)$ for unfiltered seawater samples from the eight experiments. Information is also displayed for the small particle-size fraction in the 5 μm filtrates. The values of the backscattering ratio $\tilde{b}_{bp} = b_{bp}/b_p$ are also shown.

	Unfiltered seawater			*Small particle fraction*		
ID	$\boldsymbol{b_p}$ **[m^{-1}]**	$\boldsymbol{b_{bp}}$ **[m^{-1}]**	$\boldsymbol{\tilde{b}_{bp}}$	$\boldsymbol{b_p}$ **[m^{-1}]**	$\boldsymbol{b_{bp}}$ **[m^{-1}]**	$\boldsymbol{\tilde{b}_{bp}}$
P_N	1.75	0.0135	0.008	1.57	0.0109	0.007
P_M	1.13	0.0116	0.010	0.76	0.0074	0.010
P_D	0.73	0.0078	0.011	0.33	0.0039	0.012
P_R	0.75	0.0135	0.018	0.41	0.0058	0.014
E_L	9.25	0.1690	0.018	2.56	0.0493	0.019
E_H	2.23	0.0498	0.022	0.78	0.0181	0.023
O_S	0.49	0.0068	0.014	0.35	0.0049	0.014
O_C	0.36	0.0042	0.012	0.30	0.0033	0.011

2.8. References

Aas, E. 1996. Refractive index of phytoplankton derived from its metabolic composition. J. Plankton Res. **18**: 2223–2249.

Antoine, D., D. A. Siegel, T. S. Kostadinov, S. Maritorena, N. B. Nelson, B. Gentili, V. Vellucci, and N. Guillocheau. 2011. Variability in optical particle backscattering in contrasting bio-optical oceanic regimes. Limnol. Oceanogr. **56**: 955–973, doi:10.4319/lo.2011.56.3.0955.

Babin, M., A. Morel, V. Fournier-Sicre, F. Fell, and D. Stramski. 2003. Light scattering properties of marine particles in coastal and open ocean waters as related to the particle mass concentration. Limnol. Oceanogr. **48**: 843–859.

Babin, M., and D. Stramski. 2002. Light absorption by aquatic particles in the near-infrared spectral region. Limnol. and Oceanogr. **47**: 911–915.

Balch, W. M., D. T. Drapeau, T. L. Cucci, R. D. Vaillancourt, K. A. Kilpatrick, and J. J. Fritz. 1999. Optical backscattering by calcifying algae: Separating the contribution by particulate inorganic and organic carbon fractions, J. Geophys. Res. **104**: 1541–1558.

Balch, W. M., D. Drapeau, J. Fritz, B. Bowler, and J. Nolan. 2001. Optical backscattering in the Arabian Sea: Continuous underway measurements of particulate inorganic and organic carbon, Deep Sea Res. Part I **48**: 2423–2452.

Barbieux, M., J. Uitz, A. Bricaud, E. Organelli, A. Poteau, C. Schmechtig, B. Gentili, G. Obolensky, E. Leymarie, C. Penkerc'h, F. D'Ortenzio, and H. Claustre. 2018. Assessing the variability in the relationship between the particulate backscattering coefficient and the chlorophyll a concentration from a global Biogeochemical-Argo database. J. Geophys. Res. Oceans **123**: 1229–1250, doi:10.1002/2017JC013030.

Boss, E., W. S. Pegau, W. D. Gardner, J. R. V. Zaneveld, A. H. Barnard, M. S. Twardowski, G. C. Chang, and T. D. Dickey. 2001. Spectral particulate attenuation and particle size distribution in the bottom boundary layer of a continental shelf. J. Geophys. Res. Oceans **106**: 9509–9516.

Boss, E., W. S. Pegau, M. Lee, M. Twardowski, E. Shybanov, G. Korotaev, and F. Baratange. 2004. Particulate backscattering ratio at LEO 15 and its use to study particle composition and distribution. J. Geophys. Res. **109**: C01014, doi:10.1029/2002JC001514.

Carder, K. L., P. R. Betzer, and D. W. Eggimann. 1974. Physical, chemical, and optical measures of suspended-particle concentrations: Their intercomparison and application to the west African shelf, pp. 173–193. *In*: R. J. Gibbs [ed.], Suspended solids in water, Plenum Press.

Dall'Olmo, G., T. K. Westberry, M. J. Behrenfeld, E. Boss, and W. H. Slade. 2009. Significant contribution of large particles to optical backscattering in the open ocean. Biogeosciences **6**: 947–967.

Davies, E. J., D. McKee, D. Bowers, G. W. Graham, and W. A. M. Nimmo-Smith. 2014. Optically

significant particle sizes in seawater. Appl. Opt. **53**: 1067–1074, doi:10.1364/AO.53.001067.

Gordon, H. R., O. B. Brown, and M. M. Jacobs. 1975. Computed relationships between the inherent and apparent optical properties of a flat homogeneous ocean. Appl. Opt. **14**: 417–427.

Gordon, H. R. and A. Morel. 1983. Remote assessment of ocean color for interpretation of satellite visible imagery: A Review. Springer-Verlag.

Gregg, W. W. 2002. Tracking the SeaWiFS record with a coupled physical/biogeochemical/ radiative model of the global oceans. Deep Sea Res. II. **49**: 81-105.

Gregg, W. W. and M. E. Conkright. 2002. Decadal changes in global ocean chlorophyll. Geophys. Res. Lett. **29**, doi:10.1029/2002GL014689.

Huot, Y., A. Morel, M. S. Twardowski, D. Stramski, and R. A. Reynolds. 2008. Particle optical scattering along a chlorophyll gradient in the upper layer of the eastern South Pacific Ocean. Biogeosciences **5**: 495–507.

Jonasz, M., and G. Fournier. 2007. Light scattering by particles in water: Theoretical and experimental foundations. Elsevier.

Kishino, M., M. Takahashi, N. Okami, and S. Ichimura. 1985: Estimation of the spectral absorption coefficients of phytoplankton in the sea. Bull. Mar. Sci. **37**: 634–642.

Kitchen, J. C., and J. R. V. Zaneveld. 1992. A three-layered sphere model of the optical properties of phytoplankton. Limnol. Oceanogr. **37**: 1680–1690.

Knap, A., A. Michaels, A. Close, H. Ducklow, and A. Dickson. 1996. Protocols for the Joint Global Ocean Flux Study (JGOFS) Core Measurements, JGOFS Report Nr. 19 (Reprint of the IOC Manuals and Guides No. 29, UNESCO, Paris, 1994), 170 pp.

Koestner, D., D. Stramski, and R. A. Reynolds. 2018. Measurements of the volume scattering function and the degree of linear polarization of light scattered by contrasting natural assemblages of marine particles. Appl. Sci. **8**: 2690, doi:10.3390/app8122690.

Kostadinov, T. S., D. A. Siegel, and S. Maritorena. 2009. Retrieval of the particle size distribution from satellite ocean color observations. J. Geophys. Res. **114**: C09015, doi:10.1029/2009JC005303.

Li, L., D. Stramski, and R. A. Reynolds. 2014. Characterization of the solar light field within the ocean mesopelagic zone based on radiative transfer simulations. Deep Sea Res. I. **87**: 53–69, doi:10.1016/j.dsr.2014.02.005.

Logan, B. E. 1993. Theoretical analysis of size distributions determined with screens and filters. Limnol. Oceanogr. **38**: 372–381.

Meyer, R. A. 1979. Light scattering from biological cells: Dependence of backscatter radiation on membrane thickness and refractive index. Appl. Opt. **18**: 585–588.

Mobley, C. D. 1994. Light and water: Radiative transfer in natural waters. Academic Press.

Mobley, C. D., F. Chai, P. Xiu, and L. K. Sundman. 2015. Impact of improved light calculations on predicted phytoplankton growth and heating in an idealized upwelling-downwelling channel geometry, J. Geophys. Res. Oceans **120**: 875–892, doi:10.1002/2014JC010588.

Mobley, C. D., L. K. Sundman, and E. Boss. 2002. Phase function effects on oceanic light fields. Appl. Opt. **41**: 1035–1050.

Morel, A. 1973. Diffusion de la lumière par les eaux de mer; résultats expérimentaux et approche théorique. AGARD Lect. Ser. **61**: 3.1-1–3.1-76.

Morel, A. and A. Bricaud. 1986. Inherent optical properties of algal cells including picoplankton: Theoretical and experimental results. Can. Bull. Fish. Aquat. Sci. **214**: 521–559.

Morel, A. and L. Prieur. 1977. Analysis of variations in ocean color. Limnol. Oceanogr. **22**: 709–722.

Neukermans, G., H. Loisel, X. Meriaux, R. Astoreca, and D. McKee. 2012. In situ variability of mass-specific beam attenuation and backscattering of marine particles with respect to particle size, density, and composition. Limnol. Oceanogr. **57**: 124–144, doi:10.4319/lo.2011.57.1.0124.

Neukermans, G., R. A. Reynolds, and D. Stramski. 2016. Optical classification and characterization of marine particle assemblages within the western Arctic Ocean. Limnol. Oceanogr. **61**: 1472–1494.

Organelli, E., M. Barbieux, H. Claustre, C. Schmechtig, A. Poteau, A. Bricaud, E. Boss, N. Briggs, G. Dall'Olmo, F. D'Ortenzio, E. Leymarie, A. Mangin, G. Obolensky, C. Penkerc'h, L. Prieur, C. Roesler, R. Serra, J. Uitz, and X. Xing. 2017. Two databases derived from BGC-Argo float measurements for marine biogeochemical and bio-optical applications. Earth Syst. Sci. Data **9**: 861–880, doi:10.5194/essd-9-861-2017.

Organelli, E., G. Dall'Olmo, R. J. W. Brewin, G. A. Tarran, E. Boss, and A. Bricaud. 2018. The open-ocean missing backscattering is in the structural complexity of particles. Nat. Commun. **9**: 5439, doi:10.1038/s41467-018-07814-6.

Parsons, T. R., Y. Maita, and C. M. Lalli. 1984. A manual of chemical and biological methods for seawater analysis, Elsevier.

Ritchie, R. J. 2008. Universal chlorophyll equations for estimating chlorophylls a, b, c, and d and total chlorophylls in natural assemblages of photosynthetic organisms using acetone, methanol, or ethanol solvents. Photosynthetica **46**: 115–126.

Reynolds, R. A., D. Stramski, and G. Neukermans. 2016. Optical backscattering by particles in

Arctic seawater and relationships to particle mass concentration, size distribution, and bulk composition. Limnol. Oceanogr. **61**: 1869–1890, doi:10.1002/lno.10341.

Röttgers, R., and S. Gehnke. 2012. Measurement of light absorption by aquatic particles: Improvement of the quantitative filter technique by use of an integrating sphere approach. Appl. Opt. **51**: 1336–1351.

Sheldon, R. W. 1972. Size separation of marine seston by membrane and glass-fiber filters. Limnol. Oceanogr. **17**: 494–498.

Slade, W. H., and E. Boss. 2015. Spectral attenuation and backscattering as indicators of average particle size. Appl. Opt. **54**: 7264–7277.

Sparks, T., and G. Chase. 2015. Filters and filtration handbook, 6th ed. Elsevier.

Stramski, D., E. S. Boss, D. J. Bogucki, and K. J. Voss. 2004. The role of seawater constituents in light backscattering in the ocean. Prog. Oceanogr. **61**: 27–56.

Stramski, D., A. Bricaud, and A. Morel. 2001. Modeling the inherent optical properties of the ocean based on the detailed composition of planktonic community. Appl. Opt. **40**: 2929–2945.

Stramski, D., and D. A. Kiefer. 1991. Light scattering by microorganisms in the open ocean. Prog. Oceanogr. **28**: 343–383.

Stramski, D., R. A. Reynolds, M. Babin, S. Kaczmarek, M. R. Lewis, R. Röttgers, A. Sciandra, M. Stramska, M. S. Twardowski, B. A. Franz, and H. Claustre. 2008. Relationships between the surface concentration of particulate organic carbon and optical properties in the eastern South Pacific and eastern Atlantic Oceans. Biogeosciences **5**: 171–201.

Stramski, D., R. A. Reynolds, S. Kaczmarek, J. Uitz, and G. Zheng. 2015. Correction of pathlength amplification in the filter-pad technique for measurements of particulate absorption coefficient in the visible spectral region. Appl. Opt. **54**: 6763–6782, doi:10.1364/AO.54.006763.

Stramski, D., R. A. Reynolds, M. Kahru, and B. G. Mitchell. 1999. Estimation of particulate organic carbon in the ocean from satellite remote sensing. Science **285**: 239–242.

Sullivan, J. M., and M. S. Twardowski. 2009. Angular shape of the oceanic particulate volume scattering function in the backward direction. Appl. Opt. **48**: 6811–6819.

Tilstone, G. H., P. K. Lange, A. Misra, R. J. W. Brewin, and T. Cain. 2017. Micro-phytoplankton photosynthesis, primary production and potential export production in the Atlantic Ocean. Prog. Oceanogr. **158**: 109–129, doi:10.1016/j.pocean.2017.01.006.

van de Hulst, H. C. 1981. Light scattering by small particles, John Wiley & Sons.

van der Linde, D. W. 1998. Protocol for the determination of total suspended matter in oceans and

coastal zones. Technical Note I.98.182, Joint Research Centre, Ispra, Italy.

Twardowski, M. S., E. Boss, J. B. Macdonald, W. S. Pegau, A. H. Barnard, and J. R. V. Zaneveld. 2001. A model for estimating bulk refractive index from the optical backscattering ratio and the implications for understanding particle composition in case I and case II waters. J. Geophys. Res. **106**: 14129–14142.

Twardowski, M. and A. Tonizzo. 2018. Ocean color analytical model explicitly dependent on the volume scattering function. Appl. Sci. **8**: 2684, doi:10.3390/app8122684.

Whitmire, A. L., W. S. Pegau, L. Karp-Boss, E. Boss, and T. J. Cowles. 2010. Spectral backscattering properties of marine phytoplankton cultures. Opt. Express **18**: 15073–15093.

Woźniak, S. B., and D. Stramski. 2004. Modeling the optical properties of mineral particles suspended in seawater and their influence on ocean reflectance and chlorophyll estimation from remote sensing algorithms. Appl. Opt. **43**: 3489–3503.

Woźniak, S. B., D. Stramski, M. Stramska, R. A. Reynolds, V. M. Wright, E. Y. Miksic, M. Cichocka, and A. M. Cieplak. 2010. Optical variability of seawater in relation to particle concentration, composition, and size distribution in the nearshore marine environment at Imperial Beach, California. J. Geophys. Res. **115**: C08027.

Xu, G., B. Sun, S. D. Brooks, P. Yang, G. W. Kattawar, and X. Zhang. 2017. Modeling the inherent optical properties of aquatic particles using an irregular hexahedral ensemble. J. Quant. Spectrosc. Radiat. Transf. **191**: 30–39, doi:10.1016/j.jqsrt.2017.01.020.

Zaneveld, J. R. V. 1995. A theoretical derivation of the dependence of the remotely sensed reflectance on the inherent optical properties. J. Geophys. Res. **100**: 13135–13142, doi:10.1029/95JC00453.

Zaneveld, J. R. V., D. M. Roach, and H. Pak. 1974. The determination of the index of refraction distribution of oceanic particulates. J. Geophys. Res. **79**: 4091–4095, doi:10.1029/JC079i027p04091.

Zhang, X., Y. Huot, D.J. Gray, A. Weidemann, and W.J. Rhea. 2013. Biogeochemical origins of particles obtained from the inversion of the volume scattering function and spectral absorption in coastal waters. Biogeosciences **10**: 6029–6043.

Chapter 3

Development of an approach based on polarized light scattering measurements of seawater for characterizing size and composition of marine particles

3.0. Abstract

Polarized light scattering measurements provide improved capabilities for the characterization of natural particle assemblages in terms of particle size and composition, however few studies have investigated this capability for marine particle assemblages. In this study, seawater samples representing contrasting natural assemblages of particles from coastal environments have been comprehensively characterized with measurements of angle-resolved polarized light scattering, particle size distribution and particle composition in terms of various metrics derived from mass concentration and particulate absorption. Measurements were also collected on samples following fractionation with 5 μm and 20 μm mesh filters. A decrease in the maximum value of the degree of linear polarization of light scattered by marine particles was weakly dependent on particle composition and mainly associated with increased proportions of the relatively rare large sized particles. It was also found that scattering matrix element $p_{22}(100°)$ had lower values for samples containing higher proportions of large sized particles and was relatively independent of particle composition, while $p_{22}(20°)$ had lower values for samples which are more inorganic dominated and was relatively unaffected by the presence of large sized particles. Finally, simple optically-based proxies to estimate particle size and composition were developed which rely on polarized light scattering measurements at only one or two angles. Using an incident laser which was polarized parallel to the scattering plane, light scattered around 110º with perpendicular polarization was proportional to particle size when normalized by light scattered with parallel polarization around 110º, while it was proportional to particle composition when normalized by light scattered with parallel polarization around 20º.

3.1. Introduction

The 1973 Nobel Prize in Physiology was given to Karl von Frisch in part for his pioneering work on the ability of honey bees to detect and utilize polarized ultraviolet light from the sky (von Frisch 1952). This astonishing adaptation found in honey bees gestures toward the power of polarization as a tool for broadening understanding and augmenting otherwise limited data. Following the first observations of polarized light in the ocean (Waterman 1954), studies have shown that fish and other marine organisms are sensitive to the polarization state of underwater light (Waterman 1981; Flamarique and Hawryshyn 1996). When skies are clear, the visible direct light from the sun is typically unpolarized (i.e., randomly polarized), the diffuse skylight is partially polarized, and the underwater light field is also partially polarized which depends largely on solar angle and the inherent optical properties of seawater (Waterman and Westell 1956; Timofeeva 1974). In other words, a thorough understanding of the manner in which marine particles scatter both unpolarized and polarized light is likely to enable sophisticated predictions of the polarized light field within the ocean; in turn, inversions of the observed underwater polarized light field and the use of measurements of the inherent polarization properties of light scattered by seawater (i.e., the elements of the so-called Muller scattering matrix) should enable advanced characterization of marine particles.

The use of polarized light has been explored at length in astronomical and atmospheric sciences as it relates to the determination of particle composition and size distribution using measurements and theoretical modeling of aerosol particles (Yanamandra-Fisher and Hanner 1999; Mishchenko et al. 2000; Muñoz et al. 2012; Zubko 2012). This fundamental knowledge regarding polarized light scattering by aerosol particles has been paramount for the use of polarimetry in the retrieval of atmospheric composition from satellite-based sensors (Dubovik et

al 2019). In oceanography, however, the use of polarization in light scattering measurements of marine particles has been limited (Fry and Voss 1985; Volten et al. 1998; Svenson et al. 2011), particularly with application to natural assemblages of marine particles (Beardsley 1968; Kadyshevich 1977; Voss and Fry 1984). However with improved knowledge of polarized light scattering by marine particles, the use of polarimetric sensors, in situ or airborne, has the potential to compliment traditional unpolarized radiometric measurements with refinements in particle characterization (Chami 2007; Loisel et al. 2008; Ibrahim et al. 2016; Hasekamp et al. 2019). The current study aims primarily to improve understanding of the inherent polarization properties of light scattered by particles suspended in seawater using measurements with a known artificial source of light (i.e., a laser).

Both polarized and unpolarized light scattering are foremostly a function of particle size, shape, and composition including internal structure. Additionally, both vary depending on scattering angle from the incident photon direction, ψ, and light wavelength in vacuum, λ. However, particle scattering of polarized light is far more complex, given its dependence on the incident polarization state of light. This interaction is described using a 4 x 4 scattering matrix, or Mueller matrix, which represents how a particle, or ensemble of particles, linearly transforms the 4-component incident Stokes vector into a 4-component scattered Stokes vector (Bohren and Huffman 1983). The current study focuses primarily on three of these matrix elements: $p_{11}(\psi, \lambda)$, $p_{12}(\psi, \lambda)$ and $p_{22}(\psi, \lambda)$. The degree of linear polarization of light scattered by particles, $DoLP_p(\psi, \lambda)$, describes the proportion of linearly polarized light relative to total intensity of the scattered light beam. For various assemblages of particles including suspended marine particles and when the incident light beam is unpolarized, this quantity can be derived from $p_{11}(\psi, \lambda)$ and $p_{12}(\psi, \lambda)$, which require measurements involving linear polarization (Volten et al. 1998; Hovenier

et al. 2002; Kokhanovsky 2003). The $p_{22}(\psi, \lambda)$ element also describes how linearly polarized light is transformed and has the unique property of being equal to $p_{11}(\psi, \lambda)$ for a collection of optically inactive homogeneous spheres (Hovenier et al. 1985). Few studies exist which examine $p_{22}(\psi, \lambda)$ using measurements on natural seawater samples (Beardsley 1968; Kadyshevich 1977; Voss and Fry 1984). The most recent measurements of $p_{22}(\psi, \lambda)$ for λ = 488 nm on seawater from a variety of western north-Atlantic and eastern north-Pacific waters indicate that $p_{22}(\psi, \lambda)$ decreases from ~1 at ψ = 0º to a minimum of about 0.6–0.8 at $\psi \approx$ 100º, which is in general quite agreeable with measurements by Kadyshevich (1977) in Baltic waters (Voss and Fry 1984). It is unclear, however, of the role of different particle types in the variability of $DoLP_p(\psi, \lambda)$ and $p_{22}(\psi, \lambda)$ because particle assemblages were not characterized beyond location of sampling in these studies.

The majority of studies which comprehensively measured polarized light scattering by natural marine particle assemblages are well over three decades old. Given the technological advancements of today, a reevaluation of polarized light scattering by marine particles using measurements along with comprehensive characterization of particles in terms of particle size distribution and composition is warranted. These advancements in technology have led to the development of a commercial instrument capable of measuring $p_{11}(\psi, \lambda)$, $p_{12}(\psi, \lambda)$ and $p_{22}(\psi, \lambda)$ at λ = 532 nm with high angular resolution (LISST-VSF; Sequoia Scientific). Here, the focus on angle-resolved polarized light scattering by marine particles is twofold. Firstly, the scattering measurements of well-characterized seawater samples are described for the purpose of interpretation in terms of particle size distribution and composition. Additionally, this study seeks to develop simple optical relationships which characterize marine assemblages as a function of polarized light scattering measurements at one or several angles.

3.2. Methods

Tables 3.1 and 3.2 define a list of the important measurement and statistical symbols, respectively, used throughout Chapter 3. The data presented in Chapter 3 have been acquired using experimental procedures that are described in detail in sections 1.2 and 2.2. A short description of relevant methodology follows, however more details related to particle-size fractionation and measurements of absorption spectra, particle mass concentration, and particle size distribution can be found in section 2.2 and details related to LISST-VSF instrument and light scattering measurements and data processing can be found in section 1.2. Additional details of the LISST-VSF light scattering measurements and data processing are presented here, along with the development of an alternate correction function for improved estimates of the particulate volume scattering function $\beta_p(\psi)$, degree of linear polarization $DoLP_p(\psi)$, and scattering matrix element $p_{22}(\psi)$.

3.2.1. Water samples

Sixteen seawater samples were collected in the region of San Diego, California, from June 2016 through March 2017. Two samples were collected at offshore locations aboard the R/V Sproul in mid-September. One sample was collected ~8 km offshore with Niskin bottles at a depth of ~20 m coinciding with the measurement of maximum chlorophyll-*a* fluorescence. The other sample was collected ~2 km offshore at a near-surface depth using the ship's surface seawater intake. Eleven near-shore samples were collected at the Scripps Institution of Oceanography (SIO) Pier. Three estuarine samples were collected 2 km inland in the San Diego River Estuary at different stages of high tide. The near-shore and estuarine samples were collected at a depth of about 1 m using either a bucket or a 5 L Niskin bottle. Note that one sample collected offshore

near the Santa Barbara Channel which was used in Chapter 1 has been removed from this analysis due to low signal during LISST-VSF measurements.

Approximately 30–40 L of seawater were collected from a single location for each experiment with onshore laboratory analysis completed within 8 hours after sampling except for offshore samples which were completed within 24 hours after sampling. Before analysis, water was stored in 20 L carboys and protected from light. The water in carboys was homogenized by gentle mixing immediately prior to removing samples for subsequent analysis. Special care was taken to ensure that subsamples of seawater used for different measurements and analyses were treated similarly and collected from carboys within one hour of each other. All measurements were typically completed within a 4-hour period.

Seawater for each sample was size-fractionated using woven nylon or polyester mesh filters with pore sizes of 5 μm and 20 μm (Spectrum Labs). The details of the methodology of this fractionation are described in section 2.2.2.

3.2.2. Particle characterization

The mass concentrations of suspended particulate matter (SPM), particulate organic carbon (POC), and chlorophyll-*a* (Chla) were determined with standard methodology following filtration of each original seawater sample onto 25 mm Whatman glass fiber filters (GF/F) at low (≤ 120 mm Hg) vacuum (section 2.2). Ratios of these mass concentrations additionally serve as proxies of bulk compositional characteristics of the particulate assemblage, e.g., POC/SPM or Chla/SPM. For both the SPM and POC measurements, duplicate sample filters were collected and the results averaged to obtain the final estimates of SPM and POC for a given unfiltered seawater sample. Single filters were also collected to determine both SPM and POC for the 5 μm-filtrate of all seawater samples with the exception of four samples from the SIO Pier. Single sample filters were

collected and analyzed for Chla, and no determinations were made for the filtrates. Thus, there was a total of 16 measurements of Chla, and 28 measurements of both POC and SPM available for analysis.

The measurements of particle size distribution, PSD, were made using an electronic impedance method with a Multisizer 3 (Beckman Coulter) equipped with a 100 μm aperture which allows particle counting in the size range of volume-equivalent spherical diameters, *D*, from 2 μm to 60 μm. Approximately 10 to 15 replicate measurements of 2 mL subsamples of each original (unfiltered) and two size-fractionated samples (i.e., the 5 μm and 20 μm filtrates) were collected. Assuming spherical shape of particles, the particle volume distributions were determined from the particle number distributions for each sample and the percentile-based particle diameters were calculated such as the median diameter, D_v^{50}, and the 90th percentile diameter, D_v^{90}, on the basis of particle volume distributions These parameters have been shown to provide potentially useful metrics in the analysis of relationships between the optical and particle size properties in seawater (Woźniak et al. 2010). Of the sixteen seawater samples collected for these experiments, two unfiltered samples from the SIO Pier, two 20 μm filtrate samples from the SIO Pier, and one 5 μm filtrate sample from the San Diego River Estuary were removed from further analysis because of uncertainty in the quality of Multisizer 3 measurements collected on these samples. Thus, there was a total of 43 measurements of PSD available for analysis.

For the measurement of spectral absorption coefficient of particles, $a_p(\lambda)$ [m^{-1}], unfiltered seawater samples were filtered onto 25 mm GF/F filters at low vacuum. The $a_p(\lambda)$ coefficient was determined in the spectral range from 300 to 850 nm at 1 nm intervals using a Lambda 18 UV/VIS spectrophotometer (Perkin Elmer) equipped with a 15-cm integrating sphere (RSA-PE-18, Labsphere). Following the measurement of $a_p(\lambda)$, the sample filters were immediately subject to

treatment with 95% methanol to remove extractable phytoplankton pigments and the methanol-treated filters were then measured to determine the spectral absorption coefficient of non-algal particles, denoted as $a_d(\lambda)$. The spectral absorption coefficient of phytoplankton was then calculated as $a_{ph}(\lambda) = a_p(\lambda) - a_d(\lambda)$. For this study, we evaluate the fraction $a_{ph}(\lambda)/a_p(\lambda)$ at $\lambda = 440$ for each unfiltered sample as an indication of the prevalence of phytoplankton in the sample. More details on particulate absorption measurements can be found in section 2.2.6. There was a total of 16 measurements of spectral absorption available for analysis.

3.2.3. Polarized light scattering measurements

3.2.3.1. Instrumentation and theoretical background

For the incoherent elastic scattering of light at a given wavelength λ by a collection of particles suspended in water, the Stokes vector of incident light beam $S_i = [I_i\ Q_i\ U_i\ V_i]^T$ where T represents the transpose operation, is transformed into the Stokes vector of scattered beam, $S_s(\psi)$, by a scattering matrix, $P(\psi)$. For an ensemble of randomly oriented particles exhibiting certain symmetry properties and no optical activity, the scattering matrix simplifies to 6 independent non-zero elements (van de Hulst 1981; Bohren and Huffman 1983; Hovenier et al. 2002):

$$S_s(\psi) = \begin{bmatrix} I_s(\psi) \\ Q_s(\psi) \\ U_s(\psi) \\ V_s(\psi) \end{bmatrix} = P(\psi)S_i = C \begin{bmatrix} p_{11}(\psi) & p_{12}(\psi) & 0 & 0 \\ p_{12}(\psi) & p_{22}(\psi) & 0 & 0 \\ 0 & 0 & p_{33}(\psi) & p_{34}(\psi) \\ 0 & 0 & -p_{34}(\psi) & p_{44}(\psi) \end{bmatrix} \begin{bmatrix} I_i \\ Q_i \\ U_i \\ V_i \end{bmatrix}, \qquad (3.1)$$

where λ has been omitted for brevity, C is a constant factor (for a given sample, light wavelength and measurement geometry), $p_{11}(\psi)$ represents the scattering phase function, and the reference plane is the scattering plane containing the incident and scattered directions (Bohren and Huffman 1983). This form provides a reasonable description of the measured scattering matrix by

suspensions of randomly oriented marine particles, including various specific types of particles present in seawater (Voss and Fry 1984; Fry and Voss 1985; Volten et al. 1998; Muñoz et al. 2012). In the case of unpolarized incident light (i.e., Q_i, U_i, and V_i are all zero) the volume scattering function $\beta(\psi)$ equals (to within a constant factor) $p_{11}(\psi)$, and the degree of linear polarization $DoLP(\psi)$ can be determined from (Mishchenko and Travis 1994; Volten et al. 1998):

$$DoLP(\psi) = \frac{-p_{12}(\psi)}{p_{11}(\psi)} = \frac{-Q_s(\psi)}{I_s(\psi)} \ . \tag{3.2}$$

Note that the subscript p is not included here as this is a general equation that can refer to the whole seawater sample with scattering contributions associated with both molecules and particles. Positive values of $DoLP(\psi)$ are for dominantly perpendicular polarization and negative values for dominantly parallel polarization. This definition of $DoLP(\psi)$ has been widely used for characterizing the inherent scattering properties of various types of particles beyond aquatic particles, such as aerosol particles and cosmic dust (Yanamandra-Fisher and Hanner 1999; Volten et al. 2001).

Measurements with the LISST-VSF instrument (described in detail in section 1.2.1) consist of two scans of a 15-cm path within the sample, each with a different linear polarization state of the incident beam, i.e., parallel and perpendicular to the scattering plane. Scattered intensity is measured at multiple scattering angles ψ from 0.09° to 15.17° with 32 logarithmically-spaced ring detectors and from 14° to 155° with 1° interval using a Roving Eyeball sensor equipped with photomultiplier tubes (PMTs). For the Roving Eyeball, scattered light is split between two PMTs with a polarizing prism allowing for only parallel or perpendicularly polarized light to be detected by each PMT. Detection of scattered light within the angular range 14–155° using the Roving Eyeball sensor employs measurements made with two linear polarization states of the incident beam and the corresponding two linear polarization states of the scattered light. The four

measurement configurations allow for the determination of relative values of $p_{11}(\psi)$, $p_{12}(\psi)$, and $p_{22}(\psi)$. A baseline measurement of 0.2 μm filtered water, or seawater, was collected with LISST-VSF and subtracted from sample measurements so that these scattering matrix elements refer to light scattered by suspended particles and are denoted with a subscript p for symbols related to LISST-VSF measurements, except $p_{22}(\psi)$ that represents particles (i.e., after subtraction of pure water contribution).

The scattered Stokes vector for the LISST-VSF instrument can be expressed with Eq. 3.1 by also including a polarization rotation matrix, $R(\psi)$, to account for the rotation of the scattered ray's polarization axes within the Roving Eyeball sensor and a scattering matrix for each component produced by the polarizing prism, $L^{\parallel}$ and $L^{\perp}$ where $\parallel$ designates parallel polarization and $\perp$ designates perpendicular polarization (LISST-VSF User's manual revision A). The PMT detector response is proportional to the unpolarized component of the scattered Stokes vector, I_s.

The polarization rotation matrix, $R(\psi) = \begin{bmatrix} 1 & 0 & 0 & 0 \\ 0 & cos\,2\psi & sin\,2\psi & 0 \\ 0 & -sin\,2\psi & -cos\,2\psi & 0 \\ 0 & 0 & 0 & 1 \end{bmatrix}$.

For the first eyeball rotation, the incident beam is polarized perpendicular:

$$L^{\parallel}R(\psi)P(\psi)S_i^{\perp} = \begin{bmatrix} 1 & 1 & 0 & 0 \\ 1 & 1 & 0 & 0 \\ 0 & 0 & 0 & 0 \\ 0 & 0 & 0 & 0 \end{bmatrix} R(\psi)P(\psi) \begin{bmatrix} 1 \\ -1 \\ 0 \\ 0 \end{bmatrix}$$

$$\xrightarrow{yields} \quad I_s^{\perp\parallel}(\psi) = p_{11}(\psi) - p_{12}(\psi) + \cos 2\psi \left(p_{12}(\psi) - p_{22}(\psi)\right) \tag{3.3}$$

$$L^{\perp}R(\psi)P(\psi)S_i^{\perp} = \begin{bmatrix} 1 & -1 & 0 & 0 \\ -1 & 1 & 0 & 0 \\ 0 & 0 & 0 & 0 \\ 0 & 0 & 0 & 0 \end{bmatrix} R(\psi)P(\psi) \begin{bmatrix} 1 \\ -1 \\ 0 \\ 0 \end{bmatrix}$$

$$\xrightarrow{yields} \quad I_s^{\perp\perp}(\psi) = \alpha\left[p_{11}(\psi) - p_{12}(\psi) - \cos 2\psi \left(p_{12}(\psi) - p_{22}(\psi)\right)\right] \tag{3.4}$$

For the second eyeball rotation, the incident beam is polarized parallel:

$$L^{\parallel}R(\psi)P(\psi)S_i^{\parallel} = \begin{bmatrix} 1 & 1 & 0 & 0 \\ 1 & 1 & 0 & 0 \\ 0 & 0 & 0 & 0 \\ 0 & 0 & 0 & 0 \end{bmatrix} R(\psi)P(\psi) \begin{bmatrix} 1 \\ 1 \\ 0 \\ 0 \end{bmatrix}$$

$$\xrightarrow{yields} \quad I_s^{\parallel\parallel}(\psi) = p_{11}(\psi) + p_{12}(\psi) + \cos 2\psi \left(p_{12}(\psi) + p_{22}(\psi)\right) \tag{3.5}$$

$$L^{\perp}R(\psi)P(\psi)S_i^{\parallel} = \begin{bmatrix} 1 & -1 & 0 & 0 \\ -1 & 1 & 0 & 0 \\ 0 & 0 & 0 & 0 \\ 0 & 0 & 0 & 0 \end{bmatrix} R(\psi)P(\psi) \begin{bmatrix} 1 \\ 1 \\ 0 \\ 0 \end{bmatrix}$$

$$\xrightarrow{yields} \quad I_s^{\parallel\perp}(\psi) = \alpha\left[p_{11}(\psi) + p_{12}(\psi) - \cos 2\psi \left(p_{12}(\psi) + p_{22}(\psi)\right)\right] \tag{3.6}$$

Note all elements are normalized to incident unpolarized radiance, i.e., I_i. For this notation, the measured total scattered intensity (component I_s of the scattered Stokes vector) is described in further detail with the first superscript character denoting incident laser polarization state and the second superscript character denoting detected polarization state. For example, $I_s^{\perp\parallel}$ indicates that the incident laser is perpendicularly polarized and detector is observing parallel polarized scattered light. The gain of the second PMT detector, observing only perpendicular light, relative to the first PMT detector, observing only parallel light, is described by the alpha factor, α. For each incident laser polarization state, this relative gain factor was estimated by using measurements at $\psi = \pi/4$ and $\psi = 3\pi/4$, where Eq. 3.3 and 3.4 simplify to $\alpha = I_s^{\perp\perp}(\psi)/I_s^{\perp\parallel}(\psi)$ and Eq. 3.5 and 3.6 simplify to $\alpha = I_s^{\parallel\perp}(\psi)/I_s^{\parallel\parallel}(\psi)$. It was determined from measurements with polystyrene bead suspensions that α was relatively constant throughout our experiments and can be treated as a constant for all measurements (section 1.2.1.3; α = 0.9335, coefficient of variation < 5% over ~18 months throughout the period of experiments).

Combining the above equations (Eq. 3.3–3.6) leads to:

$$p_{11}(\psi) = \frac{1}{4}\left[I_s^{\perp\perp}(\psi) + I_s^{\parallel\perp}(\psi) + \alpha\left(I_s^{\perp\parallel}(\psi) + I_s^{\parallel\parallel}(\psi)\right)\right] \tag{3.7}$$

$$p_{12}(\psi) = \frac{1}{4}\left[\alpha\left(I_s^{\perp\parallel}(\psi) - I_s^{\parallel\parallel}(\psi)\right) + \left(I_s^{\perp\perp}(\psi) - I_s^{\parallel\perp}(\psi)\right)\right] \ . \quad (3.8)$$

Note that these are determined in PMT counts and a scaling factor, S_f (described in section 1.2.1.3), is needed to compute $\beta_p(\psi)$ in absolute units, i.e.,

$$\beta_p(\psi) = \ S_f \ p_{11}(\psi) \ . \quad (3.9)$$

Note the subscript p indicates it refers only to the contribution of suspended particles larger than ~0.2 μm. Two methods (see appendix section 3.8 for derivation) are used to compute $p_{22}(\psi)$ and they are averaged for a final estimate of $p_{22}(\psi)$:

$$p_{22}(\psi) = \frac{2p_{11}(\psi) - \alpha\left[\left(I_s^{\perp\parallel}(\psi) + I_s^{\perp\parallel}(\psi)\cos(2\psi)\right) + \left(I_s^{\parallel\parallel}(\psi) - I_s^{\parallel\parallel}(\psi)\cos(2\psi)\right)\right]}{2\cos^2(2\psi)} \quad (3.10a)$$

$$p_{22}(\psi) = \frac{2p_{11}(\psi) - \left[\left(I_s^{\parallel\perp}(\psi) + I_s^{\parallel\perp}(\psi)\cos(2\psi)\right) + \left(I_s^{\perp\perp}(\psi) - I_s^{\perp\perp}(\psi)\cos(2\psi)\right)\right]}{2\cos^2(2\psi)} \ . \quad (3.10b)$$

3.2.3.2. Development of correction functions

In Chapter 1, it was found that independent corrections were needed for $\beta_p(\psi)$ and $DoLP_p(\psi)$ following comparisons of measurements on nearly-monodisperse polystyrene bead suspensions with simulations using Mie scattering theory for homogenous spheres. Corrections in Chapter 1 (section 1.2.1.4) were developed for both $\beta_p(\psi)$ and $DoLP_p(\psi)$, which were determined after combining the four measurements (Eq. 3.7 and 3.8). These corrections, however, provide no correction for $p_{22}(\psi)$ or the individual polarization combinations of measurements. Alternatively, and for the study presented in this chapter, reference values for each measurement combination were determined using above equations and $p_{11}^{Mie}(\psi)$ and $p_{12}^{Mie}(\psi)$ from Mie scattering calculations described in section 1.2.1.4 while noting that $p_{22}(\psi) = p_{11}(\psi)$ for homogenous

spheres (Hovenier et al 1985; Jonasz and Fournier 2007). For example, using perpendicularly polarized incident laser beam and parallel polarized detected light (Eq. 3.3),

$$\hat{I}_s^{\perp\parallel}(\psi) = p_{11}^{Mie}(\psi) - p_{12}^{Mie}(\psi) + \cos 2\psi \left(p_{12}^{Mie}(\psi) - p_{11}^{Mie}(\psi)\right) \tag{3.11}$$

$$\hat{\beta}_p^{\perp\parallel}(\psi) = \hat{I}_s^{\perp\parallel}(\psi)\, b_p^{REF} \ , \tag{3.12}$$

where the hat symbol denotes reference value of polarized intensities determined from Mie scattering calculations and the reference value of b_p^{REF} was computed identical to how it was in section 1.2.1.4. For comparison with measured data from the LISST-VSF Roving Eyeball sensor, S_f must be included to convert PMT counts into absolute units, e.g.,

$$\beta_p^{\perp\parallel *}(\psi) = S_f\, I_s^{\perp\parallel *}(\psi) \ , \tag{3.13}$$

and, when appropriate, the relative gain factor α, e.g.,

$$\beta_p^{\perp\perp *}(\psi) = \alpha\ S_f\, I_s^{\perp\perp *}(\psi) \ , \tag{3.14}$$

where the asterisk denotes measured and uncorrected data from the LISST-VSF Roving Eyeball sensor. Figure 3.1 shows the comparison of reference values and uncorrected measurements from the LISST-VSF for the four measurement combinations for 200 nm polystyrene beads. Similar to $\beta_p^{LISST*}(\psi)$ from Chapter 1 (Fig. 1.1), there is disagreement in both shape and magnitude and corrections are necessary. The four correction functions for each incident laser and detector polarization combination are defined as:

$$CF2^{\perp\parallel}(\psi) = \frac{\hat{\beta}_p^{\perp\parallel}(\psi)}{\beta_p^{\perp\parallel *}(\psi)}$$

$$CF2^{\perp\perp}(\psi) = \frac{\hat{\beta}_p^{\perp\perp}(\psi)}{\beta_p^{\perp\perp *}(\psi)}$$

$$CF2^{\parallel\parallel}(\psi) = \frac{\hat{\beta}_p^{\parallel\parallel}(\psi)}{\beta_p^{\parallel\parallel *}(\psi)}$$

$$CF2^{\parallel\perp}(\psi) = \frac{\hat{\beta}_p^{\parallel\perp}(\psi)}{\beta_p^{\parallel\perp *}(\psi)} \quad . \tag{3.15}$$

The above calculations were performed for all bead sizes and concentrations described in section 1.2.1 (Table 1.1). The final correction functions (with subscript *f*) were determined identical to how the final correction function $CF_f(\psi)$ for $\beta_p^{LISST*}(\psi)$ in section 1.2.1.4 was determined with 100, 200, and 400 nm beads except that $CF2_f^{\perp\perp}(\psi)$, $CF2_f^{\parallel\parallel}(\psi)$, and $CF2_f^{\perp\parallel}(\psi)$ were set to their respective value at ψ = 85° for 85–100° due to reference values near 0 around these angles (Fig. 3.1 b,c,d). The reference values in this angular range are sensitive to input PSD, refractive index and assumptions of particle shape, and measured data were subject to low signal in this region (Fig. 3.1 b,c,d). In an identical fashion to $CF_f(\psi)$ for $\beta_p^{LISST*}(\psi)$ from section 1.2.1.4 (Eq. 1.11), the final correction functions are multiplied by the LISST-VSF Roving Eyeball measurements to produce corrected results, i.e.,

$$\begin{aligned}
\beta_p^{\perp\parallel} &= CF2^{\perp\parallel}(\psi)\, \beta_p^{\perp\parallel *}(\psi) \\
\beta_p^{\perp\perp}(\psi) &= CF2^{\perp\perp}(\psi)\, \beta_p^{\perp\perp *}(\psi) \\
\beta_p^{\parallel\parallel}(\psi) &= CF2^{\parallel\parallel}(\psi)\, \beta_p^{\parallel\parallel *}(\psi) \\
\beta_p^{\parallel\perp}(\psi) &= CF2^{\parallel\perp}(\psi)\, \beta_p^{\parallel\perp *}(\psi) \quad ,
\end{aligned} \tag{3.16}$$

where the removal of the asterisk indicates the measurement has been corrected. With these corrected measurement combinations, Eq. 3.2, 3.7, 3.8, and 3.10 are modified by including steps described in Eq. 3.13 and 3.14 to determine the final results of $\beta_p(\psi)$, $DoLP_p(\psi)$, and $p_{22}(\psi)$:

$$\beta_p(\psi) = \frac{1}{4}\left[\beta_p^{\perp\parallel}(\psi) + \beta_p^{\parallel\parallel}(\psi) + \beta_p^{\perp\perp}(\psi) + \beta_p^{\parallel\perp}(\psi)\right] \tag{3.17}$$

$$DoLP_p(\psi) = \frac{\frac{1}{4}\left[\beta_p^{\parallel\perp}(\psi) + \beta_p^{\parallel\parallel}(\psi) - \left(\beta_p^{\perp\parallel}(\psi) + \beta_p^{\perp\perp}(\psi)\right)\right]}{\beta_p(\psi)} \tag{3.18}$$

$$p_{22}(\psi) = \frac{2\beta_p(\psi) - \left[\left(\beta_p^{\perp\parallel}(\psi) + \beta_p^{\perp\parallel}(\psi)\cos(2\psi)\right) + \left(\beta_p^{\parallel\parallel}(\psi) - \beta_p^{\parallel\parallel}(\psi)\cos(2\psi)\right)\right]}{2\cos^2(2\psi)\,\beta_p(\psi)} \quad (3.19a)$$

$$p_{22}(\psi) = \frac{2\beta_p(\psi) - \left[\left(\beta_p^{\parallel\perp}(\psi) + \beta_p^{\parallel\perp}(\psi)\cos(2\psi)\right) + \left(\beta_p^{\perp\perp}(\psi) - \beta_p^{\perp\perp}(\psi)\cos(2\psi)\right)\right]}{2\cos^2(2\psi)\,\beta_p(\psi)}. \quad (3.19b)$$

Note that $p_{22}(\psi)$ is normalized by $\beta_p(\psi)$ here, as it is normal notation when presenting results for scattering matrix elements (Bohren and Huffman 1983; Mishchenko and Travis 1994; Jonasz and Fournier 2007), and the average of Eq. 3.19a and 3.19b is used for the final estimate of $p_{22}(\psi)$.

3.2.3.3. Application of correction to seawater samples

For seawater samples, measurements with the LISST-VSF instrument were made in a laboratory benchtop configuration (section 1.2.2 and 2.2.5). For each sample, between four and eight sequences of 50 measurements were collected on the original (unfiltered) sample and two size-fractionated samples. The correction functions developed above were applied to the four incident and detector polarization combinations (Eq. 3.16) to determine $\beta_p^{\perp\parallel}(\psi)$, $\beta_p^{\parallel\parallel}(\psi)$, $\beta_p^{\perp\perp}(\psi)$, and $\beta_p^{\parallel\perp}(\psi)$ so that $\beta_p(\psi)$, $DoLP_p(\psi)$, and $p_{22}(\psi)$ could be computed for each measurement (following Eq. 3.17, 3.18, and 3.19). The determinations of final $\beta_p(\psi)$, $DoLP_p(\psi)$, and $p_{22}(\psi)$ involved quality control of replicate measurements, removing outliers potentially affected by measurement artifacts, deriving the median value at each angle from the remaining measurements, and then smoothing the data three times, first with a 3º and then with a 5º moving average. The final $\beta_p(\psi)$ was used to estimate the particulate scattering and backscattering coefficients, b_p and b_{bp}, following the methodology outlined in section 1.2.2. These metrics and others used throughout the text are described in Table 3.1. Of the sixteen seawater samples collected for these experiments, one unfiltered sample from the SIO Pier and one 5 μm filtrate sample from the SIO

Pier were removed from further analysis because of LISST-VSF measurement artifacts identified during processing which rendered all measurements collected on these samples erroneous. Thus, there was a total of 46 final $\beta_p(\psi)$, $DoLP_p(\psi)$, and $p_{22}(\psi)$ available for analysis.

3.3. Results and discussion

3.3.1. Validation of $CF2_f$

Before presenting results on measurements with seawater, the alternate correction functions developed in section 3.2.3 must be validated by comparing final data products $\beta_p(\psi)$, $DoLP_p(\psi)$, and $p_{22}(\psi)$, with results obtained from Mie scattering calculations for nearly-monodisperse polystyrene bead solutions (described in section 1.2.1.4). Note that the advantage of this new correction procedure is there is one single set of correction functions which provide improved results for $\beta_p(\psi)$ and $DoLP_p(\psi)$, and the previously uncorrected $p_{22}(\psi)$. Fig. 3.2 displays the final correction functions from Eq. 3.15; $CF2_f^{\parallel\perp}(\psi)$, $CF2_f^{\perp\perp}(\psi)$, $CF2_f^{\parallel\parallel}(\psi)$, and $CF2_f^{\perp\parallel}(\psi)$ as functions of scattering angle. These correction functions are generally similar in magnitude to $CF_f(\psi)$ obtained in Chapter 1 (Fig. 1.4) with some noteworthy differences related to the use of linearly polarized light and the lack of data for ψ < 16º. $CF2_f^{\parallel\perp}(\psi)$ is most similar to $CF_f(\psi)$ in shape and magnitude, increasing from ~1.7 to ~1.9 for ψ = 15–60º and beginning to decrease for ψ > 60º. Another difference here is an increase in $CF2_f^{\parallel\perp}(\psi)$ for ψ > ~130º which is not observed in $CF_f(\psi)$. It is in this region that theoretical simulations show very small values of $\hat{\beta}_p^{\perp\perp}(\psi)$, $\hat{\beta}_p^{\parallel\parallel}(\psi)$, and $\hat{\beta}_p^{\perp\parallel}(\psi)$, which is shown for the case of 200 nm polystyrene beads in Fig. 3.1 b–d. When only parallel light is detected, the values near 90º are predicted to be ~0 m^{-1} sr^{-1}, with the minimum value at 90º for $\hat{\beta}_p^{\parallel\parallel}(\psi)$ and at 95º for $\hat{\beta}_p^{\perp\parallel}(\psi)$. This is to be expected as light

scattered from a single dipole is unable to propagate in the direction of its electric field oscillations (i.e., polarization state), and in this case parallel polarization indicates electric field oscillations in the 90º scattering direction. For an ensemble of similar particles containing many dipoles, this results in interference patterns with minima near 90º, particularly so for scattered light with parallel polarization. Interestingly, the measurement combination with perpendicularly polarized incident laser and detected light also produces very small values of $\hat{\beta}_p^{\perp\perp}(\psi)$ over a larger angular range, ~85–100º, (Fig. 3.1c). Deriving such small values with the LISST-VSF is complicated due to low instrument signal relative to background signal and coupled with uncertainty of inputs into Mie scattering calculations, the values of $CF2_f^{\perp\perp}(\psi)$, $CF2_f^{\parallel\parallel}(\psi)$, and $CF2_f^{\perp\parallel}(\psi)$ for ψ = 85–100º were set to their respective value at 85º.

The validation of this new correction was performed by following similar analysis that was done in section 1.3.1. Using corrected $\beta_p^{\parallel\perp}(\psi)$, $\beta_p^{\perp\perp}(\psi)$, $\beta_p^{\parallel\parallel}(\psi)$, and $\beta_p^{\perp\parallel}(\psi)$ (Eq. 3.16), the final data products $\beta_p(\psi)$, $DoLP_p(\psi)$, and $p_{22}(\psi)$ [Eq. 3.17, 3.18, and 3.19] were determined for 100, 200, 400, and 700 nm polystyrene bead suspensions used in the statistical analysis discussed in 1.3.1 and compared with results obtained from Mie scattering calculations, DAWN-EOS scattering measurements, and $CF_f(\psi)$ and $BF_f(\psi)$ corrected LISST-VSF measurements. The results of $\beta_p(\psi)$ and $DoLP_p(\psi)$ obtained with the various methods described above are presented in Fig. 3.3. For $\beta_p(\psi)$, the results are nearly indistinguishable between $CF_f(\psi)$ corrected LISST-VSF measurements and $CF2_f(\psi)$ corrected LISST-VSF measurements and they both agree very well with reference values obtained with Mie scattering calculations and independent measurements with DAWN-EOS. The normalized root mean square error (NRMSE) from reference values is displayed in each panel (a–d), and shows that the $CF2_f(\psi)$ corrected data is slightly improved relative to $CF_f(\psi)$ corrected results. This is further evaluated in Fig. 3.4 which shows percent

differences of LISST-VSF corrected $\beta_p(\psi)$ from reference values in panels a–d. For the 400 and 700 nm beads (Fig. 3.4 c,d), there are improvements in the reproduction of the maxima and minima patterns such that disagreement with reference values is reduced by about 10% from ~40% for $CF_f(\psi)$ corrected $\beta_p(\psi)$. Outside of the maxima and minima patterns, errors for $CF2_f(\psi)$ corrected $\beta_p(\psi)$ are typically less than 5%.

For $DoLP_p(\psi)$, the results are nearly indistinguishable between $BF_f(\psi)$ corrected LISST-VSF measurements and $CF2_f(\psi)$ corrected LISST-VSF measurements and they both agree very well with reference values obtained with Mie scattering calculations and independent measurements with DAWN-EOS (Fig. 3.3 e–h). This is further evaluated in Fig. 3.4 which shows absolute differences between LISST-VSF corrected $DoLP_p(\psi)$ and reference values in panels e–h. For 100 and 200 nm beads (Fig. 3.4 e,f), the $CF2_f(\psi)$ corrected $DoLP_p(\psi)$ outperforms the $BF_f(\psi)$ corrected $DoLP_p(\psi)$ for ψ > ~130º, though the improvements are only minor (~0.02). Again, similar to $\beta_p(\psi)$, outside of the maxima and minima features for 400 and 700 nm beads, the differences are small (< 0.05). In summary, using the more featureless 100 and 200 nm beads as examples for evaluation of error, the $CF2_f(\psi)$ corrected results suggest average errors < 4% for all scattering angles 16–150º of $\beta_p(\psi)$ and < 0.007 for $DoLP_p(\psi)$. There is a slight increase in $DoLP_p(\psi)$ error centered around 90º for 100 nm beads (Fig. 3.4e) and 95º for 200 nm beads (Fig 3.4f), however this is at most 0.017.

An advantage of the $CF2_f(\psi)$ correction scheme is that it allows for improved estimations of $p_{22}(\psi)$ from measurements with 100, 200, 400, and 700 nm bead suspensions (Fig. 3.5). It is expected that for a collection of optically inactive homogenous spheres, $p_{22}(\psi)$ = 1 for all angles (Bohren and Huffman 1983; Hovenier et al 1985). Results for ψ = 35–55º and 125–145º are not

shown as recommended in manufacturer's processing code because solutions for $p_{22}(\psi)$ are unstable at ψ = 45º and 135º (Eq. 3.19). Outside these two problematic angular ranges, the results show significant improvement in the estimation of $p_{22}(\psi)$ after $CF2_f(\psi)$ correction, particularly so for ψ > 55º. For example, the RMSE displayed in each panel decreases almost an order of magnitude for 100, 200, and 400 nm beads. The dotted lines representing 25th and 75th percentile data suggest that $p_{22}(\psi)$ is more subject to uncertainty between measurements than $DoLP_p(\psi)$ because this interquartile range is on average ~30–40% larger for $p_{22}(\psi)$ than $DoLP_p(\psi)$. From these results, two angles are chosen to provide the most confident results for $p_{22}(\psi)$; ψ = 20º and 100º. At 20º, error is <0.005 for 100, 200, and 400 nm beads (Fig 3.5 a–c) and <0.01 for 700 nm beads (Fig. 3.5d). At 100º, error is identical for 100, 200, and 400 nm beads but slightly worse for 700 nm beads. Although 700 nm beads produce some increased error, it is most likely related to maxima and minima patterns related to strong constructive and destructive interference patterns produced by such particles, which are not observed as clearly with LISST-VSF measurements, perhaps owing to some effects of non-sphericity of beads related to particle aggregation or manufacturing artifacts. Additionally, 100º is outside the range significantly impacted by the fixing of $CF2_f(\psi)$ values which may result in the small feature observed for 100 and 200 nm beads centered at 92º (Fig. 3.5 a,b), however this feature results in at most 0.01 off from the expected value of 1.

Seawater samples examined in Chapter 1 (Fig. 1.11) are displayed with $CF2_f(\psi)$ corrected results in Fig. 3.6 as a final validation and evaluation of the $CF2_f(\psi)$ corrections. Parameters obtained from these measurements, in addition to those computed from the standard Petzold scattering measurements of oceanic waters, are shown in Table 3.3. These samples are now noted with their respective ID from Chapter 2 (Table 2.1). There are only minor differences between

$CF2_f(\psi)$ corrected $\beta_p(\psi)$and $CF_f(\psi)$ corrected $\beta_p(\psi)$ for nearly all scattering angles (Fig. 3.6 a–c). For $\psi \approx$ 80–110º, $CF_f(\psi)$ corrected $\beta_p(\psi)$ is about 2–8% larger than $CF2_f(\psi)$ corrected $\beta_p(\psi)$ while for $\psi <$ 50º and $\psi >$ 120º, $CF_f(\psi)$ corrected $\beta_p(\psi)$ is about 2–5% smaller than $CF2_f(\psi)$ corrected $\beta_p(\psi)$. Nonetheless, metrics derived from these measurements are similar (Table 3.3). For example, $CF2_f(\psi)$ corrections produce similar b_p (larger by at most 2.5%; sample O_C) and b_{bp} (smaller by as most ~3.5%; sample E_H). This results in slightly smaller $\tilde{b}_{bp}$ and larger $\beta_p(45º)/\beta_p(135º)$ and the angle of minimum $\beta_p(\psi)$, ψ_{min}, is decreased for $CF2_f(\psi)$ corrected $\beta_p(\psi)$. The differences outlined above, however, are minor and metrics derived from $CF2_f(\psi)$ corrected $\beta_p(\psi)$ are still quite comparable to Petzold measurements (Table 3.3) which are widely accepted within the ocean optics community (Mobley 1994; Jonasz and Fournier 2007).

The differences for $DoLP_p(\psi)$ between $CF2_f(\psi)$ and $BF_f(\psi)$ corrected results are more substantial (Fig. 3.6 d–f) and are quantified in Table 3.3. The $CF2_f(\psi)$ corrected $DoLP_p(\psi)$ has larger values for $\psi \approx$ 60–120º, the largest of which occur near 90º. This is of consequence for $DoLP_{p,max}$. The $CF2_f(\psi)$ corrections result in $DoLP_{p,max}$ values which are notably higher than $BF_f(\psi)$ corrected $DoLP_{p,max}$ (e.g., ~10% higher for O_C and ~18% higher for E_H). The angles of $DoLP_{p,max}$, ψ_{max}, are nearly identical despite the different values of $DoLP_{p,max}$ between the two corrections. Also, as a result of the larger $DoLP_{p,max}$, the full width half maximum (FWHM) values of the $CF2_f(\psi)$ corrected $DoLP_p(\psi)$ are reduced by 7–9º to values of ~66º. An additional feature of $CF2_f(\psi)$ corrected $DoLP_p(\psi)$ is reduced symmetry about ψ_{max} as observed in the symmetry parameter (Table 3.3). This is a result of reduced values of $DoLP_p(\psi)$ for $\psi >$ 120º, relative to $BF_f(\psi)$ corrected $DoLP_p(\psi)$. This symmetry parameter has not been reported in any previous literature but it identifies that $DoLP_p(\psi)$ for these seawater samples is more skewed towards

forward angles because values are larger than 1. This parameter is similar to $\beta_p(45^o)/\beta_p(135^o)$ and it indicates that although the angular pattern of $DoLP_p(\psi)$ is not perfectly symmetrical, it is significantly more symmetrical than $\beta_p(\psi)$ [Table 3.3]. As mentioned earlier, increased error from $CF2_f(\psi)$ corrections for the 100 and 200 nm beads near ψ_{max} angles are minor (< 2%); therefore, it is unlikely to result in the changes observed for $DoLP_{p,max}$ seen in Table 3.3. Although there are noticeable changes in $DoLP_p(\psi)$ between $CF2_f(\psi)$ and $BF_f(\psi)$ corrections, for reasons of consistency and the advantage associated with correction for $p_{22}(\psi)$, only $CF2_f(\psi)$ corrected $DoLP_p(\psi)$ are presented for the remainder of this study. It is also important to note that $CF2_f(\psi)$ corrected $DoLP_p(\psi)$ results are still within values obtained from previous, albeit limited, studies with seawater samples (Beardsley 1968; Kadyshevich 1977; Voss and Fry 1984).

Figure 3.6 also includes $p_{22}(\psi)$ results obtained with and without $CF2_f(\psi)$ correction for samples O_C, P_N, and E_H in panels h, i, and j, respectively. As discussed previously, uncorrected $p_{22}(\psi)$ for polystyrene beads is significantly erroneous for ψ > 55º and, accordingly, the uncorrected data for these seawater samples show a decreasing pattern which does not agree well with published results for seawater samples (Beardsley 1968; Kadyshevich 1977; Voss and Fry 1984). In contrast, after $CF2_f(\psi)$ correction, $p_{22}(\psi)$ values for ψ > 55º are increasingly higher than uncorrected results (by over 0.10 for $\psi \approx 100^o$) and $p_{22}(\psi)$ is relatively flat for ψ > 55º with small oscillations. The $CF2_f(\psi)$ corrected $p_{22}(\psi)$ values are slightly higher or about the same as literature values for seawater samples and considering validation of $p_{22}(\psi)$ presented previously, only $CF2_f(\psi)$ corrected $p_{22}(\psi)$ results are discussed in this study.

Our determinations of $p_{22}(\psi)$ for seawater samples show that these values are typically larger than 0.90 for nearly all scattering angles reported. This suggests that these seawater samples

produce scattering patterns that are close to those produced by a collection of optically inactive homogenous spherical particles (Bohren and Huffman 1983). The range of angles which seem to avoid features associated with unstable solutions of $p_{22}(\psi)$ from Eq. 3.19 are ψ < 25º and ψ = 70–110º and it is suggested that only these angles be investigated in future studies with the LISST-VSF. This range of angles also experiences reduced uncertainty as seen in the green dotted lines representing 25th and 75th percentile data. As mentioned previously, the specific angles at which $p_{22}(\psi)$ is evaluated in the remainder of this study are 20º and 100º. These angles experienced minimal error in the validation of $p_{22}(\psi)$ results with polystyrene bead suspensions. The values of $p_{22}(\psi)$ at 20º and 100º for these samples are shown in Table 3.3. Sample E_H has the lowest value at 20º with 0.93 while P_N has the highest value of 0.98. The differences of $p_{22}(100°)$ between these samples are negligible to 2 decimal places and all samples have a value of 0.94. This results in a spread of $p_{22}(20°)/p_{22}(100°)$ of 0.99–1.04 suggesting that although $p_{22}(\psi)$ is mainly flat as a function of ψ, there are some potentially significant differences between samples.

3.3.2. Particle-size fractionation and polarized light scattering

The eight seawater samples characterized in Chapter 2 were also evaluated in terms of $DoLP_p(\psi)$ and $p_{22}(\psi)$ for each original (unfiltered) and two size-fractionated samples. This provides insight into the response of polarized light scattering, specifically $DoLP_p(\psi)$ and $p_{22}(\psi)$, to the removal of medium and large sized particles as well as variations in particle composition and size between samples. The samples presented here are discussed in detail in Chapter 2 (section 2.3) and summarized only briefly in this section as it pertains to $DoLP_p(\psi)$ and $p_{22}(\psi)$ results. Recall that these eight seawater samples represent contrasting natural assemblages of particles from coastal environments, including near-shore samples dominated by organic particulate matter

with predominant role of small-celled or large-celled phytoplankton, estuarine samples dominated by inorganic particles, and offshore samples representative of phytoplankton-dominated subsurface chlorophyll-a maximum and near-surface water dominated by organic non-algal particles.

Results of $DoLP_p(\psi)$ for the unfiltered seawater sample and samples obtained following fractionation with 5 and 20 μm mesh are presented in Fig. 3.7. The most striking feature here is that resulting from fractionation. The $DoLP_p(\psi)$ increases for all filtrate samples in the angular region associated with $DoLP_{p,max}$, except the 5 μm filtrate of E_H, such that the unfiltered sample has lower $DoLP_{p,max}$ than the 20 μm filtrate and the 20 μm filtrate has lower $DoLP_{p,max}$ than the 5 μm filtrate. These changes are subtle for some samples (e.g., P_N and O_S) and more noticeable for others (e.g., P_D and P_R). In addition, the unfiltered sample also has lower $DoLP_p(\psi)$ than each size-fractionated sample for nearly all scattering angles, though it is more apparent for angles near ψ_{max}. As a result of fractionation, the value of ψ_{max} shifted towards smaller angles for some samples (e.g., P_M, P_D, and P_R). Overall, the results of size-fractionation indicate a tendency for an increase in $DoLP_p(\psi)$, especially $DoLP_{p,max}$, with a decrease in the contribution of large sized particles to particulate assemblage. The samples with the lowest unfiltered $DoLP_{p,max}$ (< 0.75) are P_D, P_R, and E_H. Recall that P_D, P_R, and E_H have a strong presence of large sized particles (D_V^{90} > 30 μm) and vary significantly in terms of composition with P_D highly organic and phytoplankton dominated, P_R inorganic dominated with non-negligible phytoplankton contribution, and E_H inorganic dominated (Table 2.3). Samples E_L and O_S are both dominated by non-algal particles and have similar PSD metrics (from Table 2.3: $D_V^{50} \approx 7$ μm; $D_V^{90} \approx 20$ μm), however the inorganic dominated E_L has lower $DoLP_{p,max}$, suggesting that composition may also play a role in decreased $DoLP_{p,max}$. Finally, the sample with the weakest contribution of large sized particles, P_N (from

Table 2.3: D_V^{50} = 5.1 µm; D_V^{90} = 14.1 µm), does not have the highest $DoLP_{p,max}$, however the changes induced to $DoLP_p(\psi)$ following size-fractionation are most insignificant of the samples shown.

The values of $p_{22}(\psi)$ for these eight samples are shown in Fig. 3.8 for ψ = 20º and 100º, the angles which are believed to have high confidence in terms of retrieval of $p_{22}(\psi)$. Similar to $DoLP_p(\psi)$, after size-fractionation $p_{22}(20°)$ and $p_{22}(100°)$ increase for all filtrate samples, except for $p_{22}(20°)$ of the 5 µm filtrate for P_N. The samples with the highest $p_{22}(20°)$ are the small and large phytoplankton dominated organic assemblages (P_N and P_D, respectively), which have values > 0.98 for unfiltered samples. The samples with the lowest $p_{22}(20°)$ are the inorganic dominated assemblages of P_R and E_H, which have values < 0.93 for unfiltered samples (Fig. 3.8a). The range of values for $p_{22}(100°)$ is more limited, however the samples with the highest values of unfiltered samples are small particle size dominated assemblages of E_L and O_S with values > 0.95, and the samples with the lowest values of unfiltered samples are the large particle size dominated assemblages of P_D and P_R with values < 0.935 (Fig. 3.8b). It is important to note here that the two samples which represent the highest values of $p_{22}(100°)$ are different in terms of composition with E_L being inorganic dominated and O_S being organic dominated, and likewise for the two samples representing the lowest values.

All 46 measurements of $DoLP_p(\psi)$ and $p_{22}(\psi)$ collected during this study are presented in Fig. 3.9 and box plots of metrics derived from these measurements are shown in Fig 3.10. For all measurements, $DoLP_{p,max}$ ranges from ~0.65 to 0.90 with the lowest value associated with an unfiltered sample and the highest value associated with a 5 µm filtered sample (Fig. 3.10a). The range of $p_{22}(20°)$ is increased relative to $p_{22}(100°)$ such that interquartile range of $p_{22}(20°)$ is 2–3 times larger than the interquartile range of $p_{22}(100°)$. A noteworthy trend seen in Fig. 3.10

(panels a and e) is an increase in the 25th, 50th, and 75th percentile values of $DoLP_{p,max}$ and $p_{22}(100°)$ as large and then medium sized particles are removed (i.e., unfiltered samples to 20 μm filtrates to 5 μm filtrates). However, changes in terms of magnitude of $DoLP_p(\psi)$ are more substantial than $p_{22}(100°)$. A similar, but weaker, trend is seen in Fig. 3.10d for $p_{22}(20°)$, however it only exists for 50th and 75th percentile data (Fig. 3.10b). There appears to be no, or very weak, changes induced to $DoLP_p$ symmetry and $p_{22}(20°)/p_{22}(100°)$ as a result of size-fractionation (Fig. 3.10 c,f). A one-way analysis of variance was performed for the data presented in Fig. 3.10 to test the statistical significance of the trends observed. These tests confirmed that the only metrics with statistically significant differences as a result of particle size-fractionation were $p_{22}(100°)$ and $DoLP_{p,max}$ (the level of marginal significance $p = 0.0002$ and $p = 0.025$, respectively). The results of this analysis suggested that $p_{22}(20°)$ differences as a result of particle size-fractionation were somewhat significant ($p = 0.07$) compared to the rest of the metrics which had $p \approx 0.2–0.8$.

3.3.3. Relationships between polarized light scattering and particle size and composition

In this section, relationships between polarized light scattering metrics derived from the 46 measurements of $DoLP_p(\psi)$ and $p_{22}(\psi)$ and particle composition and size parameters are evaluated quantitatively using Pearson correlation coefficients, *R* (Table 3.2). Each sample which has measurements with LISST-VSF and measurements of PSD or composition, is treated as an independent sample, i.e., size-fractionated samples are treated as independent of their original (unfiltered) sample to improve statistical significance of correlations. This is reasonable as changes in both composition and size distribution are observed after fractionation (Table 2.3) and changes in $DoLP_p(\psi)$ and $p_{22}(\psi)$ after fractionation are comparable to changes between different unfiltered samples (Fig. 3.7 and 3.8).

In Table 3.4, a grid of R values is shown for polarized light scattering metrics and particle composition and size parameters. Note that the particulate backscattering ratio $\tilde{b}_{bp}$ is also included as a reference light scattering metric which has been previously shown to be related to particle composition (Twardowski et al 2001; Boss et al 2004; Koestner et al 2018). The ratios POC/SPM, Chla/SPM, and $a_{ph}(440)/a_p(440)$ are used to quantify composition of particulate matter. Specifically, POC/SPM provides a proxy for contributions of organic vs. inorganic particles to total mass of particulate matter. Both Chla/SPM and $a_{ph}(440)/a_p(440)$ provide proxies for contributions of phytoplankton vs. non-algal particles although the former in the context of particulate mass concentration and the latter in the context of particulate absorption. Characterization of PSDs using the percentile particle diameters, $D_v^{50}$and D_v^{90}, reflects the contribution of small vs. large sized particles such that higher values indicate increased contributions of large sized particles to the particulate assemblage. These parameters have been shown to provide potentially useful metrics in the analysis of relationships between the optical and particle size properties in seawater (Woźniak et al. 2010).

This correlation analysis provides further evidence to some of the trends discussed previously. For the relationships between the particulate characteristics and $DoLP_p(\psi)$, the only strong correlation exists for $DoLP_{p,max}$ and D_v^{90}. Interestingly, there is only moderate correlation for $DoLP_{p,max}$ and D_v^{50} suggesting that $DoLP_{p,max}$ responds more significantly to changes in the PSD metric which is more sensitive to the presence of large sized particles. Additionally, $DoLP_{p,max}$ has weak correlation with particle composition parameters. This finding is interesting because previous measurements with individual populations of phytoplankton cells and silt particles suggested that $DoLP_{p,max}$ could distinguish between phytoplankton and mineral scatterers with lower values indicating mineral dominated assemblages. As mentioned previously,

ψ_{max} appeared to decrease following particle fractionation (Fig. 3.10b), however this analysis suggests that there is weak correlation for ψ_{max} and particle size and moderate correlation with particle composition. Although appropriate measures were taken to ensure LISST-VSF measurements were made in single scattering regime (section 1.2.1.2), it is recognized that multiple scattering is likely to result in lower $DoLP_{p,max}$. To verify that multiple scattering did not play a role in the $DoLP_{p,max}$ results, correlation coefficients (not shown) of $DoLP_{p,max}$ with both the particulate attenuation and scattering coefficients as indicators of total particle concentration were computed. No significant correlation existed ($R \approx -0.15$).

Table 3.4 shows a noticeable difference between correlations for $p_{22}(\psi)$ at ψ = 20º and ψ = 100º. Despite the particularly small range of $p_{22}(\psi)$ values (Fig. 3.10 d,e), there are strong correlations of $p_{22}(20°)$ with particle composition and $p_{22}(100°)$ with D_v^{90}. The ratio $p_{22}(20°)/p_{22}(100°)$ also shows very similar trends as $p_{22}(20°)$ and $p_{22}(100°)$ shows similar trends as $DoLP_{p,max}$ with these particle size and composition parameters. Interestingly, there is weak correlation between $p_{22}(20°)$ and particle size metrics, and $p_{22}(20°)$ has the most significant correlation with Chla/SPM (R = 0.79). Although the current study is primarily focused on polarized light scattering, it is worth noting the very strong correlation (R = –0.90) of $\tilde{b}_{bp}$ with $a_{ph}(440)/a_p(440)$ and the weak correlation of $\tilde{b}_{bp}$ with particle size parameters. As it has been shown in modeling studies that $\tilde{b}_{bp}$ is a strong function of bulk refractive index (Twardowski 2001), this result suggests the possibility that samples dominated by phytoplankton, not simply organic particles which would include non-algal particles, may have the lowest bulk refractive indices.

The polarized light scattering metrics which provided the strongest correlation with particle composition parameters, $p_{22}(20°)$ and $p_{22}(20°)/p_{22}(100°)$, are plotted in Fig. 3.11 along with

type II linear regressions of the data. Type II linear regressions were chosen here to accommodate uncertainty in both measured variables (Ricker 1973). The data points are colored based on values of D_v^{90} and the red points (D_v^{90} > 30 μm) are spread throughout high and low values of both $p_{22}(20°)$ and $p_{22}(20°)/p_{22}(100°)$ along their linear regressions. This exemplifies the insensitivity of the relationships between both $p_{22}(20°)$ and $p_{22}(20°)/p_{22}(100°)$ and particle composition to particulate assemblages with high D_v^{90}, and therefore high proportions of large sized particles. With the exception of $\tilde{b}_{bp}$ (Fig. 3.11 g,h), these polarized light scattering metrics show positive correlations with particle composition metrics in that high values of $p_{22}(20°)$ or $p_{22}(20°)/p_{22}(100°)$ relate to particulate assemblages which are organic or phytoplankton dominated and low values relate to particulate assemblages which are inorganic dominated. Although there are significant linear correlations presented here, it is not to say that these relationships are simple or necessarily linear. For example, in Fig. 11a, at $p_{22}(20°) \approx 0.985$, there exist data with POC/SPM ranging ~0.3–0.6 and D_v^{90} ranging ~12–36 μm. Nonetheless, acknowledging the complexity of natural assemblages of marine particles, these trends are remarkable in that they hold up over the dynamic range of oceanic conditions presented in this study.

The polarized light scattering metrics which provided the strongest correlation with particle size parameters are plotted in Fig. 3.12 along with type II linear regressions of the data. The data points are colored based on values of $\tilde{b}_{bp}$ and the red points ($\tilde{b}_{bp}$ > 0.018) are spread throughout high and low values of the linear regressions for both $DoLP_{p,max}$ and $p_{22}(100°)$. This exemplifies the insensitivity of the relationships between both $DoLP_{p,max}$ and $p_{22}(100°)$ and particle size parameters to particulate assemblages with high $\tilde{b}_{bp}$, and therefore containing higher refractive, and likely inorganic, particles. These polarized light scattering metrics show negative correlations

with particle size parameters in that low values of $DoLP_{p,max}$ and $p_{22}(100°)$ relate to particulate assemblages which contain higher proportions of large sized particles. As shown in Table 3.4, the correlations with D_v^{50} are only moderate and this is related to the cluster of samples which have much higher D_v^{50} than all other samples ($D_v^{50} \approx 25$ µm; Fig. 3.12 a,b). When using D_v^{90}, these data points are no longer outliers in the relationships with $DoLP_{p,max}$ and $p_{22}(100°)$. The improved correlation of D_v^{90} with $p_{22}(100°)$ compared to $DoLP_{p,max}$ is supported by the higher number of data points which fall on the line of linear fit for $p_{22}(100°)$ while data are more scattered around the line of linear fit which uses $DoLP_{p,max}$ (Fig. 12 c,d). Although there are significant linear correlations with D_v^{90} presented here, these relationships are not always straightforward. For example, in Fig. 12d, there exists samples with nearly the entire dynamic range of D_v^{90} at $p_{22}(100°) \approx 0.95$, and likewise for $DoLP_{p,max} \approx 0.80$ in Fig. 12c. Nonetheless, these trends hold up over the various complex natural assemblages of marine particles presented in this study. These findings also coincide generally with previous measurements in that the largest variability for $DoLP_p(\psi)$ and $p_{22}(\psi)$ between samples measured by Voss and Fry (1984) in mainly offshore Atlantic and Pacific waters was observed for scattering angles 90º and 100º, respectively. Although Voss and Fry (1984) did not characterize the suspended particles, it can be expected that these waters are mainly organic dominated and may vary considerably in terms of PSD.

Although variations of $p_{22}(\psi)$ from 1 are generally considered to be associated with particle nonsphericity as it is equal to 1 at all scattering angles for homogenous and optically inactive spheres, when samples contain irregularly shaped particles such a seawater, $p_{22}(\psi)$ is also related to particle size and complex refractive index. Measurements of $p_{22}(\psi)$ for aerosol particles indicate that minima of $p_{22}(\psi)$ are seen near the side-scattering angular range and lower minima are associated with samples containing larger sized particles (Volten et al. 2001). This concurs

with the findings presented in this section in that $p_{22}(100°)$ correlates negatively with D_v^{90}. Also, observed in the study by Volten et al (2001), the average $p_{22}(20°)$ for mineral-dominated aerosol particles is 0.89. This suggests that deviations from about 0.89 could be related to deviations from mineral dominated particulate assemblages. The seawater sample from this study with the lowest $p_{22}(20°)$ is the unfiltered P_R, which has a value of ~0.92. It is not unreasonable to assume that the P_R sample, which was collected at the SIO Pier after a significant rain event and has a POC/SPM value similar to estuarine samples (Table 2.1 and Table 2.3), could also have a significant proportion of mineral particles of terrestrial and atmospheric origin. Additionally, there is one seawater sample with a value of $p_{22}(20°)$ that is nearly 1 which could indicate that it contains many particles which are nearly spherical or have the shape aspect ratios close to 1. In this case, it is the 5 μm filtrate of a seawater sample collected at the SIO Pier location during high abundance of a large cylindrically-shaped diatom species (one week after sample P_D). The 5 μm filtrate of this sample is unlikely to contain the large cylindrically-shaped diatom and has the highest POC/SPM of all samples (POC/SPM = 0.64) indicating an entirely organic assemblage.

Finally, the positive correlation of $p_{22}(20°)$ with particle composition parameters such as POC/SPM and not particle size parameters is interesting because, referring to Fig. 3.8a, the increases in $p_{22}(20°)$ following fractionation indicate that small and medium sized particles may be more organic dominated than larger particles which are removed from the filtrates by the 5 μm and 20 μm mesh filters. This has been observed in POC/SPM of the 5 μm filtrate for nine out of the twelve samples which have measurements of unfiltered and size-fractionated POC and SPM (Table 2.3 includes six examples). The relationships between the particle size and composition parameters shown in Table 3.4 were also investigated during this analysis but results are not shown. These size and composition metrics have weak correlation ($|R| < 0.3$), except for D_v^{50} and

Chla/SPM which shows a moderate positive correlation of $R = 0.39$. This adds to the complexity of the relationship between particle size and composition, i.e., PSDs with significant proportions of large particles can be organic or inorganic dominated and vice versa.

3.3.4. Towards the development of simple optical sensors to estimate particle size and composition

Miniaturized single-angle scattering sensors such as the ECO Puck (WetLabs) and Seapoint Turbidity Meter (Seapoint Sensors) are increasingly being used on autonomous in situ platforms, such as autonomous underwater vehicles, floats, gliders, and moorings, to take advantage of the lower power consumption and ease of use for long-term oceanographic observations (Claustre et al. 2010; Organelli et al. 2017). The development of many commercially available in situ optical scattering sensors for oceanographic use has been driven by the desire for estimates of the backscattering coefficient, b_b, mainly because the observed water-leaving radiance important for satellite and air-borne remote sensing is to first order proportional to b_b. These sensors typically estimate b_b from measurements at a single angle chosen based on modeled and/or measured VSF shape analysis in the backward direction (Boss and Pegau 2001). An alternative approach would be to identify the optical metrics which best correlate with particulate characteristics that are of most interest to ocean biogeochemistry as is done with spectral absorption and chlorophyll or CDOM fluorometers. Optical instruments that rely on diffraction theory for estimates of the particle size distribution, such as the LISST-100 series (Sequioa Scientific), already employ this philosophy of sensor development, however these instruments lack the practicality and efficiency of other low-cost sensors like ECO Puck.

Based on the richness of the data set generated for this study, an analysis was performed to identify which simple optical measurements best correlate with particle size and composition

parameters discussed in section 3.3.3 on the basis of two statistical parameters; R and the median absolute percent difference (MAPD; Table 3.2) derived from a type II linear regression of each dataset. As mentioned in section 3.2.4, a single LISST-VSF measurement consists of two incident laser polarization states while scattered light for ψ = 14–155º with 1º resolution is detected for two polarization states creating a combination of four measurements of polarized angular light scattering; $\beta_p^{\perp\parallel}(\psi)$, $\beta_p^{\parallel\parallel}(\psi)$, $\beta_p^{\perp\perp}(\psi)$, and $\beta_p^{\parallel\perp}(\psi)$. It has previously been shown that $DoLP_p(\psi)$, and more specifically $DoLP_{p,max}$, has a negative correlation with D_v^{90}, a size parameter which is indicative of the presence of large sized particles (section 3.3.3). This suggests that large particles have a tendency to depolarize linearly polarized light, specifically at side-scattering angles near 90º. Recall from Chapter 1 (Eq. 1.3 and 1.4) that $DoLP_p(\psi)$ can also be computed as:

$$DoLP_p(\psi) = \frac{\beta_p^{\perp \mathrm{U}}(\psi) - \beta_p^{\parallel \mathrm{U}}(\psi)}{\beta_p^{\perp \mathrm{U}}(\psi) + \beta_p^{\parallel \mathrm{U}}(\psi)} \ , \tag{3.20}$$

where the superscript U indicates that the detected light is measured without any polarizing filter, hence unpolarized scattered light is measured. From this equation, it is understandable that some ratio of polarized light scattered at a side-scattering angle would produce a measurement which would serve as a proxy for a particle size parameter such as D_v^{90}.

The four polarized measurement combinations from the LISST-VSF instrument result in six unique ratio combinations, e.g., $\beta_p^{\parallel\perp}(\psi_1)/\beta_p^{\parallel\parallel}(\psi_1)$. The subscript 1 is used here to emphasize that both the numerator and denominator use the same scattering angle. For the 41 samples which contain suitable LISST-VSF measurements and PSD measurements to derive D_v^{90}, a type II linear regression was performed for D_v^{90} and each of the six possible measurement ratio combinations using ψ_1 = 20–120º. This analysis also included $DoLP_p(\psi_1)$ as a polarized light scattering measurement so that there was a total of 707 linear fits with D_v^{90}. The statistical parameters R and

MAPD were computed from each of the 707 datasets and are shown in Fig. 3.13 and 3.14, respectively. Note that R values determined here are negative but displayed as the absolute value for visualization purposes (Fig. 3.13) and MAPD is plotted inverse such that lower values of MAPD are warmer in color (towards red color in Fig. 3.14). The most significant correlation ($|R| > 0.65$) is observed for the $\beta_p^{\parallel\perp}(\psi_1)/\beta_p^{\parallel\parallel}(\psi_1)$ combination in the region ψ_1 = 95–110º. The maximum correlation for $DoLP_p(\psi_1)$ is $|R| \approx 0.60$ for ψ_1 near 90º. It is interesting that $DoLP_p(\psi_1)$ has a large angular range of moderate to strong correlation with $|R| > 0.50$ for $\psi_1 \approx$ 65–120º, and correlations with $\beta_p^{\parallel\perp}(\psi_1)/\beta_p^{\perp\perp}(\psi_1)$ behave similarly as $DoLP_p(\psi_1)$. It is important to acknowledge for experimental data such as this, the largest R does not necessarily indicate the most useful predictive relationship and an indicator of average, in this case median error is used to further hone in on an ideal measurement to serve as a proxy for D_v^{90} (MAPD in Fig. 3.14). In this case, it is now the $\beta_p^{\parallel\perp}(\psi_1)/\beta_p^{\perp\perp}(\psi_1)$ measurement combination which has the lowest error with MAPD < ~15% for $\psi_1 \approx$ 80–98º. For the angular region associated with a maximum correlation between D_v^{90} and $\beta_p^{\parallel\perp}(\psi_1)/\beta_p^{\parallel\parallel}(\psi_1)$, MAPD is ~20%, and for the angular region associated with maximum correlations with $DoLP_p(\psi_1)$, MAPD > 25%.

Two schemes were developed to determine the most useful measurement to serve as a proxy for D_v^{90}. The first sorted all values of $|R|$ in decreasing order to determine the 10 measurements which had the highest correlation with the desired parameter, in this case D_v^{90}. Of those top 10 $|R|$, the measurement which had the lowest MAPD is then chosen. The second scheme sorted all values of $|R|$ in decreasing order and recalculates each value as a percentile. This was also done for 1/MAPD (so that the higher percentile values indicate lower error). These two vectors of percentile-based $|R|$ and 1/MAPD, were then summed so that the highest combined percentile

value was indicative of the measurement which had both the highest relative $|R|$ and the lowest relative MAPD.

In terms of a simple optical proxy for D_v^{90}, the first solution is $\beta_p^{\parallel\perp}(109°)/\beta_p^{\parallel\parallel}(109°)$ with $|R| = 0.6742$ and MAPD = 20.4%, and the second solution is $\beta_p^{\parallel\perp}(96°)/\beta_p^{\perp\perp}(96°)$ with $|R| = 0.5934$ and MAPD = 14.1%. For reasons of engineering practicality, the first solution is used here because it requires only one incident state of the laser, parallel, and two detectors at 109º, one to measure perpendicularly polarized scattered light and the other to measure parallel polarized scattered light. This system would utilize a polarizing prism such as what is used in the LISST-VSF Roving Eyeball sensor. This first solution describing D_v^{90} as a function of $\beta_p^{\parallel\perp}(109°)/\beta_p^{\parallel\parallel}(109°)$ is shown in Fig. 3.16 along with D_v^{90} as a function of $DoLP_{p,max}$ (also in Fig. 3.12c) as a comparison. From the samples analyzed using a parallel incident beam, there was between ~5.5 and 7 times as much light scattered at 109º with perpendicular polarization than light scattered with parallel polarization (Fig. 3.16a). The colored data points spread throughout the linear regression suggest that there is no clear trend related to composition as assessed through $\tilde{b}_{bp}$. The correlation is also weakest for D_v^{90} for 15–30 μm as seen in the large spread of triangle points around the linear regression and there is an average positive bias for the regression (MNB = 6.5%). The observed strong correlation with D_v^{90}, and not composition, thus suggests that it is the samples which have PSDs with more significant contributions from large sized particles, that exhibit scattered light with on average more equal contributions of perpendicular and parallel polarization states.

The composition metric for this analysis is POC/SPM. As discussed in Chapter 2, simple approaches to estimate POC from b_{bp} are problematic because different scenarios of particulate composition can result in similar b_{bp} magnitude and size-based budgets. This has been observed in many other studies and an alternate approach to the estimation of POC could be a two-step

approach which relies on an estimate of POC/SPM before using a composition specific relationship for b_{bp} and POC (Woźniak et al. 2010; Reynolds et al. 2016). However, the estimation of POC/SPM from a purely optical perspective has remained elusive. As seen in this study, the backscattering ratio $\tilde{b}_{bp}$ correlates strongly with composition metrics, including POC/SPM (Table 3.4). This has also been observed for a different composition metric, Chla/$c_p(660)$ where $c_p(660)$ is the particulate attenuation coefficient at 660 nm which typically correlates well with SPM (Boss et al. 2004). Based upon this information, it is understandable that some ratio of polarized light scattering at a backwards scattering angle to polarized light scattering at a forward scattering angle would produce a measurement which would serve as a proxy for a particle composition parameter such as POC/SPM. There is additional evidence that enhancements in cross polarized light scattering in the near-forward scattering region is indicative of presence of inorganic particles, particularly particulate inorganic carbon (Guay and Bishop 2002).

It was found earlier in this section that $\beta_p^{\parallel\perp}(\psi_1)/\beta_p^{\parallel\parallel}(\psi_1)$ measurement combination correlated best with D_v^{90} at ψ_1 = 109º. In this analysis, the same measurement combination was used, however the polarized light scattering ratio $\beta_p^{\parallel\perp}(\psi_1)/\beta_p^{\parallel\parallel}(\psi_2)$ was computed for ψ_1 = 80–120º and ψ_2 = 16–50º and linear regressions were determined with POC/SPM for log-transformed data. For this analysis, a total of 27 samples were used which contained suitable LISST-VSF measurements and both POC and SPM measurements. These measurement combinations result in a total of 1435 datasets with POC/SPM of which the statistical parameters *R* and MAPD were computed and plotted as grids in Fig. 3.16. Correlations of this measurement combination with POC/SPM are in general higher than correlations with D_v^{90} ($|R|$ > 0.70 for over half of the angle combinations). The highest correlations with POC/SPM are observed for ψ_1 > ~100º and ψ_2 < ~30º, and the lowest correlations are for ψ_1 ≈ 80–100º and ψ_2 ≈ 35–50º. Interestingly, all ψ_1 angles

produce strong correlation when $\psi_2 \approx 16–25^o$ ($|R| > 0.80$). The trends for MAPD are more sporadic and only small pockets of the lowest MAPD (< 20%) exist for $\psi_1 \approx 110^o$ and $\psi_2 \approx 20^o$ or 40^o.

An identical procedure that was outlined previously for solutions of the single angle measurement combination to estimate D_v^{90} was used to identify the two most useful relationships to estimate POC/SPM assuming the measurement combination $\beta_p^{\parallel\perp}(\psi_1)/\beta_p^{\parallel\parallel}(\psi_2)$. The first solution is $\psi_1 = 111^o$ and $\psi_2 = 20^o$ with $|R| = 0.8635$ and MAPD = 19.7%, and the second solution is $\psi_1 = 111^o$ and $\psi_2 = 19^o$ with $|R| = 0.8613$ and MAPD = 18.3%. These solutions differ in only ψ_2 by 1°, which is insignificant when considering uncertainty in measurements. Nonetheless, solution two is assumed as the ideal solution because of the lower MAPD (by ~1.5%) and is shown in Fig. 3.17 along with POC/SPM as a function of $\tilde{b}_{bp}$ for comparison. From the samples analyzed using a parallel polarized incident beam, the ratio of light scattered at 111° with perpendicular polarization to light scattered at 19° with parallel polarization was between 0.006 and 0.014 (Fig. 3.17a). The improvements of POC/SPM as a function of $\beta_p^{\parallel\perp}(111°)/\beta_p^{\parallel\parallel}(19°)$ in terms of statistical parameters *R*, MAPD, and MNB, are significant when compared to POC/SPM as a function of $\tilde{b}_{bp}$ (Fig. 3.17). These improvements are related to the tighter spread of data points along the regression line with the mixed and inorganic dominated samples with POC/SPM < 0.3 (triangles and diamond points) in Fig. 3.17a compared to data in Fig. 3.17b. The colored data points spread throughout the regression line suggest that there is no clear trend related to particle size as assessed through D_v^{90}.

It is notable that the ideal solutions to estimate POC/SPM and D_v^{90} from polarized light scattering measurements both rely on a measurement of $\beta_p^{\parallel\perp}(\psi_1)$ with $\psi_1 = 109^o$ for D_v^{90} estimation and $\psi_1 = 111^o$ for POC/SPM estimation. In the case of estimating particle size, normalizing $\beta_p^{\parallel\perp}(\psi_1)$ by $\beta_p^{\parallel\parallel}(\psi_1)$ results in a measurement which correlates well with D_v^{90}

independent of the compositional proxy $\tilde{b}_{bp}$. For the case of estimating particle composition, normalizing $\beta_p^{\parallel\perp}(\psi_1)$ by $\beta_p^{\parallel\parallel}(\psi_2)$, with ψ_2 around 20º, results in a measurement that correlates well with POC/SPM independent of the PSD parametrized with D_v^{90}. Note that it was checked if $\beta_p^{\parallel\parallel}(\psi_2)$ could be replaced by $\beta_p^{\parallel\perp}(\psi_2)$ in the POC/SPM optical relationship and it was found to decrease correlations and increase errors relative to the use of $\beta_p^{\parallel\parallel}(\psi_2)$ as the normalization factor. It was also checked which angles of only $\beta_p^{\parallel\perp}(\psi)$ correlate with POC/SPM. This analysis showed that for angles ~80–140º, $R > 0.80$ and MAPD < 30% with the ideal solution at 127º ($R = 0.81$, MAPD = 26.5%, and MNB = 7.4%). Interestingly, all angles evaluated within the range 16–150º have improved correlations relative to the backscattering ratio $\tilde{b}_{bp}$ (Fig. 3.17b), but all solutions have higher MAPD. Also note that none of the solutions presented earlier in this section change if the angular range of the analysis is expanded to include ψ_1 = 121–150º and no significant changes in solutions are found if type I linear regressions are used in the determination of MAPD.

3.3.5. Determining the particle size metric D_v^{90} using percentile-based values of $DoLP_{p,max}$

Up until this point, all optical parameters evaluated for relationships with particle size and composition metrics were determined from the median values of scattering parameters based ~200–400 original replicate measurements with the LISST-VSF instrument for a given sample. Following observations of improved correlation of $DoLP_{p,max}$ with D_v^{90} as opposed to D_v^{50}, anomalous values of $DoLP_{p,max}$ associated with percentile-based values were compared using type II linear regressions with particle size parameter D_v^{90}. Briggs et al. (2013) found that fluctuations in b_{bp} or c_p measurements with clay particles in a laboratory environment could be used to estimate mean particle size. In a similar manner, it is expected that the use of variability within measurements for a given seawater sample will improve the observed relationship between the

presence of large sized particles and lower values of $DoLP_{p,max}$ discussed in section 3.3.3. To be specific, it is expected that lower percentile values of $DoLP_{p,max}$ are to be associated with the relatively rare and larger sized particles influencing D_v^{90}.

To derive the percentile based values of $DoLP_{p,max}$ in this study, $DoLP_p(\psi)$ was redefined using the desired percentile values at each ψ so that a new $DoLP_{p,max}$ could be found. The new $DoLP_{p,max}$ is notated with a superscript number associated with the percentile used in the determination of $DoLP_p(\psi)$. For example, $DoLP_{p,max}^{10}$ was derived using 10th percentile data. In Fig. 3.18, D_v^{90} is plotted as a function of the 10th, 50th, and 90th percentile values of $DoLP_{p,max}$ (i.e., $DoLP_{p,max}^{10}$, $DoLP_{p,max}^{50}$, and $DoLP_{p,max}^{90}$, respectively) derived from the ~200–400 LISST-VSF measurements for each sample. Note that $DoLP_{p,max}^{50}$ is equivalent to the median $DoLP_{p,max}$ used throughout the study and what is shown in Fig. 3.18b is identical to Fig. 3.12c. The lower percentile data corresponds to a shift towards lower values of $DoLP_{p,max}$ while the range of values remains fairly consistent. For example, $DoLP_{p,max}^{90} \approx 0.75–0.99$ while $DoLP_{p,max}^{10} \approx 0.57–0.82$. The regressions determined in the top panels (Fig. 3.18 a,b,c) were used in the comparison of estimated D_v^{90} vs. measured D_v^{90} in the bottom panels (Fig. 3.18 d,e,f). There are clear improvements in the linear relationship between $DoLP_{p,max}$ and D_v^{90} when using lower percentile data. For example, R decreases from a value of -0.42 for $DoLP_{p,max}^{90}$ to a value of -0.73 for $DoLP_{p,max}^{10}$. The estimated D_v^{90} vs. measured D_v^{90} plots also show significant improvement and the least scattered data around the 1:1 line for $DoLP_{p,max}^{10}$ compared to the higher percentile-based measures. This suggests that the rare low values of $DoLP_{p,max}$ relate most closely to the particle size parameter D_v^{90}, which is most influenced by the presence of rarer large particles. Therefore, it is the large sized particles which tend to decrease $DoLP_{p,max}$ and generate scattered light in the side angle region near 90º

which has lower degree of linear polarization. Other percentiles were also used, such as 5th, 25th, 75th, and 95th percentile data, to determine $DoLP_p(\psi)$ and $DoLP_{p,max}$. These results generally agreed with the trends discussed above in that lower percentile data provided improved correlation and statistically significant relationships between $DoLP_{p,max}$ and D_v^{90}.

This analysis was based on a time series which consisted of approximately 15–30 minutes of LISST-VSF measurements of a given sample in a controlled laboratory environment under very good mixing conditions. This analysis was also performed using only the first ~100 measurements (i.e., ~7 minutes of data acquisition) of each measurement sequence and provided similar results. It is important to note that larger particles defined here as > 20 μm in diameter are relatively rare in seawater samples compared with smaller particles, however they were still present in significant quantities during these experiments. For example in sample P_N (weakly influenced by large particles), particles counted during PSD measurements in size-bins > 20 μm were ~20 particles per mL. For sample P_D (strongly influenced by large particles), particles counted during PSD measurements in size-bins > 20 μm were ~300 particles per mL. Acknowledging that the LISST-VSF laser beam illuminates ~1 mL per measurement scan (laser is ~3 mm in diameter by 15 cm in length), it is not unreasonable that a sufficient number of larger particles were encountered over the course of ~100 measurements to influence the scattering measurements. Interestingly, this analysis did not work for $p_{22}(100°)$, i.e., correlation decreased for 10th and also 90th percentile $p_{22}(100°)$ data, despite $p_{22}^{50}(100°)$ having improved correlation with D_v^{90} compared to $DoLP_{p,max}^{50}$ (Fig. 3.12 c,d).

3.4. Summary and concluding remarks

This study involved sixteen seawater samples representing contrasting natural assemblages of particles from coastal environments, including near-shore samples dominated by organic particulate matter with predominant role of small-celled or large-celled phytoplankton, estuarine samples dominated by inorganic particles, and offshore samples representative of phytoplankton-dominated subsurface chlorophyll-a maximum and near-surface water dominated by organic non-algal particles. Each seawater sample underwent careful and comprehensive characterization in terms of angle-resolved polarized light scattering, particle composition in terms of various metrics derived from mass concentration and particulate absorption, and particle size distribution. Samples were additionally characterized in terms of angle-resolved polarized light scattering, particle size distribution, and sometimes particle composition following fractionation with 5 and 20 μm mesh. Some of the important findings are summarized below:

(i) Values of $p_{22}(20°)$ for marine particles are weakly dependent on particle size and range between about 0.92 and 1.0 with the lowest values generally associated with inorganic dominated assemblages and the highest values generally associated with organic dominated assemblages.

(ii) Values of $p_{22}(100°)$ for marine particles are weakly dependent on particle composition and range between about 0.92 and 0.97 with the lowest values generally associated with particle assemblages containing higher proportions of large sized particles and the highest values generally associated with particle assemblages containing lower proportions of large sized particles.

(iii) Reductions of $DoLP_{p,max}$ depend weakly on particle composition and are associated mainly with increased proportions of the relatively rare large sized particles.

(iv) Optically-based proxies to estimate particle size and composition were developed which rely on polarized light scattering measurements at only one or two angles.

It is remarkable that the two optically-based solutions for estimating particle size and composition share the measurement combination of $\beta_p^{\parallel\perp}(\psi_1)$ with ψ_1 centered around 110º. A simple sensor to estimate D_v^{90} and POC/SPM would thus consist of three detectors and an incident polarization state of laser parallel to the scattering plane. Two detectors would be placed at a scattering angle of around 110º utilizing a polarizing prism to partition the scattered light into two components (similar to the LISST-VSF instrument) so that one detector would sense only parallel and another detector would sense only perpendicularly polarized scattered light. A third detector would be placed at a scattering angle of around 20º to sense only parallel polarized scattered light. Using the relationships developed in this study, it is estimated that such an instrument could predict both D_v^{90} and POC/SPM to within 20% accuracy, therefore providing useful predictions of the proportions of small vs. large sized particles and organic vs. inorganic particles with unprecedented efficiency. Such particle size and composition parameters are currently achieved following lab-based analysis on aliquots of seawater which can be significantly limited in spatial and temporal scales compared to in situ optical measurements. Measurements with such an instrument could be taken relatively rapidly using autonomous or otherwise small instrument platforms.

The engineering development of such a sensor is beyond the scope of the current study, rather this data can be used as a scientific foundation for the development of a low-cost optical sensor for estimating particle size and compositional proxies, with several notes of caution. This data is limited in the sense that sample sizes are relatively small ($N = 27$ for POC/SPM; $N = 41$ for D_v^{90}) and although a broad range of oceanic conditions is included, it is lacking in environments consistent with oligotrophic open ocean or highly inorganic waters dominated by particles of

terrestrial origin. The other limitation of this study is that the PSD measurements were limited to the range of 2–60 μm, and therefore the size parameter D_v^{90} is limited in the sense that populations of smaller particles such as heterotrophic bacteria, picophytoplankton, or other colloidal particles, as well as larger particles such as large microphytoplankton have not been included in this size parameter. Finally, the evaluation of the optical relationships for particle size and composition have been performed using the "training" data and to properly quantify error of the developed relationships, an independent data set should be used.

As a final note, the basic research presented in the current study on the inherent polarization scattering properties of marine particle assemblages contributes fundamental knowledge to aid in deriving new or improved ocean biogeochemical data products from remote sensing platforms observing the ambient polarized light field. Currently, there are plans to include two polarimeters on board the NASA PACE satellite mission expected to launch in 2022 (Hasekamp et al. 2019). The findings of this current study provide a foundation for the potential use of these polarimeters for characterizing marine particle assemblages in terms of particle size distribution and composition, and further investigation, with both experimental and theoretical modeling studies, is needed to realize the full potential of polarimetry in the study of the oceans.

3.5. Acknowledgments

This work was supported by NASA Terrestrial Hydrology and Ocean Biology and Biogeochemistry Programs (Grants NNX13AN72G and 80NSSC18K0956) and the NASA Earth and Space Science Fellowship Program (Grant NNX14AK93H). Special thanks to Dariusz Stramski and Rick Reynolds for providing valuable comments on the manuscript. Additional acknowledgements to Rick Reynolds, Eric Chen, Linhai Li, and Hugh Runyan for assistance during measurements and Eric Chen and Linhai Li for assistance related to processing of data.

POC analysis of seawater samples was done at the Marine Science Institute, University of California Santa Barbara. A very special thanks to Shea Cheatham for support with editing and preparing the appendix material.

Chapter 3 material is currently being prepared to be submitted for publication with authors Koestner, D., D. Stramski, and R. A. Reynolds. The dissertation author will be the primary investigator and author of this paper.

3.6. Figures

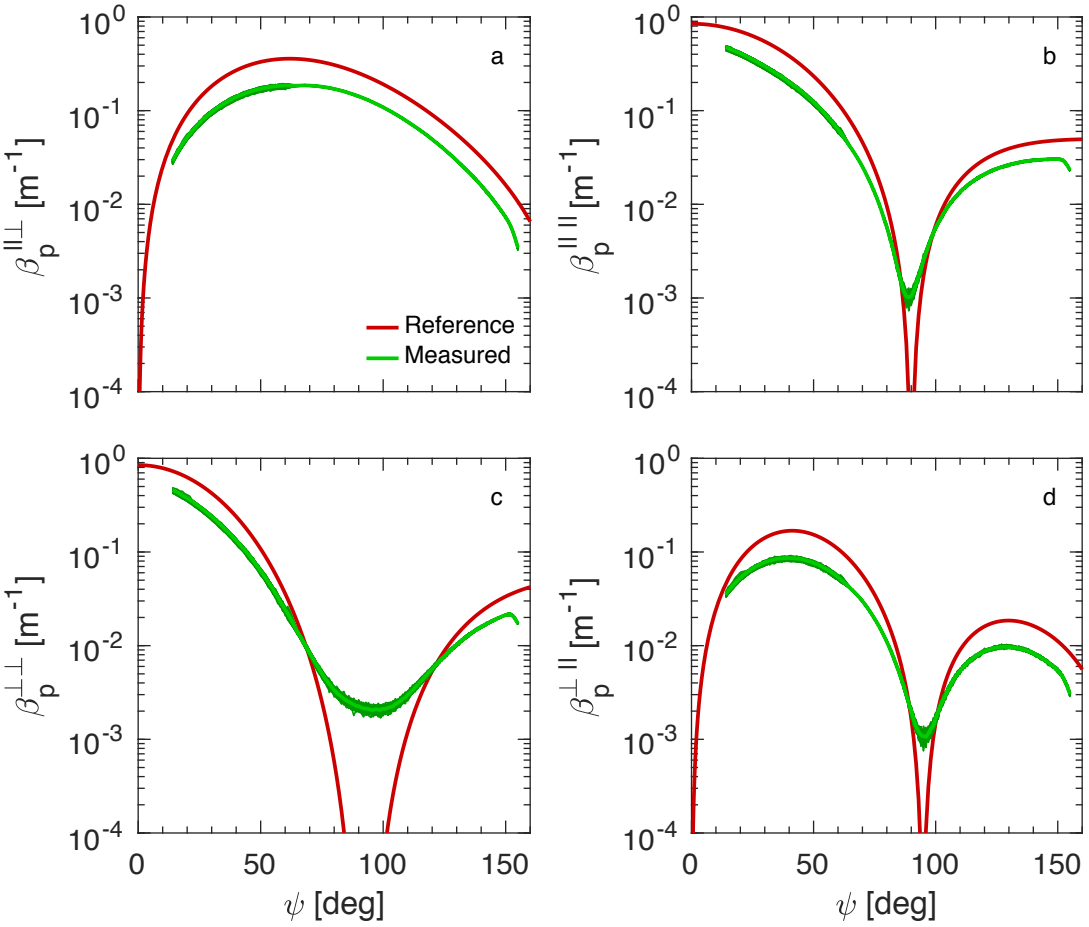

Figure 3.1. Reference values (red) and measurements (green) of the four polarized light scattering measurement combinations from the LISST-VSF for 200 nm diameter polystyrene beads suspended in water. The expected reference values obtained from Mie scattering calculations are plotted from 0.09º to 160º and measured values obtained with the LISST-VSF are plotted from 16º to 155º, both with linear scaling. Quality controlled but uncorrected measurements obtained with the LISST-VSF (dark green lines, number of measurements $N = 128$) and the median value (solid green line) are shown.

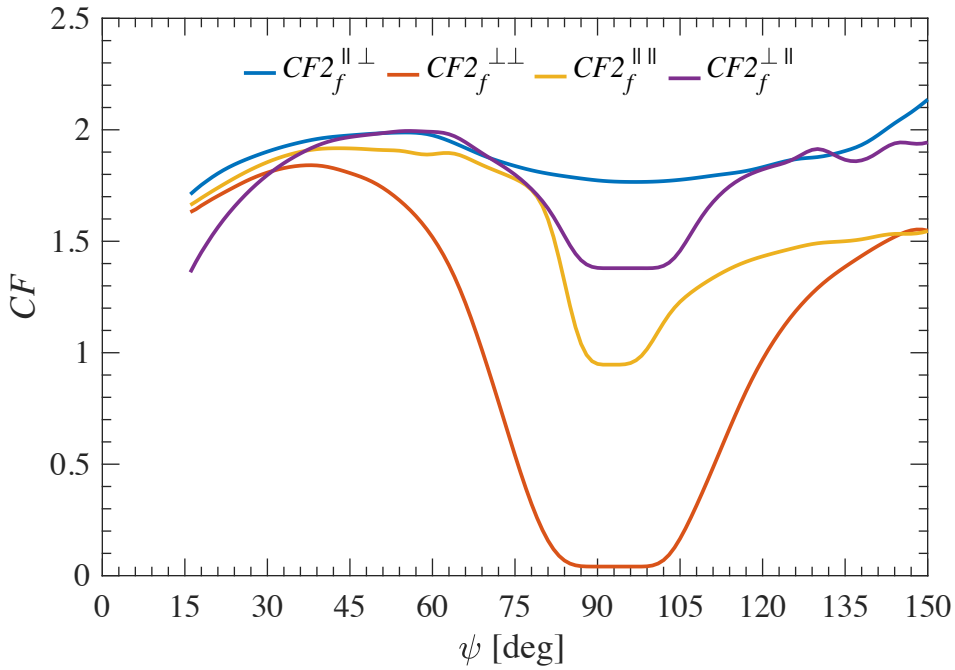

Figure 3.2. Final correction functions, $CF2_f(\psi)$, for LISST-VSF measurements of each polarized light scattering measurement combination, as indicated in legend, over the angular range 16–150° determined from 100, 200, and 400 nm polystyrene bead suspensions.

Figure 3.3. Comparison of measurements obtained with two different corrections and reference values of $\beta_p(\psi)$ [panels a–d] and $DoLP_p(\psi)$ [panels e–h] for suspensions of polystyrene beads of varying diameter as indicated in legend and for ψ = 16–150º. The reference values obtained with Mie scattering calculations are shown in red, while LISST-VSF measurement results obtained following corrections described in Koestner et al. 2018 [$CF_f(\psi)$ or $BF_f(\psi)$] are shown in blue and results obtained following $CF2_f(\psi)$ correction are shown in green. Solid lines indicate median values while the dotted lines are 25th and 75th percentile values. The normalized root mean square errors, NRMSE, from reference values of the two corrected $\beta_p(\psi)$ are displayed in panels a–d, while the root mean square errors, RMSE, from reference values of the two corrected $DoLP_p(\psi)$ are displayed in panels e–h. Independent measurements of $\beta_p(\psi)$ and $DoLP_p(\psi)$ obtained with the DAWN-EOS instrument are also shown as diamonds.

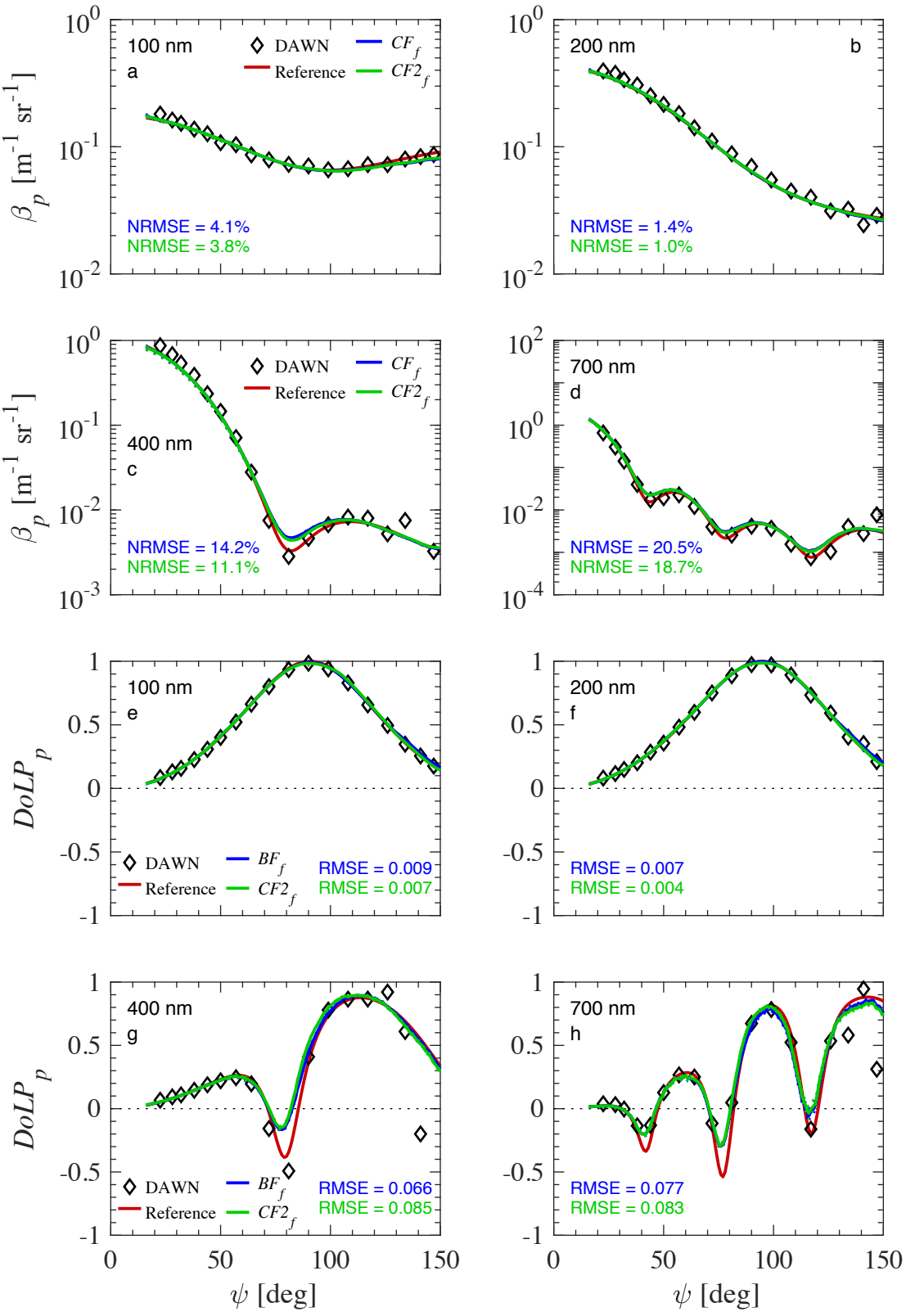

Figure 3.3. (Caption on previous page)

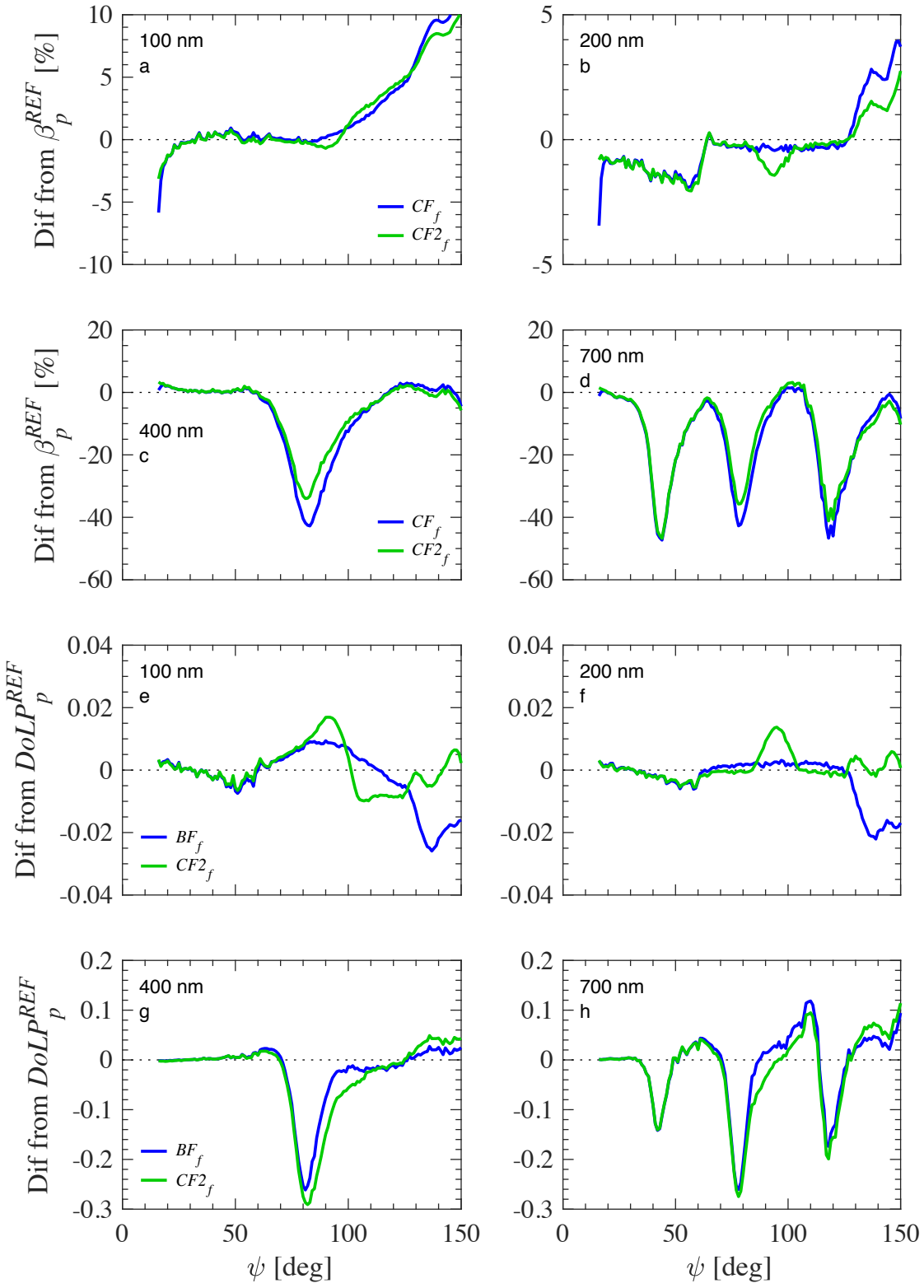

Figure 3.4. Residuals between median values for each of two different corrections and reference values from the data shown in Fig. 3.3.

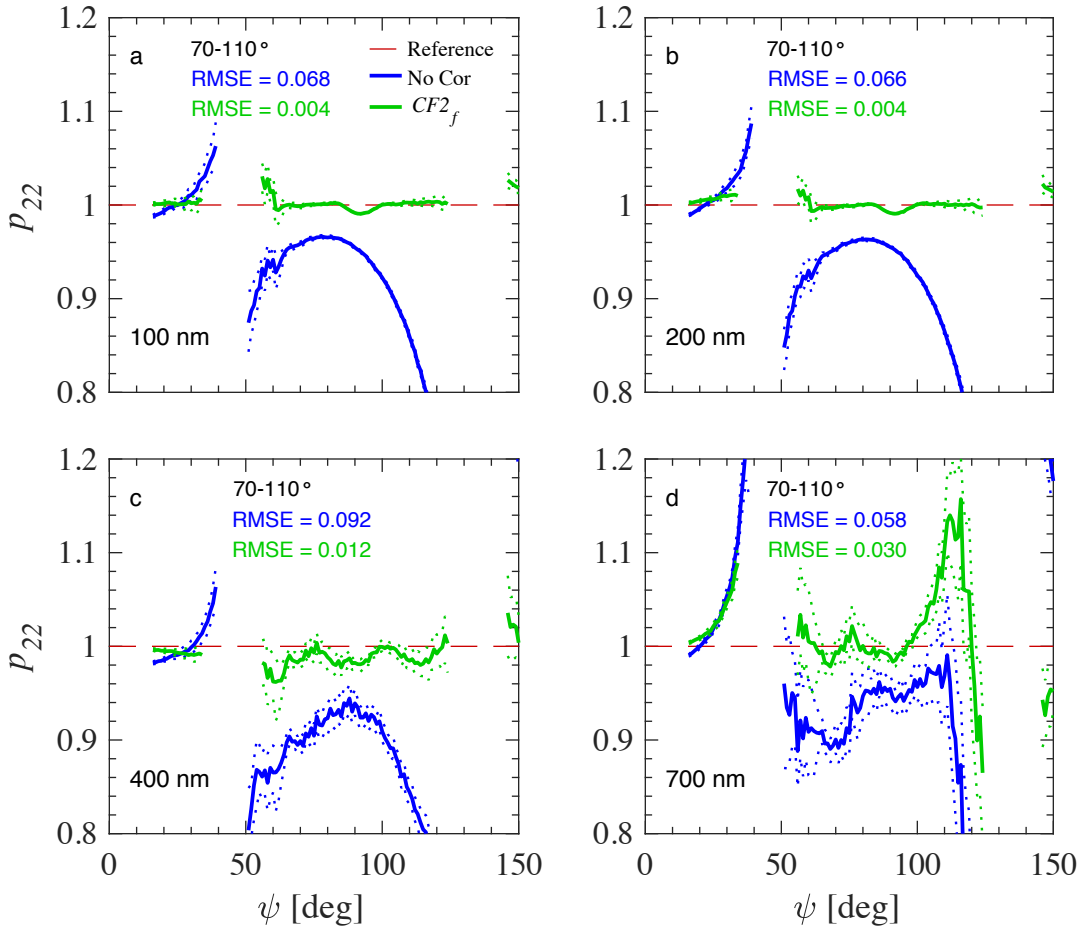

Figure 3.5. Measurements of normalized scattering matrix element $p_{22}(\psi)$ for ψ = 16–150º obtained with the LISST-VSF instrument with and without $CF2_f(\psi)$ correction for polystyrene bead suspensions as indicated in legend. Data is not shown for ψ = 35–55º and 125–145 per manufacturer's suggestion. A reference value of $p_{22}(\psi)$ = 1 for all ψ is plotted to represent homogenous spherical particles and the root mean square error, RMSE, from 1 is displayed for ψ = 70–110º. Dotted lines represent 25th and 75th percentile data from the ~128 measurements while solid lines represent median data.

Figure 3.6. Measurements of $\beta_p(\psi)$, $DoLP_p(\psi)$, and $p_{22}(\psi)$ obtained with the LISST-VSF for ψ = 16–150º on natural seawater samples from the San Diego region representing (a,d,g) subsurface offshore waters, (b,e,h) SIO Pier, and (c,f,i) San Diego River Estuary with reference sample ID indicated in legend. Results obtained following corrections described in Koestner et al. 2018 [$CF_f(\psi)$ or $BF_f(\psi)$] are shown in blue and results obtained following $CF2_f(\psi)$ correction are shown in green, with the exception that no correction is shown using blue for $p_{22}(\psi)$ results. Solid lines represent median values while dotted lines indicate the 25th and 75th percentiles obtained from a series of measurements on each sample.

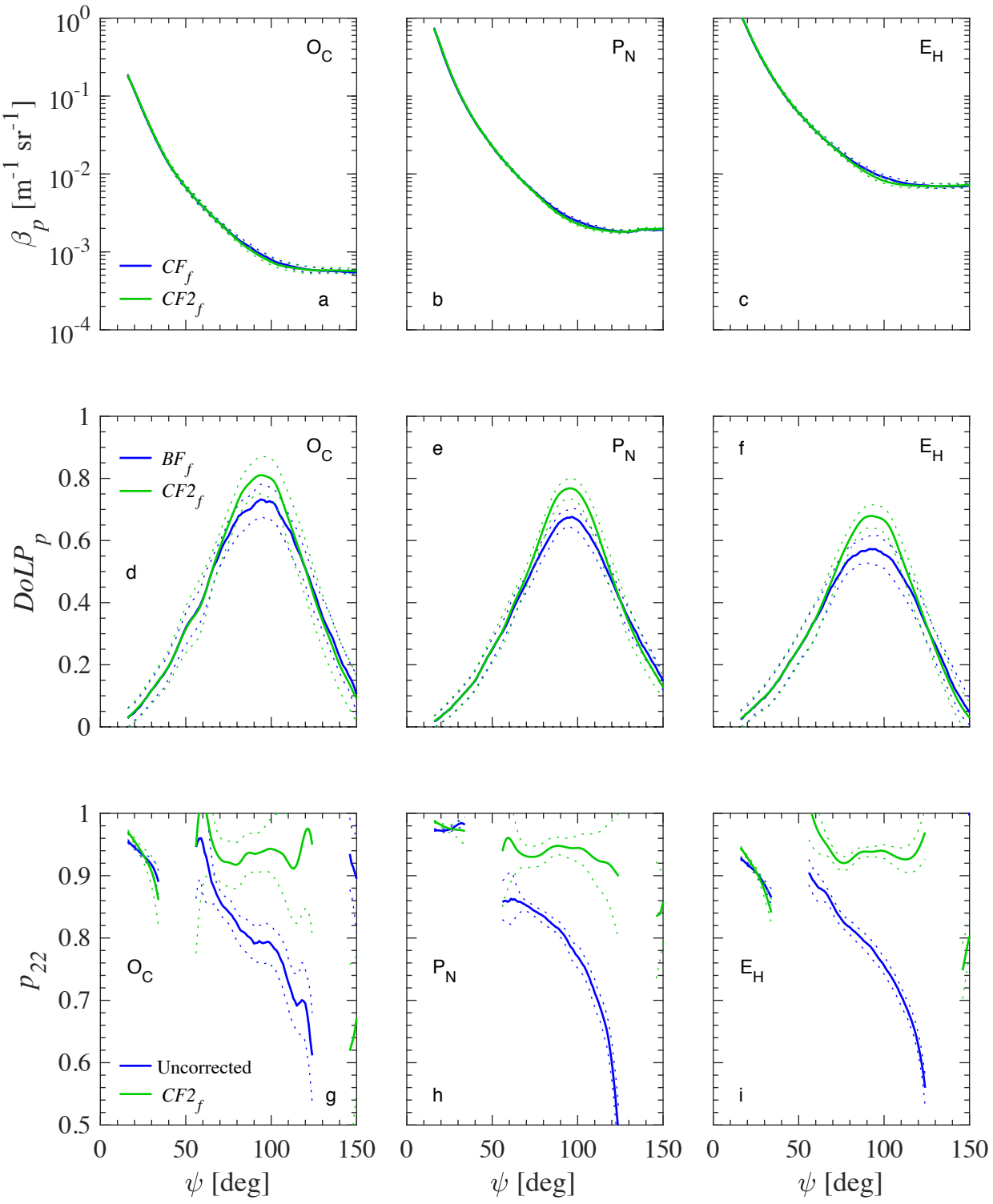

Figure 3.6. (Caption on previous page)

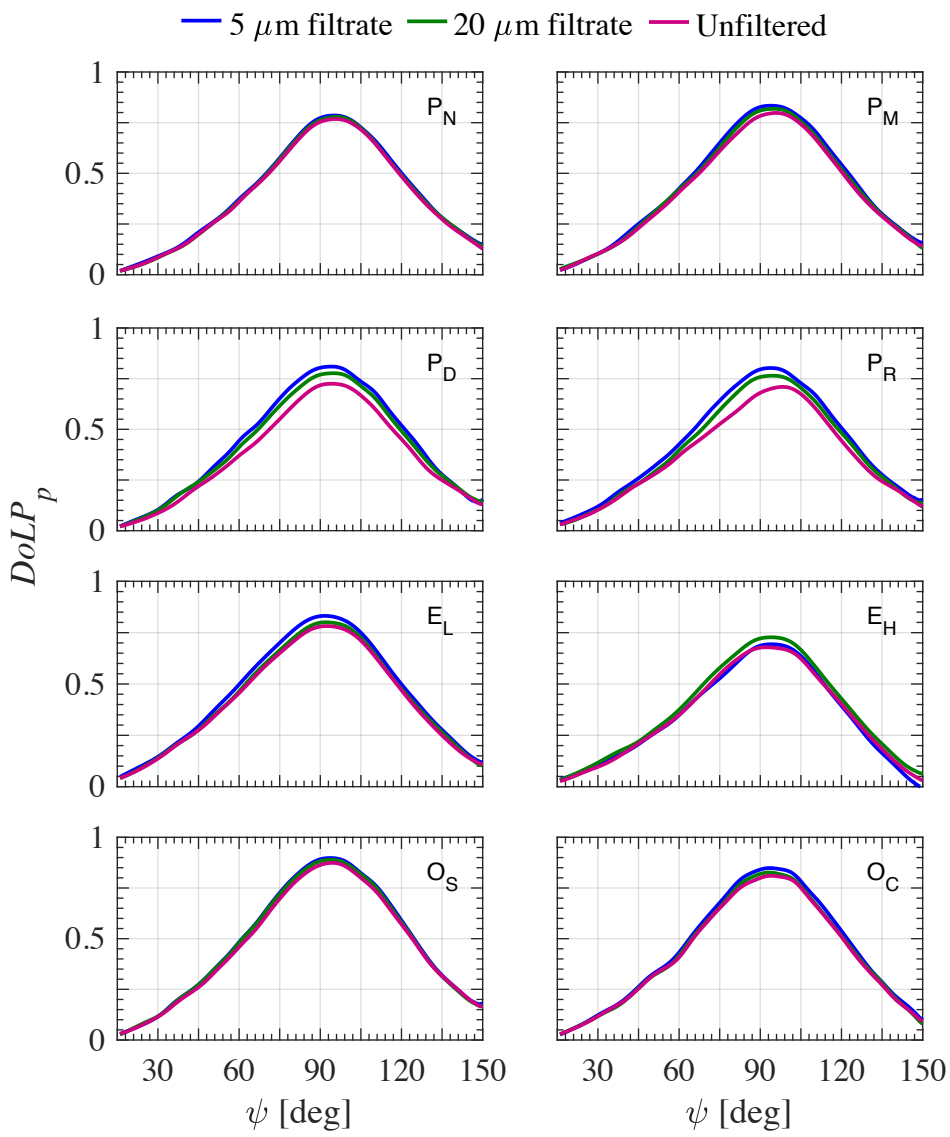

Figure 3.7. Measured $DoLP_p(\psi)$ for unfiltered and size-fractionated samples of the eight seawater samples described in Chapter 2 (Table 2.1) as indicated in legend.

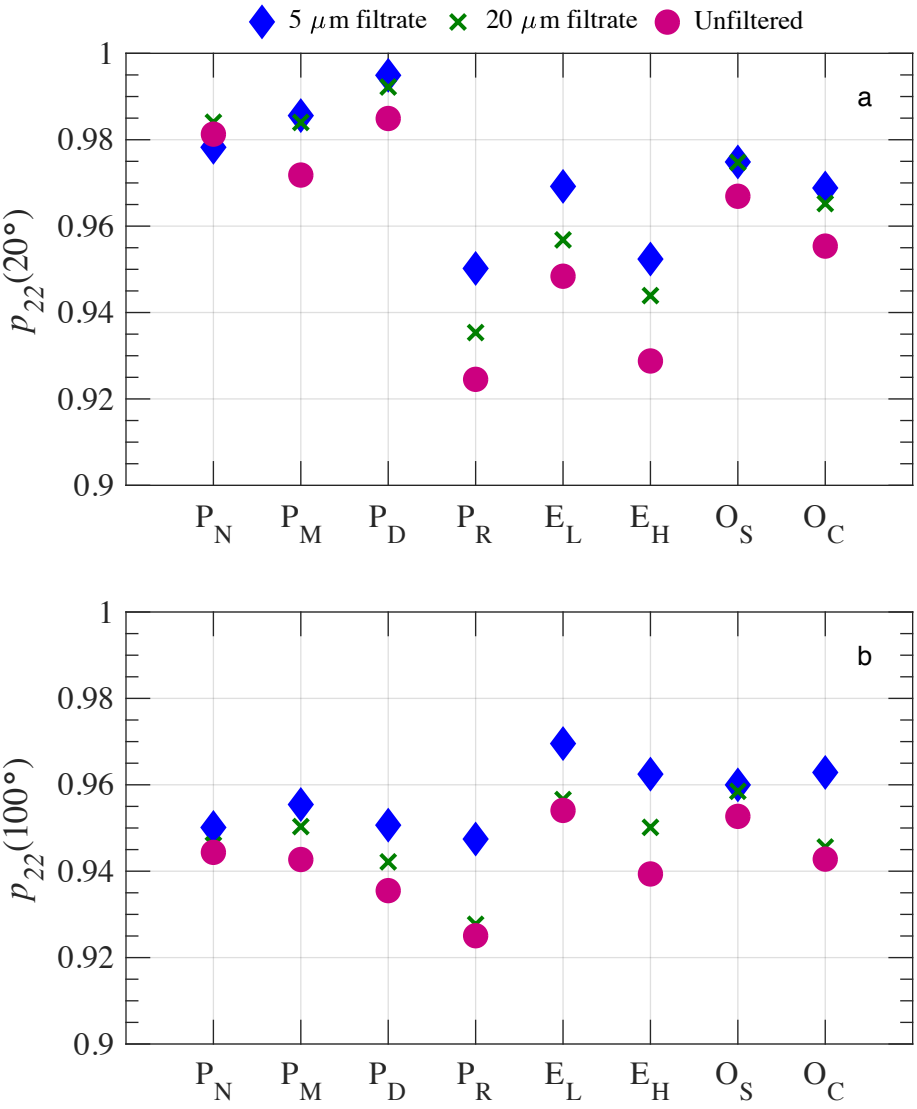

Figure 3.8. Measured values of $p_{22}(\psi)$ at (a) ψ = 20º and (b) ψ = 100º for unfiltered and size-fractionated samples of the eight seawater samples described in Chapter 2 (Table 2.1) as indicated.

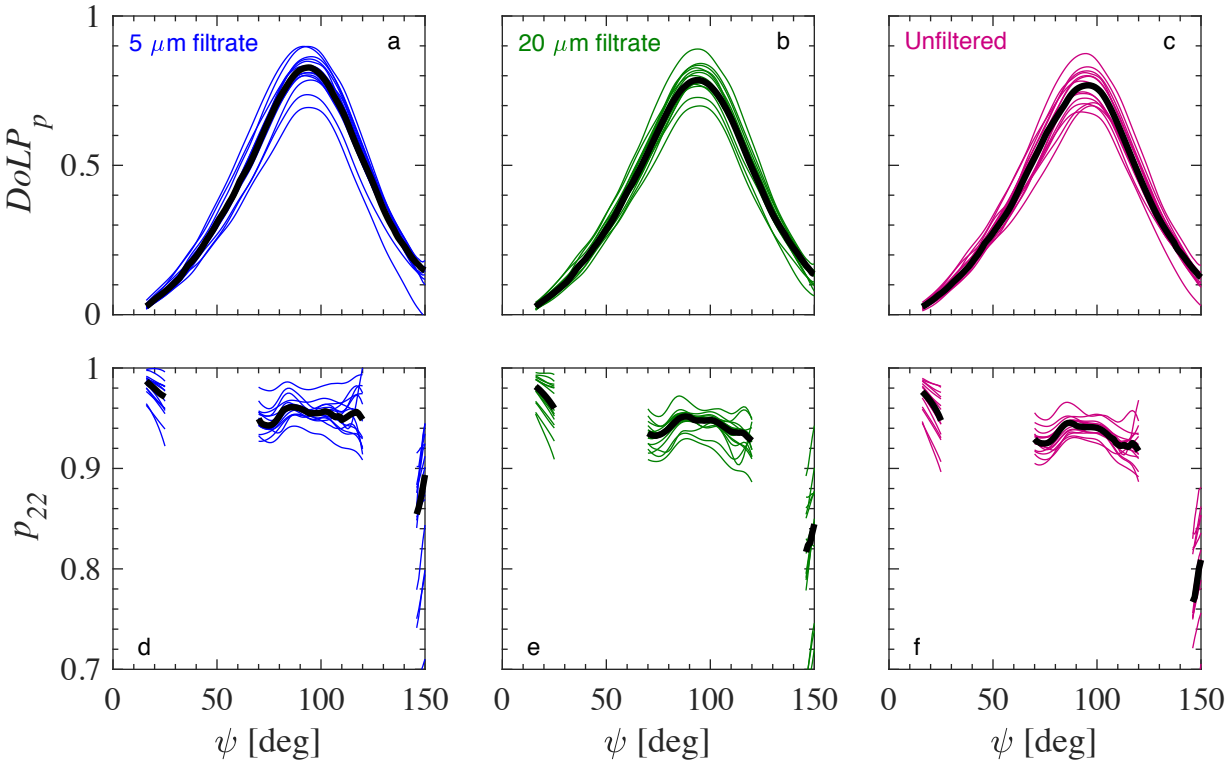

Figure 3.9. Measured (a–c) $DoLP_p(\psi)$ and (d–f) $p_{22}(\psi)$ for unfiltered and size-fractionated samples of all seawater samples as indicated in legend. Data for $p_{22}(\psi)$ is not plotted for ψ = 26–69º and ψ = 121–145º. After quality control of data from the sixteen seawater experiments, one 5 μm filtrate and one unfiltered seawater samples were removed thus (a,d) N = 15, (b,e) N = 16, and (c,f) N = 15. The solid black line indicates the median values of $DoLP_p(\psi)$ and $p_{22}(\psi)$ determined from all samples.

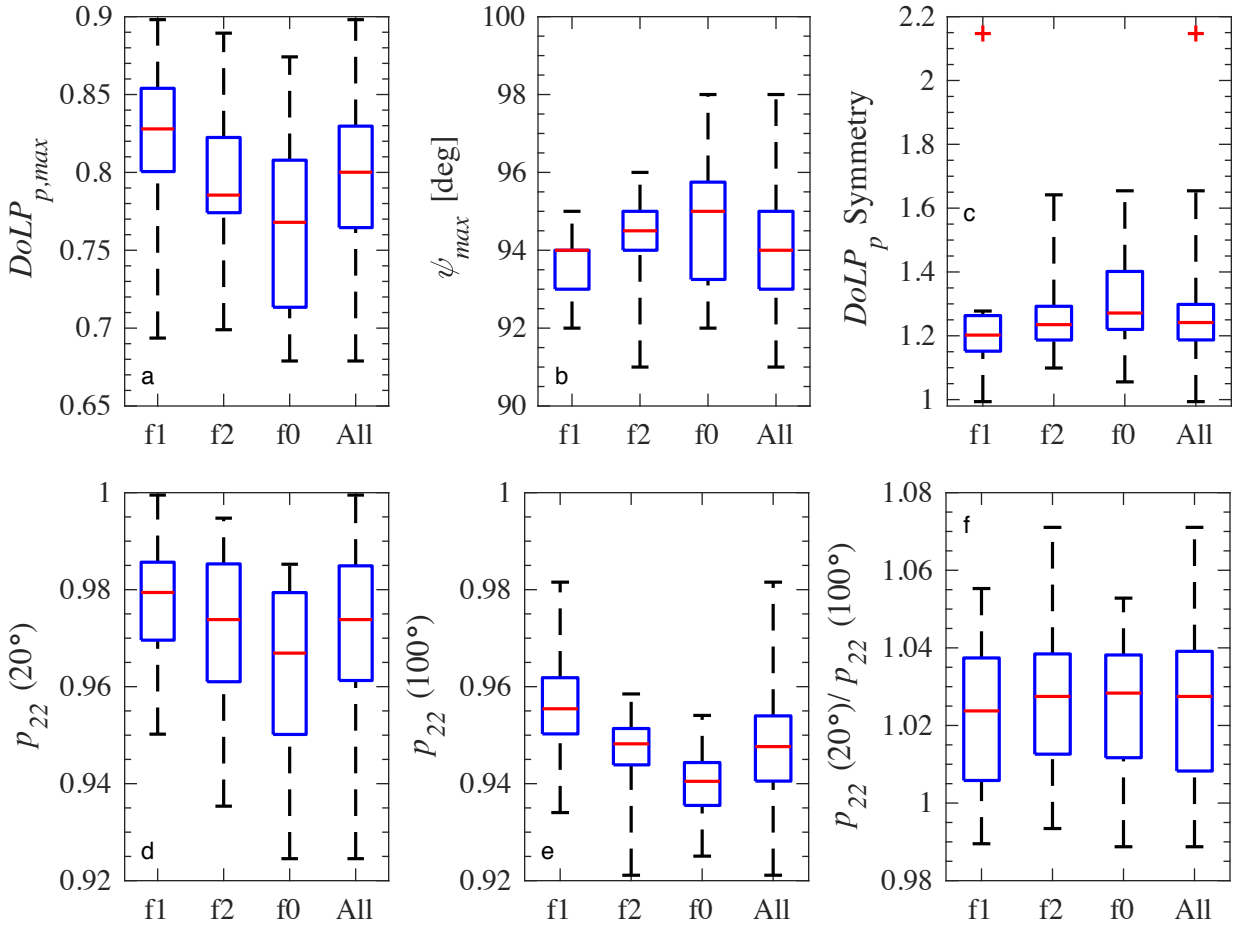

Figure 3.10. Box plots of polarized light scattering metrics derived from (a–c) $DoLP_p(\psi)$ and (d–f) $p_{22}(\psi)$ data shown in Fig. 3.9. Three box plots are shown in each panel as indicated with f1 for 5 µm filtrate, f2 for 20 µm filtrate, and f0 for unfiltered seawater, with a fourth box plot shown using all unfiltered and size-fractionated samples. Outliers are marked in panel c for being over 4 times the interquartile range from the third quartile.

Figure 3.11. Particle compositional parameters shown as a function of polarized light scattering metrics (a,c,e,g) $p_{22}(20°)$ and (b,d,f,i) $p_{22}(20°)/p_{22}(100°)$ from measurements with seawater samples. Data points are color coded by the value of D_v^{90} as indicated in legend. A type II linear regression is plotted with a black dashed line and the Pearson correlation coefficients and sample sizes are shown in Table 3.4.

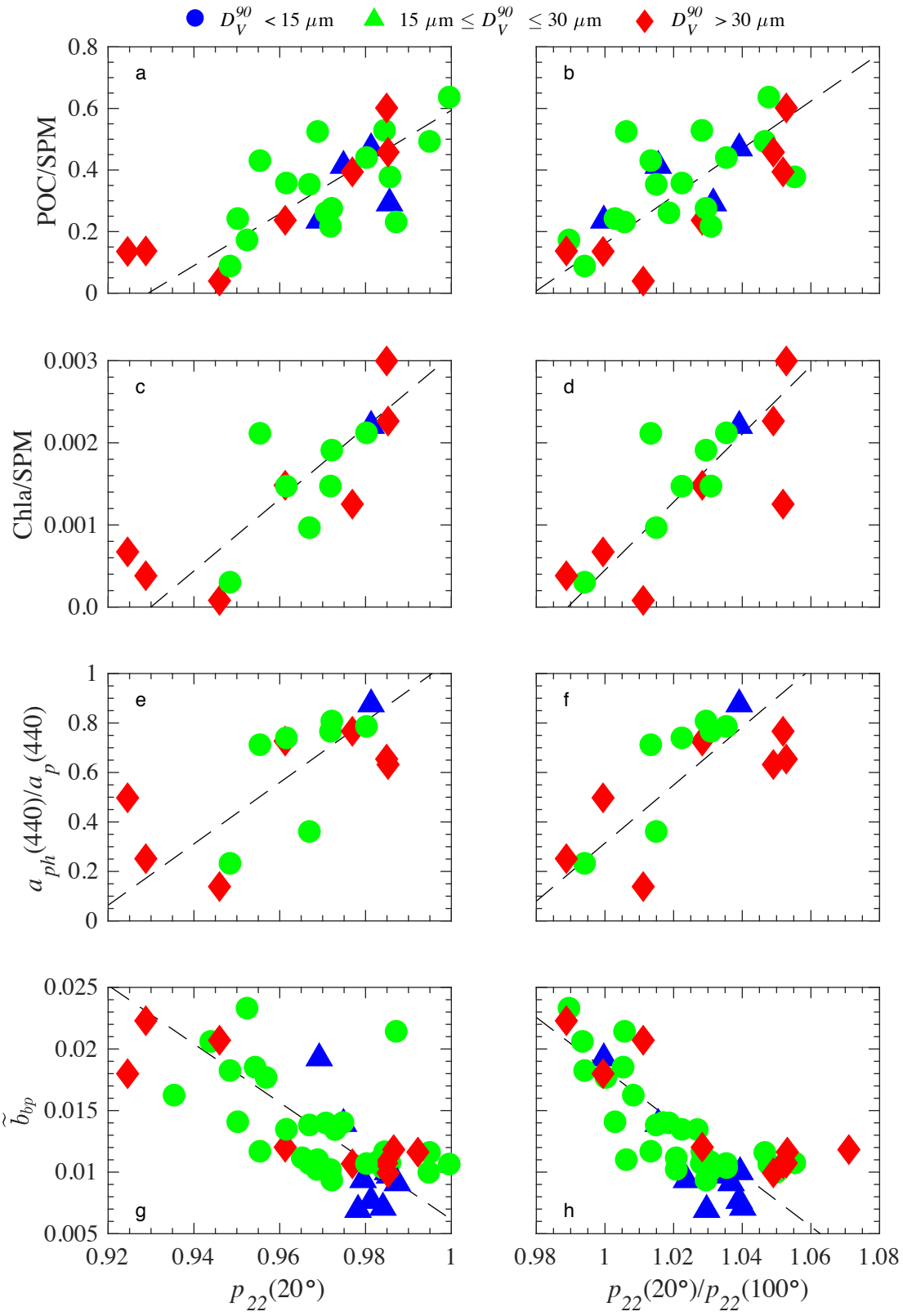

Figure 3.11. (Caption on previous page)

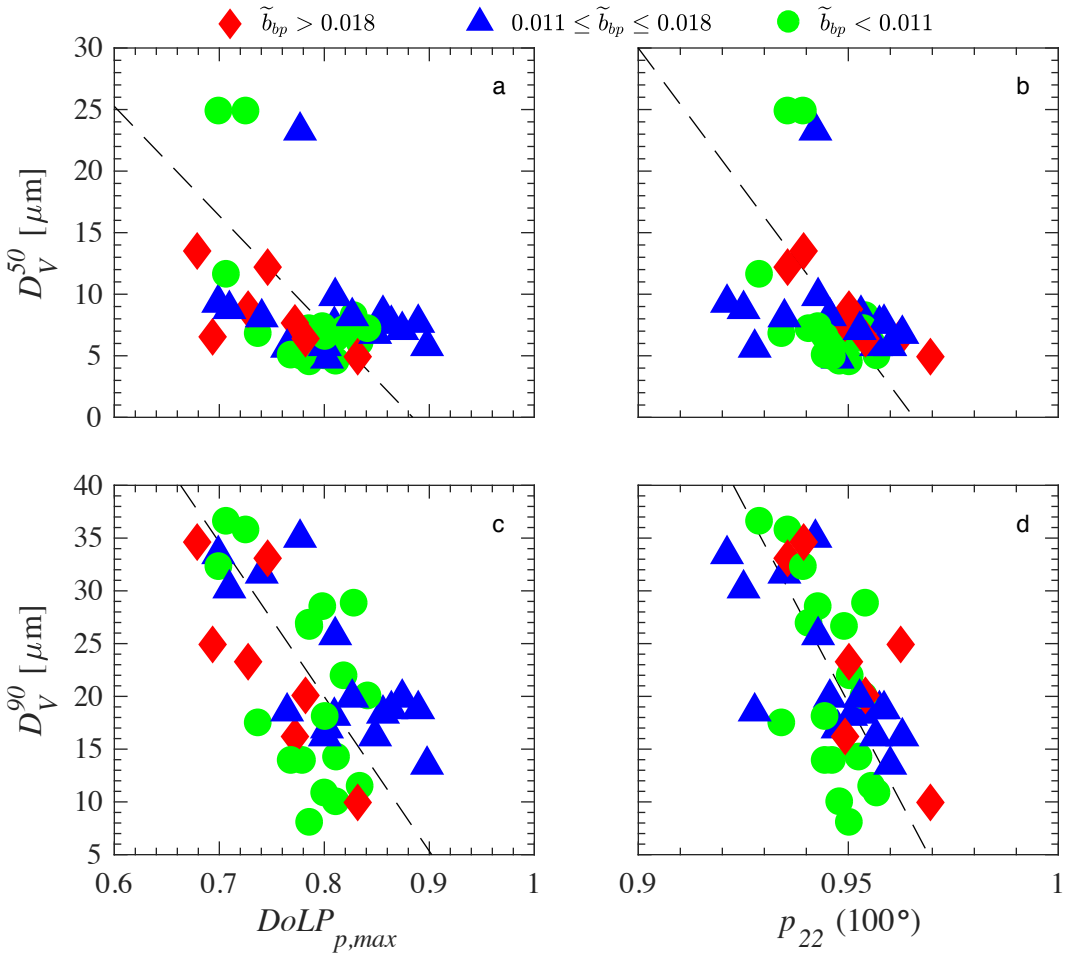

Figure 3.12. Particle size parameters shown as a function of polarized light scattering metrics (a,c) $DoLP_{p,max}$ and (b,d) $p_{22}(100°)$ obtained from measurements with seawater samples. Data points are color coded by the value of $\tilde{b}_{bp}$ as indicated in legend. A type II linear regression is plotted with a black dashed line and the Pearson correlation coefficients and sample sizes are shown in Table 3.4.

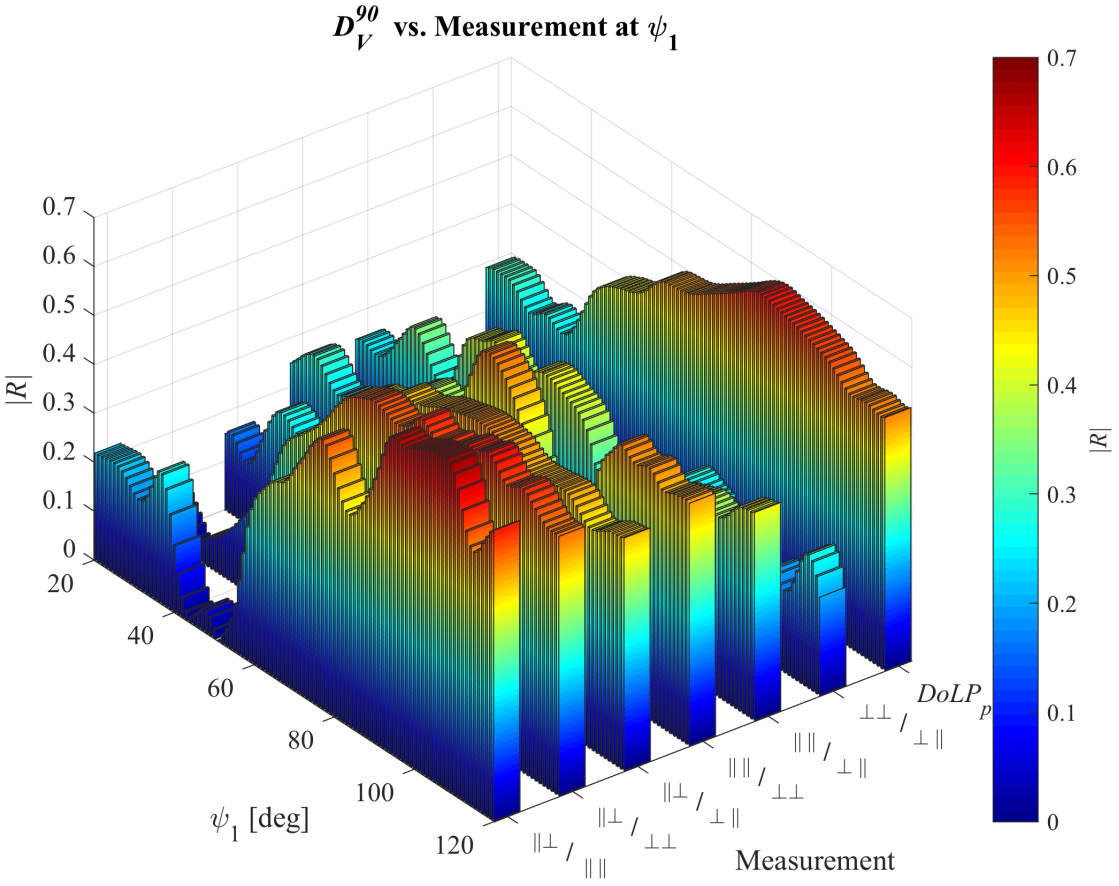

Figure 3.13. Results of the analysis of 707 datasets obtained from 41 seawater samples of particle size parameter D_v^{90} and 7 polarized light scattering measurement combinations. Each measurement is determined at ψ_1 and the symbols shown indicate the polarization state of incident light and scattered light detected. For example, $\parallel\perp/\parallel\parallel$ is equivalent to $\beta_p^{\parallel\perp}(\psi_1)/\beta_p^{\parallel\parallel}(\psi_1)$ where an incident parallel polarized beam is used in both the numerator and denominator but only perpendicularly polarized scattered light at ψ_1 is detected in the numerator and only parallel polarized scattered light at ψ_1 is detected in the denominator. Results are shown for the absolute value of the Pearson correlation coefficient, R.

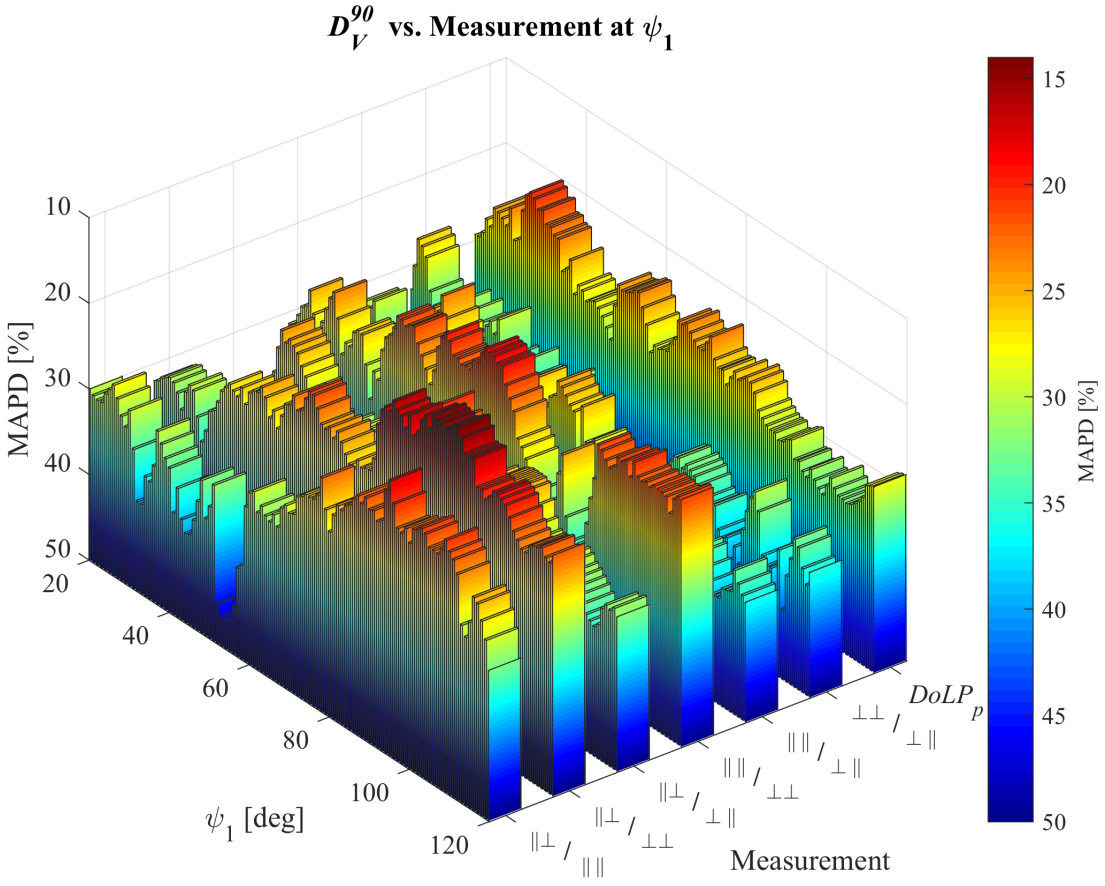

Figure 3.14. Similar to Fig. 3.13 except that results are shown for the median absolute percent difference, MAPD determined using type II linear regressions from each dataset.

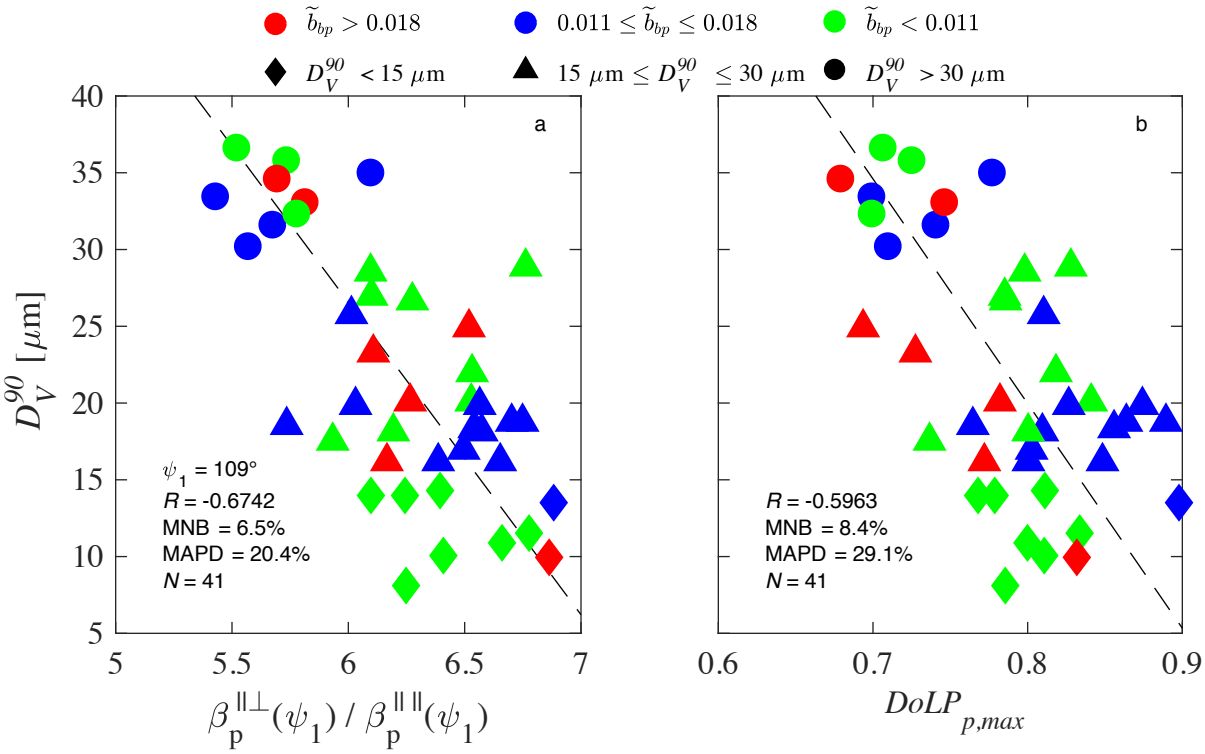

Figure 3.15. Particle size parameter D_v^{90} shown as a function of polarized light scattering metrics for seawater samples as indicated in legend by color and symbol in legend. The ideal solution determined with data in Fig. 3.13 and 3.14 is shown in (a), i.e., $\beta_p^{\parallel\perp}(\psi_1)/\beta_p^{\parallel\parallel}(\psi_1)$ with linear regression $D_v^{90} = -20.36\left(\beta_p^{\parallel\perp}(109°)/\beta_p^{\parallel\parallel}(109°)\right) + 149.7$. For comparison, $DoLP_{p,max}$ is shown in (b) with linear regression $D_v^{90} = -146.3\left(DoLP_{p,max}\right) + 137.0$. Statistical parameters from the linear regressions are displayed in each panel.

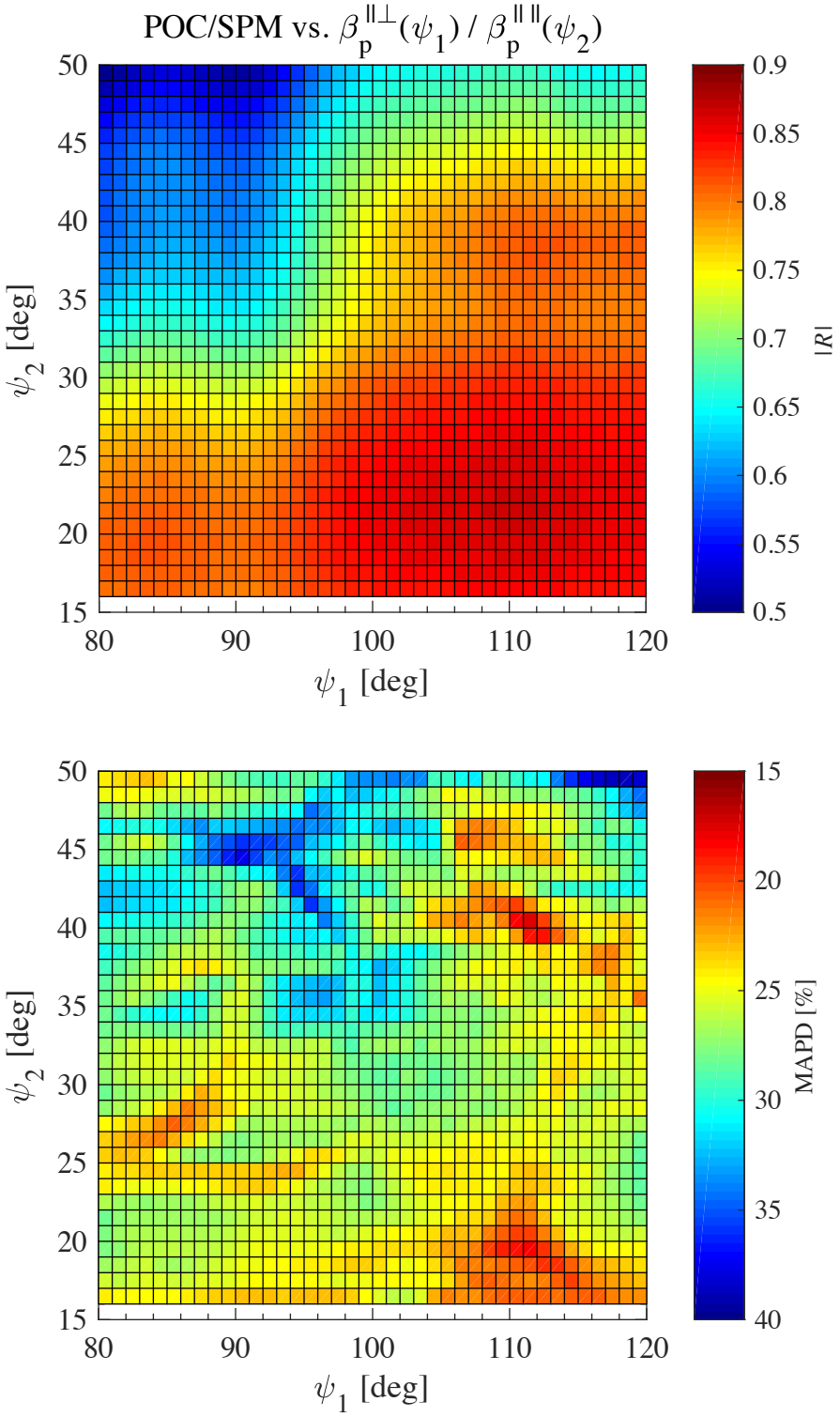

Figure 3.16. Results of the analysis of 1435 datasets obtained from 27 seawater samples of particle composition parameter POC/SPM and polarized light scattering metric $\beta_p^{\parallel\perp}(\psi_1)/\beta_p^{\parallel\parallel}(\psi_2)$. Type II linear regressions were determined for log-transformed data. Results are shown for the absolute value of the Pearson correlation coefficient, *R*, and the median absolute percent difference, MAPD.

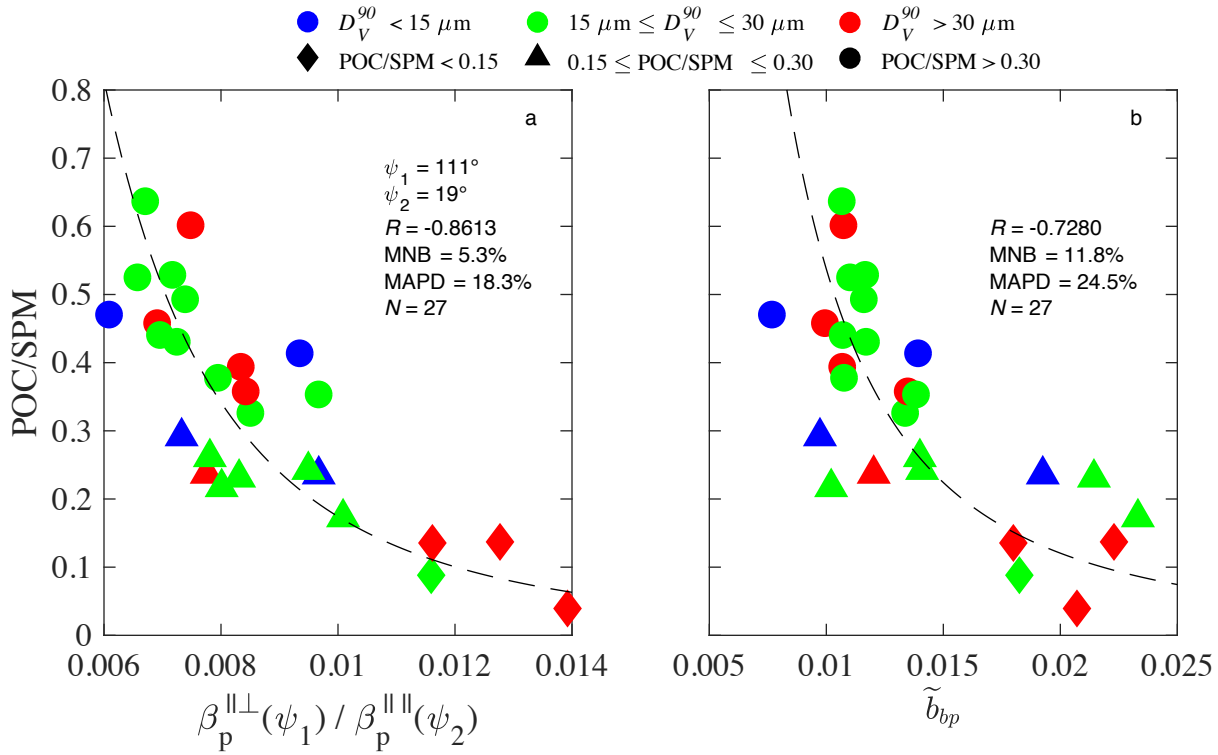

Figure 3.17. Particle composition parameter POC/SPM shown as a function of polarized light scattering metrics for seawater samples as indicated in legend by color and symbol. The ideal solution determined with data in Fig. 3.16 is shown in (a), i.e., $\beta_p^{\parallel\perp}(\psi_1)/\beta_p^{\parallel\parallel}(\psi_2)$ with linear regression POC/SPM $= 10^{-6.794}\left(\beta_p^{\parallel\perp}(111°)/\beta_p^{\parallel\parallel}(19°)\right)^{-3.02}$. For comparison, $\tilde{b}_{bp}$ is shown in (b) with linear regression POC/SPM $= 10^{-4.582}\left(\tilde{b}_{bp}\right)^{-2.16}$. Statistical parameters from the linear regressions are displayed in each panel.

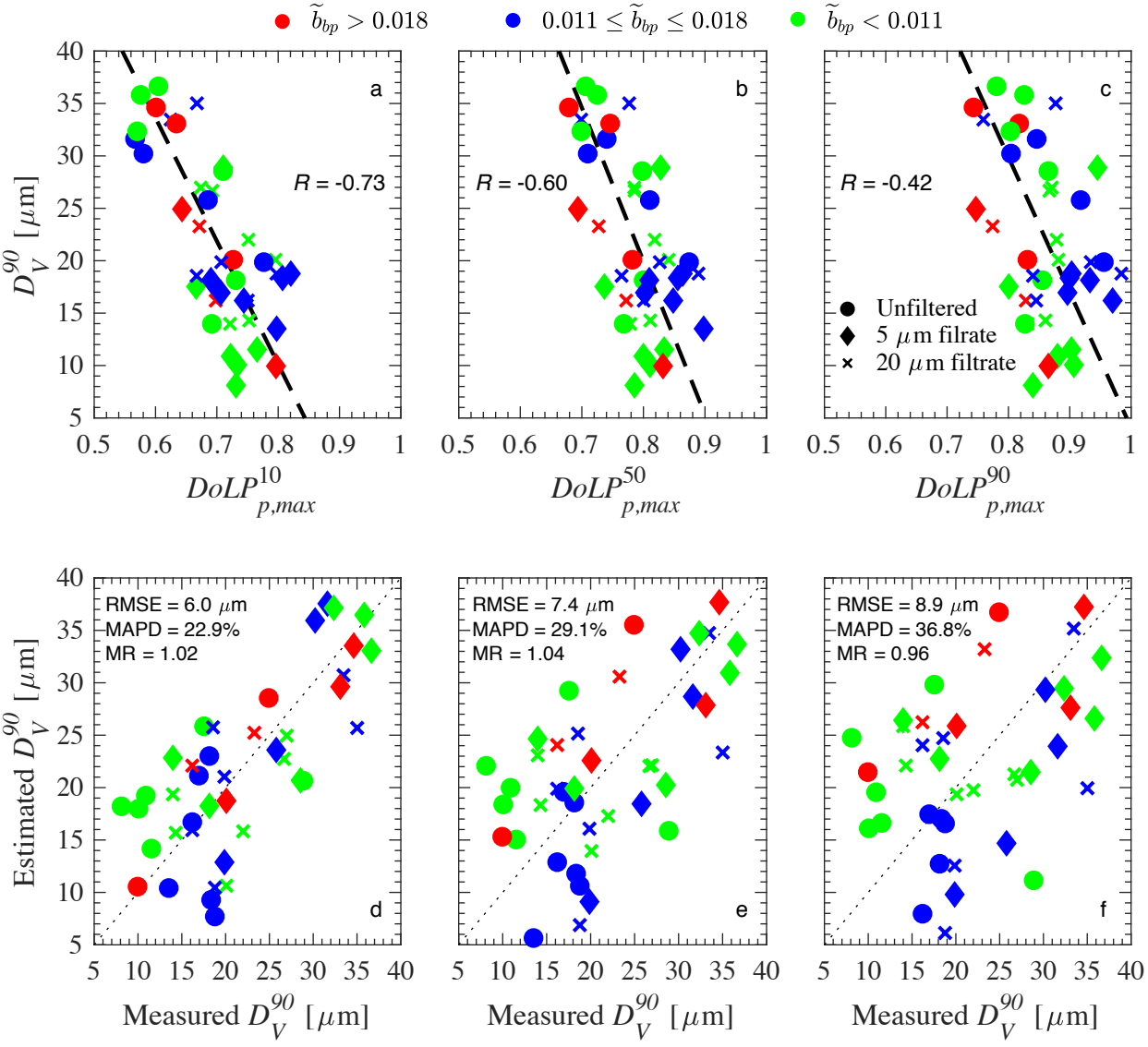

Figure 3.18. Particle size parameter D_v^{90} shown as a function (a) 10th percentile based $DoLP_{p,max}$ (b) 50th percentile based $DoLP_{p,max}$ and (c) 90th percentile based $DoLP_{p,max}$ and indicated by color and symbol in legend above and legend in panel c. Type II linear regressions are plotted with black dashed lines and Pearson correlation coefficient R is displayed in each panel. Equations for linear regressions are (a) $D_v^{90} = -117.5\left(DoLP_{p,max}^{10}\right) + 104.1$, (b) $D_v^{90} = -146.3\left(DoLP_{p,max}^{50}\right) + 137.0$ and (c) $D_v^{90} = -129.1\left(DoLP_{p,max}^{90}\right) + 133.1$. Bottom panels (d–f), show regression performance by comparing the estimated D_v^{90} using the regression from the panel above (a, b, and c, respectively) and the measured D_v^{90}. A 1:1 dotted line is plotted and statistical parameters are displayed in each panel.

3.7. Tables

Table 3.1. Table of measurement symbols and their description. All optical metrics at wavelength in vacuum λ = 532 nm unless otherwise stated.

Symbol	Description [units]
ψ	Scattering angle with 0 defined as direction of initial propagation [deg]
$\perp$ or $\parallel$	Indicates polarization perpendicular or parallel to scattering plane
$\beta_p(\psi)$	Particulate volume scattering function [m^{-1} sr^{-1}] (Eq. 3.17)
b_p	Particulate scattering coefficient [m^{-1}]; $2\pi \int_{0°}^{180°} \beta_p(\psi) \sin(\psi)\, d\psi$
b_{bp}	Particulate backscattering coefficient [m^{-1}]; $2\pi \int_{90°}^{180°} \beta_p(\psi) \sin(\psi)\, d\psi$
$\tilde{b}_{bp}$	Particulate backscattering ratio; b_{bp}/b_p
$DoLP_p(\psi)$	Degree of linear polarization of light scattered by particles (Eq. 3.18)
$DoLP_{p,max}$	Maximum value of $DoLP_p(\psi)$
ψ_{max}	Scattering angle of $DoLP_{p,max}$ [deg]
FWHM	The angular width of $DoLP_p(\psi)$ at half of $DoLP_{p,max}$ [deg]
$DoLP_p$ Symmetry	Symmetry of $DoLP_p(\psi)$ about ψ_{max}; $DoLP_p(\psi_{max} - 45°)/DoLP_p(\psi_{max} + 45°)$
$p_{22}(\psi)$	Normalized scattering matrix element row 2 column 2 (Eq. 3.19)
$a_p(\lambda)$ and $a_{ph}(\lambda)$	Spectral absorption coefficients of particles and phytoplankton [m^{-1}]
SPM	Dry mass concentration of suspended particulate matter [g m^{-3}]
POC	Particulate organic carbon mass concentration [mg m^{-3}]
Chla	Chlorophyll-a mass concentration [mg m^{-3}]
PSD	Particle size distribution [number or volume concentration]
D_v^{50} and D_v^{90}	50th and 90th percentile diameter of the cumulative volume PSD [µm]
$CF_f(\psi)$	Correction function for $\beta_p(\psi)$ from Chapter 1 (Fig. 1.4)
$BF_f(\psi)$	Bias function for $DoLP_p(\psi)$ from Chapter 1 (Fig. 1.5)
$CF2_f(\psi)$	Correction functions for polarized light scattering combinations (Fig. 3.2)

Table 3.2. Table of statistical symbols and their description.

Symbol	Description
N	Number of samples
x_i or y_i	Measured value for sample *i* of *N*
$\bar{x}$ or $\bar{y}$	Mean value; $\bar{x} = \frac{1}{N}\sum_{i=1}^{N} x_i$, and likewise for $\bar{y}$
$\hat{y}$	Predicted or reference value
R	Pearson correlation coefficient; $\frac{\sum_{i=1}^{N}(x_i-\bar{x})(y_i-\bar{y})}{\sqrt{\sum_{i=1}^{N}(x_i-\bar{x})^2}\sqrt{\sum_{i=1}^{N}(y_i-\bar{y})^2}}$
MAPD	Median absolute percent difference; 50th percentile of $\left\lvert\frac{\hat{y}_i-y_i}{y_i}\right\rvert \times 100\%$
MR	Median ratio; 50th percentile of $\frac{\hat{y}_i}{y_i}$
MNB	Mean normalized bias; $\left(\frac{1}{N}\sum_{i=1}^{N}\frac{\hat{y}_i-y_i}{y_i}\right) \times 100\%$
RMSE	Root mean square error; $\sqrt{\frac{1}{N}\sum_{i=1}^{N}(\hat{y}_i - y_i)^2}$
NRMSE	Normalized root mean square error; $\sqrt{\frac{1}{N}\sum_{i=1}^{N}(\frac{\hat{y}_i-y_i}{\hat{y}_i})^2} \times 100\%$

Table 3.3. Values of optical quantities derived from LISST-VSF measurements for the three example natural seawater samples depicted in Figure 3.6 for both correction schemes, i.e., CF_f from Koestner et al. 2018 and newly developed $CF2_f$. Values of selected optical quantities estimated from the measurements of Petzold (1972) are shown for comparison.

ID		b_p	b_{bp}	$\tilde{b}_{bp}$	$\frac{\beta_p(45°)}{\beta_p(135°)}$	ψ_{min}	$DoLP_{p,max}$	ψ_{max}	FWHM	$DoLP_p$ symmetry	$p_{22}(20°)$	$p_{22}(100°)$	$\frac{p_{22}(20°)}{p_{22}(100°)}$
O_C	Koestner et al 2018	0.35	0.0042	0.0117	16.50	146	0.73	94	74	1.28	-	-	-
	$CF2_f$	0.36	0.0041	0.0115	16.29	146	0.81	94	67	1.42	0.96	0.94	1.01
P_N	Koestner et al 2018	1.73	0.0133	0.0077	17.15	130	0.68	97	73	1.18	-	-	-
	$CF2_f$	1.74	0.0129	0.0074	17.02	125	0.77	96	66	1.24	0.98	0.94	1.04
E_H	Koestner et al 2018	2.20	0.0493	0.0225	11.93	134	0.57	92	75	1.28	-	-	-
	$CF2_f$	2.20	0.0476	0.0217	11.94	130	0.68	92	66	1.44	0.93	0.94	0.99
Petzold	Clear	0.03	0.0005	0.0151	18.01	140	-	-	-	-	-	-	-
	Coastal	0.19	0.0018	0.0094	17.83	130	-	-	-	-	-	-	-
	Turbid	1.74	0.0352	0.0202	12.25	150	-	-	-	-	-	-	-

Table 3.4. Grid of Pearson correlation coefficients, *R*, determined from optical and particle size and composition metrics. Grids are color coded with red indicating weak correlation ($|R| < 0.30$), orange indicating moderate correlation ($0.30 \leq |R| < 0.60$), and green indicating strong correlation ($|R| \geq 0.60$). The strong correlation values are bolded and the number of samples, *N*, which have data for both variables is displayed.

	$\tilde{b}_{bp}$	POC/SPM	Chla/SPM	$a_{ph}(440)/a_p(440)$	D_v^{50}	D_v^{90}
$DoLP_{p,max}$	-0.17	0.25	0.12	0.18	-0.42	**-0.60**
ψ_{max}	-0.44	0.27	0.38	0.44	0.23	0.20
FWHM	0.22	0.02	-0.37	-0.39	-0.08	-0.25
$DoLP_p$ Symmetry	0.54	-0.31	-0.30	-0.28	0.16	0.35
$p_{22}(20°)$	**-0.67**	**0.73**	**0.79**	**0.66**	0.12	-0.17
$p_{22}(100°)$	0.20	0.05	0.03	-0.11	-0.38	**-0.62**
$p_{22}(20°)/p_{22}(100°)$	**-0.76**	**0.68**	**0.78**	**0.71**	0.33	0.20
$\tilde{b}_{bp}$	**1.00**	**-0.70**	**-0.85**	**-0.90**	0.01	0.20
N	46	27	15	15	41	41

3.8. Appendix

3.8.1. Derivation of p_{22}

First eyeball rotation (incident beam polarized perpendicular)

$$I_s^{\perp\parallel} = p_{11} - p_{12} + \cos 2\psi(p_{12} - p_{22}) \tag{3.S1}$$

$$I_s^{\perp\perp} = \alpha[p_{11} - p_{12} - \cos 2\psi(p_{12} - p_{22})] \tag{3.S2}$$

Second eyeball rotation (incident beam polarized parallel)

$$I_s^{\parallel\parallel} = p_{11} + p_{12} + \cos 2\psi(p_{12} + p_{22}) \tag{3.S3}$$

$$I_s^{\parallel\perp} = \alpha[p_{11} + p_{12} - \cos 2\psi(p_{12} + p_{22})] \tag{3.S4}$$

Objective is to solve for p_{22}. There are two methods by which this can be accomplished, using equations (3.S1) and (3.S3), and (3.S2) and (3.S4), respectively.

3.8.2. Parallel solution

This method solves for p_{22} using the parallel detector; the solution is a function of p_{11}, $I_s^{\perp\parallel}$ and $I_s^{\parallel\parallel}$. Additionally, note that $I_s^{\perp\perp}$, $I_s^{\perp\parallel}$, $I_s^{\parallel\perp}$, and $I_s^{\parallel\parallel}$ are all functions of ψ.

First solve (3.S1) for p_{12}:

$$I_s^{\perp\parallel} - p_{11} = \cos 2\psi(p_{12} - p_{22}) - p_{12}$$

$$I_s^{\perp\parallel} - p_{11} = p_{12}\cos 2\psi - p_{22}\cos 2\psi - p_{12}$$

$$p_{12}(\cos 2\psi - 1) = I_s^{\perp\parallel} - p_{11} + p_{22}\cos 2\psi$$

$$p_{12} = \frac{I_s^{\perp\parallel} - p_{11} + p_{22}\cos 2\psi}{\cos 2\psi - 1}$$

Plug result for p_{12} into equation (3.S3):

$$I_s^{\|\|} = p_{11} + \frac{I_s^{\perp\|} - p_{11} + p_{22}\cos 2\psi}{\cos 2\psi - 1} + \cos 2\psi(\frac{I_s^{\perp\|} - p_{11} + p_{22}\cos 2\psi}{\cos 2\psi - 1} + p_{22})$$

$$I_s^{\|\|} = p_{11} + \frac{I_s^{\perp\|} - p_{11} + p_{22}\cos 2\psi}{\cos 2\psi - 1} + \cos 2\psi(\frac{I_s^{\perp\|} - p_{11} + p_{22}\cos 2\psi}{\cos 2\psi - 1}) + p_{22}\cos 2\psi$$

$$I_s^{\|\|} = p_{11} + \frac{I_s^{\perp\|} - p_{11} + p_{22}\cos 2\psi + I_s^{\perp\|}\cos 2\psi - p_{11}\cos 2\psi + p_{22}cos^2 2\psi}{\cos 2\psi - 1} + p_{22}\cos 2\psi$$

$$I_s^{\|\|} = \frac{I_s^{\perp\|} + I_s^{\perp\|}\cos 2\psi - 2p_{11} + 2p_{22}\cos^2 2\psi}{\cos 2\psi - 1}$$

$$I_s^{\|\|}\cos 2\psi - I_s^{\|\|} = I_s^{\perp\|} + I_s^{\perp\|}\cos 2\psi - 2p_{11} + 2p_{22}\cos^2 2\psi$$

Note that α can be redistributed as it is a constant describing relative intensity between the two PMT detectors. Thus, for consistency with processing code:

$$p_{22} = \frac{2p_{11} - \alpha[(I_s^{\perp\|} + I_s^{\perp\|}\cos 2\psi) + (I_s^{\|\|} - I_s^{\|\|}\cos 2\psi)]}{2\cos^2 2\psi}$$

3.8.3. Perpendicular solution

A likewise solution exists for the perpendicular detector, which gives:

$$p_{22} = \frac{2p_{11} - [(I_s^{\|\perp} + I_s^{\|\perp}\cos 2\psi) + (I_s^{\perp\perp} - I_s^{\perp\perp}\cos 2\psi)]}{2\cos^2 2\psi}$$

3.9. References

Beardsley, G. F. Jr., 1986. Mueller Scattering Matrix of Sea Water. J. Opt. Soc. Am. **58**: 52.

Bohren, C. F. and D. R. Huffman. Absorption and Scattering of Light by Small Particles; Wiley: New York, NY, USA, 1983.

Boss, E. and W. S. Pegau. 2001. Relationship of light scattering at an angle in the backward direction to the backscattering coefficient. Appl. Opt. **40**: 5503–5507.

Boss, E., Pegau, W. S., Lee, M., Twardowski, M., Shybanov, E., Korotaev, G., and F. Baratange. 2004. Particulate backscattering ratio at LEO 15 and its use to study particle composition and distribution. J. Geophys. Res. **109**: C01014, doi:10.1029/2002JC001514.

Briggs, N. T., W. H. Slade, E. Boss, and M. J. Perry. 2013. Method for estimating mean particle size from high-frequency fluctuations in beam attenuation or scattering measurements. Appl. Opt. **52**: 6710–6725.

Chami, M. Importance of the polarization in the retrieval of oceanic constituents from the remote sensing reflectance. J. Geophys. Res. 2007, **112**: C05026, doi:10.1029/2006JC003843.

Claustre, H., J. Bishop, E. Boss, B. Stewart, J. F. Berthon, C. Coatanoan, K. Johnson, A. Lotiker, O. Ulloa, M. J. Perry, F. D'Ortenzio, O. Hembise Fanton D'Andon, and J. Uitz. 2010. Bio-optical profiling floats as new observational tools for biogeochemical and ecosystem studies: Potential synergies with ocean color remote sensing, in Proceedings of OceanObs'09: Sustained Ocean Observations and Information for Society (Vol. 2), Venice, Italy, 21–25 Sept. 2009, ESA Publ. WPP-306, edited by J. Hall, D. E. Harrison, and D. Stammer, 7 pp., Eur. Space Agency, Rome,

Dubovik, O., Z. Li, M. I. Mishchenko, D. Tanré, Y. Karol, B. Bojkov, B. Cairns, D. J. Diner, W. R. Espinosa, P. Goloub, X. Gu, O. Hasekamp, J. Hong, W. Hou, K. D. Knobelspiesse, J. Landgraf, L. Li, P. Litvinov, Y. Liu, A. Lopatin, T. Marbach, H. Maring, V. Martins, Y. Meijer, G. Milinevsky, S. Mukai, F. Parol, Y. Qiao, L. Remer, J. Rietjens, I. Sano, P. Stammes, S. Stamnes, X. Sun, P. Tabary, L. D. Travis, F. Waquet, F. Xu, C. Yan, and D. Yin. 2019. Polarimetric remote sensing of atmospheric aerosols: Instruments, methodologies, results, and perspectives. J. Quant. Spectrosc. Radiat. Transf. **224**: 474–511.

Flamarique, I. N. and C. W. Hawryshyn. 1996. Is the use of underwater polarized light by fish restricted to crepuscular time periods? Vision Res. **37**: 975–989.

von Frisch, K. 1952. Orienting Ability and Communication Among Bees, Bee World, 33:2, 19-25.

Fry, E. S., and K. J. Voss. 1985. Measurement of the Mueller matrix for phytoplankton. Limnol. Oceanogr. **30**: 1322–1326.

Guay, C.K. and J. K. Bishop. 2002. A rapid birefringence method for measuring suspended CaCO3 concentrations in water, Deep Sea Res., Part I, **49**: 197–210.

Hasekamp, O. P., G. Fu, S. P. Rusli, L. Wu, A. D. Noia, J. aan de Brugh, J. Landgraf, J. M. Smit, J. Rietjens, and A. van Amerongen. 2019. Aerosol measurements by SPEXone on the NASA PACE mission: expected retrieval capabilities. J. Quant. Spectrosc. Radiat. Transf. **227**: 170–184.

Hovenier, J. W., H. C. van de Hulstm and C. V. M. van der Mee. 1985. Conditions for the elements of the scattering matrix. Astron. Astrophys. **157**: 301–310.

Hovenier, J. W., H. Volten, O. Muñoz, W. J. Van der Zande, and L. B. F. M. Waters. 2002. Laboratory studies of scattering matrices for randomly oriented particles: Potentials, problems, and perspectives. J. Quant. Spectrosc. Radiat. Transf. **79**: 741–755.

van de Hulst, H. C. 1981. Light scattering by small particles, John Wiley & Sons.

Ibrahim, A., A. Gilerson, J. Chowdhary, and S. Ahmed. 2016. Retrieval of macro- and micro-physical properties of oceanic hydrosols from polarimetric observations. Rem. Sens. Environ. **186**: 548–566.

Jonasz, M., and G. Fournier. 2007. Light scattering by particles in water: Theoretical and experimental foundations. Elsevier.

Kadyshevich, Y. A. 1977. Light-Scattering Matrices of Inshore Waters of the Baltic Sea. Izv. Acad. Sci. USSR Atmos. Oceanic Phys. **13**: 77.

Kokhanovsky, A.A. 2003. Parameterization of the Mueller matrix of oceanic waters. J. Geophys. Res. **108**: 3175, doi:10.1029/2001JC001222.

LISST-VSF Multi-angle polarized light scattering meter: User's manual revision A; Sequoia Scientific: Bellevue, WA, USA

Loisel, H., L. Duforet, D. Dessailly, M. Chami, and P. Dubuisson. 2008. Investigation of the variations in the water leaving polarized reflectance from the POLDER satellite data over two biogeochemical contrasted oceanic areas. Opt. Express **16**: 12905–12918.

Mishchenko, M. I. and L. D. Travis. 1994. Light scattering by polydisperse, rotationally symmetric nonspherical particles: linear polarization. J. Quant. Spectrosc. Radiat. Transf. **51**: 759–778.

Mishchenko, M. I., J. W. Hovenier, and L. D. Travis, Eds., 2000: Light Scattering by Nonspherical Particles: Theory, Measurements, and Applications, Academic Press, San Diego.

Mobley, C. D. 1994. Light and water: Radiative transfer in natural waters. Academic Press.

Muñoz, O., F. Moreno, D. Guirado, D. D. Dabrowska, H. Volten, and J. W. Hovenier. 2012. The Amsterdam–Granada light scattering database. J. Quant. Spectrosc. Radiat. Transf. **113**: 565–574.

Organelli, E., M. Barbieux, H. Claustre, C. Schmechtig, A. Poteau, A. Bricaud, E. Boss, N. Briggs, G. Dall'Olmo, F. D'Ortenzio, E. Leymarie, A. Mangin, G. Obolensky, C. Penkerc'h, L. Prieur, C. Roesler, R. Serra, J. Uitz, and X. Xing. 2017. Two databases derived from BGC-Argo float measurements for marine biogeochemical and bio-optical applications. Earth Syst. Sci. Data **9**: 861–880.

Petzold, T. J. 1972. Volume Scattering Functions for Selected Ocean Waters. SIO Ref. 72–78, Scripps Institution of Oceanography Visibility Lab: University of California, San Diego, CA, USA,1972.

Ricker, W. E. 1973. Linear regressions in fishery research. J. Fish. Res. Board Can. **30**: 409–434.

Reynolds, R. A., D. Stramski, and G. Neukermans. 2016. Optical backscattering by particles in Arctic seawater and relationships to particle mass concentration, size distribution, and bulk composition. Limnol. Oceanogr. **61**: 1869–1890, doi:10.1002/lno.10341.

Svensen, Ø., J. J. Stamnes, M. Kildemo, L. M. S. Aas, S. R. Erga, and Ø Frette. 2011. Mueller matrix measurements of algae with different shape and size distributions. Appl. Opt. **50**: 5149–5157.

Timofeeva, V. A. 1974. Optics of turbid waters (results of laboratory studies). In Jerlov, N. and Steeman Nielsen, E. (Eds), Optical aspects of oceanography (pp 177–218). New York: Academic Press.

Twardowski, M. S., E. Boss, J. B. Macdonald, W. S. Pegau, A. H. Barnard, and J. R. V. Zaneveld. 2001. A model for estimating bulk refractive index from the optical backscattering ratio and the implications for understanding particle composition in case I and case II waters. J. Geophys. Res. **106**: 14129–14142.

Volten, H., J. F. De Haan, J. W. Hovenier, R. Schreurs, W. Vassen, A. G. Dekker, H. J. Hoogenboom, F. Charlton, and R. Wouts. 1998. Laboratory measurements of angular distributions of light scattered by phytoplankton and silt. Limnol. Oceanogr. **43**: 1180–1197

Volten, H., O. Muñoz, E. Rol, J. D. Haan, W. Vassen, J. W. Hovenier, and T. Nousiainen. 2001. Scattering matrices of mineral aerosol particles at 441.6 nm and 632.8 nm. J. Geophys. Res. **106**: 17375–17401.

Voss, K. J. and E. S. Fry. 1984. Measurement of the Mueller matrix for ocean water. Appl. Opt. **23**: 4427–4439.

Waterman, T. H. 1954. Polarization patterns in submarine illumination. Science **120**: 927–932.

Waterman, T. H. 1981. Polarization sensitivity. In Autrum, H. (Ed.), Handbook of sensory physiology, Vol VII/6B, pp. 281–469. Berlin, Heidelberg, New York: Springer.

Waterman, T. H. and W. E. Westell. 1956. Quantative effect of the sun's position on submarine light polarization. J. Mar. Res. **15**: 149–169.

Woźniak, S. B., D. Stramski, M. Stramska, R. A. Reynolds, V. M. Wright, E. Y. Miksic, M. Cichocka, and A. M. Cieplak. 2010. Optical variability of seawater in relation to particle concentration, composition, and size distribution in the nearshore marine environment at Imperial Beach, California. J. Geophys. Res. **115**: C08027.

Yanamandra-Fisher, P. A. and M. S. Hanner. 1999. Optical properties of nonspherical particles of size comparable to the wavelength of light: Application to comet dust. Icarus **138**: 107–128.

Zubko, E. 2012. Light scattering by irregularly shaped particles with sizes comparable to the wavelength. In Light Scattering Reviews 6; Kokhanovsky, A.A., Ed.; Springer: Berlin, Germany, 2012; pp. 39–74.